

UNIVERSITÀ DELLA CALABRIA



UNIVERSITA' DELLA CALABRIA

Dipartimento di Ingegneria per l'Ambiente e il Territorio e Ingegneria Chimica

Dottorato di Ricerca in

Scienze e Ingegneria dell'Ambiente, delle Costruzioni e dell'Energia (SIACE)

CICLO XXXI

Preparazione e caratterizzazione di fotocatalizzatori per la valorizzazione del CO₂ in reattori a membrana

Settore Scientifico Disciplinare CHIM/07

Coordinatore:

Ch.mo Prof. Salvatore Critelli

Firma 

Supervisore/Tutor: Ch.mo Prof. Giuseppe Marci

Firma 

Ch.mo Prof. Giuseppe Barbieri

Firma 

Ch.mo Prof. Raffaele Molinari

Firma 

Dottoranda: Dott.ssa Francesca Rita Pomilla

Firma 



Department of Environmental and Chemical Engineering, DIATIC

Doctorate School in Environmental Sciences and Engineering, of
Buildings and Energy (SIACE) XXXI Cycle

SSD CHIM/07

Ph.D. thesis

**Preparation and Characterisation of Photocatalysts for
CO₂ valorisation in Membrane Reactors**

Tutors

Professor Giuseppe Marcì
Engineer Giuseppe Barbieri
Professor Raffaele Molinari

Ph.D. Student

Francesca Rita Pomilla
Matr. 030664

Summary

Abstract.....	5
Sommario.....	10
Outline	15
Chapter 1 The Environmental problem and CO ₂ valorisation	16
1.1 Aim of this dissertation.....	17
1.2 The Environmental problem	19
1.3 CO ₂ utilization: conversion to high added value compounds.....	21
1.3.1 Activation of CO ₂	23
1.3.2 Methods	24
1.4 Photocatalytic reduction of CO ₂	32
1.4.1 Basic principles of photocatalysis.....	32
1.4.2 Photocatalytic reduction of CO ₂ : Overview	40
1.4.3 Photocatalytic reduction of CO ₂ : Metal oxide materials, TiO ₂ and ZrO ₂	44
1.4.4 Photocatalytic reduction of CO ₂ : Graphene composite materials.....	49
1.4.5 Photocatalytic reduction of CO ₂ by C ₃ N ₄ pristine, O doped and composite TiO ₂ /g-C ₃ N ₄	53
1.4.6 Photocatalytic Reactors for CO ₂ reduction: batch vs continuous	59
1.5 Photocatalytic Membrane Reactor.....	64
1.5.1. Membrane reactors: basic principles and applications	64
1.5.2 Photocatalytic membrane reactor for CO ₂ reduction.....	73
Chapter 2 Experimental section.....	75
2.1 Material and Methods	76
2.2 Material synthesis	76
2.2.1 ZrO ₂ based materials.....	76
2.2.2 G/TiO ₂ composites.....	77

2.2.3	Pristine and base g-C ₃ N ₄ materials	78
2.2.4	g-C ₃ N ₄ pure and O doped materials and their immobilization: g-C ₃ N ₄ , O _R -C ₃ N ₄ and O _T -C ₃ N ₄	78
2.2.5	Pristine Nafion and photocatalytic C ₃ N ₄ and C ₃ N ₄ -TiO ₂ Membranes	79
2.3	Materials characterizations	80
2.3.1	Powder characterizations.....	80
2.3.2	Characterisations of supported materials.....	81
2.3.3	Characterization of membranes	82
Chapter 3	Results and discussion.....	83
3.1	Doped and pristine ZrO ₂ for CO ₂ photoreduction	84
3.1.1	Photocatalytic test conditions	84
3.1.2	Characterisation of ZrO ₂ based materials	85
3.1.3	Photocatalytic activity study	94
3.1.4	Conclusion	99
3.2	G/TiO ₂ composites for CO ₂ photoreduction	100
3.2.1	Photocatalytic test conditions	100
3.2.2	Characterization of G/TiO ₂ materials	100
3.2.3	Photocatalytic activity of G/TiO ₂ samples.....	105
3.2.4	Conclusion	110
3.3	O-doped and pristine C ₃ N ₄ : structural changes after use for CO ₂ photoreduction.	111
3.3.1	Photocatalytic test conditions	111
3.3.2	Characterisations of pure and O doped C ₃ N ₄ materials.....	113
3.3.3	Photocatalytic tests	116
3.3.4	Conclusion	131
3.4	Photocatalytic CO ₂ reduction in continuous membrane reactor: C ₃ N ₄ Nafion membrane.....	133

3.4.1	C ₃ N ₄ powder	133
3.4.1.1	Powder characterisation	133
3.4.1.2	Preliminary powder photocatalytic test condition and results	136
3.4.2	Photocatalytic membrane test conditions	137
3.4.3	Characterisations of C ₃ N ₄ -Nafion membrane	140
3.4.4	Results and discussions	142
3.4.5	Conclusion	153
3.5	Photocatalytic CO ₂ reduction in continuous membrane reactor: C ₃ N ₄ -TiO ₂ /Nafion membrane.....	155
3.5.1	C ₃ N ₄ -TiO ₂ powder.....	155
3.5.1.1	Powder characterization.....	155
3.5.1.2	Preliminary photocatalytic tests: experimental conditions and results by using C ₃ N ₄ -TiO ₂ photocatalyst.....	158
3.5.2	Photocatalytic membrane test conditions	160
3.5.3	Characterisation of C ₃ N ₄ -TiO ₂ /Nafion membrane	162
3.5.4	Results and discussions	164
3.5.5	Conclusion.....	173
	Conclusions.....	175
	Appendix A. Publications	177
	Appendix B. Training <i>Ph.D</i> school activity	180
	Acknowledgements.....	183
	Index Figure.....	185
	References.....	191

*Only the chemist can tell, and not always the chemist,
what will result from compounding
Fluids or solids.
And who can tell
How men and women will interact
On each other, or what children will result?
There were Benjamin Pantier and his wife,
Good in themselves, but evils toward each other:
He oxygen, she hydrogen,
Their son, a devastating fire.
I Trainor, the druggist, a mixer of chemicals,
Killed while making an experiment,
Lived unwedded.*

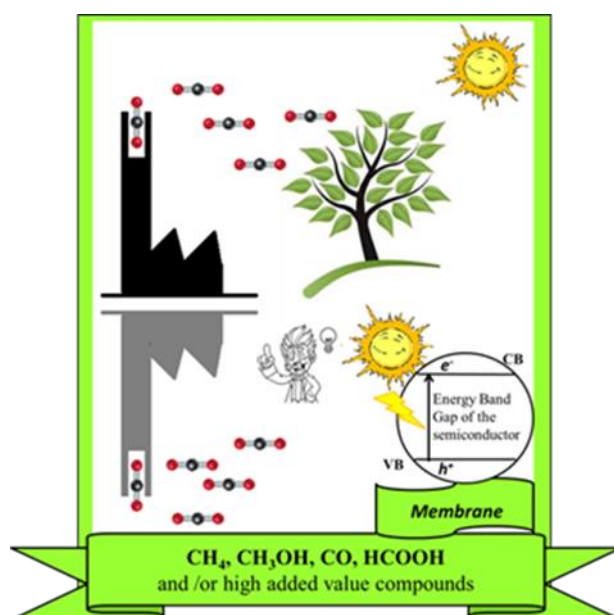
Edgar Lee Masters

Abstract

Carbon dioxide is a gas that is constantly exchanged among the atmosphere, oceans, and land surface due to its continuous production and absorption by many microorganisms, plants and animals. These processes tend to balance the CO₂ content in the atmosphere; however, since the Industrial Revolution, human activities are perturbing this equilibrium causing global warming and climate change. Due to this problem, an increasing concern has brought the scientific community to devote huge efforts to the CO₂ reduction and/or valorisation.

The published researches demonstrate that photocatalytic reduction of CO₂ in the presence of H₂O as reductant is a promising green way to obtain CH₄, CO, CH₃OH, EtOH, HCHO, acetaldehyde, and other products. Albeit, some aspects should be still improved in the use of the current technology, mainly related to the fact that TiO₂, the most known photocatalyst, absorbs light in the ultraviolet region of the electromagnetic spectrum and the use of the visible light is by far desirable. Beside the use of the best light source, also the high recombination hole-electron photogenerated charges (h⁺ e⁻) should be reduced or, in the best prospective, suppressed.

The aim of the current *PhD* dissertation is the CO₂ reduction by renewable methods, by using sunlight in order to obtain molecules that eventually could be used as fuels. This challenge aims to miming the natural process.



In this context, heterogeneous photo-catalysis assisted by the choice of reactor such as the continuous membrane reactor can improve the process performance.

The current research is focused to improve the activity in CO₂ reduction by two way: (i) the improvement of catalyst photoactivity and (ii) the optimization of the reactor set up. The first approach regards the catalyst modification by composites formation or doping material. The second approach aims to enhance the performance of the photoreaction by the incorporation of the photocatalyst in a membrane. In this way, the photocatalytic membrane should play a double role: (i) as (photo)catalyst support (ii) as separating barrier shifting the equilibrium versus the products formation, all in one step avoiding also a possible back reaction.

Several materials were prepared: (i) C₃N₄ from melamine by two thermal treatments, (ii) the C₃N₄ composite with TiO₂ sample by mechanical mixing, (iii) the O doped C₃N₄ samples by chemical and/or thermal method, (iv) graphene/TiO₂ composites with a graphene loading percentage weights equal to 0.5, 1, 3 and 10% obtained by a hydrothermal method. Beside to these powder samples, by solvent evaporation method, also the photocatalytic membranes were prepared embedding C₃N₄ and C₃N₄-TiO₂ in to polymeric Nafion matrix. In addition to these materials, also ZrO₂ bare and doped with Er or Ce were prepared. These photocatalysts were characterised and then used to perform CO₂ photoreduction experiments.

By concerning the characterization, FTIR, DRS, and XRD analyses were carried out for all powder samples, whilst the morphology and the structure of the photocatalytic and bare Nafion membrane were studied by SEM image and FTIR-ATR analysis.

In order to evaluate the photocatalytic activity versus the CO₂ photoreduction, all powder sample (TiO₂, C₃N₄, C₃N₄-TiO₂, bare and doped ZrO₂ materials, graphene/TiO₂ were tested in a Pyrex gas/solid batch reactor in the presence of a gaseous mixture CO₂/H₂O, at atmospheric pressure and under simulated sunlight. Besides, the pure and O doped C₃N₄, after immobilisation in a glass supports, were tested in a batch reactor at 2 bar. In both cases, the evolution of the species present in the reacting mixture, during the irradiation time, was followed by a GC-FID-TCD.

The flat sheet photocatalytic C_3N_4 and C_3N_4/TiO_2 Nafion membranes were assembled in a stainless steel module equipped with a quartz window allowing UV-Vis irradiation of the catalytic membrane surface. Once placed in UV-Vis exposure chamber, the membrane module was fed continuously with CO_2 and H_2O by means of a mass flow controller and an HPLC pump, respectively.

In the case of C_3N_4 Nafion membrane, particular attention was devoted to analysing the effect of contact time (2, 9.8 and 18.7 s) and CO_2/H_2O (0.5, 2 and 5) feed molar ratio on membrane reactor performance. Whilst, in the $C_3N_4-TiO_2$ /Nafion membrane the experimental set up allowed also to define the pressure system effect on reaction performance.

In this photocatalytic membrane reactor, the gaseous fraction of retentate and permeate flows were analysed by means of a GC-FID-TCD. To ensure the catalysts and the membrane photoactivity, in all case, the blank test was carried out in the same experimental reaction conditions but replacing CO_2 by argon.

The results obtained in these three years are below briefly described.

During the test of **graphene/ TiO_2** materials, methane was the main product in all case. The highest methane production ($1000 \mu M g^{-1}$) was observed for the 1% graphene/ TiO_2 composite and it was the highest ever reported for similar systems in the presence of metal free photocatalysts. This research may open a new doorway for new significant application of graphene for the selective production of methane and methanol as a promising material in membrane photocatalytic continuous reactor. However further investigations are needed.

The tests carried out in the presence of **ZrO_2 based materials** highlight that the new photocatalysts are able to absorb portions of UV ($\lambda=365$ nm) and solar light. Pristine ZrO_2 as well as Ce and Er-doped ZrO_2 resulted photoactive in gas-solid regime for CO_2 reduction to form mainly acetaldehyde. This uncommon behaviour for an insulator like ZrO_2 (with a band gap of more than 5 eV) is explained by the formation of intra band gap states due to the O vacancies.

During the tests in the presence of **C_3N_4 and oxygen doped C_3N_4** used as photocatalysts for CO_2 reduction, the detected product was CO. The pure material was

observed to be more active than the oxygen modified analogue. A decrease in the rate of CO generation, under irradiation, was observed during both single runs and repeated test cycles with the same catalyst. During control tests in the absence of CO₂, the production of CO was observed under irradiation, raising questions about the origin of CO and the stability of C₃N₄. Both analyses such as the diffuse FTIR and XPS before and after use, showed that the thermal and the photocatalytic treatments produce similar changes to the functional groups, which are consistent with oxidation of the C₃N₄ structure. This study allowed an interesting examination of where and how oxidation disrupts the material structure, showing changes in the heptazine base units along with changes in the bonds between units due to the thermal oxidation or photocatalytic use.

By using **C₃N₄ Nafion membrane**, photocatalytic CO₂ conversion was carried out in a continuous photocatalytic reactor with an exfoliated C₃N₄-based membrane irradiated by UV-vis light. The effect of H₂O/CO₂ feed molar ratio and contact time on species production, reaction selectivity and converted carbon were investigated. The rate of total converted carbon per gram of catalyst used varied between 5 to 47.6 μmol g_{catalyst}⁻¹ h⁻¹, with the latter value obtained at an H₂O/CO₂ feed molar ratio of 5 and 2 s as contact time. Alcohols were prevailing product. The membrane reactor converted at least 10 times more carbon than the batch system, as a result of the better dispersion of the catalyst which was embedded in the Nafion matrix.

The photocatalytic CO₂ reduction experiments carried out by using **C₃N₄-TiO₂ Nafion** membrane produced mainly MeOH and formaldehyde with trace of acetone and EtOH. The obtained MeOH production confirms the trend previously found for C₃N₄ Nafion membrane about the feed molar ratio and residence time effect. In particular the MeOH production increased with the feed molar ratio and is higher at lower residence time (2 s). Then, the best set up conditions were: a H₂O/CO₂ feed molar ratio and residence time equal to 5 e 2 s, respectively. Under these experimental conditions, MeOH production was higher; in addition, at the lower pressure (3 bar) the reaction exhibited ca. 80% of selectivity that decreased at ca. 50% when there action pressure raised to 5 bar.

On the contrary, the selectivity towards formaldehyde increases from 10 to 45% when the feed pressure increases. By comparing the experiments obtained in the presence of

C₃N₄ loaded Nafion and C₃N₄-TiO₂ loaded Nafion membranes with those present in the literature for TiO₂ loaded Nafion membrane, the selectivity toward MeOH production increases with TiO₂ content. On the contrary, the C₃N₄-TiO₂ loaded Nafion membrane showed the best value of total carbon converted, equal to 60 μmol g⁻¹ h⁻¹, compared with the other two membranes aforementioned. This value is ca. 7 time higher than that obtained in the batch test with the C₃N₄-TiO₂ powder catalyst, confirming the enhancement owing to the continuous membrane reactor versus the batch.

In conclusion, the CO₂ was valorised by using several type of catalysts (pure, doped and composite graphitic materials) in different reactors. In all the cases, CO₂ photoreduction occurs giving CH₄ and CO or alcohol and acetaldehyde as the main products as a function of reactor type (batch or membrane reactor) and experimental conditions operated.

This *Ph.D* dissertation, in the CO₂ photoreduction field, provided (i) an interesting structural study of C₃N₄ before and after use, (ii) a remarkable study of catalyst photoactivity by using oxide and graphitic material in batch reaction, (iii) a promising route for the optimisation of the photocatalytic continuous membrane reactor in terms of feed molar ratio of reagents mixture, residence time and reaction pressure.

Sommario

Il diossido di carbonio (CO_2) è un gas che viene costantemente scambiato tra l'atmosfera, gli oceani e la superficie terrestre grazie alla attività biologica di una grande varietà di microrganismi, piante e animali. I fenomeni di emissione e di assorbimento del CO_2 in questi processi naturali tendono ad equilibrarsi. Tuttavia, a partire dalla rivoluzione industriale, le attività umane hanno perturbato questo equilibrio, causando un preoccupante aumento della concentrazione di CO_2 nell'atmosfera con il conseguente riscaldamento globale i fenomeni climatici ad esso connessi. Questo problema ha portato la comunità scientifica a dedicare enormi sforzi alla riduzione e/o alla valorizzazione del CO_2 .

Le ricerche riportate in letteratura dimostrano che la riduzione fotocatalitica del CO_2 in presenza di H_2O come agente riducente è un modo promettente per ottenere CH_4 , CO , CH_3OH , $\text{C}_2\text{H}_5\text{OH}$, HCHO , $\text{C}_2\text{H}_4\text{O}$, etc. Tuttavia i piccoli valori di conversioni ottenuti hanno spinto ad accoppiare la fotocatalisi eterogenea con la tecnologia dei reattori continui a membrana per migliorare le prestazioni del processo.

Questo è il punto di partenza del presente lavoro di tesi il cui obiettivo è di ottimizzare l'attività nella riduzione del CO_2 attraverso: (i) il miglioramento della fotoattività del catalizzatore e (ii) l'ottimizzazione della configurazione del reattore. Il primo approccio riguarda la modifica del catalizzatore mediante formazione di compositi o di materiali dopati, mentre il secondo mira a migliorare le prestazioni della reazione mediante l'incorporamento del fotocatalizzatore in una membrana e l'uso di un reattore continuo. Il reattore continuo fotocatalitico a membrana così ideato conduce la reazione in un unico step e consente di ottimizzare l'esposizione del catalizzatore alla luce e ai reagenti e di spostare l'equilibrio chimico verso la formazione dei prodotti riducendo in tal modo la possibilità che i prodotti possano reagire a loro volta secondo reazioni termodinamicamente più favorite ma indesiderate che diminuiscono l'efficienza globale del processo.

Per perseguire lo scopo prefissato sono stati preparati i seguenti materiali:

- (a) nitruro di carbonio (C_3N_4)
- (b) C_3N_4 con TiO_2

- (c) C_3N_4 dopato con O mediante metodo chimico e/o termico
- (d) compositi di grafene/ TiO_2 con un peso percentuale di carico del grafene dello 0.5, 1, 3 e 10%
- (e) ossido di zirconio (ZrO_2) puro e dopato con Erblio (Er) o Cerio (Ce).

In aggiunta a questi materiali, sono state preparate membrane fotocatalitiche mediante il metodo di evaporazione del solvente. Nella matrice polimerica delle membrane (Nafion) sono stati aggiunti C_3N_4 puro o accoppiato a TiO_2 .

Tutti i fotocatalizzatori sono stati caratterizzati attraverso la spettroscopia UV-vis, la spettroscopia ad infrarossi a Trasformata di Fourier (FTIR) e la diffrazione dei raggi X. Alcune polveri sono state caratterizzate tramite spettroscopia fotoelettronica a raggi X (XPS). Per quanto riguarda le membrane fotocatalitiche, l'analisi strutturale, ottica e morfologica è stata condotta tramite spettroscopia a infrarossi, di riflettanza diffusa e tramite microscopia elettronica a scansione. Tutti i materiali preparati sono stati infine testati per la fotoriduzione del CO_2 in presenza di acqua.

Per valutare l'attività fotocatalitica dei materiali nei confronti della riduzione del CO_2 , tutti i materiali in polvere sopra elencati sono stati testati in un reattore batch di Pyrex riempito da una miscela gassosa CO_2/H_2O a pressione atmosferica e sotto irraggiamento UV-vis (luce solare simulata, SOLARBOX). Il C_3N_4 puro e quello drogato con ossigeno, sono stati utilizzati previa immobilizzazione su un supporto di vetro e testati in un reattore batch in acciaio con una finestra in quarzo attraverso la quale si è effettuata l'irradiazione UV-vis necessaria per condurre la reazione. Anche in questo caso la reazione è stata condotta in presenza di H_2O come agente riducente ma ad una pressione di CO_2 pari a 3 bar.

Diversamente dai materiali in polvere, le membrane fotocatalitiche sono state invece testate in un reattore continuo. Il reattore era composto da un modulo in acciaio dotato di una finestra in quarzo per consentire l'irradiazione UV-vis della superficie della membrana posta all'interno del reattore. Il modulo così composto è stato collegato a dei controllori di portata mediante i quali è stato possibile controllare le quantità di reagenti da miscelare e introdurre nel sistema. Questo strumento ci ha permesso di studiare la distribuzione dei prodotti, la quantità di carbonio convertito, la selettività al variare del

tempo di residenza della miscela dei reagenti all'interno del reattore e l'effetto del rapporto molare della miscela reagente $\text{H}_2\text{O}/\text{CO}_2$.

In tutti i casi, sia in presenza del catalizzatore in polvere, su supporto di vetro o su membrana, l'evoluzione nel tempo della reazione fotocatalitica è stata seguita con campionamenti periodici. Le analisi dei campioni sono state effettuate tramite gas cromatografo dotato di rilevatori a ionizzazione a fiamma e a termo-conducibilità elettrica.

Tutti i fotocatalizzatori hanno mostrato foto-attività nella riduzione del CO_2 e i risultati sono qui di seguito brevemente discussi.

Nel caso dei composti **grafene/TiO₂** il CO_2 è stato trasformato preferenzialmente in metano che ha raggiunto una concentrazione massima per grammo di catalizzatore di $1000 \mu\text{M g}^{-1}$ nel caso in cui il grafene era presente al 1%. I risultati in generale hanno confermato quanto riportato in letteratura dimostrando l'esistenza di un caricamento ottimale di grafene sul TiO_2 . Successivi studi e implementazioni dal punto di vista reattoristico sono comunque necessari.

Nel caso dei test condotti in presenza dei materiali a base di **ZrO₂ drogati e non**, i risultati hanno evidenziato un'attività fotocatalitica di conversione di CO_2 tendenzialmente ad acetaldeide. Lo studio strutturale delle polveri fotocatalitiche ha consentito di comprendere e giustificare l'insolita attività del ZrO_2 che, in quanto semiconduttore con band gap di circa 5 eV, generalmente non assorbe radiazione nel campo UV-vis. La fotoreattività riscontrata è dovuta alla formazione di vacanze di ossigeno nella struttura dell'ossido che si comportano come stati energetici intermedi all'interno del band gap che consentono l'assorbimento di radiazione UV-vis. Inoltre nel caso del ZrO_2 drogato con Er o Ce, è stato possibile identificare la formazione di bande energetiche intermedie all'interno del band gap capaci di generare un "doppio salto dell'elettrone eccitato".

Nel caso dei catalizzatori immobilizzati a base di **C₃N₄ (puro e drogato con ossigeno)**, i test fotocatalitici di riduzione del CO_2 hanno evidenziato il CO come unico prodotto. Dal confronto delle reattività ottenute con tutti i materiali supportati si evince una maggiore attività del materiale puro C_3N_4 che però diminuisce con il riutilizzo. Lo

stesso andamento decrescente è stato riscontrato per i catalizzatori dopati con ossigeno. A seguito delle analisi FTIR e XPS, effettuate prima e dopo l'utilizzo, è stato possibile identificarne la causa nell'introduzione di atomi di ossigeno all'interno della struttura al posto dei centri di azoto. L'incremento del contenuto di ossigeno interno alla struttura può essere visto come una foto-ossidazione del materiale che quindi ne causa la progressiva perdita di attività fotocatalitica.

Questo studio ha permesso di comprendere dove e come l'ossidazione muta la struttura del materiale a causa dell'ossidazione termica o dell'uso fotocatalitico, mostrando cambiamenti nelle unità di base di eptazina e nei legami tra esse.

Utilizzando la membrana fotocatalitica contenente il C_3N_4 , la conversione fotocatalitica del CO_2 è stata effettuata in un reattore fotocatalitico continuo irradiato da luce UV-vis. Sono stati studiati gli effetti del rapporto molare di alimentazione H_2O/CO_2 e il tempo di contatto della miscela all'interno del reattore sulla produzione e la distribuzione dei prodotti, sulla selettività della reazione e sul carbonio convertito totale. In generale, gli esperimenti hanno prodotto principalmente metanolo, etanolo, formaldeide, e tracce di acetone. In termini di efficienza della reazione condotta, gli esperimenti fotocatalitici hanno mostrato valori di carbonio convertito totale tra i 5 e $47.6 \mu\text{mol g}^{-1} \text{h}^{-1}$. Il più alto valore, in particolare, è stato raggiunto adottando un rapporto molare di H_2O/CO_2 di 5 e un tempo di residenza di 2 s. In ogni caso, comunque, il valore di carbonio convertito totale ottenuto nel reattore continuo a membrana è stato almeno 7 volte maggiore rispetto a quello ottenuto in condizioni analoghe ma in presenza delle polveri di C_3N_4 nel reattore batch. Quest'ultima evidenza sottolinea l'importanza di opportune condizioni reattoristiche per la reazione considerata e in particolare del reattore continuo a membrana per incrementare l'efficienza del catalizzatore in esso disperso.

Gli esperimenti di fotoriduzione del CO_2 effettuati utilizzando la membrana Nafion $C_3N_4-TiO_2$ hanno prodotto principalmente metanolo e formaldeide con tracce di acetone ed etanolo. La quantità di metanolo ottenuto conferma la tendenza precedentemente menzionata per la membrana di Nafion in presenza di C_3N_4 , in merito all'effetto del rapporto molare e del tempo di residenza. In particolare, la produzione di metanolo aumenta con il rapporto molare e con il diminuire del tempo di residenza. Per quanto riguarda l'effetto della pressione di reazione, la selettività verso la produzione di

metanolo mostra valori maggiori (*ca.* 80%) a pressioni minori (3 bar). Viceversa si sono ottenute selettività a metanolo (*ca.* 50%) minori a pressioni di reazione maggiori (5 bar).

La selettività della reazione nei confronti della produzione di formaldeide aumenta dal 10 al 45% quando la pressione di alimentazione aumenta da 3 a 5 bar. Sia negli esperimenti in presenza delle membrane fotocatalitiche in Nafion contenenti C_3N_4 e $C_3N_4-TiO_2$ che nei risultati di letteratura relativi a membrane in Nafion con TiO_2 , la selettività in metanolo aumenta con il contenuto di TiO_2 . In termini di carbonio totale convertito, la membrana Nafion $C_3N_4-TiO_2$ ha mostrato una più alta efficienza raggiungendo un totale carbonio convertito rispetto alle altre due membrane sopra menzionate pari a $60 \mu\text{m g}^{-1} \text{h}^{-1}$. Questo valore come già detto, risulta essere di *ca.* 7 volte superiore a quello ottenuto nel test in batch con il catalizzatore $C_3N_4-TiO_2$ in polvere. Questo risultato evidenzia l'incremento delle performance del reattore a membrana fotocatalitico continuo rispetto a quello batch.

In conclusione, diversi tipi di catalizzatori (materiali grafittici puri, drogati e compositi) sono stati preparati, caratterizzati e testati per la trasformazione fotocatalitica del CO_2 in diversi reattori. In tutti i casi, la fotoriduzione di CO_2 si verifica dando metano, monossido di carbonio, alcol e formaldeide come prodotti principali in funzione del tipo di reattore (reattore batch o membrana) e delle condizioni sperimentali utilizzate. Questa tesi di dottorato, nel campo della fotoriduzione della CO_2 , ha fornito (i) un interessante studio strutturale del C_3N_4 e dei materiali dopati con ossigeno prima e dopo l'uso, (ii) un ampio studio della fotoattività di catalizzatori ossidici e materiali grafittici in reattori batch, (iii) uno studio per l'ottimizzazione del reattore fotocatalitico continuo a membrana in termini di rapporto molare di alimentazione dei reagenti della miscela, tempo di residenza e pressione di reazione.

Outline

The present dissertation deals with the preparation and characterisation of photocatalysts active under UV-vis light irradiation for CO₂ reduction to high value added compounds. The first chapter introduces the environmental problem of the global warming caused by the increasing CO₂ concentration in the atmosphere. The sections therein survey the various methods investigated in the relevant literature in order to exploit CO₂ as building block for the synthesis of fuels. Due to its green features, photocatalysis is proposed as one of the most promising methods among them, and its basic mechanisms, along with the main photocatalysts and some reactor design issues are briefly presented.

The second chapter describes the synthesis and characterization of all of the photocatalysts tested for CO₂ reduction. Results of the reactivity test in batch reactors are reported in chapter 3. The section 3.1, 3.2 and 3.3 present the CO₂ photoreduction results obtained in the presence of graphene/TiO₂ composites, bare and doped ZrO₂ materials and bare and doped C₃N₄ samples, respectively.

The following 3.4 and 3.5 sections present the results of the fuels production in a continuous photoreactor by using C₃N₄ and C₃N₄-TiO₂ embedded in Nafion membranes.

This dissertation ends with a summary highlighting the main results and the appendix A and B which report the publications and the training Ph.D school activity, respectively.

Chapter 1
The Environmental problem and CO₂
valorisation

1.1 Aim of this dissertation

The presented literature overview testify the attention of the scientific community towards the challenging problem of CO₂ activation. Different materials have been already proposed as promising photocatalysts and their activity has been tested and reported in many papers.

The starting point of the present dissertation was to identify the most promising materials among them and to investigate the relationship between their physico-chemical features and their activity for CO₂ photoreduction. These basic materials were TiO₂, ZrO₂, and C₃N₄. TiO₂ is the most studied semiconductor due to its abundance, non toxicity and chemical stability so that it is often considered as a reference materials for a wide class of photocatalytic reactions. The use of ZrO₂ for CO₂ photoreduction is appealing because of its surface basicity favours CO₂ adsorption. Even if this material has been only rarely used as a photocatalyst due to its wide band gap (ca. 5 eV), recent studies highlighted its visible light harvesting capability due to the presence of oxygen vacancies acting as colour centres. Graphitic carbon nitride (C₃N₄) is very attracting material recently investigated for CO₂ photoreduction because of its narrow band gap, the basicity of the constituting nitrogen atoms and the particularly negative potential of the photogenerated electrons.

With the aim of increasing the CO₂ photoreduction efficiency of these materials, two approaches were adopted: (i) modifying the bare semiconductors by means of metal and non-metal doping or by coupling them with opportune graphitic materials (such as graphene or the graphitic C₃N₄), and (ii) tailoring design and operating parameters influencing the reaction efficiency, by using continuous photocatalytic membrane reactors, different reactants molar ratio, and residence times.

As far as the first point is concerned, TiO₂ was loaded with different amounts of graphitic materials such as graphene and carbon nitride, whilst ZrO₂ was modified with Erbium and Cerium metals. Moreover, C₃N₄ was doped with oxygen in order to enhance its visible light absorption capability.

These materials were tested for CO₂ photoreduction in batch reactors by using water as the reductant. However, in order to avoid back reaction of the products, which is the main hurdle hindering the reaction efficiency, and to optimize the light exposure of the photocatalyst, the activity tests were performed in a continuous photocatalytic membrane reactor. To this aim giving the high versatility, the UV transparency, the photostability and the high proton exchange efficiency of Nafion, the C₃N₄ and C₃N₄-TiO₂ samples were embedded into the Nafion membrane. C₃N₄ materials were chosen to be coupled with Nafion because of the reported compatibility and strong interaction with the sulfonic groups of Nafion.

The photocatalytic materials both powdered and embedded in the membrane were thoroughly characterized in order to evidence the correlation between their physico-chemical properties and CO₂ photoreduction efficiency.

1.2 The Environmental problem

Since the last century, the scientific community is placing particular attention on a world phenomenon called “Global warming”.^{1, 2} In climatology, the expression global warming indicates the change in the Earth's climate that assumed remarkable effects during the 20th century and is still ongoing.

Atmosphere and oceans have warmed, the amounts of snow and ice have diminished and sea level has risen. These changes are largely attributed to emissions in the Earth's atmosphere of increasing quantities of greenhouse gases and to other factors that the scientific community has identified as attributable to human activity.

By definition, a greenhouse gas is a gaseous compound, generally present in the atmosphere, which is transparent to the solar radiation but consistently retains the infrared radiation emitted by the Earth's surface, atmosphere and clouds. These properties are known from spectroscopic analyses. Greenhouse gases can be of both natural and anthropogenic origin, and absorb and emit at specific wavelengths in the infrared radiation region. This causes the phenomenon known as a greenhouse effect. In fact, these gases are capable to re-radiate into the atmosphere the absorbed solar IR radiation simultaneously blocking the IR emission from the Earth thus causing the above mentioned global warming.

Water vapour, carbon dioxide, nitrous oxide, methane and sulphur hexafluoride (SF_6) are the main greenhouse gases in the Earth's atmosphere. In addition to these gases, there is a wide range of greenhouse gases of exclusive anthropogenic origin, such as halocarbons. Among the most known are chlorofluorocarbons (CFC), and many other chlorine and fluorine containing molecules whose emissions are regulated by the Montreal Protocol.

The molecules mostly contributing to the greenhouse effect are those characterised by a non-linear molecular structure and by an intrinsic dipole moment. In fact, not all of the diatomic gases constituting the atmosphere are IR active as they have a definite linear structure. On the other hand, ozone, water vapour, nitrous oxide, fluorinated gases (hydrofluorocarbons, sulphur hexafluoride, perfluorocarbons, chlorofluorocarbons) behave as greenhouse gases due to their non-linear structure.

As an exception, CO₂, despite its symmetric and linear structure, has a strong IR absorption due to its asymmetric stretching, which affords a significant dipole moment. Even if other gases have a greater greenhouse potential, CO₂ is considered one of the biggest responsible for the global warming due to its greater abundance in the atmosphere.²

Before the second industrial revolution (which conventionally began in 1870, along with the large-scale use of electricity, oil and chemicals), the atmospheric CO₂ concentration was 280 part per million (ppm), as shown by measurements in glaciers and poles.

Recently, the World Meteorological Organization published a series of data related to 2016, which show a significant increase in the concentration of carbon dioxide in the atmosphere. For instance, the CO₂ concentration rose from 400 to 403.3 ppm in only one year (from 2015 to 2016).

Due to the strong correlation between the global warming and the CO₂ concentration³ (Figure 1), the European Commission⁴ set greenhouse gas emissions targets in order to limit the warming to well below 2°C above pre-industrial temperatures within 2050.

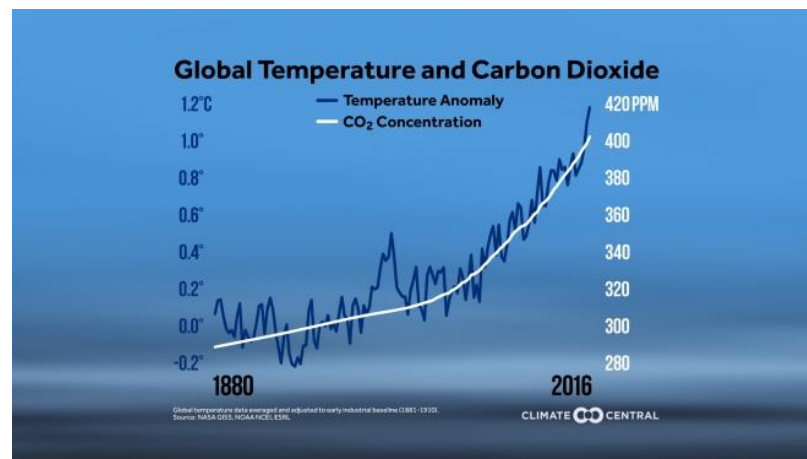


Figure 1. Global temperature and CO₂ atmosphere concentration (ppm) trend from 1880 to 2016.⁴

European key climate and energy targets are set in two particular actions called: (i) 2020 climate and energy package and (ii) 2030 climate and energy framework.

These targets are defined in order to address the EU activities towards a low-carbon economy as detailed in the 2050 low-carbon roadmap. The EU tracks its progress on cutting emissions through regular monitoring and reporting.

1.3 CO₂ utilization: conversion to high added value compounds

Even if naturally present in the atmosphere as a transparent and odourless gas at a low percentage (0.04%) with respect to the other air components, CO₂ plays a key role in the “Carbon cycle”, i.e., the biogeochemical cycle by which carbon is exchanged among the biosphere, pedosphere, geosphere, hydrosphere, and atmosphere. In fact, CO₂ is solubilised in the seawater as CO₃²⁻ and HCO₃⁻ depending on pH, and it is a primary worker in the biological process. In particular, CO₂ represents the building block in the chlorophyll photosynthesis where it is fixed from the plants in the presence of light and from them rejected as waste in the dark.

Carbon is the main component of biological compounds as well as a major component of many minerals such as limestone. Along with the nitrogen and water cycles, the carbon cycle comprises a sequence of events, which are essential to the Earth capability of sustaining life. In theory, being a cycle, it should be capable to balance in the environment the content of carbon, in all of its forms. Unfortunately, this equilibrium is perturbed by human activities, which produce tons of CO₂ per capita at years, as reported in “The global carbon budget 1959–2011” published from Quéré et al. (Figure 2).⁵

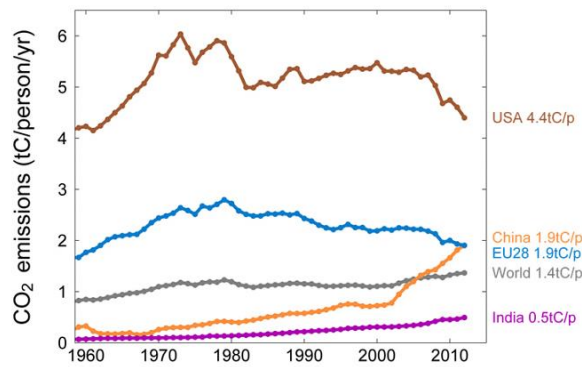


Figure 2. Average emissions per capita from 1960 to 2012.⁵

In a more recent study (2017), Quèrè et al.,⁶ in collaboration with sixty world institutes, estimate that ca. 87% of the current anthropogenic CO₂ total emission, derives from fossil fuel combustion (Figure 3a).

In particular, their studies found that the electricity and heat generation is the economic sector that produces the largest amount of man-made carbon dioxide emissions (Figure 3b).

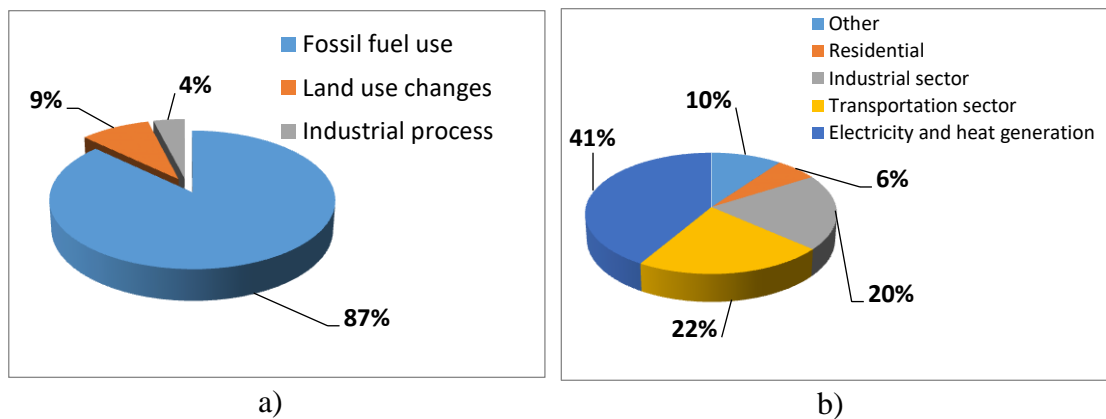


Figure 3. (a) Anthropogenic sources of Carbon dioxide and (b) Carbon dioxide emissions from fossil fuel combustion.

Fossil fuels have been exploited up to now as the main energy source for human activities. This is due to their fundamental characteristics of (i) high compactness concerning the energy to volume ratio, (ii) easy storage, and (iii) low cost. Because of the extremely long process of natural formation of fossil fuels, which makes them a non-renewable energy source, an inevitable and progressive depletion of

the stocks occurred. This has caused a continuously rising cost of the fossil fuels and of related goods.

Experts from all over the world estimate the predictable exhaustion of resources in a period of around 40 years.

These problems, along with the environmental disasters recently occurred (CO₂ increasing, deforestation, desertification, etc.), moved industrialised Countries to greater attention towards environmental issues by using alternative and renewable energy sources. In particular, the European Union aimed at promoting the use of renewable resources according to targets to be fulfilled within 2020.

In other words, the goal is to generate energy by wind, sun, tides, or other renewable sources, at least at the same rate of consumption. Furthermore, these technologies to produce green energy are environmental friendly, as they do not pollute, not jeopardise the natural resources for the needs of future generations, and not produce emissions of toxic substances or greenhouse gases into the atmosphere.

1.3.1 Activation of CO₂

Even if CO₂ contains polar bonds, it is a nonpolar molecule, due to the high symmetry of its linear structure. Furthermore, CO₂ in principle could give rise to nucleophilic and electrophilic attack through its carbon and oxygen atoms, respectively.

According to the Molecular Orbital Theory, its highest occupied molecular orbital (HOMO), is susceptible to electrophile attack due to the localized electron density of oxygen (lone pairs). On the contrary the lowest unoccupied molecular orbital (LUMO) is susceptible to nucleophile attack due to the antibonding orbital at the lowest energy represented by the central carbon atom.

Furthermore, the CO₂ HOMO degenerated orbitals have four electrons with the same energy ready to be released, while CO₂ LUMO have four unoccupied states to which four electrons can transfer. If one of four electrons from HOMO orbital is released or transferred, the degeneration is broken⁷ with the consequent activation

of CO₂. Unfortunately this electron transfer is not favoured so that it has been often represented as a “Holy Grail”.⁸

Therefore, CO₂ is a very stable molecule with a $\Delta G^0 = -394$ kJ/mol also because the carbon atom is in its highest oxidation state. Consequently, CO₂ activation is the crucial step in CO₂ transformation to high added value molecules.

1.3.2 Methods

Three principal methodologies are reported to transform CO₂ into useful chemicals:

- (i) Use high-energy starting materials such as hydrogen, unsaturated compounds, small-membered ring compounds, and organometallics
- (ii) Address the selectivity towards oxidized low-energy synthetic products such as organic carbonates
- (iii) Supply energy such as light, electricity or biological driving forces.

Selecting the appropriate method and shifting the equilibrium to the product side by removing a particular compound, can lead to a negative Gibbs free energy of the reaction.

Significant researches have been devoted to use CO₂ as the raw material for different reactions, as summarised in Figure 4. In particular, CO₂ reduction performed under photoirradiation, or under electrochemical conditions, generally, affords simple molecules such as carbon monoxide, methane and formic acid⁹ or syngas by means of reforming reactions.

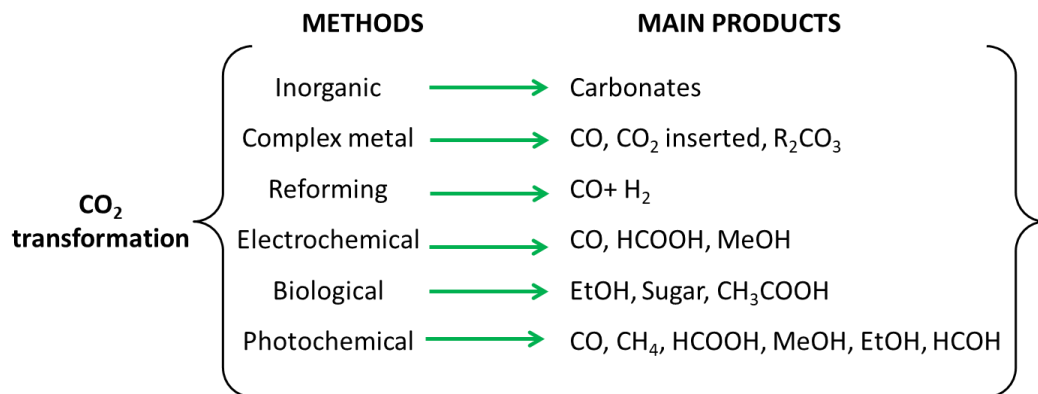
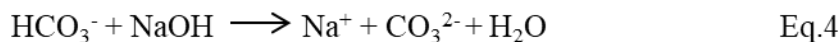
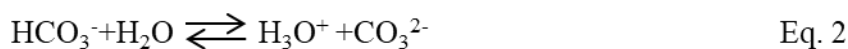
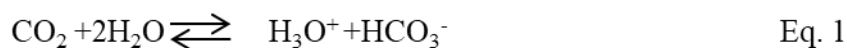


Figure 4. The main reaction/process type from CO₂ transformation to obtain high added value compounds.^{9,10}

The inorganic CO₂ reaction (Eq. 1-2) is just a pH depending to equilibrium as showed in the below reactions (Eq. 3-4).



This method is not very useful due to the very low economic value of products (carbonate and bicarbonate salts) and additionally to the large amount of base needed to obtain carbonate.

With the exception of this first kind of transformation, all of the other CO₂ activation routes require the presence of some catalyst to decrease the high activation energy.

Metal complexes (inorganic or organic type) have been used to activate CO₂ in order to obtain high added value compounds as CO or to fix CO₂ in an organic substrate (carboxylation process).

This reaction occurs because CO₂ can efficiently coordinate with transition metal compounds.¹¹ Figure 5 shows the different coordination modes of CO₂ in transition metal complexes, even at room temperature.¹²

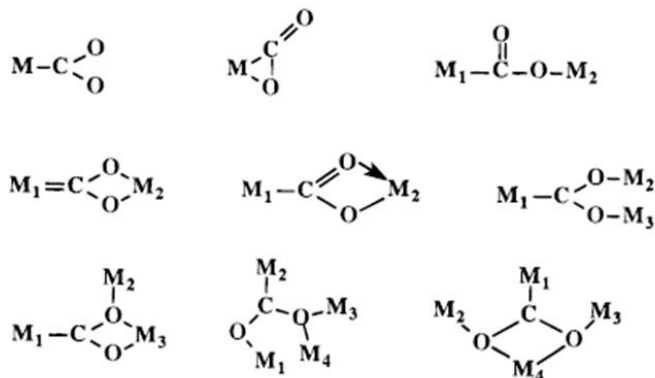


Figure 5. Modes of bonding of carbon dioxide with transition metal.

In particular, high valence metal complexes with nucleophilic ligands as alkoxides or amides,^{13, 14} permit the formation of the carboxyl group through nucleophilic attack to CO₂. This reaction occurs by CO₂ insertion in the M-O or M-N bond giving a metal-alkyl carbonate or metal-alkyl carbamate, respectively. In general, apparently because the metal alkoxide and metal-alkyl carbonate have similar M-O bond strengths, most metal alkoxide complexes react reversibly with carbon dioxide.¹⁵⁻²¹ CO₂ insertion has been reported for different transition metals. Zinc complexes, as Zn₂Br₄(μ-OCHRCH₂NC₅H₅)₂ (R = H, CH₃),²² or Cobalt complexes, as [Co (TCT)(OR)]BPh₄ (R = Et, Ph; TCT = cis,cis-1,3,5-tris(cinnamylideneamino) cyclohexane),²³ activate CO₂ for insertion reactions. Similar behaviour has been found for organic metal complexes such as Rhenium fac-(CO)₃L₂-ReOCH₃ (L = PMe₃; L₂ = diars),²⁴ alkyl vanadium(III) alkoxide,²⁵ Molybdenum systems²⁶ like Mo₂(OiPr)₄(L)₄ (L = PMe₃, HOiPr), or Titanium(IV) butoxide²⁷, which promote reversible carbon dioxide insertion into the M-O bond. Interestingly, also zirconia catalysts,²⁸ vanadium based heterogeneous catalysts²⁹ and organotin alkoxides immobilized on mesoporous silica³⁰ exhibit similar CO₂ insertion. This kind of reaction was also hypothesized to occur in CO₂-starting syntheses catalysed by tin³¹, nickel³², and niobium³³ complexes.

Metal-organic or inorganic compounds are currently used as catalysts in relevant industrial processes to produce for instance acetic acid, salicylic acid, urea, polycarbonate and propylene carbonate from CO₂.

Even if this type of complexes are used in industrial processes, they suffer several disadvantages mainly because the transition metals are toxic and, especially in the metal-organic form, capable to interact with human tissues and DNA. Some of them are not stable in the presence of water or give leaching making difficult their separation from the reacting mixture and their reuse. Moreover, some transition metals such as Rh, Os, Pt, Au, Ru, and Pd are rare earth elements, which considerably affect the overall cost of the process.

A very efficient alternative method is CO₂ reforming, a thermal catalytic process affording syngas (CO + H₂). This process attracted great attention as a clean and efficient method for hydrogen production from waste material as CO₂. Notably, H₂ is envisaged as the fuel carrier of the future especially for its application to fuel cells.³⁴

The industrial CO₂ reforming occurs in the presence of Ni based catalysts,³⁵ starting from methane and CO₂ as the reagents. (Eq. 5).



CO₂ reforming processes are industrially carried out at a high temperature to enhance reaction rates and syngas yields, due to the highly endothermic nature of reaction.

The main drawback of the thermal catalytic reforming processes is the large amount of heat required for the processes.³⁴ Typically, a temperature ranges of 500-950°C³⁶ and a pressure between 20-40 bar are applied. These hard operating conditions make the process expensive and energetically demanding. Furthermore, with respect to the steam reforming process (i.e., the analogous process when H₂O is used instead of CO₂), the CO₂ reforming is 40 kJ more endothermic and the higher carbon concentration favours coke deposition, with the consequent faster poisoning of the catalyst.

Albeit the aforementioned drawback, the high interest to obtain H₂ has driven researchers to design opportunely catalysts and reactors in order to improve the efficiency of the process, set mild conditions, and reduce the costs.³⁶⁻⁴⁰

A promising method to avoid the above-mentioned catalyst poisoning, is to use electricity as the driving force by means of electrochemical processes. These systems are typically comprised of an anode and a cathode placed in two chambers separated by an ionic conducting membrane. In the anodic compartment, water is oxidised to molecular oxygen, while CO₂ (used as carbon source) is reduced at the cathodic side to high added value molecules.

The electrocatalysts used for this application can be divided into three groups: metallic, non-metallic, and molecular catalysts as summarised in Figure 6.⁴¹⁻⁵⁹

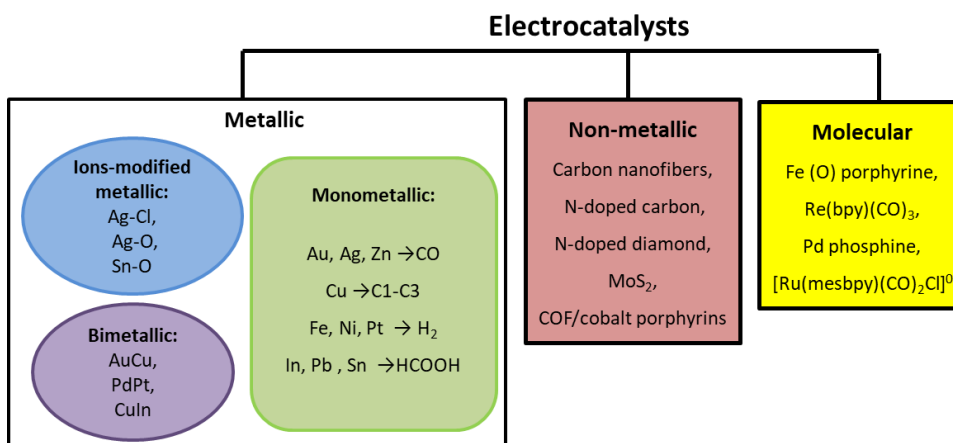
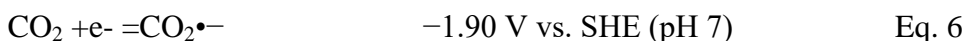


Figure 6. Schematic illustration of the three major categories of electrocatalysts for CO₂ reduction.⁶⁰

Due to the thermodynamically uphill nature of one electron CO₂ reduction (Eq. 6) an external bias is required.



On the other hand, a smaller electromotive force in the range of -0.2 to -0.6 V vs. SHE (Standard Hydrogen Electrode) is required for CO₂ reduction with proton-assisted electron transfer processes.

Unfortunately, due to the similar redox potentials for all of the reaction pathways (i.e., CO_2 to HCOOH and CO_2 to CH_3OH have E_0 equal to -0.58 and -0.51 V, respectively),⁶⁰ the proton-assisted processes can lead to a wide range of CO_2 -derived products, thus giving rise to poor selectivity towards the desired chemicals. However, generally only CO and HCOO^- are reported as the main products of CO_2 electrocatalytic reduction.⁶⁰

Notably, a key factor, to be carefully controlled is the competition of water with CO_2 , which decreases the efficiency of the process producing H_2 instead of the CO_2 reduction products.⁶⁰ Furthermore, the costs related to the consumption of electricity are bottleneck for this process. In addition, the electricity is currently mainly produced from fossil fuel oxidation, which in turn is a source of CO_2 .

Every living being must extract energy from the environment in order to carry out the metabolic processes. In particular, plants harvest solar light in order to perform photosynthesis, which uses CO_2 as building block to synthesise carbon chains molecules (e.g., glucose and cellulose). For this reason, plants, algae and cyanobacteria are called photoautotrophs, i.e., they are capable to produce complex organic compounds from simple molecules, generally using light as energy source. Photosynthesis is largely responsible producing and maintaining the oxygen content of the atmosphere, and it supplies the organic compounds and the energy necessary for life on Earth. Even if photosynthesis is differently performed by different species, the process always begins when energy from light is absorbed by proteins called reaction centres that contain green chlorophyll pigments. These proteins (enzyme function) coordinate with Cu (Cu(I) and Cu(II)) and Mg, playing a key role on the photosynthesis process.

Different pathways are known for the fixation of inorganic carbon into organic compounds used for cell biomass.⁶¹ Among them the reductive pentose phosphate (Calvin–Benson–Bascham) cycle^{61, 62} is the predominant mechanism by which many prokaryotes and all plants fix CO_2 into biomass.

The enzymes required to carry out these important metabolic pathways, which have evolved over billions of years, and they use readily abundant materials from the environment to achieve these important energy conversion processes. All of these

metabolic pathways involve the storage and utilization of energy in the form of chemical bonds. Our ability to carry out the same transformations in a controlled and efficient way will be critical to our future energy security. In fact, a huge number of literature reports focus understand these complex processes in order to convert CO₂ in high added value compounds in vitro and in vivo conditions. In particular, it has been demonstrated the photosynthetic functions of microalgae *Chlorella* or unicellular cyanobacteria *Synechocystis* can be energetically convenient compared to catalytic conversions requiring energy-intensive reaction conditions (high temperature ca. 300–600 °C and pressure higher than 10 bar).⁶³⁻⁶⁶ Furthermore, algae such as *Chlorella*, *Scenedesmus*, *Spirulina*, *Nannochloropsis*, and *Chlorococcum* are characterized by rapid growth, tolerance to stress factors, and to high concentrations of CO₂.⁶⁷⁻⁶⁹ A recent kinetic study on *Chlorella vulgaris* reports the bio-fixation rate and cell concentration value more than 1.4 g/L/day and 1.3×10^7 cells/mL, respectively.⁷⁰

Unicellular microorganisms such as Cyanobacteria have been used in several ways to produce renewable biofuel. However, recent studies suggest that biofuel production from cyanobacteria is unfeasible, as the energy return to energy invested ratio (EROEI) is unfavourable.⁷¹ In fact numerous large, closed loop bioreactors with ideal growth conditions (sunlight, fertilizers, concentrated carbon dioxide, oxygen) need to be built and operated, and this in turn consumes fossil fuels.⁷¹ Additional energy is required to work up the cyanobacterial products.

A hybrid type of photo bioreactor was developed for the growth of algae and cyanobacteria by considering the influence of various parameters such as CO₂ concentration, availability of light, temperature, pH, and O₂ removal rate.⁷² For instance, Kumar et al. developed a composite (or mixed) bioreactor getting maximum yield and maximum energy efficiency of the process.⁶⁸

A class of enzymes widely studied are those belonging to the crotonase superfamily, characterized by presence of oxyanion holes that stabilize the formation of enolate anions in their substrates. Furthermore, these enzymes are biotin dependent. Biotin is a vitamin linked to the active site of the enzyme, which plays the role of cofactor in different ATP-dependent carboxylases. The carboxylation reaction involves the capture of bicarbonate by the biotin, which in

turn transfer CO_2 to an acceptor. Generally, the acceptor is Acetyl-CoA so that the enzyme operating carboxylation is called Acetyl-CoA carboxylase.

In other words, this vitamin is responsible for the C-C formation through CO_2 fixation.^{41, 73-75}

Several possible advantages exist for using biotin-dependent carboxylases as catalysts for fuel production. Firstly, a wide variety of enzymes is available, all of the genes encoding the enzymes have been cloned, and activity overexpressed. Secondly, even if the enzymes operate at low concentration of bicarbonate, it is possible to enhance the reaction rate by using other enzymes, which locally increase the bicarbonate concentration and allow to doubling the turn over number even at room temperature and atmospheric pressure.

The major disadvantage for fuel production is that these processes require a continuous input of ATP and of acceptor molecule (acetyl-CoA).⁴¹ Furthermore, biological systems are based on complex and delicate equilibria whose control is demanding. However, investigating the mechanisms of the biological systems is of paramount importance to mimic their ability of exploiting CO_2 as a building block molecule (i.e., photosynthesis process shown in Figure 7).



Figure 7. Simplified scheme of natural photosynthesis process by plant.

In this way, it would be possible to develop a green industry to produce and to solve the environmental problems. This vision is clearly expressed by the famous sentence of G. Ciamician:

“On the arid lands there will spring up industrial colonies without smoke and without smokestacks; forests of glass tubes will extend over the plains and glass buildings will rise everywhere; inside of these will take place the photochemical processes that hitherto have been the guarded secret of the plants, but that will have been mastered by human industry which will know how to make them bear even more abundant fruit than nature, for nature is not in a hurry and mankind is. And if in a distant future the supply of coal becomes completely exhausted, civilization will not be checked by that, for life and civilization will continue as long as the sun shines!”^{76,77}

In this contest, the photocatalysis may be a promising tool to realize this dream.

1.4 Photocatalytic reduction of CO₂

1.4.1 Basic principles of photocatalysis

Sun is considered an unlimited source of energy and a promising driving force for chemical reaction.

The term of Photocatalysis refers to a catalytic process induced by light. Generally, photocatalysts are semiconductors, which are characterized by their unique electric conductive behaviour, intermediate between that of a conductor and an insulator.

In detail, when light of suitable energy is absorbed by the catalyst (semiconductor) one electron is promoted to the conduction band (CB) from the valence band (VB) where a hole is generated (step 1-Figure 8). The energy required to produce this effect is an intrinsic factor for each semiconductor and it is equal to its band gap (ΔE_g), i.e., the difference between the energy of the edges of the conduction and valence bands.

The light absorption occurs when the photon energy (E) is higher or at least equal to ΔE_g . The relationship between the energy of photon E and the wavelength λ of the light is expressed by equation 7,

$$E = \frac{h \cdot c}{\lambda} \quad \text{Eq. 7}$$

where h is Plank constant ($6.626 \cdot 10^{-34}$ J s) and c is light velocity ($2.998 \cdot 10^8$ m s⁻¹). The charges generated upon light absorption (step 1) can either undergo primary recombination, emitting light or heat (step 2), or can be trapped at reactive surface sites (step 3). The trapped charges can either recombine (secondary recombination, process 4), or undergo an Interfacial Electron Transfer Process, whereby the electron reduces an electron acceptor species A to a primary reduction product $A^{\cdot-}$ (step 5a), and the hole oxidizes an electron donor species to $D^{\cdot+}$ (step 5b). In order to avoid back electron transfer (step 7) $A^{\cdot-}$ and $D^{\cdot+}$ must then undergo a rapid conversion to the final products A_{red} and D_{ox} (from step 5a to 6a and from step 5b to 6b).

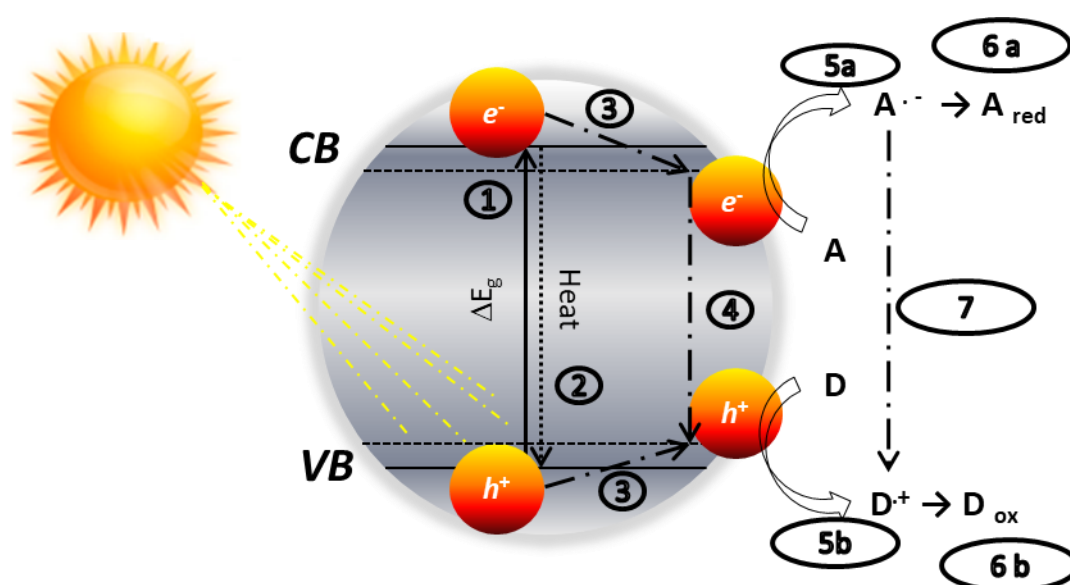


Figure 8. Schematic key processes representation of a photocatalytic reaction at level of a semiconductor particle.

Under the best conditions, thus the electrons and holes may reduce and oxidize, respectively, species adsorbed or in proximity of the surface of the catalyst.

Generally, heterogeneous photocatalysis is carried out in the presence of a solid dispersed in a fluid phase (liquid or gas) similarly to the case of thermal heterogeneous catalysis, and the overall process consists of five independent steps:

1. Transfer of the reactants from the fluid phase to the surface of the catalyst
2. Adsorption of a least one of the reactants
3. Reaction in the adsorbed phase
4. Desorption of the product(s)
5. Removal of the products from the interface region.

These steps are summarised in Figure 9 a and b for catalytic and photocatalytic reactions, respectively.

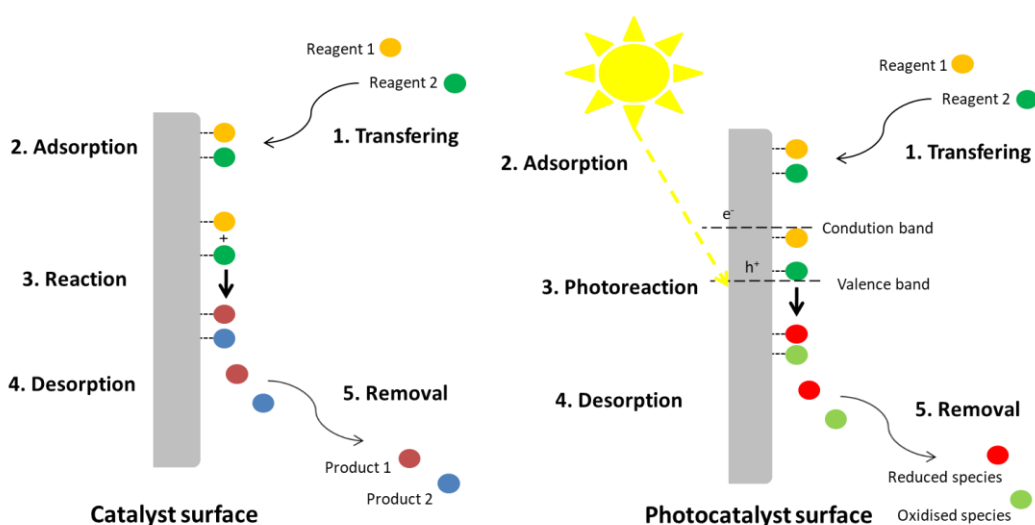


Figure 9. Catalytic and photocatalytic simplified mechanisms.

The main difference between catalysis and photo-catalysis is that the activation process (step 3) is enhanced by heat and light, respectively.

The electron promotion from valence band to conduction band continuously occurs under irradiation, but the consequent reaction of photogenerated charges (e^- and h^+) is lower than the number of promotion events. The charges which are not efficiently trapped or reacted, recombine releasing the surplus of acquired energy either as photons or heat, as above described.

Heterogeneous photocatalysis is a suitable methodology to carry out a large variety of reactions such as metal deposition, organic synthesis, water splitting,

photoreduction, hydrogen transfer, $O_2^{18}-O_2^{16}$ and deuterium–alkane isotopic exchange, water disinfection, anti-cancer therapy, water detoxification, gaseous pollutant removal, isomerisation, etc.^{34, 78-90}

In general, several factors affect the catalyst photoactivity as reported by Rajeshwar et al.⁹¹ and summarized in Table 1.

Table 1. Factors responsible of photoreactivity of semiconductors.

Proprieties	Factors
Optical	Band gap, ΔE
Electronic	Carrier mobility, redox potential of the charges
Structural and morphological	Surface Area, crystallinity, particles size, defects, crystal phase, exposed facets, particle morphology
Surface	Acid-base character, surface groups, defects

These effects are crucial to determine the catalyst photoactivity and capability to perform a selected reaction. These properties acting individually or synergistically, affect UV-vis adsorption, quantum efficiency, reactant adsorption and/or orientation, charge recombination, etc. Sometimes the effect of some properties may be contrasting, so that it is difficult to predict the photocatalytic behaviour. For instance, high specific surface areas generally imply higher adsorption and higher reactivity. On the other hand, materials with a high surface area are generally poorly crystalline with the consequent reduced oxidation/reduction power due to the lower mobility of charges in the lattice.⁹²⁻⁹⁴

From these considerations, it appears clear the importance of the studies on synthesis and characterization of tailored materials. In fact, different techniques are reported to synthesise and to design photocatalysts for specific aims, modulating their proprieties such as crystallinity, defectivity (vacancies in the crystal lattice), surface functionalization, etc.

Titanium dioxide (TiO_2) is the most popular photocatalyst due to its abundance, chemical stability, easy synthesis, no toxicity, low price, easy structural modulation and remarkable photoactivity. The commercial TiO_2 labelled as Evonik ® P25,

comprises of ca. 80% anatase and 20% rutile phases, and it is the most reported one, due to its high activity, so that it is often used as reference catalyst⁷⁸ in many photocatalytic studies.

On the other hand, the main drawback of TiO₂, as well as of other semiconductors absorbing in the UV light range, is that it is able to absorb only at wavelengths shorter than 400 nm so that only 4% of the solar irradiation (the UV portion) is useful for its excitation.

In order to exploit a larger part of the solar spectrum, different techniques have been used as summarised below in Figure 10.

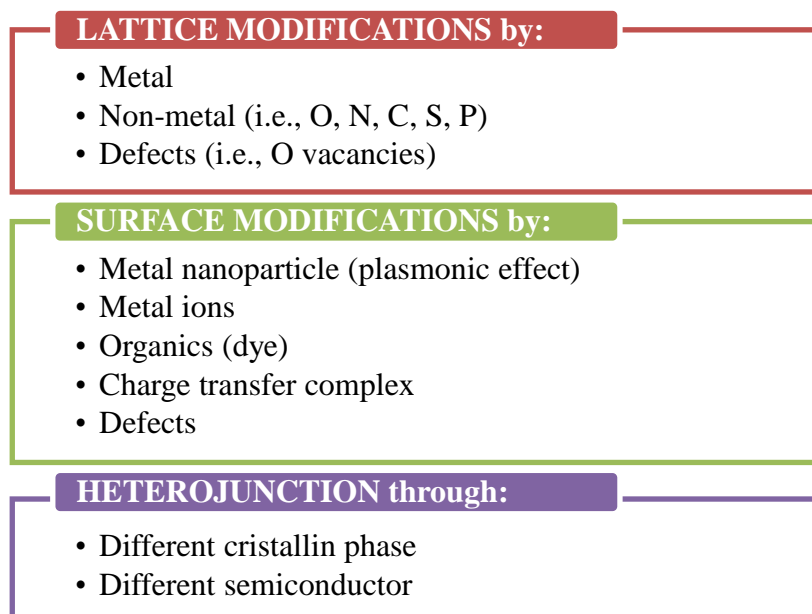


Figure 10. Schematic presentation of principal catalyst modifications.

Structural (lattice) modifications of the semiconductors are characterised by the introduction of foreign atoms into their lattice. This generates intermediate energy states in the band gap thus endowing the material with visible light activity. Similar effect is also achieved by introducing lattice defects such as O vacancies.

Surface modifications are the most commonly used technique to photosensitise the catalyst. To this aim, several techniques are reported in literature based on modification through chromophoric or chromogenic species. Chromophoric species (dyes, metal nanoparticles, metal organic complexes) can be grafted on the semiconductor surface. They absorb visible light (the adsorbate itself is coloured) and subsequently inject electrons into the conduction band of the semiconductor. This mechanism is also known as *photo-induced electron transfer*.

In particular, the visible light absorption, in the case of metal nanoparticles, is due to the so-called plasmonic resonance. This effect gives rise to a local electric field, which further boosts photoexcitation.

On the other hand, the chromogenic species allow visible light activation of a system in which neither the catalyst nor the adsorbate (generally enediols, chlorophenols) absorb visible light. The adsorbate is colourless but becomes coloured when adsorbed on TiO_2 . This mechanism is also known as *optical electron transfer*.

The heterojunction modifications can be built between two or more different semiconductors (TiO_2 and CeO_2) or by means of two different crystal phases belonging to the same type of semiconductor (TiO_2 anatase and rutile). In order to form a heterojunction, the requirement that each material is a semiconductor with unequal band gaps is somewhat lost, especially on small length scales, where electronic properties depend on spatial properties.

There are three typical types of heterojunction: Type I (Figure 11A), Type II (Figure 11B) and Type III (Figure 11C). In all cases, both semiconductors are in a photoexcited state.

In the heterojunction of type I, both photogenerated charges just migrate to SC-I (semiconductor I) from SC-II (semiconductor II) with any effect on charge separation in each semiconductor. Similarly, no separation of charges is caused in type III heterojunction where each couple e^- and h^+ works alone without any cooperative effect, as shown in Figure 11C.

In contrast, the type II heterojunction, as shown in Figure 11B, presents thermodynamic compatibility of valence band (VB) and conduction band (CB) of

SC-I and VB and CB of SC-II. In fact, the photogenerated h^+ migrate from VB of SC-I (more positive potential) to VB of SC-II (less positive potential). The opposite migration occurs for the e^- photogenerated on the SC-II, decreasing the recombination e^-h^+ events.

Clearly, only type II heterojunctions are beneficial because they give rise to enhancement of charges separation, and consequently the photocatalytic activity improves.

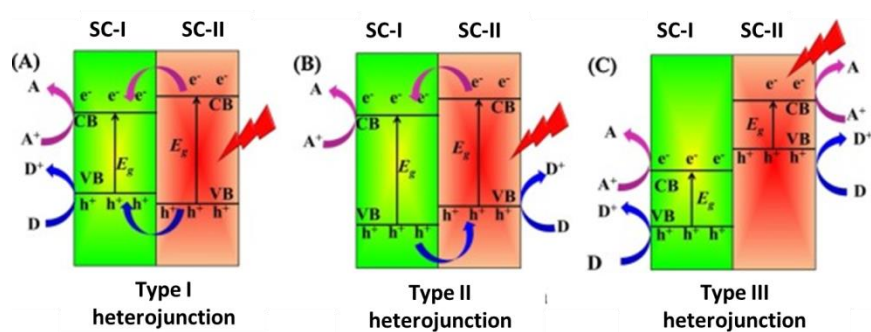


Figure 11. Separation charges in the different types of heterojunctions as reported from Li et al.⁹⁵

A particular situation occurs when the heterojunction is formed by one material with two different crystalline phases. In this case, the enhanced charges separation effect is lower than above reported, due to the very similar values of CB and VB.

Another possible charge migration pathway, which may occur in the type II heterojunction, is called “Z-scheme”, due to the Z shaped path of the electron transfer (Figure 12).⁹⁶

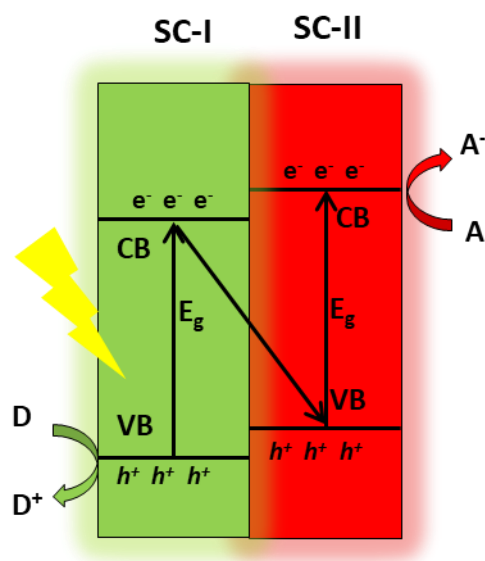


Figure 12. Z scheme representation.

In both cases, spatial charge separation is achieved. However, in the Z-scheme electrons and holes mostly populate CB and VB of SC-II and SC-I, respectively. On the contrary, in the type II heterojunction electrons and holes mostly populate CB and VB of SC-I and SC-II, respectively.

In addition, it should be noted that charge-carrier migration for the direct Z-scheme photocatalyst is physically more feasible than that for type-II heterojunction photocatalysts (Figure 12), since the migration of photogenerated electrons from the CB of TiO₂ semiconductor to the photogenerated hole-rich VB of GaP, for instance, is favourable due to the electrostatic attraction between the electron and hole.⁹⁵ Notably, even if it is a difficult task, experimental measurements of the potential of the photogenerated charges may be useful to discriminate between the two mechanisms.

Depending on the desired composite, the synthesis of mixed semiconductors can be carried out by co-precipitation methods (heterojunction formation), by impregnation methods (heterojunction formation or surface functionalization), by hard mechanical treatments by using planetary ball milling (heterojunction formation), by electro or photo-deposition (nanoparticle metal-catalyst), by thermal

treatment in air or in controlled atmosphere (doped-catalyst or nanoparticle metal-catalyst), etc.

Notably, considerations about charges (e^- and h^+) lifetime would result very interesting. In fact once created, these carriers need to transfer to the surface of the catalyst and maintain their separation as long as the desired reactions occur. The carrier lifetimes are on the nanosecond order in typical semiconductors.⁹⁷ In contrast, i.e., the water reduction and oxidation half-reaction need milliseconds and seconds, respectively, to proceed. Clearly, the carrier lifetimes are not long enough for single semiconductors. In nano-crystalline materials, the diffusion length is not too small; the problem usually lies in too short lifetime on the surface. To improve the charge separation, and thereby their lifetime, and to increase the rate of the surface reactions, some modification techniques are also used such as introduction in the lattice of metals and non-metals, metal ions and metal nanoparticle surface loading, and the heterojunction formation.

In this contest, a huge number of researches found heterogenous photocatalysis as a promising green method to perform CO_2 valorisation in order to obtain high added value compounds.

1.4.2 Photocatalytic reduction of CO_2 : Overview

Photocatalysis has been reported as a method for activating and converting CO_2 into high added value compounds. Given the high CO_2 stability, the adsorption strategy of CO_2 onto a photocatalyst surface is a key factor to decrease the energy barrier. In particular, through adsorption, the linear structure of CO_2 should possible bend in order to decrease the energy of the lowest unoccupied molecular orbital level. Thereafter, sequential of CO_2 reduction should begin with one-electron transfer to form the corresponding anion radical $CO_2^{\cdot-}$ (Eq. 6). Further reactions mostly involve the transfer of electrons or protons, to break C-O bonds, and create new C-H bonds.⁹⁸ To this aim the potential of the charge carriers, the operating conditions and the type of reductant play a key role. All of these features influence the different distribution of the final products.⁹⁹⁻¹⁰¹ First of all,

photocatalytic reduction of CO₂ required the presence of reductant species in order to scavenge the photogenerated hole making the electron photogenerated more available. The main reductants used to this purpose are H₂O, H₂, CH₄, and CH₃OH,¹⁰² which, undoubtedly, differently affect the reaction pathways.

It is reported that, carbon-free reductants such as H₂O and H₂ lead to the formation of C₁ and C₂ products. Even if H₂ is favoured in agreement with the eq. 8, its use is not the best choice for economic and safety reasons.



On the contrary, H₂O being an excellent green and cheap compound represents the best alternative, and it is commonly used to CO₂ photoreduction.

Unfortunately, there is limited knowledge on the actual reaction routes, so that several pathways have been proposed.

The first step is the formation of CO₂^{·-} anion radical through one electron transfer from the CB of the photocatalyst to CO₂ (Eq. 6).^{103, 104}

By observing Figure 13, it can be seen that electrons photogenerated in the conduction band of the most candidate semiconductors do not have enough negative potential driving force to carry out the one-electron reduction of CO₂ to CO₂^{·-}.^{105, 106}

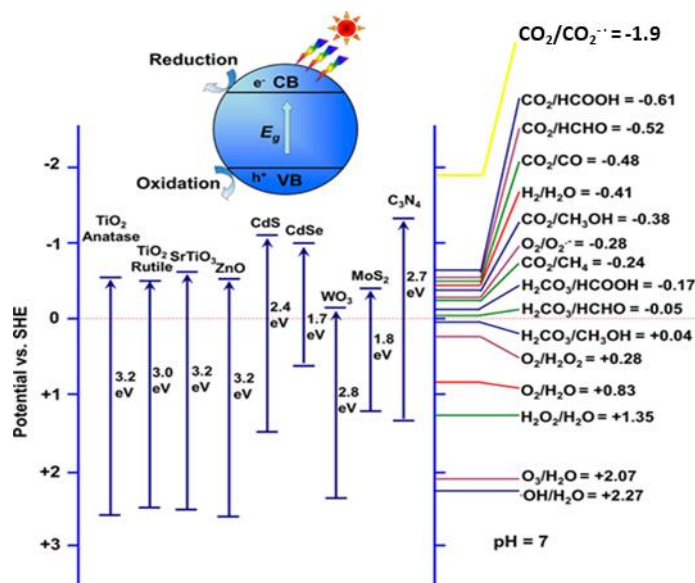


Figure 13. Potentials for various redox couples in water (pH 7) and the band-edge positions of semiconductor photocatalysts reported by Kou et al.⁹⁰

Figure 13 summarizes the association between band-edge positions of photocatalysts and the potentials for various redox couples in water (pH 7).^{90, 102, 107}

The thermodynamic limitations would make impossible the activation of the CO₂ molecule.¹⁰

However, multi-electron transfer reactions coupled with proton exchange possess suitable redox potential so that the formation of a high-energy CO₂^{•-} radical can be bypassed (Table 2). This Proton Coupled Electron Transfer has been firstly highlighted in a pioneering photoelectro-chemical study carried out in liquid phase from Inoue et al. on 1979.

Table 2. The main products of CO₂ reduction using water as reductant and the corresponding reduction potentials with reference to SHE (Standard Hydrogen Electrode) at pH 7 in aqueous solution, 25 °C and 1 bar gas pressure.¹⁰

Reaction	E ₀ (V vs SHE)	Equation (n ^o)
$\text{H}_2\text{O} + 2\text{H}^+ = \frac{1}{2} \text{O}_2 + 2 \text{H}^+$	+1.23	9
$\text{CO}_2 + 2\text{H}^+ + 2\text{e}^- = \text{CO} + \text{H}_2\text{O}$	-0.51	10
$\text{CO}_2 + 2\text{H}^+ + 2\text{e}^- = \text{HCOOH}$	-0.58	11

$\text{CO}_2 + 6\text{H}^+ + 6\text{e}^- = \text{CH}_3\text{OH} + \text{H}_2\text{O}$	-0.39	12
$\text{CO}_2 + 8\text{H}^+ + 8\text{e}^- = \text{CH}_4 + 2\text{H}_2\text{O}$	-0.24	13
$2\text{CO}_2 + 12\text{H}^+ + 12\text{e}^- = \text{C}_2\text{H}_5\text{OH} + 3\text{H}_2\text{O}$	-0.33	14
$2\text{CO}_2 + 14\text{H}^+ + 14\text{e}^- = \text{C}_2\text{H}_6 + 4\text{H}_2\text{O}$	-0.27	15

By considering the number of electrons transferred, formation of CO and HCOOH, requiring just two electrons (Eq. 10 and 11 in Table 2, respectively), should be kinetically favoured. On the other hand, CH₄ formation should be thermodynamically favoured by considering its reduction potential.

However, in the relevant literature it is reported that the product distribution strongly depends on the operating conditions. For instance, being the same number of electrons required (2e⁻) formation of CO is favoured in gas phase, whilst formation of HCOOH is favoured in liquid phase. Furthermore, even if CH₄ formation is thermodynamically favoured with respect to CH₃OH, it has been detected only in gas phase reactions while CH₃OH formation (6e⁻ required, eq. 12 in Table 2) was observed both in liquid and gas phase reactions.

Recently, Olivo et al.,¹⁰⁸ compared the product distribution in vapour and liquid phase tests, and they found that the reduction of H⁺ to H⁻ strongly affects the process activity and selectivity depending on the reaction medium. As shown in Figure 14, in this the study authors pointed out that in the gas phase the deoxygenation step is faster than hydrogenation thus causing the preferential formation of CH₄. On the contrary, in liquid phase CH₃OH, HCHO and HCOOH are the main products as the hydrogenation step is faster than the deoxygenation.

Another method to enhance the reduction efficiency of CO₂ is the use of a hole-scavenger. Several low molecular weight organic compounds such as MeOH, EtOH or TEOA (triethanolamine) are suitable to this aim. Unfortunately, these compounds are also products of CO₂ photoreduction, (Table 2); therefore, their use should be avoided. Inorganic sacrificial agents are more appropriate such as Na₂SO₃ or Na₂S salts.

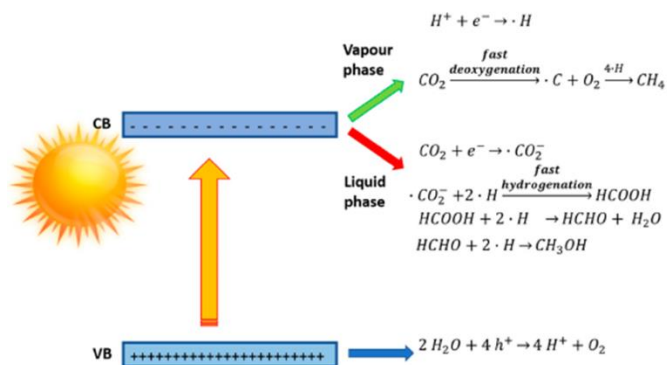


Figure 14. Different reaction mechanisms in liquid and gas phase reported from Olivo et al.¹⁰⁸

Stolarczyk et al.⁹⁷ observed that the use of sacrificial agents reduces the overall efficiency of the process. The difference between the redox potentials of the reduction and oxidation half-reaction determines the amount of energy stored in the photocatalytic process. The use of a sacrificial agent provides an additional loss mechanism, because the stored energy is accordingly decreased by the difference between the redox level of the scavenger and that of CO₂ reduction.⁹⁷

From all of the above-mentioned considerations, the choice of the opportune photocatalyst is extremely relevant and still a challenging task. Suitable surface characteristics should allow a better CO₂ reduction and water oxidation.

In the following sections, detail on CO₂ reduction carried out in the presence of TiO₂, ZrO₂, C₃N₄ and graphene based material will be presented because they are relevant for the aim of this Ph. D thesis.

1.4.3 Photocatalytic reduction of CO₂: Metal oxide materials, TiO₂ and ZrO₂

For the first time, Inoue et al.¹⁰⁵ carried out photocatalytic CO₂ reduction in liquid phase by using several semiconductors such as TiO₂, WO₃, ZnO₂, CdS, GaP, and SiC using H₂O as reducing agent. This pioneering work, reported the production of

HCHO, HCOOH, CH₃OH and trace of CH₄, under 500W Xenon or 500 W high-pressure mercury arc lamp.

Titanium dioxide is a white solid, thermal stable, no toxic, and a cheap material used in a huge number of industrial products such as sunscreens, toothpastes, paint, food additives (E171), etc.

TiO₂ is naturally occurring in three allotropic forms named anatase, rutile, and brookite. TiO₂ can be also synthesised starting from inorganic or organic precursor, by hydrolysis of TiCl₄, TiOSO₄, or alkoxides such as titanium isopropoxide and butoxide. By opportunely tailoring the operating conditions of the synthesis (appropriate precursor, pH, thermal treatment, additives, separation process), it is possible to obtain only one, two or all of the above mentioned crystal phases and to set the particle size and specific surface area.¹⁰⁹⁻¹¹² Furthermore, with the aim of CO₂ photoreduction, a recent research published by Yang et al.,¹¹³ focused the attention on TiO₂ precursors. By diffuse reflectance infrared Fourier transform spectroscopy and isotopically labelled ¹³CO₂, this study demonstrates that carbon residues deriving from precursors and solvents participate to the CO formation. Therefore, authors^{114, 115} suggest to “cleaning” the photocatalysts under irradiation prior to their use for CO₂ reduction.

The three allotropic TiO₂ forms have different band gap energies. As reported by Monai et al.,¹¹⁶ anatase and rutile show band gap approximately equal to 3.2 and 3.02 eV, respectively. The values reported for brookite ranges between 3.1 and 3.4 eV.¹¹⁶ The conduction band edge for TiO₂ is ca. -0.5 eV (Figure 13). So that, it is a candidate for the CO₂ reduction.

As above-mentioned, until 1979 to now a huge number of investigations on CO₂ reduction were published, especially using titanium dioxide, and some of these reports are summarised in Table 3.

Table 3. Literature survey of photocatalytic CO₂ reduction catalysed by pristine and doped TiO₂ based materials using H₂O as the reducing agent in batch reactor.

Photocatalyst	Light source, phase, Pressure, Temperature, etc	Products, $\mu\text{mol g}^{-1}\text{h}^{-1}$	Ref.
TiO ₂	75 W high pressure Hg, gaseous, 2 °C	CH ₄ ($3.5 \cdot 10^{-3}$), CH ₃ OH ($2.4 \cdot 10^{-3}$), CO traces	117
TiO ₂	4.5kW Xenon lamp, liquid and gaseous, NaOH, 0.25 μbar , 20°C	CH ₄ (0.08),CH ₃ OH (0.15), H ₂ (0.18), C ₂ H ₅ OH (0.25), C ₂ H ₄ (traces) Total product in gas and liquid phase.	118
TiO ₂	990 W Xenon lamp, liquid, 65 bar, 25°C	HCOOH (0.6)	119
TiO ₂ (P25)	15 W GTE F15T8/BLB lamp, liquid, 25°C	CH ₃ OH (0.41 $\mu\text{M g}^{-1}\text{h}^{-1}$)	120
TiO ₂ (TiCl ₄)	400 W medium pressure Hg, gaseous	CH ₄ (0.01),CH ₃ CHO (traces),HCHO(0.03)	110
TiO ₂ (P25)	125 W medium pressure Hg, liquid, 7 bar, 80°C, Na ₂ SO ₃ hole trap	CH ₄ (0.01),CH ₃ OH (0-351),HCHO(0-16560), CO (0.7-13),H ₂ (0-103),HCOOH (59-2960)	108
TiO ₂	A300W HRC UV-VIS and 400 W Xe-Halogen lamp, liquid, NaOH, NaHCO ₃ , 25°C	HCOOH (16-23)	121
Cu/TiO ₂	75 W high pressure Hg, 2 °C	CH ₃ OH ($6 \cdot 10^{-3}$)	117
1% Cu/TiO ₂ (TiCl ₄)	400 W medium pressure Hg, gaseous	CH ₄ (0.017),CH ₃ CHO (0.01), HCHO(0.2)	110
TiO ₂ (P25) GaP/TiO ₂	1500Whigh pressure Xe lamp, gaseous, 70°C	CH ₄ (0) CH ₄ (0.52)	122
Me/Porphirine/TiO ₂ (Me=Zn,or Cu)	300W HRC UV-VIS and 400 W Xe-Halogen lamp, liquid, NaOH, NaHCO ₃ , 25°C	HCOOH (6.5-26)	121
1-7% Ag/TiO ₂	8W Hg lamp, liquid,	CH ₄ (0.36), CH ₃ OH (0.072) CO (0.048), H ₂ (5.6)	105
CuO/TiO ₂	250 W high pressure Hg lamp, liquid, 25 °C, MeOH, CTAB	HCOOCH ₃ (1600)	123
TiO ₂ CeO ₂ /TiO ₂	500 W Xenon lamp, liquid, NaOH,	CH ₄ (6 $\mu\text{mol g}^{-1}$) CH ₄ (18.6 $\mu\text{mol g}^{-1}$)	124
Pd/RuO ₂ /TiO ₂ Pd/TiO ₂ , TiO ₂	450 W Xe short arc lamp, liquid, NaOH, NA ₂ SO ₃ hole trap,	HCOO ⁻ (72 ppm) HCOO ⁻ (69 ppm) HCOO ⁻ (20 ppm)	125
TiO ₂ N-TiO ₂ nanotubeN-TiO ₂	500 W tungsten-halogen lamp, liquid, NaOH,	HCOOH (20) HCOOH (334), HCHO (70) HCOOH (1040), HCHO (77), CH ₃ OH (94)	126
Cu/Ce/TiO ₂	125 W UV lamp, liquid, NaOH, 50-70-90 °C,	CH ₃ OH (5-11.3)	127
TiO ₂ (P25) TiO ₂ /Cu/C	32 W Hg lamp, liquid, NaOH, 25 °C	CH ₄ (1.5), CO (7.7) CH ₄ (2.5), CO (20)	128
TiO ₂ /SBA-15	120 W high-pressure Hg lamp, gaseous, H ₂ O or H ₂ as reducing agent	CH ₄ (4.3-2.1 ppm) C ₂ H ₄ (2.5-1.4 ppm) C ₂ H ₆ (3.7-0.8 ppm)	129
TiO ₂ /SBA-15 Au/TiO ₂ /SBA-15	200 W Hg/Xe lamp, gaseous, He	CH ₄ + C ₂ H ₆ + C ₃ H ₈ + C ₄ H ₁₀ (ca. 30 ppm) CH ₄ + C ₂ H ₆ + C ₃ H ₈ + C ₄ H ₁₀ (ca. 37 ppm)	114

TiO ₂ TiO ₂ /Y-zeolite Pt TiO ₂ /Y-zeolite	high-pressure Hg lamp, gaseous, 55 °C,	CH ₄ (0.5) CH ₄ (5), CH ₃ OH (0.5) CH ₄ (8), CH ₃ OH (5)	130
Cd/Se/ TiO ₂	300 W Xe arc lamp, liquid	CH ₄ (48 ppm g ⁻¹ h ⁻¹), CH ₃ OH (3.3 ppm g ⁻¹ h ⁻¹), H ₂ and CO (traces)	131
TiO ₂ micro-size 1% Pt/TiO ₂	300 W Xe lamp, gaseous	CH ₄ (2.5), CH ₄ (6)	132
P25 TiO ₂ Pt/ TiO ₂ Cu ₂ O/ TiO ₂	300 W Xenon arc lamp, 0.8 bar, gaseous, porous structure	CH ₄ (3.7 ppm g ⁻¹ h ⁻¹) CH ₄ (2.4 ppm g ⁻¹ h ⁻¹) CH ₄ (3.2 ppm g ⁻¹ h ⁻¹) CH ₄ (28.4 ppm g ⁻¹ h ⁻¹)	133
TiO ₂ Anatase Ni- TiO ₂ Ni-CNT/TiO ₂	75 W visible daylight lamp, gaseous	CH ₄ (0.04) CH ₄ (0.05) CH ₄ (0.07)	134

As reported in Table 3, TiO₂ has been differently modified in order to improve the CO₂ reduction efficiently. For instance, TiO₂ has been decorated with metal (Ag, Pt, and Rh) nanoparticles in order to take advantage of the plasmonic effect and of the resulting visible absorption. Metal ions loaded on the TiO₂ surface acting as electrons sink in order to enhance the available electrons. TiO₂ has been also coupled with other metal oxide such as CeO₂ able to increase the CO₂ absorption.

Another promising way to increase the TiO₂ photocatalytic performance toward the CO₂ reduction is its coupling with graphitic materials such as graphene or carbon nitride (C₃N₄). In the first case the electron hole recombination phenomena, generally limiting the TiO₂ efficiency, are reduced due to the outstanding conductivity of graphene. Coupling TiO₂ and C₃N₄ not only favours spatial charges separation (see section 1.3.1), but also enlarges the absorption of the composite towards visible light, being C₃N₄ a yellow coloured powder. The graphitic C₃N₄ and graphene TiO₂ composite will be discussed later in the 1.3.4 and 1.3.5 sections.

While the TiO₂ based materials have been extensively investigated, few researches have explored the potential of Zirconium dioxide (ZrO₂) to obtain high added value molecules from CO₂ photoreduction. ZrO₂ is a white solid, most naturally occurring in its monoclinic crystalline structure, in baddeleyite minerals (ZrSiO₄).

ZrO₂ is industrially prepared from natural ores, ZrSiO₄, by the alkali fusion, plasma fusion or a carbon reduction methods. Zirconium is a transition metal electronically similar to titanium. Due to its ion conductivity^{135, 136} high chemical stability and resistance to corrosion, ZrO₂ is used for biomedical application¹³⁷ as an implant biomaterial,¹³⁸ for dental crown,¹³⁹ femoral heads for total hip replacement.¹⁴⁰

Due to its proprieties, ZrO₂ finds also applications as solid oxide in fuel cell¹⁴¹ and catalysis,^{135, 141} for reaction of hydrogenation, dehydration and skeletal isomerization of hydrocarbons.¹⁴²⁻¹⁴⁴

The reason for the poor interest to use ZrO₂ as photocatalyst is due to the wide band gap value ranging from 5 to 7 eV depending on the phase (cubic, tetragonal, monoclinic, or amorphous). However, due to its outstanding thermal stability and to the presence of both surface acid and basic sites, ZrO₂ has found applications in photo-oxidation of chemicals¹⁴⁵⁻¹⁴⁷ and water photo splitting.¹⁴⁸

Furthermore, the very negative potential of photogenerated electrons makes ZrO₂ a good candidate for photoreduction reactions. In fact, the conduction band edge lies at ca. -1.0 V (vs. SHE, pH 0),¹⁴⁸ i.e., much more negative than that of TiO₂ anatase (-0.1 V), whereas the potential of the valence band is ca. +4.0 V, more positive than that of TiO₂ (+3.1 V). Introduction of new electronic states in the wide band gap ZrO₂ by defects or doping with rare earth elements modifies the optical properties of ZrO₂ giving rise to an active photocatalyst, which can absorb also fractions of the visible light as reported by Gionco et al.^{147, 149}

Furthermore, favourable CO₂ adsorption onto ZrO₂ is reported in the relevant literature. In fact, structural studies, reported high concentration of acid and basic sites, as measured by the amount of irreversibly adsorbed ammonia and CO₂, respectively.¹⁴³ In detail, ZrO₂ calcined at 600°C exhibits 0.6 μmol/m² of acidic and 4 μmol/m² of basic sites. Additionally, infrared spectroscopic studies revealed the presence of Lewis type acid sites, but not protonic (Bronsted acid) sites.

Some studies report ZrO₂ induced CO₂ photoreduction by water as the reductant. For instance, Lo et al., obtained 0.1 μmol g⁻¹ h⁻¹ of CO from CO₂ and H₂O under UV light set at 43°C and at 1.1 bar in the presence of ZrO₂.¹⁵⁰ In particular high

products yield was obtained using H₂-H₂O mixture or just H₂ but not with only water.¹⁵⁰

However, the best results are reported by Sayama et al., which tested ZrO₂, 0.1% Pt-ZrO₂, 0.1% Au-ZrO₂, 1% Cu-ZrO₂, 1% RuO₂ – ZrO₂ photocatalysts. The highest values of CO and H₂ formation i.e., 1.1 and 285 μmol h⁻¹ respectively, were obtained in the presence of bare ZrO₂.¹⁴⁸

1.4.4 Photocatalytic reduction of CO₂: Graphene composite materials

Graphene is a planar 2D material characterized by a honeycomb-like structure of sp² carbon atoms. The synthesis of graphene from graphite essentially involves mechanical or chemical exfoliation.¹⁵¹ The mechanical exfoliation represents the easiest method, but unfortunately affords low yields and requires long production time.¹⁵² On the contrary, chemical exfoliation appears suitable for large-scale production. One of the most common chemical exfoliation methods is called colloidal suspension and it was developed by Brodie,¹⁵³ Staudenmaier,¹⁵⁴ and Hummers.¹⁵⁵ In the presence of strong acids and oxidants, graphite is converted to exfoliated graphene oxide, which in turn can be chemically reduced to graphene.

Graphene is a low cost material with high versatility, tuneable physicochemical, mechanical and chemical stability, opto-electronic properties, excellent electron and thermal conductivity.¹⁵⁶⁻¹⁵⁹ The number of layers, the lateral size, dimensionality, edge structure, defect density, and reduction degree can be also easily controlled.^{160, 161}

Because of these peculiarities, this material finds several applications in electronics,¹⁶² optoelectronics,¹⁶³ and mass and energy transport.¹⁶⁴

Graphene has been used as support for various nano-hybrids materials as semiconductors, being an electron collector and transporter capable to efficiently hinder electron-hole recombination.¹⁶⁵ This action extends the lifetime of the photo-generated charge carriers,¹⁶⁶ making electrons more available for the reduction of

species present in the reacting mixture, while the holes remain localised in the semiconductor valence band. This results in a high spatial charge separation of the photo-induced electron-hole pairs.

Graphene nanosheets present huge theoretical specific surface area,¹⁶⁷ commonly believed as the highest among all of the known materials. Another peculiarity of this material concerns the possibility, during the synthesis by chemical method, to improve the nanoparticles dispersion, and to reduce their size owing to the large volume/surface ratio and to the presence of opportune functional groups. Recent studies demonstrate that these functional groups (i.e., C=O, COOH, etc.) can act as anchoring sites and allow the growth of the photocatalyst particles on their surface.¹⁶⁸ Hence, photocatalysts can be uniformly deposited on the surface of graphene nanosheets, thus inhibiting aggregation. Additionally, because of its black colour and being a conductor (zero band gap), graphene can absorb almost throughout the whole spectrum of solar light, enhancing light absorption of composite. Unlike the good light absorption ability, graphene does not create active electrons or holes for the photocatalytic reactions but it can efficiently transport electrons. Finally, graphene can increase the temperature around the photocatalyst to create a confined photothermal effect.^{169, 170}

Due to the lower cost with respect to noble metals and because of its peculiar physic-chemical proprieties, the photocatalytic application of graphene has been largely investigated. A huge number of researches reports the graphene as cocatalyst for a wide range of photocatalytic applications.¹⁷¹ For example, graphene can prevent CdS from photocorrosion in the visible-light photocatalytic H₂ production.¹⁷² It can address the selectivity of CdS towards aldehydes in alcohols oxidation reactions, under mild conditions.¹⁷³

By wrapping the photocatalyst such as Cu₂O and CdS and avoiding their photocorrosion induced by the attack of active species, such as •OH radicals,¹⁷⁴ graphene increases the cocatalyst stability.

Furthermore, graphene can be used as cocatalyst to increase the reduction ability such as in the case of metal oxide. As shown in Figure 15, the best photocatalysts

for the occurring of reduction reactions are carbon nitride (C_3N_4), CdS, Cu_2O , ZnS. Notably, on the contrary, the metal oxide material exhibits oxidation ability.

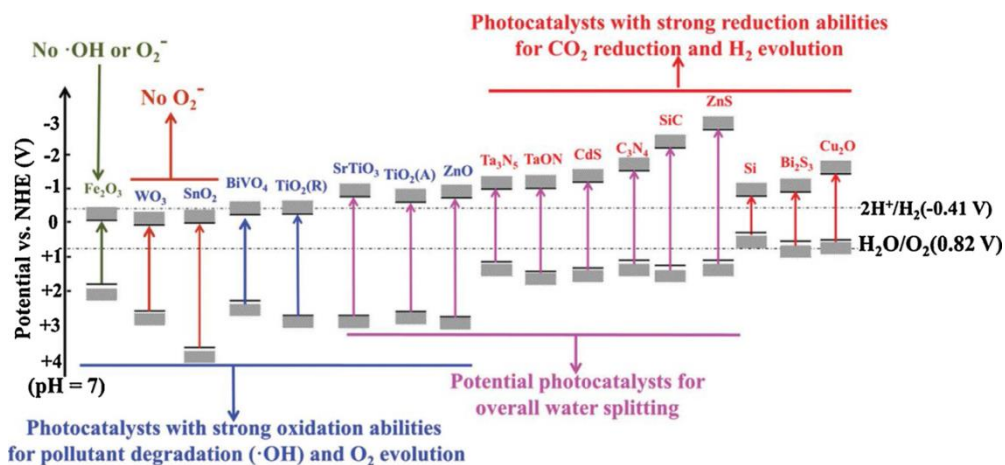


Figure 15. Band positions and potential applications of some typical photocatalysts at pH = 7 in aqueous solutions, reported from Li et al.¹⁷⁵

In fact, several researches propose the graphene/ TiO_2 heterojunctions as promising photocatalysts in the field of energy conversion and environmental applications.^{165, 166, 176}

Two key points make graphene a promising cocatalyst for the photocatalytic CO_2 reduction: (i) Electron conductivity: the electron density¹⁷⁷ on the graphene nanosheet is high and favours multi-electron reactions for photocatalytic CO_2 reduction (Table 2). (ii) CO_2 adsorption and activation. Due to the graphene large 2D π -conjugated structure and the delocalized π -conjugated binding π^*_3 of CO_2 , a π - π conjugation interaction can be established between graphene and CO_2 . The graphene π - π conjugation interaction can significantly facilitate the adsorption of CO_2 molecules on the graphene-based photocatalysts, thereby improving the photocatalytic CO_2 reduction activity. Notably, this interaction can also cause destabilization and activation of CO_2 molecules enhancing photocatalytic CO_2 reduction reactions.¹⁷⁴

Table 4. Literature survey of photocatalytic CO_2 reduction catalysed by G based materials, focusing to TiO_2 /graphene composites, using H_2O as reductant in batch reactor.

Photocatalyst	Light source, phase, Pressure, Temperature, etc.	Products, $\mu\text{mol g}^{-1} \text{h}^{-1}$	Ref.
0.27 % G/P25 (0.27, 0.55, 1.09, 2.15 G%)	100W Hg lamp or 60W, Halco Lighting, Pure Lite Neodymium Vis lamp, gas phase, film catalyst 6.45 cm^2	CH_4 ($8.3 \mu\text{mol m}^{-2} \text{h}^{-1}$) under UV CH_4 ($4 \mu\text{mol m}^{-2} \text{h}^{-1}$) under Vis	178
8.5 % G/TiO ₂ (2.21, 8.5, 16.39 G%)	150W Vis lamp, 25 °C, liquid phase, 1 mol/L NaOH	CH_3OH (15) HCOOH (16)	179
0.5 % G/P25 ₂ (0.25, 0.5, 1 G%)	100W Hg lamp or 60W, Halco Lighting, Pure Lite Neodymium Vis lamp, gas phase, film catalyst 6.45 cm^2	CH_4 ($9.3 \mu\text{mol m}^{-2} \text{h}^{-1}$) under UV CH_4 ($0.15 \mu\text{mol m}^{-2} \text{h}^{-1}$) under Vis	180
2 % G/P25 ₂ (0, 1, 2, 5 G%)	300 W Xe lamp, gas phase	CH_4 (8) C_2H_6 (16.8)	181
TiO ₂ /G N-TiO ₂ /G	15 W Vis Lamp TORNADO 220–240 V Philips, 25 °C, gas phase	CH_4 (3.21) CH_4 (3.60)	182
GO/P25 G/P25 B-G/P25	300 W Xe lamp, 25 °C, liquid phase, Na ₂ SO ₃ hole trap	CH_4 (0.32) CH_4 (0.7) CH_4 (1.25)	183
G/WO ₃	300 W Xe lamp, 1 mL H ₂ O, gas phase,	CH_4 (1.11)	184
GO N doped G N doped G/CuC	20W-F-Hope LED Opto-Electric, DMF and H ₂ O, liquid phase,	CH_3OH (16) CH_3OH (31) CH_3OH (70)	185
1% NiO _x - Ta ₂ O ₅ /G	400 W metal halogen lamp, liquid phase, HCO ₃ ⁻ , CO ₂ , NaOH	CH_3OH ($1 \mu\text{mol h}^{-1}$) H ₂ ($0.82 \mu\text{mol h}^{-1}$)	186
Cu ₂ O/ G	six lamps at 8.3 mW/cm ² USHIO G8T5, gas phase, NaOH, 35 °C	$\text{CH}_3 \text{CH}_2\text{OH}$ (20) H ₂ (140)	187
GO/TiO ₂ Cu-GO/TiO ₂	UV/vis Heraeus TQ 150 medium-pressure Hg vapour lamp, 25°C, liquid phase, He/CO ₂ , at different pH, several Cu precursor	CH_3OH (12-45) $\text{CH}_3 \text{CH}_2\text{OH}$ (17-150) CH_3OH (8-60) $\text{CH}_3 \text{CH}_2\text{OH}$ (17-90)	188
G/TiO ₂ in spheres of PMMA or PEI	300 W Xe arc lamp, gas phase,	CH_4 (1.2) CO (9)	189

*where GO and G are graphene oxide and graphene respectively.

Table 4 presents a survey of relevant reports focusing on the use of graphene-based materials for CO₂ photoreduction, in particular between graphene and TiO₂.

As reported in the Table 4, the graphene-based materials produce preferentially CH₄ and methanol from CO₂ photoreduction. In all the reported studies, the materials are generally synthesised by means of solvothermal, hydrothermal, or electrostatic self-assembly strategies ultrasound assisted methods or through.

1.4.5 Photocatalytic reduction of CO₂ by C₃N₄ pristine, O doped and composite TiO₂/g-C₃N₄

Recently, due to its facile synthesis, no toxicity, reduction activity, enhanced photoexcited charge conductivity,¹⁹⁰ appealing electronic band structure and high (claimed) physicochemical stability,¹⁹¹ 2D graphitic carbon nitride (g-C₃N₄), a new metal free polymer has been introduced as an emergent photocatalyst.

g-C₃N₄ consists of earth-abundant C and N elements bond in a π rich aromatic structure easy to be modify without significant structural and composition changes.¹⁹¹

The g-C₃N₄ exists in seven different phases, i.e., α -C₃N₄, β -C₃N₄, cubic C₃N₄, pseudo cubic C₃N₄, g-h-triazine, g-h-heptazine and g-o-triazine with band gap energy of 5.49, 4.85, 4.30, 4.13, 2.97, 2.88 and 0.93 eV, respectively.^{192, 193} Although all these phases are semiconductors, only g-h-heptazine and g-h-triazine, containing 14 and 28 of C and N atoms respectively in the elementary cells, possess suitable band gap and band edge potentials to drive photocatalytic processes.^{192, 193} However, by considering the position of the valence band, only the g-h-heptazine phase meets the potential requirements for water oxidation.^{192, 193} For this reason g-C₃N₄ in this form, is one of the most frequently investigated photocatalysts for H₂ production. Additionally, in principle, the CB edge of g-C₃N₄ is enough negative to reduce CO₂ (Figure 16).^{191, 194, 195}

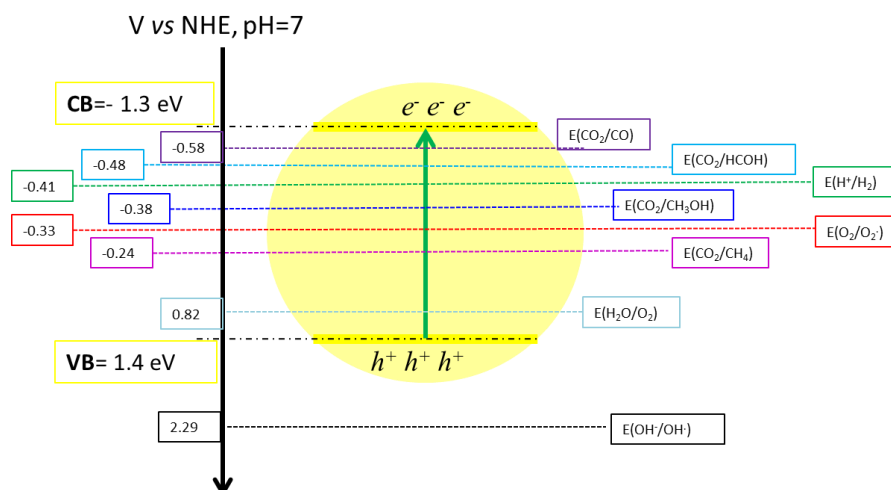


Figure 16. The redox potentials of the relevant products of CO₂ reduction with respect to the estimated position of the g-C₃N₄ conduction and valence band edges (CB and CV) at pH 7.¹⁹⁵

g-C₃N₄ shows other advantages for CO₂ photoreduction because it is rich of N basic sites, which favour the CO₂ adsorption step. Due to these outstanding properties, several reports were published on different synthetic strategies affording specific crystal phase, surface area, band gap position and band gap energy.

The most common g-C₃N₄ synthesis consists in the thermal condensation of Melamine, or of its precursors (cyanamide or dicyanamide), as reported by Ong et al. (Figure 17).¹⁹¹

g-C₃N₄ results from condensation of various melem units (monomer) having C/N molar ratio of ca. 0.75, which is the theoretical value of the final polymer (Figure 17).

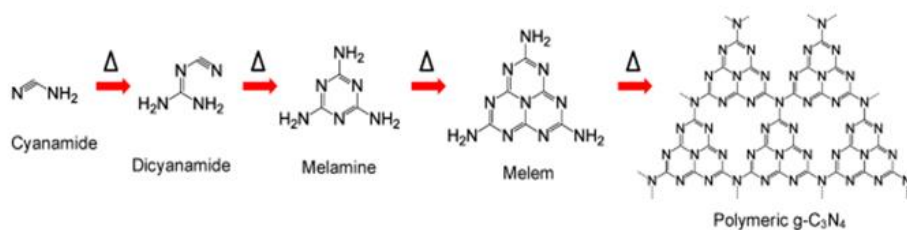


Figure 17. Schematic g-C₃N₄ synthesis by three different precursors, reported by Ong et al.¹⁹¹

The as synthesised polymer generally presents low specific area (ca. $10 \text{ m}^2 \text{ g}^{-1}$), so that the exfoliation process, that can occur by chemical and thermal methods, is used to increase the exposed surface. The thermal treatment seems to be a most simple and effective method also to enhance the photocatalytic and electronic proprieties of $\text{g-C}_3\text{N}_4$.^{196, 197} In fact, thermal treatments reduce the starting bulky material to a layered one.

In this field, computational studies demonstrated that the number of layers influences also the light absorption ability and the corresponding photoactivity (photoelectric proprieties),¹⁹⁸ as reported in Table 5.

Table 5. Band gaps (ΔE_g) of heptazine and triazine $\text{g-C}_3\text{N}_4$ nanosheets with different thickness, obtained by means of computational studies.

Geometry	ΔE_g Heptazine $\text{g-C}_3\text{N}_4$, eV	ΔE_g Triazine $\text{g-C}_3\text{N}_4$, eV
1 layer nanosheet	3.03	3.81
2 layer nanosheet	2.85	3.51
3 layer nanosheet	2.79	3.42
4 layer nanosheet	2.75	3.38
Bulk	2.70	3.31

In order to increase the CO_2 photoreduction activity of carbon nitride, doping is a suitable method to change the band structure and the adsorption properties. By changing opportunely the precursor, it is possible to introduce non-metal atoms into the lattice of $\text{g-C}_3\text{N}_4$, as shown in Figure 18.

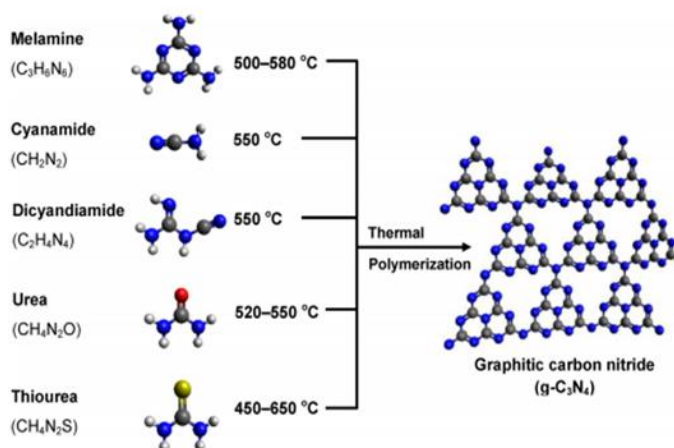


Figure 18. Thermal synthesis to obtain pure and non-metal doped $g-C_3N_4$, reported by Ong et al.¹⁹¹

S doping is generally obtained by using thiourea like precursor O doping derives from urea like precursor or from successive oxidation of $g-C_3N_4$ with H_2O_2 .¹⁹⁹ Treatment of $g-C_3N_4$ with ethylene diphosphonic acid²⁰⁰ or with red phosphor²⁰¹ produces P doping.

The incorporated heteroatoms increase the delocalization of π -electron in the $g-C_3N_4$ structure. This effect causes a red-shift of the optical absorption toward longer wavelengths¹⁹⁴ and generally enhances the photocatalytic activity. The operating conditions used during the doping such as the precursor, additives such as barbituric acid, temperature, pressure, etc.,^{202, 203} affect the dopant position (C or N site), the molar ratio relative C/dopant and, consequently, the theoretical C/N ratio. Recently, Huang et al. reported the formation energies of O-doped $g-C_3N_4$ ($O-C_3N_4$) by substituting N and C atoms using O atom.²⁰⁴ Additionally, this study analyses the formation energy of $O-C_3N_4$ distinguishing the different C and N positions present in the C_3N_4 structure shown in Figure 19.

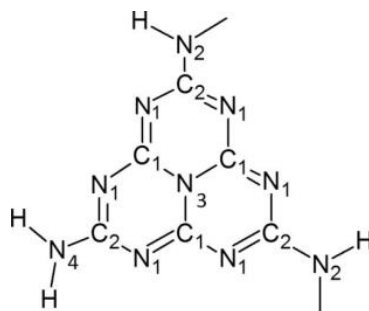


Figure 19. Melem structure repeated in the polymeric C_3N_4 with the corresponding atomic assignment according to XPS analysis as Dante et al. report.²⁰⁵

In general, doping generates a “second semiconductor” whose heterojunction may decrease the charge recombination^{199, 206} increasing the photocatalytic activity. In particular, non-metal dopants generate a cathodic shift of the valence band edge in combination with a higher conduction band minimum causing a slightly reduced absorbance. The effect of O doping is to promote a downshift of the CB minimum by 0.21 eV without modifying the valence band maximum. Furthermore, the O-doping induces intrinsic electronic and band structure modulations, leading to improved surface area, extended visible light response, and enhanced separation efficiency of the photo-generated charge carriers¹⁹⁹. By taking into account these properties, a recent study develops a promising O doped C_3N_4 for CO_2 reduction.²⁰⁶

g- C_3N_4 was successfully coupled with metal oxides to promote CO_2 photoreduction. In fact, it has a more negative conduction band edge (ca. -1.2 eV) than the most common oxide semiconductors (Figure 15), and this should favour CO_2 reaction even under visible light irradiation.

Hydrothermal methods²⁰⁷ coupled with thermal treatments²⁰⁸⁻²¹⁰, impregnation methods²¹¹ and vigorous mixing by milling ball²¹² are the principal strategies used to form heterojunction between TiO_2 and g- C_3N_4 .

g- C_3N_4/TiO_2 composites showed enhanced CO_2 photoreduction activity towards high added value compounds with respect to the pristine materials.

Some reports on CO_2 photoreduction reactions induced by using g- C_3N_4 pure, O- C_3N_4 and C_3N_4/TiO_2 catalysts, are summarised in Table 6.

Table 6. Literature survey of photocatalytic CO₂ reduction catalysed by pristine, O doped and based C₃N₄ materials, using H₂O as reductant in batch reactor.

Photocatalyst	Light source, phase, Pressure, Temperature, etc.	Products, $\mu\text{mol g}^{-1}\text{h}^{-1}$	Ref.
m-g-C ₃ N ₄ u-g-C ₃ N ₄	300 W Xe-lamp with 420 nm cut off filter, liquid phase, NaOH, 1 bar, 20 °C	CH ₃ OH (traces), CH ₃ CH ₂ OH (3.64) CH ₃ OH (6.28), CH ₃ CH ₂ OH (4.51)	213
u-g-C ₃ N ₄ 0.03 ba-u-g-C ₃ N ₄ 0.03 ATCN-u-g-C ₃ N ₄	300 W Xe-lamp with 420 nm cut off filter, liquid phase, 2.2 bypyridine, TEOA, CoCl ₂ , 1 bar and 30 °C, several loading of BA	H ₂ (ca. 1 μmol), CO (2.3 μmol) H ₂ (ca. 5 μmol), CO (31.1 μmol) H ₂ (ca. 7 μmol), CO (37.9 μmol)	214
t-g-C ₃ N ₄ u-g-C ₃ N ₄	300 W Xe-lamp with 420 nm cut off filter, gas phase	CH ₄ (traces), CH ₃ CHO (0.3), CO (0.4) CH ₄ (traces), CH ₃ CHO (0.5), CO (0.6)	215
t-g-C ₃ N ₄ u-g-C ₃ N ₄ P25(TiO ₂)	300 W Xe-lamp with 200 nm cut off filter (UV-Vis light), gas phase	CH ₄ (0.14), H ₂ (0.17), CO (2.1) CH ₄ (0.154), H ₂ (0.22), CO (1.46) CH ₄ (0.1), H ₂ (0.39), CO (0.22)	215
t-g-C ₃ N ₄ m-g-C ₃ N ₄	300 W Xe-lamp UV-vis light, liquid phase, NaHCO ₃ HCl, H ₂ PtCl ₆ , 1 bar	CH ₃ OH (0.37) CH ₃ OH (0.3)	216
m-g- C ₃ N ₄ O- C ₃ N ₄ tube	350 W Xe-lamp with 420 nm cut off filter, gas, NaHCO ₃ and H ₂ SO ₄	CH ₃ OH (0.17) CH ₃ OH (0.88)	206
u-g-C ₃ N ₄ BTN (TiO ₂ nanotube) C ₃ N ₄ /BTN	300 W Xe-lamp with 420 nm cut off filter, gas phase, NaHCO ₃ and H ₂ SO ₄	CH ₄ (1.80), CO (7.10) CH ₄ (0.17), CO (0.74) CH ₄ (5.21), CO (0.84)	208
u-g-C ₃ N ₄ BTN (TiO ₂ nanotube) C ₃ N ₄ /BTN	300 W Xe-lamp with 200 nm cut off filter, gas phase, NaHCO ₃ and H ₂ SO ₄	CH ₄ (2.5), CO (9.3) CH ₄ (0.73), CO (3.31) CH ₄ (6.94), CO (1.27)	208
m-g- C ₃ N ₄ m-porous-g- C ₃ N ₄	300 W Xe-lamp with 420 nm cut off filter, gas phase	CO (4.37) CO (0.94)	217
m-bulk- C ₃ N ₄ m-g- C ₃ N ₄	300 W Xe-lamp with 420 nm cut off filter, 15 °C, 25 kPa, gas phase	CH ₄ (0.33) CH ₄ (0.94)	218
dc- g- C ₃ N ₄ B-dc- g- C ₃ N ₄ B-dc- g- C ₃ N ₄ / TiO ₂	300 W Xe-lamp with 420 nm cut off filter, liquid phase	CH ₄ (5) CH ₄ (44) CH ₄ (67)	219
dc- g- C ₃ N ₄ B-dc- g- C ₃ N ₄ B-dc- g- C ₃ N ₄ / TiO ₂	300 W Xe-lamp, liquid phase	CH ₄ (14) CH ₄ (50) CH ₄ (70)	219
u- g- C ₃ N ₄ u- g C ₃ N ₄ / N-TiO ₂	300 W Xe-lamp, gas phase, 30°C	CO (3.8) CO (12.2)	220
m-g-C ₃ N ₄ m-g-C ₃ N ₄ / TiO ₂	8 W Hg lamp, gas phase, 120 kPa, 50 % humidity	CH ₄ (4.7), CO (1), H ₂ (17.5) CH ₄ (8.7), CO (2.8), H ₂ (41.3)	221
g-C ₃ N ₄ g-C ₃ N ₄ /Cu g-C ₃ N ₄ /Cu/TiO ₂	Mercury gas UV lamp with an intensity of 5.4 mW/cm ² , liquid phase, UV light, 25°C, NaOH	CH ₃ OH (40), HCOOH (1200) CH ₃ OH (210), HCOOH (2250) CH ₃ OH (470), HCOOH (1000)	222
m-g-C ₃ N ₄ m-g-C ₃ N ₄ /Cu m-g-C ₃ N ₄ /Cu/TiO ₂	500 W Xe-lamp, liquid phase, visible light, 25 °C, NaOH	CH ₃ OH (240), HCOOH (2250) CH ₃ OH (350), HCOOH (3100) CH ₃ OH (450), HCOOH (2250)	222

(*Where m, u, t, dc and ba indicate melamine; urea, thiourea, dicyanamide and barbituric acid, respectively.

1.4.6 Photocatalytic Reactors for CO₂ reduction: batch vs continuous

The systems currently used for artificial photocatalytic CO₂ reduction result still inefficient and the maximum quantum yields are estimated much below 0.1 %.^{223, 224} Therefore, the design of proper reacting systems and the investigation of the related engineering issues are of paramount importance to enhance the efficiency of this reaction.

In general, a chemical reactor used to perform a catalysed reaction must exert at least three functions. In particular, it has to (i) guarantee a proper residence time to perform the chemical reaction, (ii) implement heat exchange, and (iii) allow the direct interaction between reactants and catalyst to facilitate the reaction.

In the case of photocatalytic reactor photons can be considered as immaterial reactants, so that phenomena related to the presence of light must be carefully considered. First of all the materials of which the photoreactor is comprised may absorb light acting as filters for the impinging radiation. Therefore, transparent materials such as quartz or Pyrex should be used. In this dissertation, the batch reactors are made of Pyrex, which cut off light at wavelengths less than 320 nm. In these conditions, the photocatalyst is the light absorbing species and the occurrence of photolytic reactions can be neglected.

Furthermore, an optimal light distribution within the reactor must be ensured so that all of the photocatalysts particles can efficiently activated. For this reason the reactor configuration, the amount of photocatalyst, and light penetration depth are key parameters to be optimised.

Different reactor configurations can be used, which can be mainly divided into two groups: batch and continuous.

A typical batch reactor consists of a tank with agitator mixer with an integrated heating/cooling system where reagents and catalyst are loaded. A batch reactor is a closed reactor where there is not exchange of mass between the reactor and the environment during the reaction. Depending on the aims, also open reactors can be used where one or more reagents are fed to ensure the best conditions (i.e., flux of

oxygen or air in oxidation photoreaction). These vessels may vary shape and size (from less than 1 litre to more than 15,000 litres). They are usually fabricated in steel, glass, stainless steel, glass-lined steel, or other alloys. Liquids and solids are usually charged via connections in the top cover of the reactor. Vapours and gases can be discharged through connections in the top. Liquids are usually discharged out of the bottom. A batch system is the generic term for a type of vessel widely used in the process industries for a variety of process operations such as solids dissolution, product mixing, chemical reactions, batch distillation, crystallization, liquid/liquid extraction and polymerization. Batch reactors are frequently used in wastewater treatment. They are effective in reducing BOD (biological oxygen demand) of influent untreated water. There are also many laboratory applications, such as small-scale productions, for testing new processes that have not been fully developed, for the manufacture of expensive products, and for processes that are difficult to convert into continuous operations. They are also used for experiments of reaction kinetics and thermodynamics. Batch reactors are generally considered expensive to run, as well as with variable product distribution reliability.

The photocatalytic CO₂ reduction has been generally performed in batch reactors. This reaction mainly produces volatile compounds; thus, after the introduction of reagents and catalyst, the vessel is generally closed. In this type of system, the residence time coincides with the reaction time. Therefore, generally, the concentration of products (or the amount of consumed reactants) is calculated as a function of the reaction time per gram of catalyst present in the reactor (or per irradiated specific surface area and per number of catalytic sites).

The advantages of the batch reactor consist in its versatility and easy design. A single vessel can carry out a sequence of different operations without any loss in performance terms. This is particularly useful when processing toxic, highly reactive compounds. However, this type of reactor suffers some disadvantages such as high processing costs, difficulties in large-scale productions and in treating unstable reacting mixtures. Furthermore, reactions carried out in batch reactors present low selectivity values especially when undesired secondary routes or back reactions are thermodynamically favoured.

In order to enhance the selectivity towards a target compound, the residence time must be carefully optimized. In fact, if the target compound is a reaction intermediate it may undergo further transformations thus reducing the selectivity of the process. In a batch system, this can be achieved only by stopping the reaction when the target compound concentration reaches its maximum, with relevant disadvantages in terms of plant flexibility and operational costs. On the other hand, in a continuous reactor the residence time distribution can be simply controlled by optimizing the fluid dynamics of the system. The relevance of this issue is even more evident in synthetic applications, especially in cases where the back reaction of the products is faster than their formation, as for instance in the semiconductor induced photocatalytic CO₂ activation for the synthesis of high value added products such as fuels.

Continuous-flow systems may assume two extreme configurations, named continuous stirred tank reactor (CSTR) and plug flow reactor (PFR). In the CSTR system, the flow is perfectly mixed so that the concentration is constant throughout the reactor. On the other hand, the concentration decreases along the flow direction in the PFR. Although PFR has been chosen as the configuration used in the ISO norms for standardization of photocatalytic reactions, CSTR presents relevant advantages. Even if a PFR is more efficient than a CSTR having the same volume,²²⁵ in a CSTR all the catalyst surface is exposed to the same (output) concentration.²²⁶ In steady state conditions, the CSTR can be mathematically described by a set of algebraic equations whereas the PFR requires a set of ordinary differential equations. For these reasons, the European Standard Organization is currently working on standard test methods performed in CSTR configurations.

Continuous processes are used in the chemical industry since decades. Recently, they are used for pharmaceutical,^{227, 228} water treatment,²²⁹⁻²³¹ and fine chemicals²³²⁻²³⁵ applications due to the high safety and quality standards, cost efficiency and overall production flexibility. Furthermore, continuous reactors allow to well performing highly exothermic reactions impossible in discontinuous reactors.

In general, continuous reactors possess several advantages such as the possibility of easy scale-up and the efficiency to control the fluid dynamics and the residence time of reactants and products to enhance the selectivity towards target compounds.

Even if batch systems were often applied for CO₂ photo-reduction, fluidised bed reactors and fixed bed reactors are generally the most efficient configurations. In fluidised bed reactors, the photocatalyst is in a fluid-like state so that substrate adsorption and reaction rate are maximized. The problem of product-catalyst separation is in this case negligible by considering the rather volatile nature of the obtained compounds. However, the problems of low surface-area-to-volume ratio, of non-uniform light distribution and poor light utilization efficiency are usually encountered in existing photoreactors.

Notable, being the CO₂ photoreduction strongly depending on parameters such as reactor type, catalyst type and structure, intensity and range of wavelength, pressure, temperature, pH, residence time and reactants molar ratio, comparing results reported in literature research is very difficult due to the various experimental conditions used.

Recently, Hurtado et al. demonstrated under the same experimental conditions the higher efficiency of continuous reactors with respect to the batch reactors for CO₂ photocatalytic reduction. In detail, the reaction has been carried out in water and in the presence of Cu₂O supported on multi-layers graphene in a slurry batch reactor and in a continuous capillary reactor with the catalyst immobilized on the wall. In both cases, authors detected hydrogen as the major photoproduct in the gas phase, along with traces of ethanol in the aqueous solution. The maximum production rates of hydrogen and ethanol were respectively 2031 and 545 $\mu\text{mol g}^{-1} \text{h}^{-1}$ in continuous mode and 140 and 20 $\mu\text{mol g}^{-1} \text{h}^{-1}$ in batch reactor.¹⁸⁷

Table 7 reports the relevant literature on CO₂ photoreduction carried out in continuous systems.

Table 7. Literature survey of photocatalytic CO₂ reduction, using H₂O as reductant, in continuous reactors.

Operative conditions	Products, $\mu\text{mol g}^{-1} \text{h}^{-1}$	Selectivity, %	Ref
G-Pt/TiO ₂ (1.7 cm × 1.7 cm), 500W W-halogen lamp with a high-pass UV filter, gas phase, 100 mL min ⁻¹	CH ₄ = 3 $\mu\text{mol m}^{-2} \text{h}^{-1}$	100	²³⁶ (2015)
NiO/InTaO ₄ , 500 W halogen, liquid phase, KHCO ₃ continuous flow	CH ₃ OH= 1.4	100	²³⁷ (2007)
TiO ₂ , 200 UV lamp, He/CO ₂ feed 50 mL min ⁻¹ , gas phase, H ₂ O/CO ₂ molar ratio 0.1	H ₂ = 50 CH ₄ = 3.5 CO= 6	84 6 10	²³⁸ (2015)
Metal NP/TiO ₂ , 200 W Hg lamp, 8 mL min ⁻¹ , gas phase, 25°C	CH ₄ = 1.6 C ₂ H ₆ = 0.2	89 11	²³⁹ (2017)
Pt/ TiO ₂ , 400 W Xe lamp, gas phase, 3 mL min ⁻¹	CH ₄ = 1361	100	²⁴⁰ (2012)
Cu ₂ O/TiO ₂ , six USHIO G8T5 lamps, NaOH, liquid phase, 9 mL min ⁻¹	H ₂ = 2031 CH ₃ CH ₂ OH= 545	79 21	¹⁸⁷ (2016)
CuO/SiC, 500W Xe lamp, UV filter NaNO ₂ solution, liquid phase, NaOH, Na ₂ SO ₃	CH ₃ OH= 38	100	²⁴¹ (2011)
Metal/TiO ₂ , 500 W Halogen lamp, gas phase, 1 bar, 4 mL min ⁻¹	H ₂ = 63 CH ₃ OH= 26 CH ₃ CH ₂ OH =19 CH ₃ CHO= 20	49 20 15 16	²⁴² (2015)

*NP is nanoparticle

Recently, the combination of continuous photoreactor and membrane technologies resulted in a promising hybrid system called Photocatalytic Membrane Reactor. Such combination offers several advantages. First of all, membranes can allow separation of the photo-catalytically produced target compounds thus avoiding their overreaction and increasing the selectivity of the process. Furthermore, membranes offer large surface-area-to-volume ratio, uniform light and catalyst distribution, better catalyst exposition to light and to reactants, enhanced mass transfer and fine flow control.

1.5 Photocatalytic Membrane Reactor

1.5.1. Membrane reactors: basic principles and applications

A huge number of natural processes occur in the presence of membranes such as vegetal or animal cellular membranes. By definition, membrane is a thin sheet of natural or synthetic material that is semipermeable to substances in solution. Membranes can be constituted of organic, inorganic or hybrid materials. Inorganic membranes are generally made of glass, metal or ceramics. A general classification distinguishes the membranes on the basis of their shape in flat sheet and tubular.²⁴³ Tubular membranes can have different diameter size and can be divided in hollow fiber, capillary, and tubular membranes as shown in Figure 20.



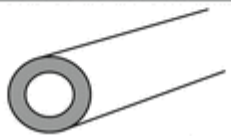
Hollow fiber membranes		outer D ~ 0.08-0.8 mm inner D ~ 0.04-0.5 mm
Capillary membranes		inner D ~ 0.5-5 mm outer D ~ 0.8-7 mm
Tubular membranes		outer D ~ 5 -25 mm

Figure 20. Diameter range of tubular membranes.

The principal function of a membrane is to exert the selective separation of species in a homogeneous or heterogeneous mixture in gas or liquid phase.

This function is possible owing to a dense or porous structure. Generally, dense structures are suitable for gas separation while the porous one for filtration processes. As reported in Table 8, the field of application of the membranes changes depending on their (i) pore size, (ii) molecular weight cut off, (iii) membrane matrix, (iv) type of compounds to be separated, and (v) applied pressure as the driving force of the separation process.

Table 8. Membrane process and corresponding characteristics required.²⁴⁴

Parameter	Microfiltration	Ultrafiltration	Nanofiltration	Reverse Osmosis
Pore size, μm	0.01-1.0	0.001-0.01	0.0001-0.001	<0.0001
Molecular Weight Cut off	>100,000	1,000-300,000	300-1,000	100-300
Operating Pressure, psi	<30	20-100	50-300	225-1,000
Membrane Materials	Ceramics, polypropylene, polysulfone, polyvinylidenedifluoride	Ceramics, polysulfone, polyvinylidenedifluoride, cellulose acetate, thin film composite	Cellulose acetate, thin film composite	Cellulose acetate, thin film composite, polysulfonated polysulfone
Membrane Configuration	Tubular, hollow fiber	Tubular, hollow fiber, spiral wound, plate and frame	Tubular, spiral wound, plate and frame	Tubular, spiral wound, plate and frame
Types of micro-organisms and Species Removed	Clay, bacteria, viruses, suspended solids	Proteins, starch, viruses, colloid silica, organics, dyes, fats, paint solids	Starch, sugar, pesticides, herbicides, divalent anions, organics, BOD, COD	Metal cations, acid, sugars, aqueous salts, amino acids, monovalent salts, BOD, COD

A further structural grouping can be done for porous membranes in symmetric and asymmetric type (Figure 21). In symmetric membranes, the structure and the mass transport properties are identical over the entire cross section, and the thickness of the membrane determines the flux. Asymmetric membranes present a not homogeneous pore distribution so that structural and transport properties vary over the cross section. They generally consist of an extremely thin surface layer supported on a much thicker porous, dense substructure. The surface layer and its substructure may be formed in a single operation or in different steps. An asymmetric membrane consists of a 0.1 – 1 μm thick ‘skin’ layer on a highly porous 100 – 200 μm thick substructure. The skin represents the actual selective barrier whose nature determine the separation properties and the permeation rate. The thickness is an important parameter influencing the mass flux. The separation properties and permeation rates of the membrane are determined by the surface layer, while the substructure acts as a mechanical support. The advantages of asymmetric dense membranes are generally related to the higher fluxes provided

and to the good mechanical stability, so that almost all of the commercial pressure driven processes such as reverse osmosis and gas and vapour separation, are based on this kind of membranes. An important application is the desalination of sea, river, or brackish water. Desalination plants were built especially in the USA, in Israel, and recently in Germany. The permeate water is sterile, desalted, and completely free from particles.²⁴⁵

Two techniques are generally used to prepare asymmetric membranes. The first is the phase-inversion process, which in a single step leads to an integral overall structure in which the skin and the support are comprised of the same material. The second is a two-step process producing a (multilayers) composite structure where a thin barrier layer is deposited on a porous substructure. In this case, barrier and support structures are generally made of different materials.

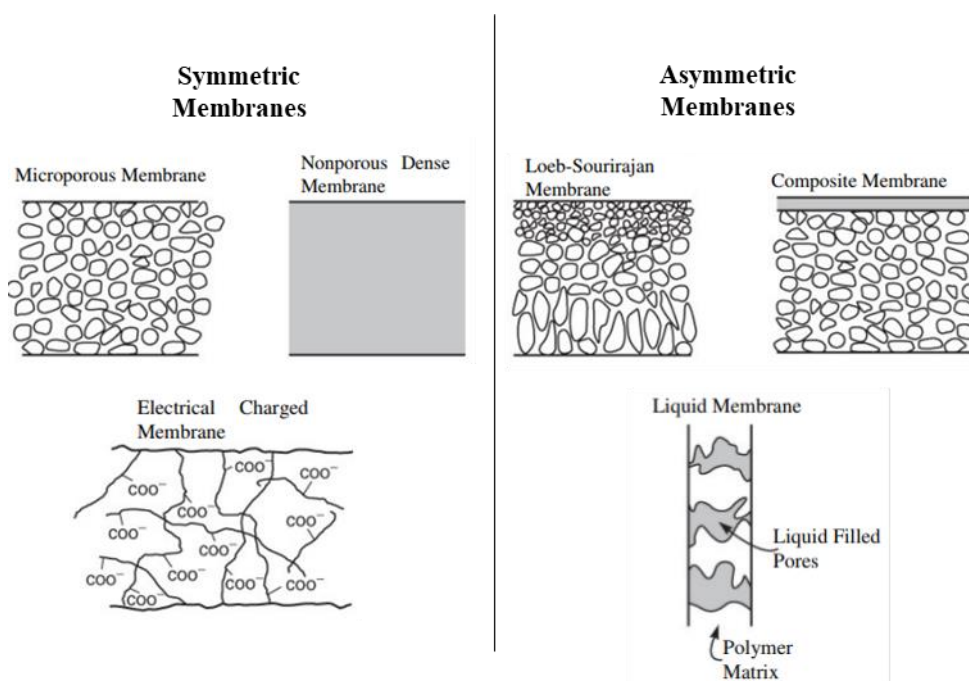


Figure 21. Simplified scheme of symmetric and asymmetric membrane²⁴⁶.

As above mentioned in Table 8, gradient of partial pressure between the retentate and permeate sides is one of the parameters generally driving the separation process. However, species migration can be also performed through an electrochemical or concentration gradient between the two chambers (donor and acceptor phases) as shown in Figure 22.

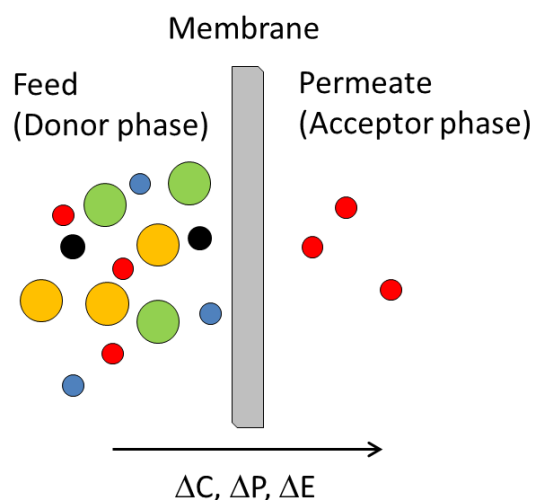


Figure 22. Permeation through a membrane of liquids or gases where ΔC , ΔP , ΔE are the concentration, pressure and electrochemical gradient, respectively.

In detail, when a driving force is applied through a membrane, three different streams can be distinguished: (i) the feed, (ii) the permeate, and (iii) the retentate. The species pass through the membrane with a concentration profile, which affect the mass transport phenomenon.²⁴⁷ In addition, the transport rate of a species through the membrane is inversely proportional to its thickness. High transport rates are desired in membrane separation processes for economic reasons, so that it is important to use membrane as thin as possible. A crucial point is the mechanism of mass transport through membranes. Two basic models can describe the mass transfer: (i) the solution-diffusion model and (ii) the hydrodynamic model. In the first case, typically occurring in dense membranes, the transport occurs only by diffusion, thus the component that needs to be transported must first dissolve (solution) within the membrane. The hydrodynamic model described satisfactorily the behaviour of porous membranes and the mass transport mechanism is a pure convective motion of molecules through the membrane pores due to the superimposed pressure gradient.

Several methods have been developed to synthesize the membranes with specific properties as reported in Figure 23.

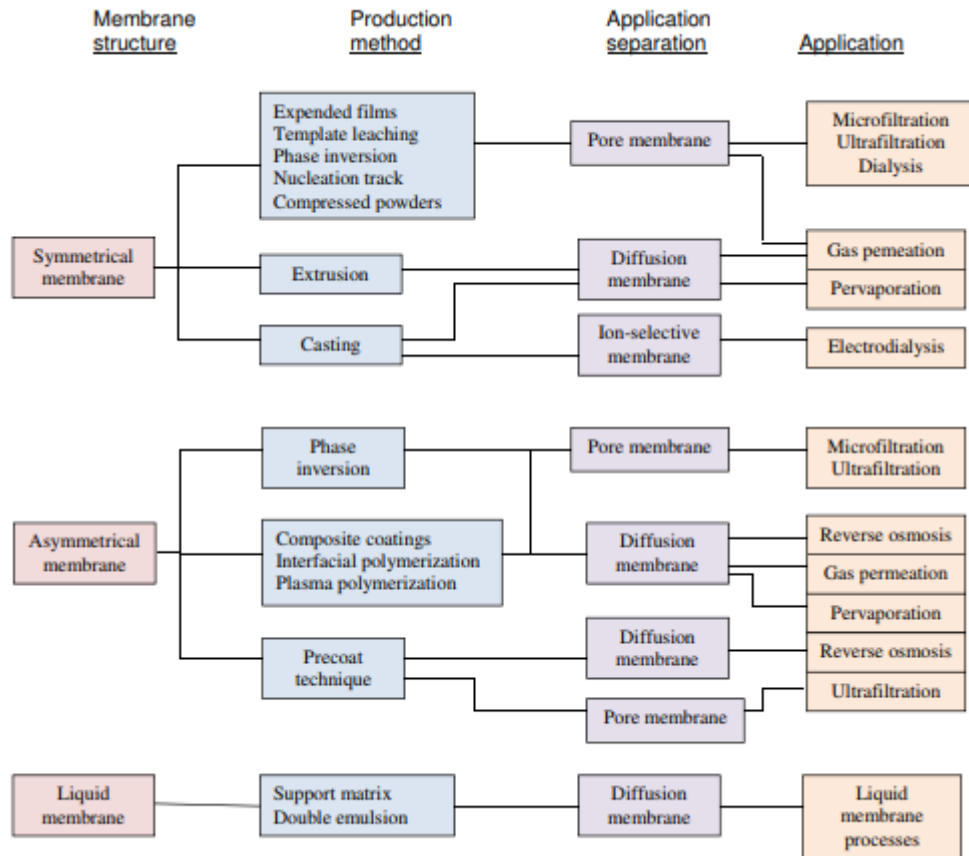


Figure 23. Membrane production methods and application fields of the obtained membranes.

For instance, dense membranes are generally polymeric. The selection of the starting polymer is not arbitrary, but based on the specific properties, which the membrane should possess, mainly structural factors, such as molecular weight, chain flexibility, and chain interactions. In fact, structural factors determine the thermal, chemical and mechanical properties of polymers, but also permeability.

The polymeric membranes used in this dissertation work have been prepared by means of the solvent evaporation method. The polymer is dissolved in a solvent and a homogenous solution (named casting) is obtained. Then, the solution is casted on a suitable support, e.g., a glass plate or another type of porous (non-woven fabric) or non-porous (polymer) support. Thereafter, the solvent is evaporated in controlled atmosphere (e.g., room chamber maintained at constant temperature and humidity) thus leading a dense and homogenous membrane.²⁴⁸ Tuning the experimental conditions permits to tailor the properties of the polymeric dense membrane.²⁴⁹

The Perfluorinated ionomer known as Nafion (Figure 24) is the most widely used polymer for the synthesis of polymeric membrane for PEM fuel cells.^{250, 251} The resulting membranes show high proton conductivity, super acidity and high mechanical and chemical stability.

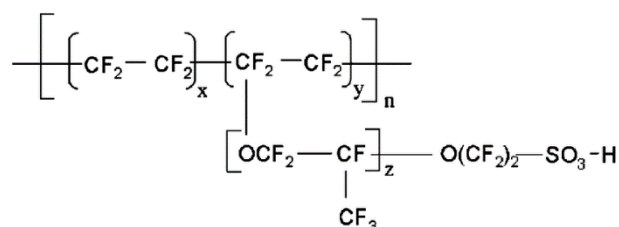


Figure 24. Chemical structure of Nafion polymer.

In general, to enhance the physic-chemical properties of the membranes, various additives can be used during their synthesis. The compounds can be homogeneously embedded inside the matrix or just functionalize the membrane surface. For instance, C₃N₄ or graphene oxide embedded into a Nafion membrane, showed an improvement toward water selectivity and a higher performance of Nafion membrane in fuel cells, respectively.^{252, 253}

The latest development in membrane material design is the use of hybrid (inorganic–organic) materials, which overcome most of the limitations associated with polymeric membrane systems. Inorganic materials explored to this aim are metal oxides (e.g., Al₂O₃, TiO₂, SiO₂, ZnO, and Fe₂O₃), metals (e.g., Cu, Ag) and carbon-based materials (e.g., graphene and carbon nanotubes). Introducing inorganic moieties into a polymeric matrix system can offer multi-functionality beyond the mere separation and can enhance hydrophilicity, mechanical strength, water permeability, rejection rate, antifouling properties and/or introduce photocatalytic activity.²⁵⁴

The main role of membranes is known to be the separation of desired species. However, membranes can be used also as expositors or contactors. The membrane acts as an expositor when it enables or facilitates, for instance, the exposition of a photocatalyst to the light. In this case the photocatalyst particles, dispersed in the membrane matrix, harvest more photons (increasing the efficiency of the reaction) and at the same time may be better exposed to reactants (higher available surface

contact area). The membrane acts as a contactor when merely contact two phases and enhance the mass transport between them. Membrane contactors have been widely studied by Boyadzhiev et al. for recovery of organic acids, antibiotics, alkaloids, bio-surfactant, and metals.²⁵⁵

Membrane reactors are an interesting alternative to traditional reactors owing to their unique characteristics.²⁵⁶

Membrane reactors can consist of one or more modules. As shown in Figure 25, two operating ways are possible: single pass or recirculated reactors. In order to increase the productivity, several modules can be added and located in parallel. On the contrary, in series arrangement it is preferred to enhance the selectivity of the process.

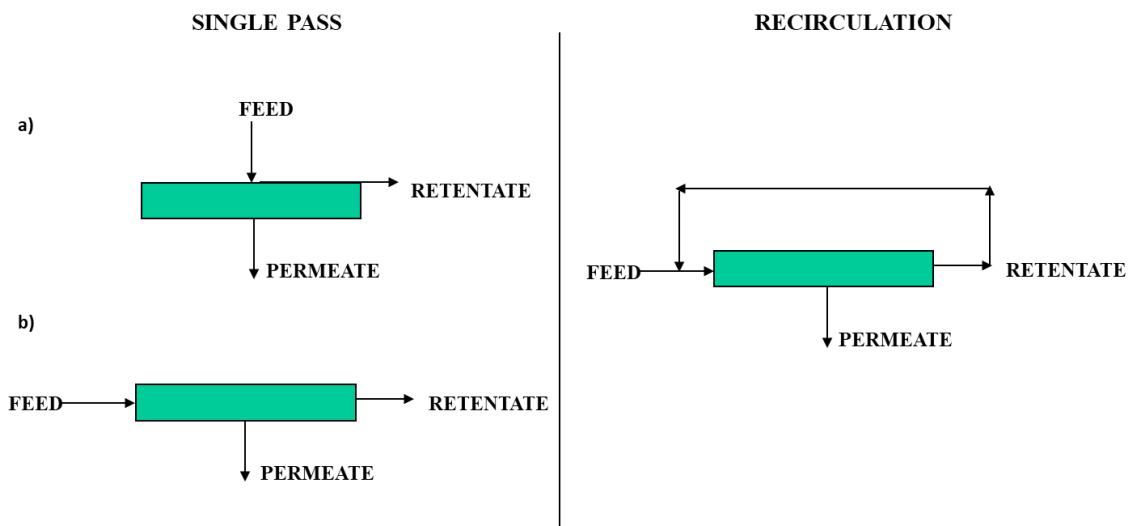


Figure 25. Module arrangements: two types of single pass (a and b) and recirculation mode.

Due to the high potential offered, the use of membranes is continuously increasing in several fields such as water treatment, food and pharmaceutic industries,²⁵⁷ chemistry, etc. Cold separation using membrane technology is widely used in food, biotechnology and pharmaceutical industries. In fact, it was demonstrated that among polymeric materials, polymeric membranes are attractive for their selectivity and bio-stability characteristics in the use of bio-hybrid systems for cell culture. Semipermeable membranes act as a support for the adhesion of anchorage-dependent cells and allow the specific transport of metabolites and nutrients to cells

and the removal of catabolites and specific products. Moreover, new membrane systems that have been recently realized might also potentially contribute to regenerative medicine and tissue engineering.²⁵⁸ Furthermore, using membranes enables to separate species impossible to be performed by using thermal separation methods. For example, it is impossible by distillation to separate the constituents of azeotropic liquids or solutes, which form isomorphous crystals by distillation or recrystallization, but such separations, can be achieved using suitable membranes. For instance, several studies report this technology as a promising method for H₂ and N₂ separation, air-drying and in particular for CO₂ capture.^{259,260} Important technical applications include the production of drinking water by reverse osmosis (worldwide approximately 7 million cubic metres annually), filtrations in the food industry, the recovery of organic vapours such as petro-chemical vapour recovery and the electrolysis for chlorine production. In wastewater treatment, membrane technology is becoming increasingly important. With the help of ultra/microfiltration it is possible to remove particles, colloids and macromolecules, so that wastewater can be disinfected. About half of the market is dedicated to medical applications such as the use of membranes for artificial kidneys to remove toxic substances by haemodialysis and as artificial lung for bubble-free supply of oxygen in the blood. The importance of membrane technology is growing in the field of environmental protection (NanoMemPro IPPC Database). Even in modern energy recovery techniques, membranes are increasingly used, for example in fuel cells and in osmotic power plants which generates renewable and emissions-free energy and thus contributes to eco-friendly power production by water treatment at different salinity.

The integration of photocatalysis with a membrane based separation unit has been recently proposed as a promising tool to transfer photocatalytic syntheses from lab to industrial scale. The reason why photocatalytic membrane reactors could produce great advantages is based on a simple idea. The target molecule, generally a reaction intermediate, can be continuously separated from the photocatalytic system by means of suitable membranes in order to avoid its further oxidation. This not only provides higher selectivity and efficiency with respect to the sole photocatalytic process, but also enables direct separation of the product of interest.

Furthermore, the dense membranes are generally not affected by possible fouling and allow the complete retention of the photocatalytic powder. This avoids further separation steps, thus strongly reducing the operating costs. Finally, the possibility of operating in a continuous or semi-continuous mode, the easy control and the modularity of the system endow the integrated process with versatility and flexibility. It is worth to note that the integration of the two processes is straightforward due to the similar operating conditions at which they generally operate (mild temperature, low pressure, diluted solutions, low energy demand). This solution has been often applied for environmental²⁶¹ (i.e., water treatment) purposes by considering the synergistic effects of the integration, i.e., the possibility of pollutant removal with rates higher than the sum of those obtained by the single technologies.²⁶² On the other hand, applications for the synthesis of high value added compounds might be still defined at a nascent level. Notably, while some interesting syntheses have been investigated from a “chemical” point of view, the highly specific engineering issues related to them should be still approached. Therefore, various competences and different research approaches must be interdisciplinary connected and scientific collaborations are often required to prove the applicative viability of photocatalytic membrane reactors (PMRs) for synthetic purposes. Up to now a limited number of photocatalytic oxidation, reduction and syntheses of high added value chemicals were carried out in PMRs.^{261, 263-265} In fact, few photo-oxidation reactions (i.e., partial oxidation of benzene to phenol and alcohols to aldehydes and the synthesis of vanillin), photo-reduction (i.e., reduction of nitrate to ammonia and acetophenone to phenylethanol) and only two photocatalytic synthetic reductions (CO₂ to fuels and the synthesis of phenylethanol) have been carried out in PMRs, to the best of my knowledge.

More recently, the incorporation of photocatalyst into membrane matrix was studied to develop a newly PMR for the CO₂ photoreduction with good performance.

1.5.2 Photocatalytic membrane reactor for CO₂ reduction

Despite the attractive features of PMRs, their application to heterogeneous CO₂ photoreduction has been up to now scarce.

Pioneering researches on CO₂ reduction in a photocatalytic membrane reactor have been carried out from Pathak et al. in a batch reactor at 139 bar.^{266 267} Authors reported that homogeneously dispersing the photocatalyst in Nafion thin films resulted in improved efficiency of CO₂ photocatalytic reduction with respect to the case where the photocatalyst was dispersed in the reacting mixture. In their first report²⁶⁶ commercial TiO₂ (Degussa) was immobilized in Nafion matrix films and tested in the presence of supercritical CO₂. The products detected were HCOOH, CH₃OH and CH₃COOH (190, 280 and 30 μmol g_{catalyst}⁻¹, respectively) after 5 hours of irradiation.

Recently, an innovative CO₂ photoreduction system in mild conditions (pressure of ca. 3 bar) was reported by Sellaro et al.²⁶⁸. TiO₂ (1.2% wt.) was embedded in a Nafion membrane prepared by solvent method evaporation. The main product was methanol with a production rate of 45 μmol g_{catalyst}⁻¹ h⁻¹, which is one of the highest values reported for photocatalytic systems operating in similar conditions. This work showed that PMRs might be a promising technology for CO₂ reduction.

Both the above-mentioned papers demonstrated the Nafion capability of dispersing and supporting photocatalysts active for the CO₂ photoreduction. Being a stable and UV-vis transparent material with high proton conductivity, Nafion seems to be the best polymeric choice in order to carry out CO₂ photocatalytic reduction in PMRs.

Recently, the influence of reactants molar ratio and contact time on CO₂ photoreduction efficiency has been demonstrated in optofluidic membrane microreactor.²⁶⁹ In this study, a mesoporous CdS/TiO₂/SBA-15@carbon paper composite membrane was used for the reaction affording an outstanding methanol production of ca. 800 μmol g_{catalyst}⁻¹ h⁻¹.

In general, microreactors show several advantages such as: minimal amounts of reagent required under precisely controlled conditions, rapid screening of reaction

conditions, improved overall safety conditions of the process,²⁷⁰ excellent mass and heat transfer, shorter residence time, lightweight and compact system design, laminar flow, effective mixing and better process control.

By taking into consideration all of the mentioned advantages, it is obvious that they could have many areas of application but those systems are still not perfect. Frequently quoted disadvantages of microreactors are high fabrication cost, low throughput, incompatibility with solids and the omission of cost reduction by scale up effects which lead to still poor industrial acceptance.²⁷¹ To ensure a stable flow in microreactors it is necessary to use low pulse or pulseless pumps; pumps are one of the most expensive parts of the microreactor apparatus. Due to the small dimensions of micro-channels one of the biggest problems is clogging²⁷² when operating with small diameter solids (for example enzyme dispersion) in a microreactor or with highly viscous solvents. It is also important to mention that microreactors can operate a very short residence time so in this case a fast reaction is carried out. Fast reactions also require very active catalysts with high stability in the microreactor. Consequently, microreactors still cannot be used as a replacement for all traditional processes. Another very important problem concerns the analysis of the products. In fact, off-line analyses, although easy to perform, are time demanding. Therefore, there are many efforts in developing on-line analytical techniques for micro-structured devices.

From these considerations, only few reports are available to the best of my knowledge, focus on CO₂ reduction in PMRs, so that further investigations are needed.

Chapter 2
Experimental section

2.1 Material and Methods

All the following materials were used as received without any further purification: $ZrOCl_2$ (Sigma Aldrich, 98%), $Ce(SO_4)_2$ (Sigma Aldrich, 100%), $Er(NO_3)_3 \cdot 5H_2O$ (Sigma-Aldrich, 99.9%), TiO_2 P25 (Evonik, 100%), melamine (Sigma Aldrich, 99%), H_2O_2 (Sigma Aldrich, 30% wt./wt. in H_2O), Graphite (Sigma Aldrich, -), H_2SO_4 (Sigma Aldrich, 95-98%), $NaNO_3$ (Sigma Aldrich, 99%), $KMnO_4$ (Sigma Aldrich, 99%), Nafion solution (Quintech e.K Brennstoffzellen Technologie, 5 wt. %). Distilled deionized water used throughout the experiments, for washing processes, as solvent and reagent was purified by means of a Milli-Q system. All liquid analytical standards such as methanol (anhydrous, 99.8%), absolute ethanol (reagent ISO, reagent Pharmacopoeia European, $\geq 99.8\%$), acetone (analytical standard), acetaldehyde (ACS reagent, $\geq 99.5\%$), propanal (reagent grade 97%), propanol (anhydrous, 99.7%) and formaldehyde (37% wt. in H_2O contains 10-15 % methanol as stabiliser) were obtained from Sigma-Aldrich.

Gasses such as CO_2 , CO , CH_4 , Ar, He and N_2 were purchased from Air Liquide with a purity of 99.998%.

2.2 Material synthesis

2.2.1 ZrO_2 based materials

The ZrO_2 based samples have been prepared by means of a hydrothermal process, starting from an aqueous solution containing the zirconium precursor ($ZrOCl_2 \cdot 8H_2O$) in 1.0 M concentration and the rare earth precursor, ($Ce(SO_4)_2$ or $Er(NO_3)_3 \cdot 5H_2O$). The pH of the solution was then adjusted to 11 by using a 4.0 M NaOH aqueous solution. The solution, with the precipitates, was then transferred into a 125 mL Teflon lined stainless steel autoclave, 70% filled, which was heated at 175 °C overnight in an oven. The precipitates were hence centrifuged and washed three times with deionized water, then dried at 60 °C. For comparison, pure ZrO_2 was prepared by the same procedure, without the presence of the rare earth metal. Finally, the prepared powders were calcined at 500 °C for 2 h. For each dopant (Ce or Er), two samples were prepared with different rare earth metal

content, namely 0.5%, and 10% molar percentage. Samples will be labelled indicating the molar percentage of the dopant, then the dopant followed to the ZrO₂.

2.2.2 G/TiO₂ composites

Graphene oxide was prepared from graphite flakes via an improved Hummers method.¹⁵⁵ In detail, 4 g of graphite were added to 2 g of NaNO₃ in 92 mL of H₂SO₄ and stirred for ca. 15 minutes at 0°C in an ice bath. Because of heat evolution due to the exothermic process, 12 g of KMnO₄ were slowly (in 15–20 min) introduced to maintain the temperature below to room value (20°C). Then, after removal of the ice bath, the solution was stirred for 90 minutes assuming a green colour. Firstly, 184 mL of Milli-Q H₂O (reaching 98 °C) were added to the acid solutions, and later 560 mL of Milli Q hot H₂O. A change of the solution colour, from green to yellow, was observed after treatment with 20 mL of H₂O₂.

Upon treatment with the peroxide, to reduce the residual permanganate and manganese dioxide to colourless soluble manganese sulphate, the suspension was filtered resulting in a yellow-brown filter cake. It was washing three times with a total volume of 560 mL of warm H₂O. Filtering was carried out while the suspension was still warm to avoid precipitation of the slight soluble salt of mellitic acid formed as a side reaction.

Unlike the Hummer's method, the resulting product was dispersed in H₂O under stirring using ultrasound in order to obtain a 2D material. The solid was separated by centrifugation at 1000 rpm for 2 minutes. This procedure was repeated 2 times. However, to remove all possible residues from the synthesis steps, the resulting solid was washed by water and centrifuged for 15 minutes at 800 rpm. The precipitated powders were dried at 70°C overnight and labelled GO.

The graphene/commercial TiO₂ composites was obtained via hydrothermal method based on modified Nethravathi's work at four different G percentage weights equal to 0.5, 1, 3 and 10%.²⁷³ Briefly, 6 mg of GO was dissolved in a solution of H₂O (60 mL) and ethanol (30 mL) by ultrasonic treatment for 1 h, and 0.6 g of TiO₂ was added to the obtained GO solution and stirred for 2 h to get a homogeneous

suspension. The ethanol was used to facilitate both the dispersion of reagents and as reductant of GO to G in these hydrothermal conditions. The suspension was then placed in a 100 mL Teflon-sealed autoclave and maintained at 120 °C for 3 h to simultaneously achieve the reduction of GO and the deposition of TiO₂ on the carbon substrate. The system pressure reached the 25 psi as result of CO₂ formation from ethanol oxidation. Finally, the resulting composite was recovered by filtration, rinsed by water several times, and dried overnight at 60°C. The resulting powder was labelled as 1% G/TiO₂. By following the same procedure, also the 0.5% G/TiO₂, 3% G/TiO₂ and 10% G/TiO₂ composites were prepared.

2.2.3 Pristine and base g-C₃N₄ materials

Graphitic carbon nitride (g-C₃N₄) was prepared by heating (at 2 °C min⁻¹) 10 g of melamine up to 520 °C, temperature kept for 2 h, in a covered crucible exposed in static air. The yellow solid was pounded and then heated again, without coverage, at 3 °C min⁻¹ up to 500 °C keeping this temperature for 4 h.

g-C₃N₄-TiO₂ photocatalyst was prepared by mechanically milling both solids with a Retsch RM200 mortar grinder. The procedure of preparation was as follows: 3 g of TiO₂ (commercial P25) powder were mixed in the ball-milling tank with 1 g of g-C₃N₄ (ratio of 3:1) for 1 h at 250 rpm (30 minutes clockwise, 5 minutes of pause, and 30 minutes by inverting the rotation).

2.2.4 g-C₃N₄ pure and O doped materials and their immobilization: g-C₃N₄, O_R-C₃N₄ and O_T-C₃N₄

Oxygen doped g-C₃N₄, was prepared by a modified thermal polymerization method.²⁷⁴ Briefly, 1 g of g-C₃N₄ (as synthesized previously, see section 2.2.4) was dispersed in 80 mL of 30% H₂O₂ solution and placed in a Teflon vessel of 100 mL. The vessel was then heated up to 130 °C and kept at this temperature for 24 h in an autoclave. After cooling, the dispersion was filtered, and the orange coloured powder was washed with hot water to remove the H₂O₂. Once no H₂O₂ was

detected in the washings (by KMnO_4 method), the powder was dried at 60°C and designated $\text{O}_\text{R}-\text{C}_3\text{N}_4$. $\text{g}-\text{C}_3\text{N}_4$ and $\text{O}_\text{R}-\text{C}_3\text{N}_4$ catalysts were immobilised in a glass supports by the following procedure. 8 mg of powder was immobilized on borosilicate glass ($3 \times 2.5 \text{ cm}^2$) by spray coating using a water dispersion of 25 g L^{-1} . Each coated borosilicate glasses were dried at 70°C . The $\text{g}-\text{C}_3\text{N}_4$ powder coated was used without further treatment or annealed at 450°C (2 h with ramp up and down rate 2°C min^{-1}) to produce $\text{O}_\text{T}-\text{C}_3\text{N}_4$ prior to testing.

2.2.5 Pristine Nafion and photocatalytic C_3N_4 and $\text{C}_3\text{N}_4\text{-TiO}_2$ Membranes

Nafion and photocatalytic Nafion membranes were prepared following the same procedure reported by Sellaro et al.²⁶⁸ Nafion 5 wt. % solution (20 g) was dried at ca. $60\text{--}70^\circ\text{C}$ under stirring; then, the resulting powder was dissolved in $\text{EtOH}/\text{H}_2\text{O} = 50:50$ w/w at room temperature under stirring for 1 h to obtain the polymeric solution. Two types of flat sheet membranes were prepared: a Nafion membrane (not including catalyst) and a photocatalytic Nafion membrane (Table 9). For the catalytic membranes, after complete polymer dissolution, the catalyst (C_3N_4 or $\text{C}_3\text{N}_4\text{-TiO}_2$) was added to the obtained solution, and the resulting dispersion was left under stirring for 1 h more. Then, it was sonicated for 3 h more at room temperature to favour the homogenization of the dispersion. The catalyst-polymer dispersions obtained were then cast in a Petri dish (diameter = 7.1 cm), and the solvent evaporation was carried out in a climatic chamber ($60 \pm 4^\circ\text{C}$ and $12 \pm 5\%$ as relative humidity) for about 20 h. The membranes obtained were treated thermally, heating at $10^\circ\text{C min}^{-1}$ up to 100°C , then at $0.5^\circ\text{C min}^{-1}$ up to 120°C , and kept at this temperature for 4 h. No specific investigation on catalyst loading content was carried out, and the chosen photocatalyst percentage was 1.23 wt. %. In the case of the Nafion membrane, the same procedure was followed but without catalyst dispersion. Then, the flat sheet membranes obtained were detached from the Petri dishes with a small amount of water and then dried at room temperature. In all the membranes, two membrane sides were distinguished as the casting-plate-facing and air-facing surfaces.

Table 9. Composition of solutions used to prepare pristine and photocatalytic membranes

	Membrane, wt.%	
	Photocatalytic Nafion	Nafion (bare)
<i>Polymeric solution</i>		
Solvent (EtOH:H ₂ O, 50:50)	97.8	97.827
Polymer	2.173	2.173
<i>Catalyst addition</i>		
Catalyst	0.027	0
<i>Resulting membrane</i>		
Catalyst in membrane	1.23	0
Polymer in membrane	98.77	100

2.3 Materials characterizations

2.3.1 Powder characterizations

Bulk and surface of all catalysts prepared in the above (2.2.1 - 2.2.4) sections and commercial TiO₂ were characterised for defining the physicochemical properties of the powder.

Their crystalline phase structures were analysed at room temperature by powder X-ray diffraction by using a Panalytical Empyrean instrument, equipped with Cu K α radiation and a PixCel-1D (tm) detector.

The Brunauer–Emmett–Teller specific surface area of the synthesized catalysts was measured by nitrogen adsorption–desorption isotherms using a Micromeritics Asap instrument. Infrared spectra of the samples in KBr (Aldrich) pellets were obtained with an FTIR-8400 Shimadzu spectrophotometer and recorded with 4 cm⁻¹ resolution and 256 scans.

The diffuse reflectance spectra were measured in air at room temperature in the 200–800 nm wavelength range using a Shimadzu UV-2401 PC spectrophotometer, with BaSO₄ as the reference material.

However, in order to define the fine structure of the graphene materials, the Raman spectra were also performed in three points for each sample. The spectra were recorded by a Reinshaw in-via Raman equipped with an integrated microscope and

with a charge-coupled device (CCD) camera. He/Ne laser operating at 532 nm was used as the exciting source (20x lens, focal length ca. 4-5 μm and work power ranged from 1% to 50% of 100mW).

Additionally in collaboration with Giamello's group of University of Turin, Electron Paramagnetic Resonance analyses were carried out on ZrO_2 base materials in order to explain the unusual photoreactivity. Then, Electron Paramagnetic Resonance spectra were recorded at room temperature and at liquid nitrogen temperature (-196 °C) on an X-band CW-EPR Bruker EMX spectrometer equipped with a cylindrical cavity operating at 100 kHz field modulation. The effect of light on EPR spectra was investigated by using 1600W Mercury/ Xenon lamp (Oriental Instruments) and an IR water filter. A 400 nm cut off filter was used to eliminate part of the UV radiation, leaving a 5–8% of UVA component comparable to that present in the solar spectrum.

2.3.2 Characterisations of supported materials

All the materials supported on glass (2.2.4 section) were characterized, before and after their use, by a Perkin Elmer Varian 640-IR FTIR was used for FTIR characterization. FTIR analysis was performed with a resolution of 10 cm^{-1} step size, compiled from 50 scans and measured in triplicate.

The crystalline phase structures were analyzed at room temperature by powder X-ray diffraction by using a Panalytical Empyrean, equipped with Cu K_α radiation (1.5406 Å) and PixCel-1D (tm) detector.

Diffuse reflectance was used to determine the optical characteristics of the materials and measured with a Shimadzu UV-2401 PC spectrophotometer, with BaSO_4 as the reference material. X-ray photoelectron spectroscopy (XPS) of the used and unused material plates were recorded by means of a Kratos Axis Ultra system equipped with a monochromatic Al K_α X-ray source ($h\nu$ 1486 eV). Triplicate analysis was performed, sampling from different areas of the material plates. For all the elements, the coefficient of variance was less than 10%. The binding energy at 284.8 eV was used for calibration of C 1s chemical shifts. Survey

scans covering the entire energy range were performed with 160 eV energy window, whilst high-resolution scans of specific elemental regions were performed at a reduced 20 eV. The data were fitted using a mixed Gaussian-Lorentzian (GL30) function on a Shirley background.

2.3.3 Characterization of membranes

After cleaning as described in the section 3.4.2, the membranes prepared (2.2.5 section) were characterized by different techniques. The morphologies of the membrane surfaces (air- and plate-facing) and cross section were examined by an EVO MA10 Zeiss Scanning Electron Microscope. The samples were sputtered with gold prior to these analyses.

A PerkinElmer Spectrum One was utilized for Fourier Transform Infrared spectroscopy analyses in attenuated total reflectance mode of both air-facing and casting-plate-facing membrane surfaces.

Diffuse reflectance spectroscopy (Shimadzu UV-2401 PC) analyses were carried out in three different points for both casting sides.

Permeability to N₂ and CO₂ were also measured to evaluate the membrane mass transport properties and integrity.

Chapter 3
Results and discussion

3.1 Doped and pristine ZrO₂ for CO₂ photoreduction

The results presented in this chapter have been published in:

E.I. García-López, G. Marci, F.R. Pomilla, M.C. Paganini, C. Gionco, E. Giamello, L. Palmisano. ZrO₂ Based materials as photocatalysts for 2-propanol oxidation by using UV and solar light irradiation and tests for CO₂ reduction. *Catalysis Today* 313, **2018**, 100–105.¹⁴⁷

3.1.1 Photocatalytic test conditions

Previously the photocatalytic test, a possible presence of products deriving from C impurities was checked by treating the photocatalysts under irradiation (before the photoactivity experiments in the presence of CO₂) with a flow of humid inert gas according to Strunk et al.,¹¹⁴ which allowed also to clean the surface. Notably no organic species were observed during the treatment.

The CO₂ photoreduction tests were carried out by using a batch photoreactor constituted by a Pyrex vessel with a volume of 25 mL and equipped with a septum to permit the sampling (Figure 26). 0.06 g of photocatalyst were spread in the bottom of the photoreactor and N₂ was flushed for 2 h inside the system under irradiation in order to photo-desorb possible impurities and/or carbon residues from the catalyst surface. Subsequently, the photoreactor was saturated with CO₂ containing the vapour pressure of water at 25 °C. In order to start the experiment in the presence of humid CO₂, the stream of CO₂ was continuously flushed for at least 1 h inside the reactor, after bubbling it in a flask containing water. Then the reactor was closed and the lamp (1500W high-pressure Xenon lamp) of SOLARBOX (CO·FO·ME·GRA) apparatus, simulating the solar light, was switched on.

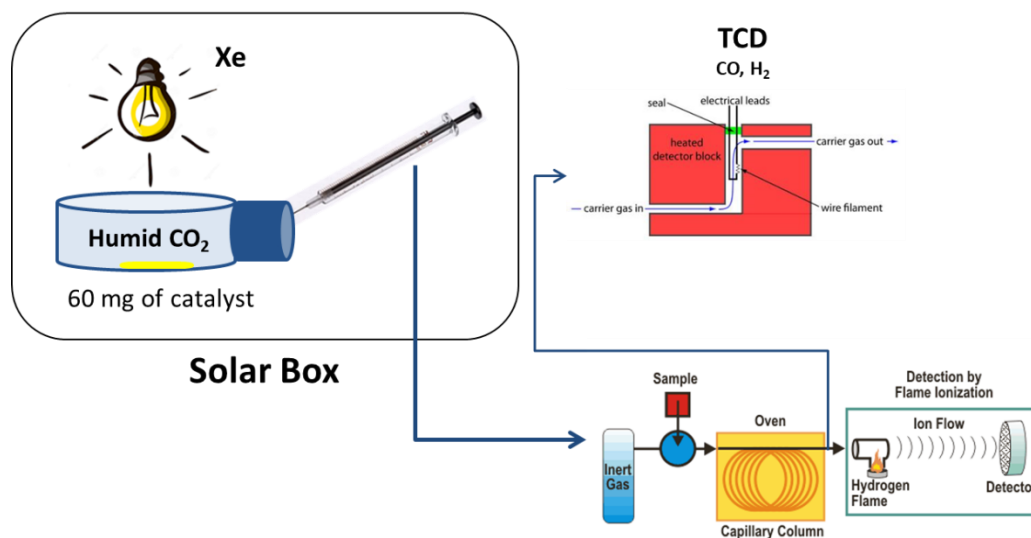


Figure 26. Photocatalytic apparatus consisting by Solar Box and glass batch reactor equipped with GC TCD-FID instruments.

Aliquots of the gaseous reaction mixture were withdrawn from the reactor at fixed irradiation times by using a gas-tight micro syringe. The evolution of the formed organic products was followed by a GC-2010 Shimadzu equipped with a Phenomenex Zebron Wax-plus column by using He as the carrier gas and a FID. CO was analysed by a HP 6890 GC equipped with a packed column GC 60/80 Carboxen-1000 and a TCD. The latest analysis were useful to check the tight of the system by monitoring the amount of N₂ and O₂ inside the reactor.

3.1.2 Characterisation of ZrO₂ based materials

XRD patterns of prepared samples are reported in Figure 27. A mixture of both monoclinic (m-ZrO₂) and tetragonal (t-ZrO₂) polymorphs of zirconia was observed in all of them. In agreement with Gionco et al.²⁷⁵ the increasing of rare earth (RE) dopant amount led to the stabilization of the tetragonal polymorph.

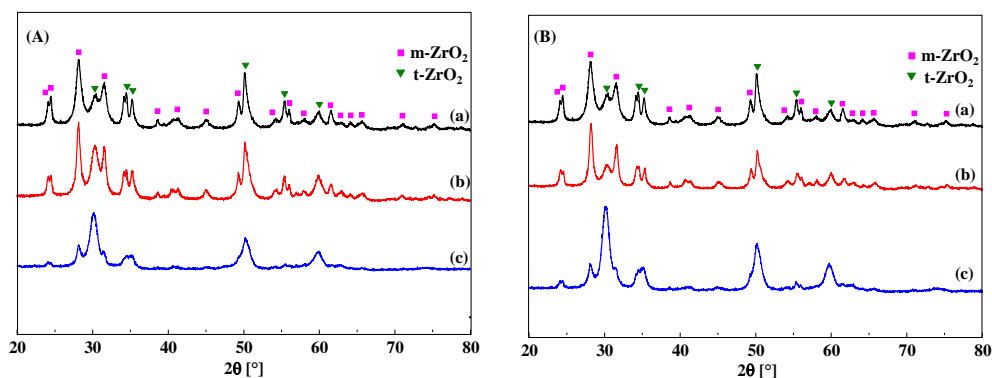


Figure 27. XRD patterns of the prepared samples. Ce doped (A) and Er doped (B) ZrO_2 samples, along with the pristine ZrO_2 . (A): ZrO_2 (a); 0.5%Ce/ ZrO_2 (b) and 10%Ce/ ZrO_2 (c) and (B): ZrO_2 (a); 0.5%Er/ ZrO_2 (b) and 10%Er/ ZrO_2 (c).¹⁴⁷

A Rietveld refinement was performed on the XRD patterns and the results are reported in Table 10.

Table 10. Cell parameters, weight percentage and crystallite size obtained from Rietveld refinement: (wt.) weight percentage of a given phase; (a), (b) and (c) lattice parameters; (β) angle between a and c axes for the monoclinic cell; (D) and (d) maximum and minimum crystallite sizes for the anisotropic m- ZrO_2 ; (d') crystallite size for t- ZrO_2 ; (E_g) estimated band gap for all of the samples prepared.¹⁴⁷

Sample	Phase	wt. [%]	a [\AA]	b [\AA]	c [\AA]	β [$^\circ$]	d, d' [nm]	D [nm]	E_g [eV]
ZrO_2	m- ZrO_2	66	5.18	5.22	5.34	99.59	9	43	5.2
	t- ZrO_2	34	3.58		5.23		7		
0.5% Ce/ ZrO_2	m- ZrO_2	61	5.19	5.22	5.35	99.71	13	40	5.1/4.0
	t- ZrO_2	39	3.62		5.16		10		
10% Ce/ ZrO_2	m- ZrO_2	24	5.16	5.20	5.32	99.35	17	20	3.0
	t- ZrO_2	76	3.62		5.17		10		
0.5% Er/ ZrO_2	m- ZrO_2	76	5.17	5.21	5.33	99.51	15	31	5.2
	t- ZrO_2	24	3.61		5.16		11		
10% Er/ ZrO_2	m- ZrO_2	28	5.18	5.22	5.35	99.58	12	63	5.1
	t- ZrO_2	72	3.64		5.16		12		

The weight percentages of phases obtained are in agreement with the qualitative considerations. The cell parameters of the m- ZrO_2 phase are poorly influenced by the insertion of the RE dopant, while the lattice constants of t- ZrO_2 undergo a distortion which increases with the RE content, as shown in Table 10. Moreover,

the m-ZrO₂, both in the bare and doped oxides, presents some degree of anisotropy. Indeed, the peaks broadening is not constant; for this reason it was used the Popa model²⁷⁶ for the refinement of this phase and we have listed in Table 10 the maximum (D) and minimum (d) crystallite sizes obtained from the Rietveld refinement, along with the (110) and (-111) plans, respectively. The maximum crystallite sizes for the monoclinic phase are generally larger than those tetragonal. Raman spectra obtained for all of the samples are reported in Figure 28 and Figure 29

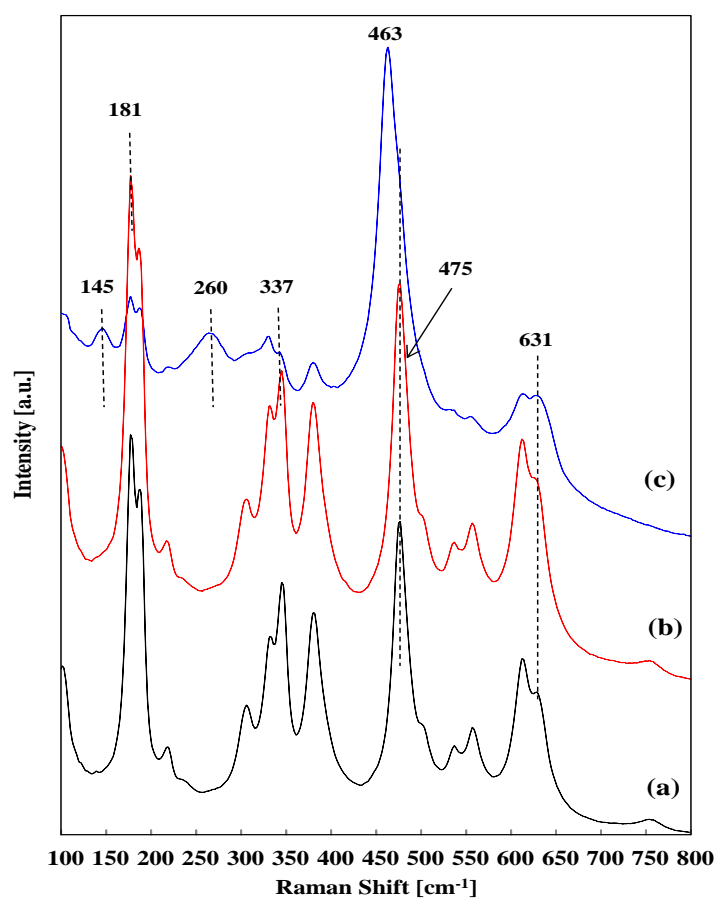


Figure 28. Raman spectra of the samples: ZrO₂ (a); 0.5% Ce/ZrO₂ (b) and 10% Ce/ZrO₂ (c).¹⁴⁷

Raman spectroscopy has been used to further investigate the structural features of the synthesized samples. Figure 28 shows micro-Raman spectra of Ce doped samples along with that of pristine ZrO₂ in the range from 100-800 cm⁻¹. Each measurement has been done at different positions on the surface of the powders in order to verify the homogeneity of the material. Raman spectroscopy is a very

sensitive technique to determine the phase composition in transition metal oxides. According to the literature, tetragonal ZrO_2 presents six active modes: 148, 164, 266, 322, 339, 467, 609, and 642 cm^{-1} ²⁷⁷ whereas monoclinic ZrO_2 shows sixteen active modes in the range $100\text{-}700 \text{ cm}^{-1}$: 102, 179, 190, 224, 235, 270, 305, 320, 334, 360, 375, 385, 476, 500, 553, and 636 .²⁷⁸

The micro-Raman spectrum of the pristine ZrO_2 showing the bands reported in literature results the presence of monoclinic and tetragonal phases in good agreement with the crystalline phases revealed by XRD. The Raman bands located at 145 and 260 cm^{-1} can be assigned only to the tetragonal phase and the bands at 181 and 337 cm^{-1} to the monoclinic phase. The perusal of Figure 28 indicates that the mentioned bands, attributed to the tetragonal phase, are more evident in the sample $10\% \text{ Ce/ZrO}_2$ than in the ZrO_2 , indicating the stabilization of the tetragonal polymorph in agreement to XRD results. The bands at 475 and 631 cm^{-1} are close to those typical of both polymorphs and could change their relative intensities for the two phases; often these two bands present ca. the same intensity in the tetragonal phase, but the band at 475 cm^{-1} becomes much stronger than that at 631 cm^{-1} in the case of the monoclinic phase. This insight, also observed in Figure 28, confirms the previous conclusion, i.e., the consolidation of the tetragonal phase by increasing Ce in the ZrO_2 sample. It is very important to note that in Figure 28, line (c), the spectrum of the $10\% \text{ Ce/ZrO}_2$ sample shows a peak at 463 cm^{-1} that corresponds to the typical band attributable to the presence of the cubic fluorite structure of CeO_2 . Because of the high Raman scattering of the CeO_2 cubic phase, the intensity of this band corresponding to the F_{2g} first-order symmetrical stretching mode of the Ce-O vibration unit, is remarkable. Hence, the Raman spectrum confirms the presence of CeO_2 in the $10\% \text{ Ce/ZrO}_2$ sample. Further differences between the spectrum of the ZrO_2 pristine sample and that of the doped samples, particularly $10\% \text{ Ce/ZrO}_2$, are attributable to distortions in the structure due to the presence of Ce.

In Figure 29(A) the micro-Raman spectra of Er doped samples are reported along with that of pristine ZrO_2 in the range from 100 to 800 cm^{-1} . As observed for the $10\% \text{ Ce/ZrO}_2$ sample, also in the Raman spectrum of the $10\% \text{ Er/ZrO}_2$, the 475 cm^{-1}

¹, band decreased in intensity indicating the consolidation of the tetragonal polymorph in the 10% Er/ZrO₂ powder.

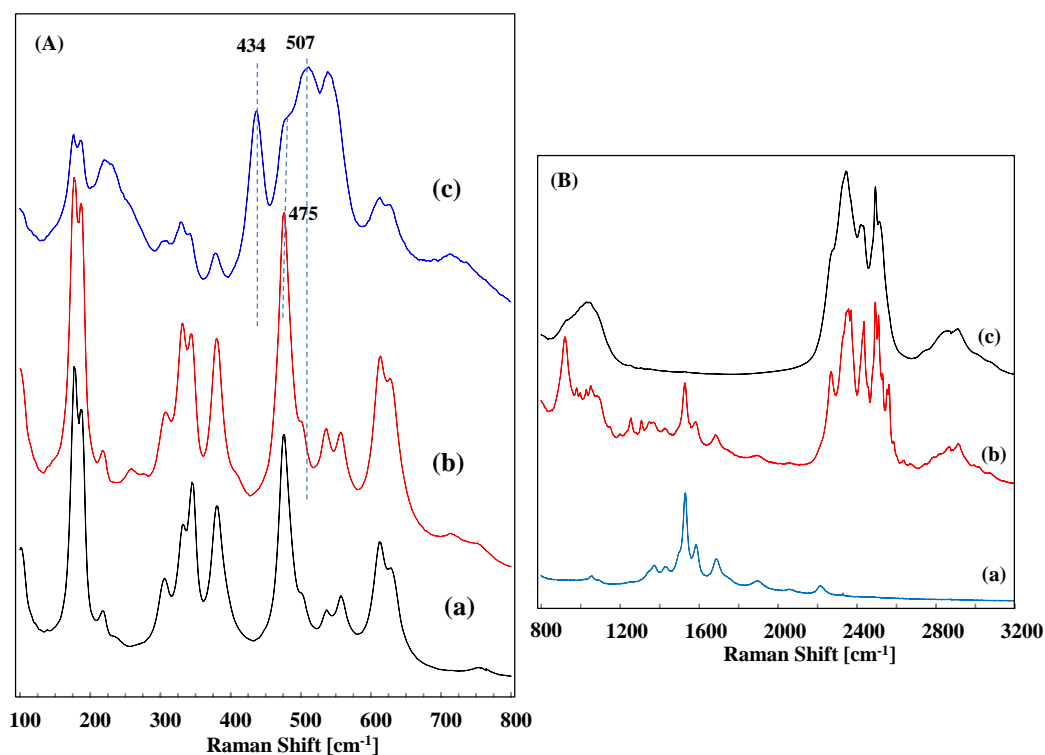


Figure 29. Raman spectra of the samples: ZrO₂ (a); 0.5% Er/ZrO₂ (b) and 10% Er/ZrO₂ (c).¹⁴⁷

By taking into account the ionic radii size of Zr⁴⁺, Ce⁴⁺ and Er³⁺, it should be considered that the incorporation of the rare earth ion into the zirconia structure is expected to modify the host lattice. Raman spectroscopy is an appropriate technique to detect the incorporation of dopants and the possible host lattice disorder and defects appearance due to their presence. The lattice defects induce disorder, which breaks the symmetry in Raman transitions giving rise to variations of some signals of spectrum. This occurs for the Er containing ZrO₂, where some Raman transitions appeared shifted with respect to the pristine ZrO₂ due to the doping with the trivalent cations Er³⁺ by virtue of the size of this cation (ionic radius Er³⁺ 0.881 Å, Zr⁴⁺ 0.790 Å) generating oxygen ion vacancies, as before reported.^{279, 280} Notably, Ce⁴⁺ presents an ionic radius of 0.92 Å, so the difference in size between Zr⁴⁺ and Ce⁴⁺ can favour also the partial segregation of CeO₂.

Figure 29(A) the band at 434 cm^{-1} of the 10% Er/ZrO₂ sample can be due to the presence of Er₂O₃. The bands at about 507 cm^{-1} can be assigned to the t-ZrO₂ (ca. 475 cm^{-1} in the pristine ZrO₂) and to the presence of Er₂O₃.²⁸¹ Consequently, for the sample 10% Er/ZrO₂ the presence of some segregated distorted sesquioxide species cannot be excluded. Indeed, the study of the spectra at higher energies (Figure 29(B)) appeared completely different from that of the pristine ZrO₂, but no data about the bands present in the range $2200\text{--}2600\text{ cm}^{-1}$, confirming the presence of Er₂O₃, were found in literature.

Concerning the band gap measurements, Figure 30 shows the Kubelka-Munk transformation of the diffuse reflectance spectra normalized to 1 for all of the previous mentioned samples.

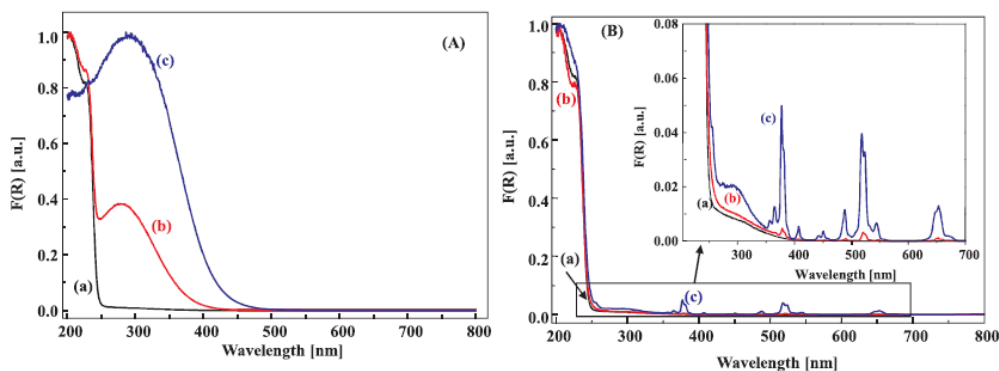


Figure 30. Absorbance spectra of the samples obtained by applying the Kubelka-Munk function, $F(R_{\infty})$, to the diffuse reflectance spectra. (A): ZrO₂ (a), 0.5% Ce/ZrO₂ (b), 10% Ce/ZrO₂ (c) and (B): ZrO₂ (a), 0.5% Er/ZrO₂ (b), and 10% Er/ZrO₂ (c) The inset is a magnification of the squared region.¹⁴⁷

An absorption shoulder, centred at ca. 300 nm, is clearly observed for the Ce doped samples in Figure 30(A). The absorption in the UV–vis range increases for all of the samples by adding the RE but the effect of Ce and Er ions is largely different as reported before.²⁷⁵ The presence of the absorption band centred at 300 nm dominates the spectra of the 10% Ce/ZrO₂ sample overlapping the fundamental transition of zirconia. The shape of the spectrum is strongly similar to that of pure CeO₂ indicating that this absorption could be related to the charge transfer transition from O 2p to Ce 4f. This finding could indicate the presence of CeO₂ on the surface of ZrO₂ for the X% Ce/ZrO₂ samples in accord with Raman results. Probably the CeO₂ was very well dispersed on ZrO₂ and consequently its presence

was not revealed by XRD analysis. The Er containing samples, on the other hand, show a smaller modification of the optical properties of the materials; indeed all of the spectra are very similar each other, except for the small region enlarged in the inset of Figure 30(B). Both the Er/ZrO₂ samples present many absorption bands which are the fingerprint of the Er³⁺ ion, and the shoulder centred at 300 nm already present in the undoped materials. This band intensity increases with the Er content. The values of E_g (eV) were calculated by using the Tauc plot²⁸² and are reported in Table 10. The values were calculated by considering a direct transition for all of the samples except for 10% Ce/ZrO₂, where an indirect transition was considered due to the high concentration of CeO₂. Thus, the CeO₂, as in the case of TiO₂ (anatase structure), shows an indirect band gap.²⁸³ For the 0.5% Ce/ZrO₂ sample two values are reported, one ascribable to the fundamental VB→CB transition of ZrO₂, and a second one due to the absorption band ascribable to the O 2p→Ce 4f charge transfer transition. The value of the band gap of ZrO₂ is not highly affected by the insertion of dopants, while the overall absorption is largely modified. Both 10% Er/ZrO₂ and 10% Ce/ZrO₂ samples are indeed coloured.

The photoluminescence emission spectra at $\lambda_{exc}=365$ nm (i.e., 3.40 eV) are reported in Figure 31.

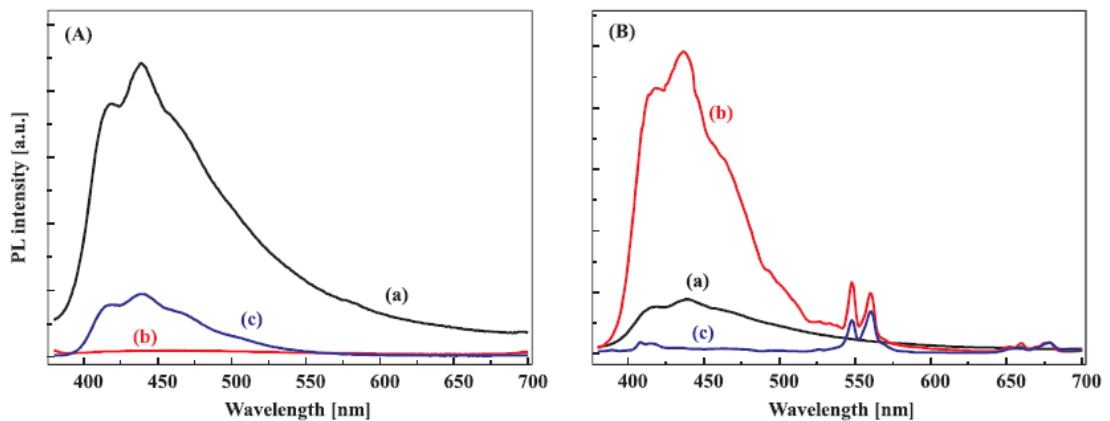


Figure 31. Photoluminescence spectra of (A): ZrO₂ (a); 0.5% Ce/ZrO₂ (b) and 10% Ce/ZrO₂ (c) and (B): ZrO₂ (a); 0.5% Er/ZrO₂ (b) and 10% Er/ZrO₂ (c).¹⁴⁷

Since the excitation energy is lower than E_g, the PL spectra can reflect the intra band gap defects present in the ZrO₂ samples. The pure ZrO₂ (Figure 31(a) both (A) and (B)) presents a broad, asymmetric emission band centred at around 440 nm

(i.e., 2.82 eV). This emission band was already reported in literature, and it is generally assigned to the radiative recombination of photogenerated holes with electrons occupying oxygen vacancies.²⁸⁴⁻²⁸⁶ In the case of Ce doped samples (Figure 31(A)), there is an evident suppression of the luminescence intensity, indicating a lower amount of intra band gap defects and thus a lower electron hole recombination rate. This effect is higher for the 0.5% Ce/ZrO₂ sample for which the luminescence intensity is nearly zero, while in the case of the 10% Ce/ZrO₂ sample the luminescence intensity is lower than that of pure zirconia but higher than that of the 0.5% Ce/ZrO₂ sample, probably because the 10% Ce/ZrO₂ sample absorbed more energy during the excitation due to its lower band gap (presence of well dispersed CeO₂). In the case of Er doped samples (Figure 31(B)), the effect is different, depending on the rare earth metal concentration. The 0.5% Er/ZrO₂ sample, indeed, shows an enhanced luminescence, indicating the formation of many oxygen vacancies as charge compensation for the introduction of Er³⁺ ions. The 10% Er/ZrO₂ sample, on the contrary, shows a total suppression of the luminescence intensity, except for the bands related to its f–f transitions, suggesting that in this case the main recombination centres are actually the Er ions and not the formed oxygen vacancies. EPR is a suitable technique to monitor the photo-induced charge separation process and, thus, to assess the photoactivity of a material under irradiation. Indeed, the direct charge separation is obtained by irradiating in situ the solid at the temperature of liquid nitrogen to avoid the rapid recombination of the carriers. If the photogenerated charges are stabilized by the solid (at different sites of the oxide, usually a cation for the electron and an oxide anion for the hole), paramagnetic centres can be formed (i.e. the O⁻ ion) and they can be monitored by the electron paramagnetic resonance. The effect of UV–vis light on hydrothermally synthesized ZrO₂ was already reported by Gionco et al.²⁷⁵ The as prepared sample does not show paramagnetic centres and its spectrum is a barely flat line. Upon irradiation, a new signal appeared ascribable to the photogenerated holes localized at an anion centre.

Figure 32 reports the EPR spectra recorded at liquid nitrogen temperature for the Ce/ZrO₂ (Figure 32(A)) and Er/ZrO₂ (Figure 32(B)) samples.

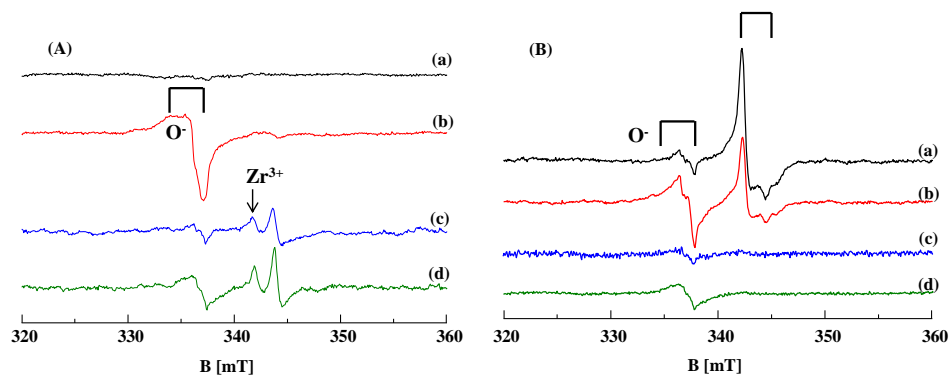


Figure 32. EPR spectra recorded at liquid nitrogen temperature for the Ce/ZrO₂ (A) samples: (a) 0.5% Ce/ZrO₂ before irradiation; (b) 0.5% Ce/ZrO₂ after irradiation; (c) 10% Ce/ZrO₂ before irradiation; (d) 10% Ce/ZrO₂ after irradiation and Er/ZrO₂ (B) samples: (a) 0.5% Er/ZrO₂ before irradiation; (b) 0.5% Er/ZrO₂ after irradiation; (c) 10% Er/ZrO₂ before irradiation; (d) 10% Er/ZrO₂ after irradiation. Irradiation time: 15 min.¹⁴⁷

For all of the samples, both the spectra before ((a), (c)) and after ((b), (d)) irradiation for 15 min, are reported. The spectrum of the as prepared 10% Ce/ZrO₂ sample shows some intrinsic defectivity. Spectra in Figure 32 are reported against the external applied magnetic field B₀. Eq. 16 allows extrapolating the related values of the g factors.

$$\Delta E = h\nu = g_e * \mu_B * B_0 \quad \text{Eq. 16}$$

The factor g_e is very useful being a dimensionless quantity that characterizes the magnetic moment and gyromagnetic ratio of electron. In fact, it is essentially a proportionality constant that relates the observed magnetic moment μ of a particle to its angular momentum quantum number and a unit of magnetic moment, usually the Bohr magneton (μ_B) or nuclear magneton (eq. 16).

In detail, Figure 32 A (spectrum c) shows two signals: the one centred at g=1.978 (B=342) is assignable to Zr³⁺ species¹⁴⁹, the assignment of the one at B = 344, related with g_{||}=1.96 and g_⊥=1.94, reported in literature, is still under debate.²⁸⁷⁻²⁸⁹

Under irradiation a new signal ascribable to O⁻ species appears in both 0.5% Ce/ZrO₂ and 10% Ce/ZrO₂ samples. The effect of irradiation is much more evident in the case of the 0.5% Ce/ZrO₂ sample, whilst for 10% Ce/ZrO₂ the intensity of the new signal is much lower. This can be due to spin-orbit coupling effects that affect the localization of the photogenerated charges. The spectrum of the as prepared

0.5% Er/ZrO₂ sample also shows the presence of a well-defined axial signal at $g_{\parallel}=1.978$ and $g_{\perp}=1.955$, which is assigned to Zr³⁺ ions, probably due to the Er³⁺ ions and the consequent formation of oxygen vacancies. Upon irradiation, both the spectra of the 0.5% Er/ZrO₂ and 10% Er/ZrO₂ samples show the formation of the signal related to the localized hole. In addition, in this case the intensity of the spectrum of 0.5% Er/ZrO₂ is higher than that of 10% Er/ZrO₂.

3.1.3 Photocatalytic activity study

Concerning the photoreactivity experiments, blank tests, carried out under the same experimental conditions (section 3.1.1) and they ensured that no organic compounds were produced in the absence of catalyst as well as under dark or in the absence of CO₂.

On the contrary, in all of tests carried out in the presence of CO₂, all of the samples showed activity for CO₂ photo-reduction giving rise to small organic molecules and CO which increased by increasing the irradiation time as shown in Figure 33, i.e., in the presence of ZrO₂ catalyst.

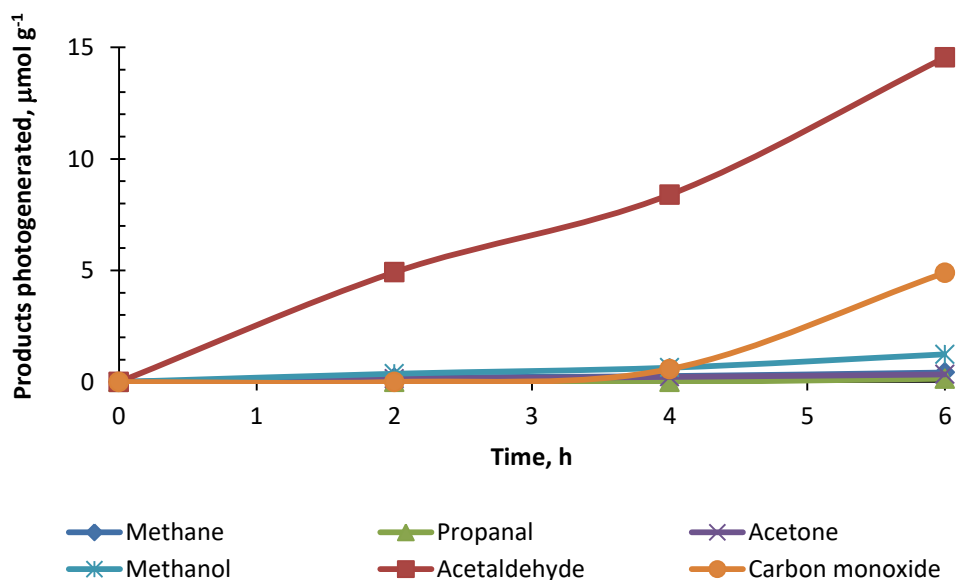


Figure 33. Photogenerated products versus irradiation time in the presence of ZrO₂ catalyst, CO₂ and H₂O.

Generally, during the first 6 h of irradiation acetaldehyde, CO and traces of methane, methanol, methanal, propanal and propanone were obtained for all of the catalysts used. Data are summarized in Figure 34.

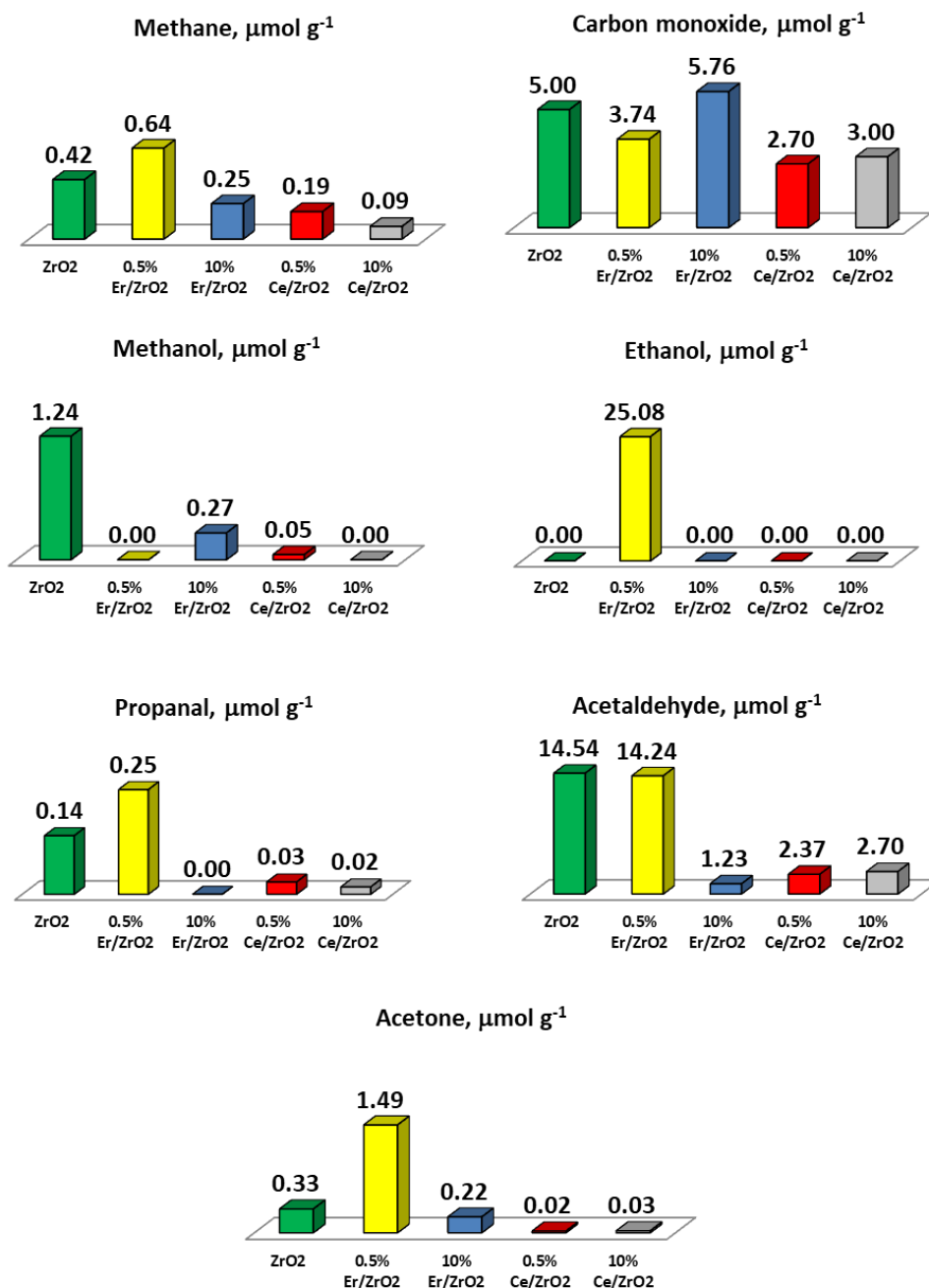


Figure 34. Photocatalytic reactivity (in terms of $\mu\text{mol g}^{-1}$) towards CO_2 reduction after 6 hours of irradiation time obtained with the following catalysts ZrO_2 , 0.5% Er/ZrO_2 , 10% Er/ZrO_2 , 0.5% Ce/ZrO_2 and 10% Ce/ZrO_2 coloured green, yellow, blue, red and grey, respectively.

The presence of ZO_2 catalyst induces formation of ca. 5 and 15 $\mu\text{mol g}^{-1}$ of CO and acetaldehyde, respectively.

At longer irradiation times (up to 24 h) the maximum amount of acetaldehyde increased from ca. 15 $\mu\text{mol g}^{-1}$ (after 6 h) to 25 $\mu\text{mol g}^{-1}$. Similar behaviour was observed in the presence of 0.5% Er/ ZO_2 sample, where acetaldehyde production increased from 14 to 17 $\mu\text{mol g}^{-1}$ after 6 h and 24 h of irradiation, respectively. For both samples the CO_2 reduction rate declines for long-term irradiation. Although this effect is more pronounced in the presence of 0.5% Er/ ZO_2 , this sample showed the best activity producing also 25 $\mu\text{mol g}^{-1}$ of ethanol after 6 h irradiation. This amount remained constant even after 24 h irradiation.

As shown in Figure 34, increasing the extent of Er doping on ZrO_2 (10% Er/ ZO_2 sample) results in a reduction of the CO_2 conversion efficiency and no ethanol could be detected. In detail, in the presence of 10% Er/ ZO_2 sample the amount of acetaldehyde produced decreased more than 10 times with respect to 0.5% Er/ ZO_2 , while a slight increase of the photogenerated CO was observed (from 3.74 to 5.76 $\mu\text{mol g}^{-1}$), which hence becomes the main product.

A different behaviour was observed in the presence of Ce doped photocatalysts. CO and acetaldehyde remained the main products of CO_2 photoreduction, but the amount of photoreduction products increased with increasing the Ce doping. However, the overall efficiency of Ce doped materials was always lower than both that of bare ZO_2 and Er doped materials.

Therefore, in all photocatalytic test, traces of methane, methanol, propanal and acetone detected were lower than 1 $\mu\text{mol g}^{-1}$, excepted for the acetone (1.49 $\mu\text{mol g}^{-1}$) and methanol (1.24 $\mu\text{mol g}^{-1}$) produced in the presence of 0.5% Er/ ZO_2 and ZO_2 respectively, after 6 h of irradiation time.

As above discussed, ZO_2 and 0.5% Er/ ZO_2 catalysts exhibited the best photoreduction performance towards CO_2 reduction. This fact are highlighted in Figure 35 where the total carbon converted after 6 h irradiation time, is calculated according to eq. 17.

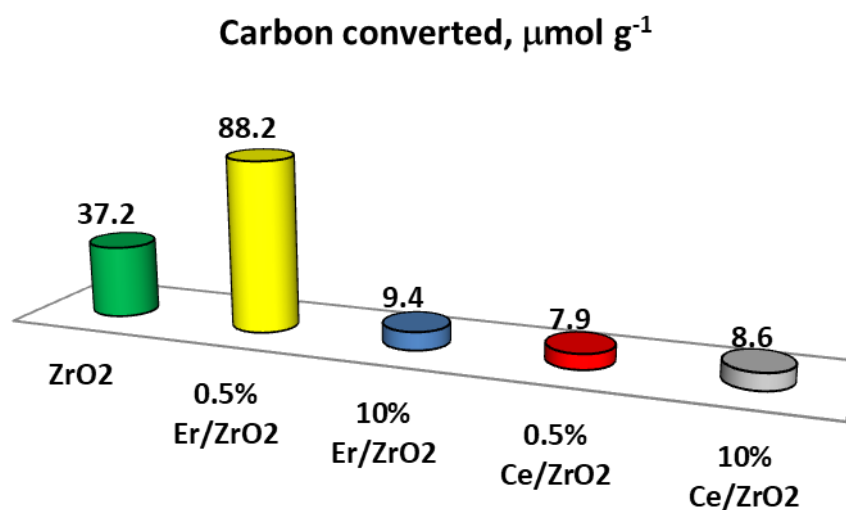


Figure 35. Carbon converted obtained after 6 hour of irradiation time with the following catalyst ZO₂, 0.5% Er/ZO₂, 10% Er/ZO₂, 0.5% Ce/ZO₂ and 10% Ce/ZO₂.

$$\frac{\text{Converted carbon}}{\text{catalyst weight}} = \frac{\sum \text{Carbon for each produced species}}{\text{Amount of catalyst}}, \frac{\mu\text{mol}}{\text{g}_{\text{catalyst}}} \quad \text{Eq. 17}$$

By comparing the obtained results, the best photoreduction activity was achieved in the presence of 0.5% Er/ZO₂ and ZO₂ affording ca. 88 and 38 $\mu\text{mol g}^{-1}$ of carbon converted, respectively. 0.5 % Er doping enhanced the ZrO₂ performance more than 2 times. An opposite trend was observed by increasing the amount of Er from 0.5 to 10%, which caused a drastic reduction in the CO₂ reduction efficiency (3 times less with respect the ZO₂ sample and ca. 10 times less with respect to 0.5% Er/ZO₂ catalyst). Ce doped materials presented the lowest efficiency. However, increasing Ce doping resulted in higher amount of carbon converted (from 7.9 to 8.6 $\mu\text{mol g}^{-1}$) comparable with that obtained with 10% Er/ZO₂ catalyst (9.4 $\mu\text{mol g}^{-1}$).

As literature reports, the same reaction has been carried out by using the same set-up in the presence of TiO₂ photocatalysts obtained from TiCl₄ as the precursor.¹¹⁰ In that case, depending on the type of catalyst, a different selectivity was observed, but the main reaction product observed was also ethanal in a maximum amount of ca. 1 $\mu\text{mol g}^{-1}$ after 5 h of irradiation. Also, GaP/TiO₂ materials were used before in the same system.¹²² In that case, the main product obtained by the CO₂ reduction

was methane in an amount of ca. $12 \mu\text{mol g}^{-1}$ after 6 h of irradiation. However, a more thorough investigation is necessary in order to understand the different selectivity of the various photocatalysts reported in the literature.

The photo-activity of bare ZrO_2 under UV irradiation can be explained by taking into account the photoluminescence and EPR studies indicating that this material was able to photo-produce electron-hole pairs under UV light irradiation (in the PL $\lambda_{\text{exc}}=365 \text{ nm}$), although its band gap is 5.2 eV.

To sum up, the CO_2 photoreduction activity of the ZrO_2 based samples can be explained by considering their defectivity, which mainly consists in the presence of oxygen vacancies. Even if ZrO_2 presents a wide band gap (5.2 eV), the high defectivity not only induces visible light harvesting capability, but also the possibility of dissociative adsorption of CO_2 . In fact, as schematically depicted in Figure 36 and reported in the relevant literature,²⁹⁰ oxygen vacancies allow formation of intermediate complexes (a) characterized by lower activation energy with respect to the species formed by interaction of CO_2 with a perfect ZrO_2 surface (b).

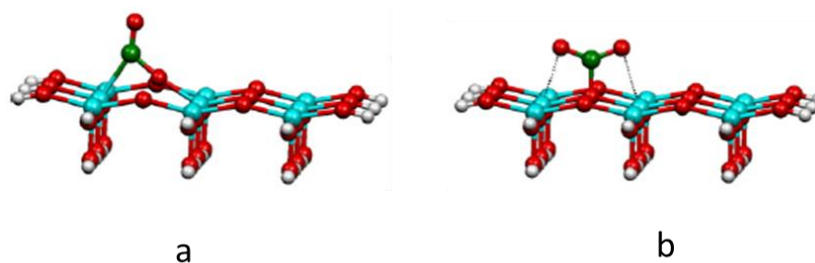


Figure 36. CO_2 adsorption on defective (a) and perfect (b) ZrO_2 surface.

Doping with Ce^{4+} stabilizes the tetragonal polymorphous structure of ZrO_2 thus diminishing the defectivity. As a result, CO_2 conversion for all of the Ce doped materials was lower than that observed for the bare ZrO_2 sample. On the other hand, low amounts of Er^{3+} in the ZrO_2 lattice (0.5% Er/ZrO_2 sample) increase the defectivity of the material as demonstrated by EPR and Raman spectroscopy results. As a result, this sample showed the highest photocatalytic CO_2 reduction efficiency. However, increasing the Er doping extent tentatively favoured

segregation of erbium containing oxides, which led a detrimental effect on the CO₂ reduction activity.

3.1.4 Conclusion

The preparation of ZrO₂ by a solvothermal method and the introduction of new electronic states in this high band gap semiconductor by doping with Ce and Er, led to new photocatalysts able to absorb portions of UV ($\lambda=365$ nm) and solar light. Pristine ZrO₂ as well as Ce and Er-doped ZrO₂ resulted photoactive in gas-solid regime for CO₂ reduction to form mainly acetaldehyde. This uncommon behaviour for an insulator like ZrO₂ (with a band gap of more than 5 eV) is explained by the formation of intra band gap states due to the O vacancies. The intra band states are responsible for the “double jump” absorption leading to excitation of the electrons from the valence band to the conduction band. In the doped materials, the lanthanides doping showed two opposite CO₂ reduction capability. In the Er doped materials, lower doping resulted in an enhancement of the activity due to the increasing of O vacancies with respect to bare ZrO₂. At higher Er contents and in both Ce doped materials, lower photoreduction capability was achieved with respect to pure ZrO₂. Seen the promising behaviour, further investigation could be useful to improve the structure understanding and the reduction capability of this type of catalysts.

3.2 G/TiO₂ composites for CO₂ photoreduction

The results presented in this chapter have been published in:

F. R. Pomilla, R. Molinari, G. Marci, E.I. Garcia-Lopez and L. Palmisano. Photocatalytic CO₂ valorisation by using TiO₂, ZrO₂ and graphitic based semiconductors. *Research and Technologies for Society and Industry (RTSI)*, ISBN: CFP18C29-ART, Part Number: 978-1-5386-6286-3, , **2018, 478-483**. I participated with an oral presentation in the relative 4^o International Forum EEI, RTSI, inside the section Nanomaterials for 4.0, 10-13 September 2018, Scuola Politecnica of University of Palermo, Palermo, Italy.

3.2.1 Photocatalytic test conditions

In order to test the G/TiO₂ catalysts at different graphene loadings (0.5, 1, 3 and 10) for CO₂ photoreduction, the same apparatus described in the section 3.1.1 was used. In addition, in this case, blank tests were performed.

3.2.2 Characterization of G/TiO₂ materials

FTIR spectra of the home-prepared G/TiO₂ samples are reported in Figure 37. The FTIR spectrum of graphene oxide (GO) in Figure 37 (black spectrum) shows the presence of abundant hydroxyl, carboxyl, and epoxide groups, as indicated by the characteristic peaks of the C=O stretching vibration at 1733 cm⁻¹, the O-H deformation at 1404 cm⁻¹, the C-O (epoxy) stretching vibration at 1227 cm⁻¹, the C-O (alkoxy) stretching vibration at 1049 cm⁻¹, and the epoxy or peroxide group peak at 957 cm⁻¹. After reduction of GO by hydrothermal synthesis in the presence of TiO₂ (see section 2.2.2), the intensities of the bands related to oxygen containing groups significantly decrease in all of the spectra of the composites G/TiO₂, while the peak at 1624 cm⁻¹, which corresponds to non-oxidized graphitic domains remains virtually the same. This confirms the reduction of GO to graphene.¹⁷⁶ In addition, it is evident the broad band in the low frequency region (600-1000 cm⁻¹) of the spectra of the

composite materials due to the presence of TiO_2 (Ti-O-Ti stretching). However, the band centre shifts towards higher wavenumbers at higher graphene loadings. This effect has been reported in literature¹⁷⁶ and it is due to the presence of Ti-O-C vibrations which combine with the Ti-O-Ti vibrations of TiO_2 . This result confirms formation of G/ TiO_2 composites by chemical interaction of TiO_2 and graphene.

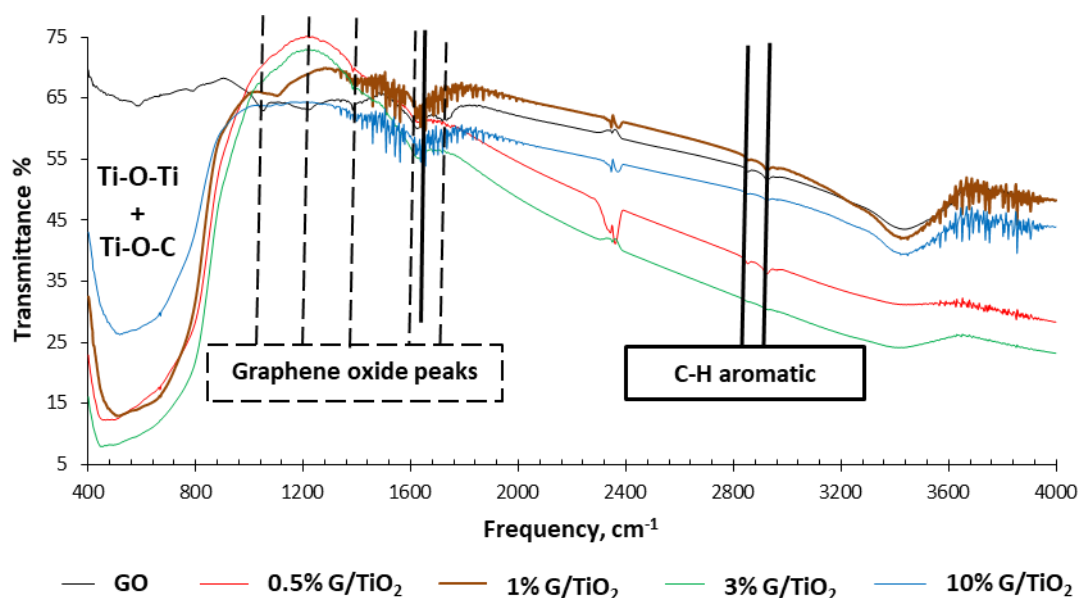


Figure 37. FTIR spectra recorded from 400 to 4000 cm^{-1} of pure graphene oxide (black) and G/ TiO_2 composites at different graphene loading. The vertical black dashed and full black lines indicate the graphene oxide (GO) and graphene (G) characteristic peaks, respectively.

In order to obtain information about structural defects of graphene, Raman analysis has been performed and the results are reported in Figure 38. By the analysis of the characteristic peaks labelled in Figure 38 as D and G, Raman spectroscopy is capable not only to identify the presence of graphene but also to provide information such as the amount of disorder, doping, and the atomic arrangements at the edges.²⁹¹ Briefly, all carbons show common features in their Raman spectra in the 800–2000 cm^{-1} region, the so-called G and D peaks, which lie at around 1580 and 1360 cm^{-1} , respectively.²⁹² The D peak is due to the breathing modes of sp^2 rings and requires a defect for its activation.²⁹³ This band derives from transvers optical phonons around the K point of the Brillouin zone.²⁹² The G peak corresponds to the E_{2g} phonon at the Brillouin zone center.²⁹² The Raman spectra of graphite and graphene also show

second-order scattering.²⁹⁴ The *D* peak and its second-order peak *2D* are activated by resonance processes.^{295, 296} Notably, the *G* peak of the composites is shifted towards higher frequencies with respect to the *G* peak of the spectrum of bare GO. This indicates that the graphitic structure present in the composites is graphene rather than graphene oxide as reported in literature.²⁹⁷

The *D* band is an indication of disorder, which may arise from certain defects such as vacancies, grain boundaries,²⁹³ and amorphous carbon species.²⁹⁸ The intensity ratio of these two bands indicates the quality of the product. The band intensity ratio I_d/I_g found equal to 1.00 for GO, decreased a little bit for all the G/TiO_2 composites. This difference indicates a decrease of defects by recovery of the aromatic structures. Lee et al. reported,²⁹⁹ in fact, an increase of the I_d/I_g ratio of reduced graphene oxide treated with hydroiodic acid and acetic acid, indicating that the reduction process altered the structure of GO with a large quantity of structural defects.

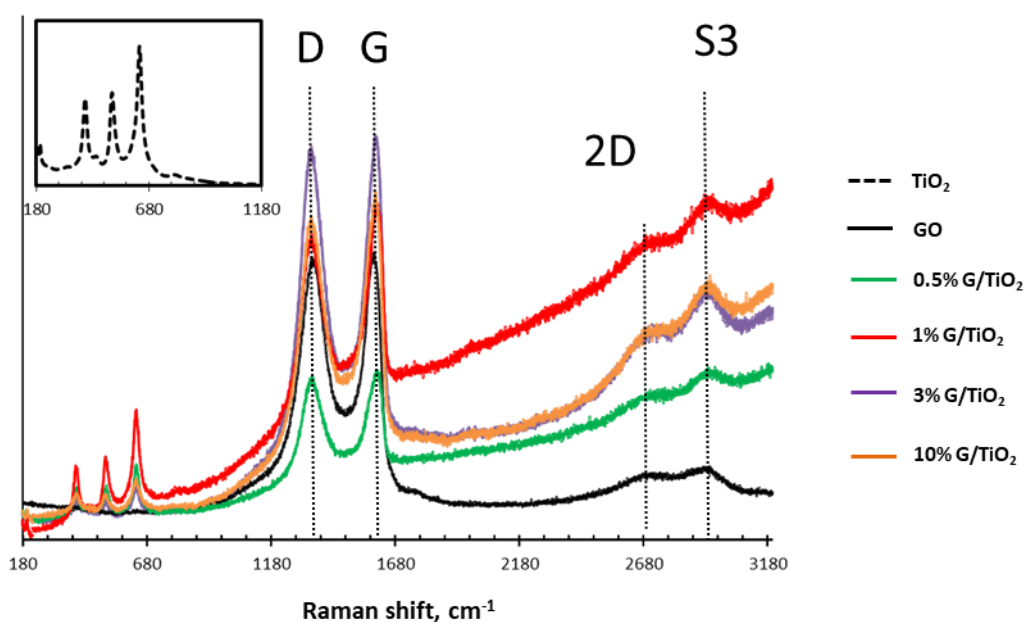


Figure 38. Raman spectra analysis of G/TiO_2 composites, pure GO and TiO_2 by using a laser at 532 nm. The TiO_2 Raman spectrum is shown in the inset (dashed line).

Based on this information, it can be deduced that the composite prepared herein contains less defects than the GO. The band at 2700 cm^{-1} is particularly interesting.

Monolayer graphene shows a sharp peak at ca. 2700 cm^{-1} known as the 2D band. Hence, the width of this band is considered an indicator of the number of graphene layers. Casiraghi found that while the intensity of the *G* peak is not affected by doping, the 2D peak intensity is strongly sensitive to doping and in particular to the dynamics of the photoexcited electron-hole pairs.²⁹¹ In Figure 38, the band at 2700 cm^{-1} is related to the graphene structure.

The band, known as S3 (2900 cm^{-1}), is a second-order peak derived from the D–G peak combination. The intensity ratio between the bands S3 and 2D is proportional to the decrease of the defects.²⁹⁷ The GO spectrum shows a large S3 band with low intensity appearing as a shoulder of the 2D band. When the GO is reduced to graphene, as in the case of the G/TiO₂ composites, the band S3 (indicated in Figure 38) increases in intensity and is more defined in terms of shape. These changes are more evident in the sample with loading starting from 1% wt.

This reduction, in terms of defects, is accompanied by lower oxygen content in graphene as FTIR suggests.

Three spot analyses have been performed for each sample. Some images were taken and are reported in Figure 39.

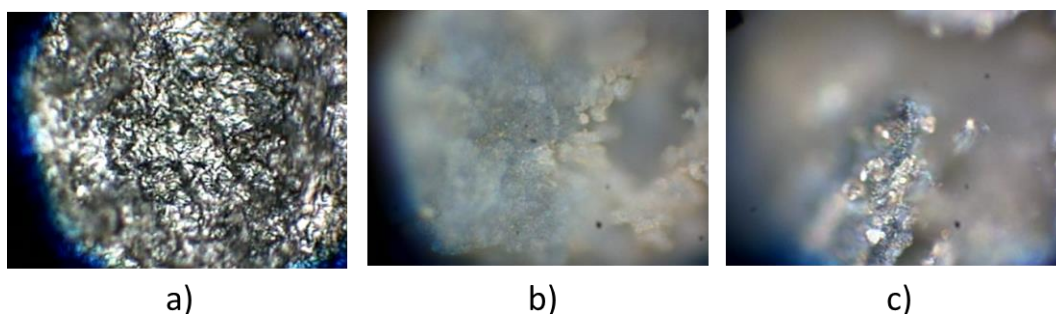


Figure 39. Microscopy images of a) GO, b) 0.5% G/TiO₂, and c) 3% G/TiO₂ samples.

Figure 39 shows that the composite 0.5% G/TiO₂ is less homogeneous with respect to GO sample. This evidence is probably due to the very low graphene loading along with its not complete dispersion. In these samples (blue/grey) the TiO₂ and G/TiO₂ domains are evident. At higher graphene loadings, higher homogeneity can be observed.

In order to study the effect of the G % wt. loading on the optical properties, DRS spectra were performed. Results are shown in Figure 40. All of the samples present a red shift of the absorption edge compared to bare TiO₂, which shows standard absorption edge at ca. 410 nm, except the sample at lower G loading equal to 0.5%. Probably this G loading is too low to generate a UV light absorption modification on composite. Whilst, 1 wt. % G composite presents an adsorption at ca. 420 nm, which correspond in a red shift of TiO₂ absorption edge equal to 410 nm. This result is in accord with the relevant literature.¹⁷⁶ When, in the G/TiO₂ composites, the G wt. % loading increases at 3% and at 10, the relative absorption edge rises to 440 and 470 nm, respectively. These results indicate that the introduction of graphene causes the narrowing of the band gap, as shown in Figure 40 (intersection between the dashed lines and the wavelength axis) with a consequently catalyst visible light absorption. This narrowing should be attributed to the chemical bonding between TiO₂ and G, by formation of Ti-O-C bond, as previously observed (FTIR analysis, Figure 37) and as suggested by Zhang et al.¹⁷⁶ As a result of the extended photo-responding range a more efficient utilization of the solar spectrum could be achieved, especially under visible light irradiation. The visible light harvesting capability of the 10% G/TiO₂ catalysts is expected to improve its photoactivity.

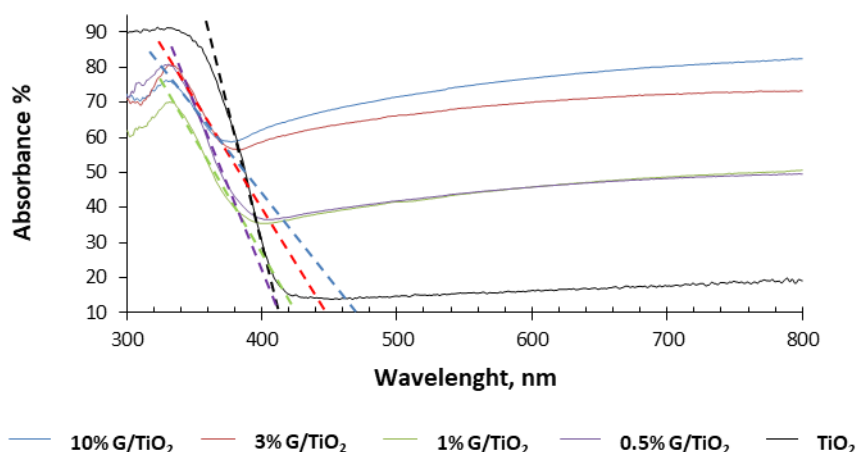


Figure 40. Diffuse Reflectance spectra recorded for all G/TiO₂ composites.

Table 11 summarises the media of specific surface area (SSA) of the samples in desorption and adsorption of N₂. The SSA is higher than that of TiO₂ for samples at

high graphene content (3 and 10%) whilst is lower than TiO₂ at low graphene content (0.5% and 1% G/TiO₂). This effect is probably due to the inhomogeneity of samples at low wt. % (0.5 and 1% of G) where the G particle are not well dispersed thus blocking the access to TiO₂ channels. On the other hand, in the sample at 3 and 10 % G/TiO₂, G is well dispersed in the composite and the SSA of the material (TiO₂) increases making easier the adsorption of the reagent.

Table 11. Specific Surface Area (SSA) obtained by a single point measurements of desorption and adsorption of N₂.

SSA, m ² g ⁻¹	10% G/TiO ₂	3% G/TiO ₂	1% G/TiO ₂	0.5% G/TiO ₂	TiO ₂
A _{media}	58	57	45	46	52

3.2.3 Photocatalytic activity of G/TiO₂ samples

The photocatalytic tests for CO₂ reduction were performed in a gas phase batch photoreactor under the conditions detailed in section 3.1.1, in the presence and in the absence of CO₂, cleaning by N₂ under irradiation prior to CO₂ feeding. The same products were qualitatively detected during 6 hours of irradiation by using the G/TiO₂ photocatalysts, but with a different amount depending on the graphene loading. In particular, the amount of CO₂ reduction products increased by increasing irradiation time. The G/TiO₂ composites produced methane (Figure 41) and methanol (Figure 42) as the major products, and in some cases also acetaldehyde and carbon monoxide were detected.

In particular, the 1% G/TiO₂ sample exhibited the best CO₂ photoreduction capability reaching a methane concentration of ca. 1000 μMg⁻¹, corresponding to a methane production rate of 5 μmol g⁻¹ h⁻¹. This result is in accord with that reported by Tu and coworkers which found a methane production rate of 7.3 μmol g⁻¹ h⁻¹ after 4 h of irradiation time (reactor volume: 25 mL).

0.5% and 1% G/TiO₂ composites produced a methane concentration of ca. 200 μM g⁻¹ after 6 h of irradiation. The worst methane production (120 μMg⁻¹) was detected in the presence of 10% G/TiO₂, with the highest G content, showing reactivity at least 4 times lower with respect to that measured for 1%G/TiO₂ catalyst.

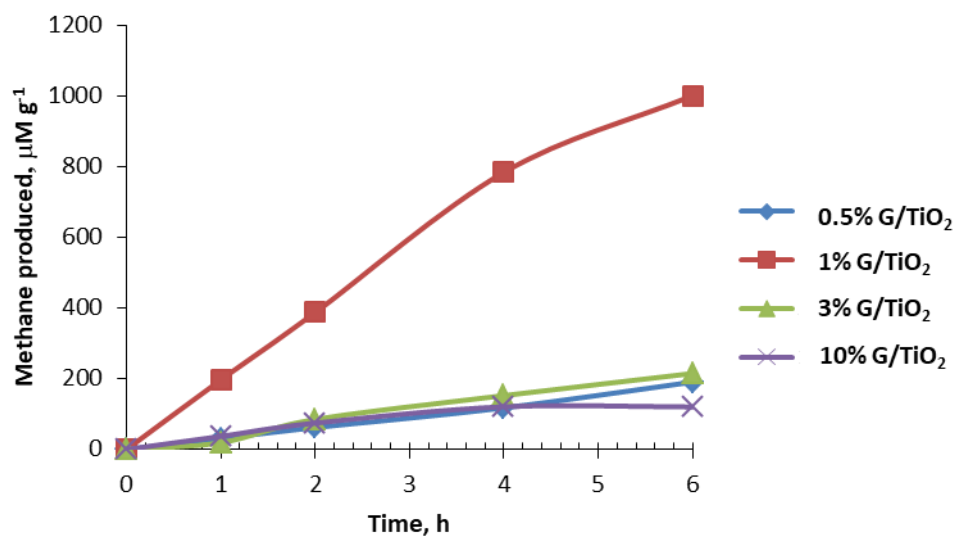


Figure 41. Methane photo-generated versus irradiation time in the presence of G/TiO₂ composites.

As far as the methanol formation is concerned, generally during the first two hours of irradiation its concentration strongly increases and after slows down or decreases. As in the case of methane production, the maximum concentration was obtained in the presence of 1% G/TiO₂ which allowed to produce 172 µM g⁻¹, whilst 15 and 43 µM g⁻¹ were detected in the presence of 0.5% G/TiO₂ and 3% G/TiO₂ catalysts, respectively. (Figure 42)

In addition, in this case, the 10% G/TiO₂ sample exhibited the worst photoactivity and methanol produced in the first hours of irradiation was degraded during the following irradiation.

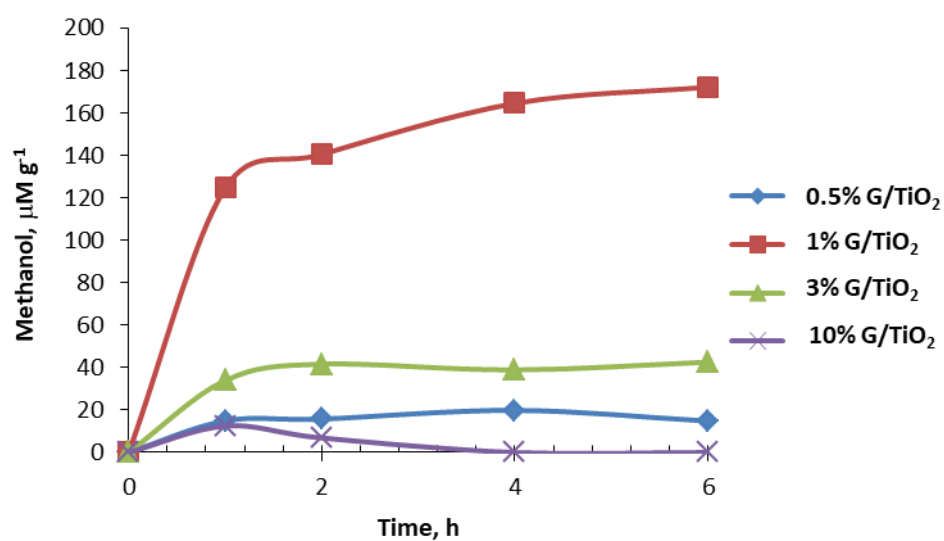


Figure 42. Methanol photo-generated versus irradiation time in the presence of G/TiO₂ composites.

As shown in Figure 43, only the samples 1% and 10% G/TiO₂ were capable to photoreduce CO₂ to carbon monoxide, which reached a concentration of 100 and 90 µM g⁻¹, respectively. In the presence of the other samples, no CO was detected.

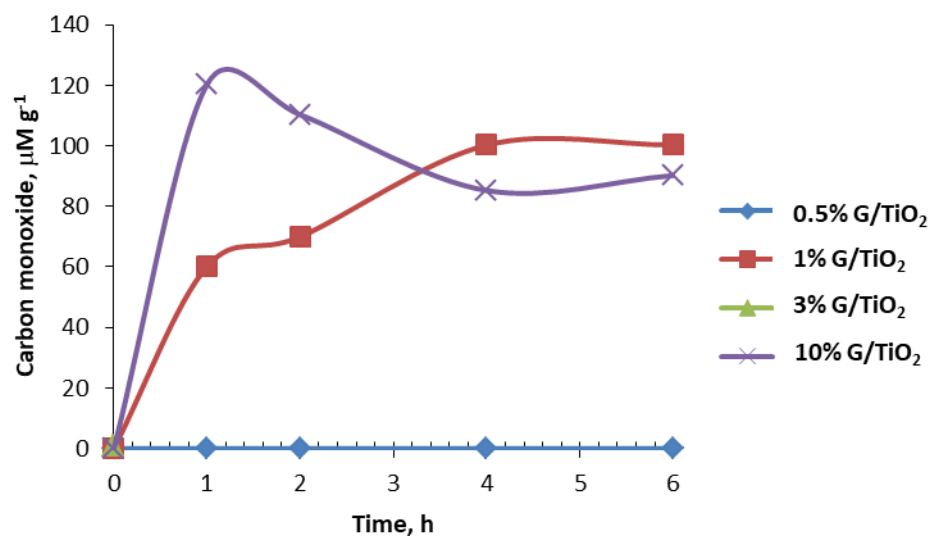


Figure 43. Carbon monoxide photo-generated versus irradiation time in the presence of G/TiO₂ composites.

Acetaldehyde was detected only for the samples with low graphene amount (Figure 44). In particular, after 6 h irradiation concentrations of ca. 243 and 12 µM g⁻¹ was detected in the presence of 1% G/TiO₂ and 0.5% G/TiO₂ photocatalysts, respectively.

Notably, the presence of acetaldehyde as a CO₂ photoreduction product has been never observed before in other reports in the presence of graphene modified TiO₂.

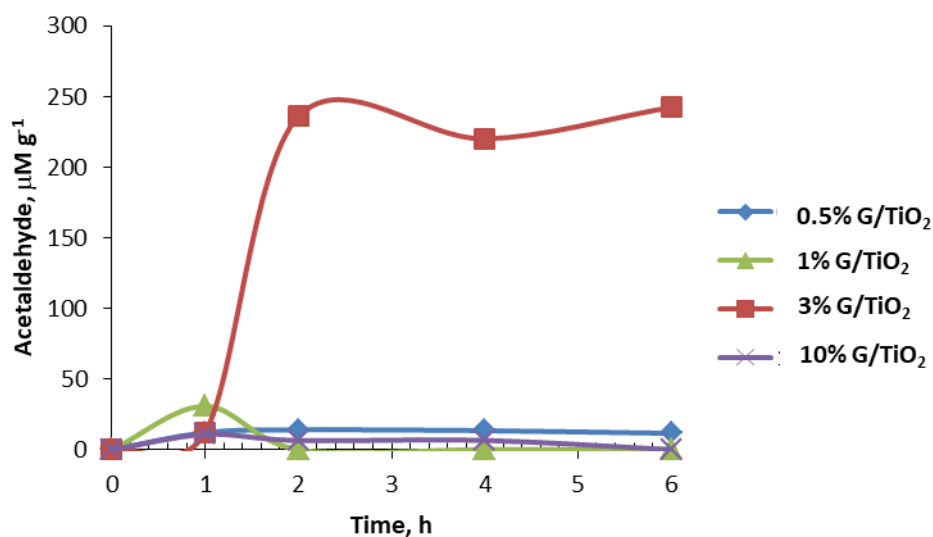


Figure 44. Acetaldehyde photo-generated versus irradiation time in the presence of G/TiO₂ composites.

In order to evaluate the CO₂ photoreduction improvement, due to the graphene loading, TiO₂ alone was also tested under the same experimental conditions. In these experiments, no products were detected highlighting the scarce reduction capability of pure commercial TiO₂ with respect to the composites. This is also evident from the values of total carbon converted which are reported in Figure 45. In detail, a loading of 0.5 % wt of G increases the total carbon converted (Eq. 17 section 3.1.3) from 0 to 5.7 µmol g⁻¹. Further increasing the amount of G from 0.5 to 1% wt in the composite results in an important improvement of the amount of total carbon converted, which reaches a value of 44 µmol g⁻¹ (ca. 9 times more just by doubling the graphene content). This result is in accord with the literature studies previously summarized in Table 4. When the amount of G in the composite rises from 1 % to 3 wt %, the photoreduction capability of the material drastically falls from 44 to 7.2 µmol g⁻¹ h⁻¹ (in terms of total carbon converted). As Figure 45 shows, further increments of graphene loading up to 10% wt, decreases the photoreactivity of material to values comparable with those retrieved for 0.5% G/TiO₂. The existence of an optimum graphene content has been already highlighted in literature.¹⁸¹ However, by comparing the best results obtained with the 1% G/TiO₂ catalyst in this

dissertation with those reported in literature, the carbon-converted values hereby reported are the highest ever reported in the presence of metal free photocatalysts.

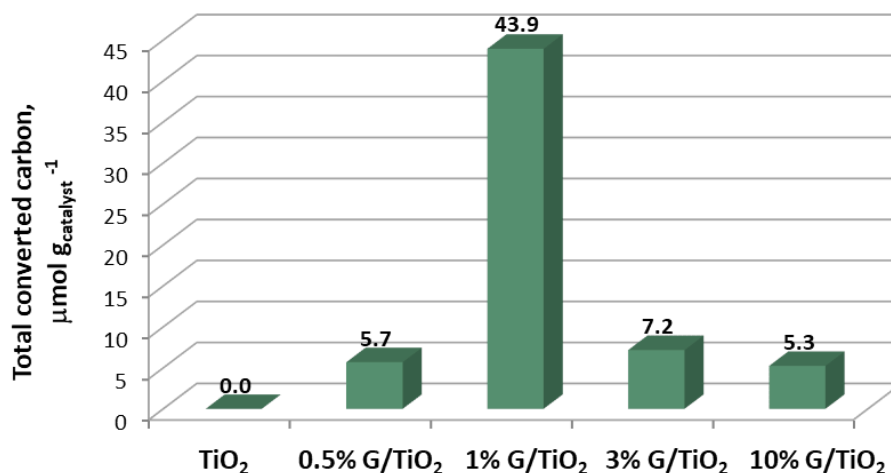


Figure 45. Total carbon converted after 6 h of irradiation time in the presence of G/TiO₂ composites.

Even if 1% G/TiO₂ photocatalyst shows the best photoreduction capability in terms of CO₂ conversion, it shows the lowest selectivity (Eq. 18) towards methane with respect to the other composites tested (Figure 46).

$$Selectivity_i = \frac{i\text{-species produced}}{\sum_i^n \text{species produced}}, \quad \text{Eq. 18}$$

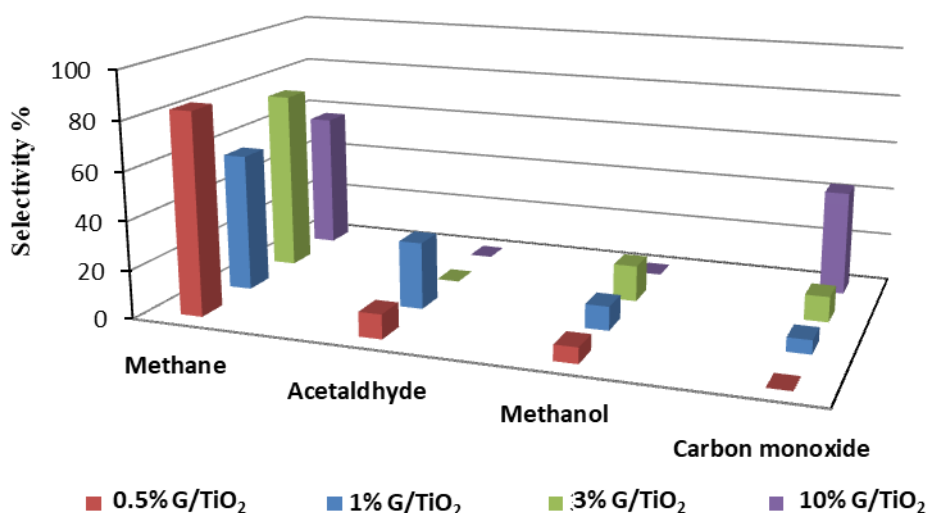


Figure 46. Selectivity of methane, carbon monoxide, acetaldehyde and methanol photogenerated after 6 h of irradiation in the presence of G/TiO₂ composites.

In detail, 0.5% G/TiO₂ shows the best selectivity to methane (83.5%). An interesting trend is observable with respect to the methanol selectivity, which increases with increasing the graphene loading and reaches the highest value (14 %) in the presence of 3% G/TiO₂.

10% G/TiO₂ catalyst converts CO₂ only to two products, i.e., methane and CO. In particular, it shows the best selectivity (43%) towards CO. Notably, the selectivity values decrease with decreasing the graphene loading for all of the composites.

3.2.4 Conclusion

The hydrothermal technique was used to prepare G/TiO₂ hybrid materials at different G loading from GO as the precursor. Characterization results highlighted chemical interaction between G and TiO₂ particles through Ti-O-C bonding formation. The electrons photogenerated by excitation of the TiO₂ nanoparticles can transfer through graphene thus reducing losses related to charge recombination. Furthermore, the higher electron availability enables photoreduction of CO₂ into hydrocarbon fuel.

Notably, products deriving from multi-electron transfer processes, such as methane, are preferentially formed. This is due to the less endergonic nature of these processes (-0.24 V vs SHE at pH 7) with respect to the mono-electron transfer one (-1.9 V vs SHE at pH7), and to the synergistic effect of TiO₂ and G. In fact, the latter efficiently conducts the photogenerated electrons, thus reducing charges recombination and enhancing the electron availability. The highest methane production (1000 μM g⁻¹) was observed for the 1% G/TiO₂ composite and it is the highest ever reported for similar systems in the presence of metal free photocatalysts. This research may open a new doorway for new significant application of graphene for the selective production of methane and methanol as a promising material in membrane photocatalytic continuous reactor. However further investigation is needed.

3.3 O-doped and pristine C₃N₄: structural changes after use for CO₂ photoreduction

The results presented in this chapter give the following manuscript

F. R. Pomilla, M. A. L. R. M. Cortes, J. W. J. Hamilton, R. Molinari, G. Barbieri, G. Marcì, L. Palmisano, P. K. Sharma, A. Brown, J. A. Byrne. Graphitic C₃N₄ physical changes following photocatalytic tests in the presence of CO₂ and water. Accepted to the *Journal of Physical Chemistry C*, **2018**, 122, 28727-28738

3.3.1 Photocatalytic test conditions

Photocatalytic tests were performed in a stainless steel T-shaped reactor, composed of UHV vacuum parts (Swagelok and Kurt J. Lesker) with an internal volume of 120 mL. The reactor was fitted with a quartz window to allow irradiation of the catalyst (Figure 47).

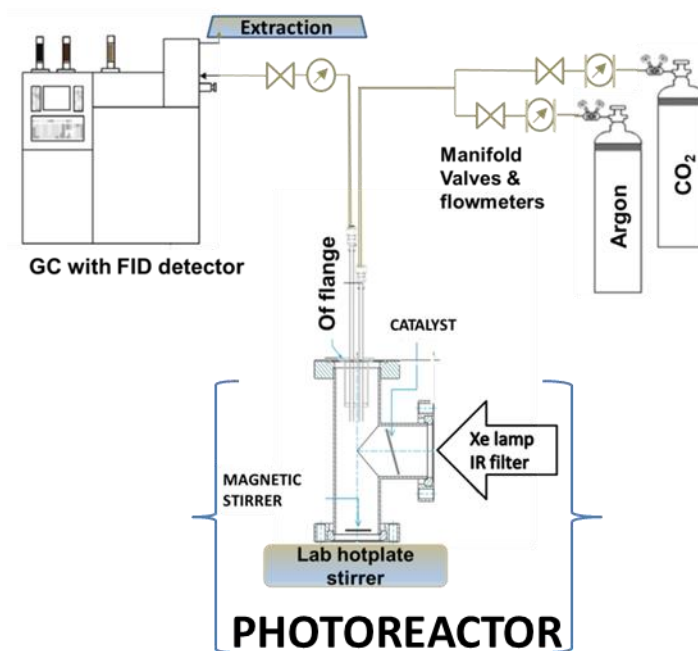


Figure 47. Batch photoreactor scheme equipped with a mass flow controller and light source reported from Cortes et al.³⁰⁰ The system is on line connected with a GC-FID/TCD.

The catalyst-coated plate was placed inside the reactor facing the quartz window. High purity water (1 mL, Merck, SupraSolv 7732-18-5) was added to the bottom of the reactor at the start of each experiment. The reactor was purged for 10 min with 20% CO₂ (BOC, UN1013, 99.99% purity) in Ar (BOC, UN1006, 99.998% purity) before sealing at a pressure of 2 bar. For the control tests in the absence of CO₂, the reactor was instead purged for 10 min with Ar, and 1 mL of heated water was added to the reactor.³⁰⁰ The temperature of the reactor was maintained with thermal tape at 70°C for all tests. The light source was a 100 W Xe lamp (LOT Oriel) equipped with an IR filter. The resulting light intensity is reported in Figure 48.

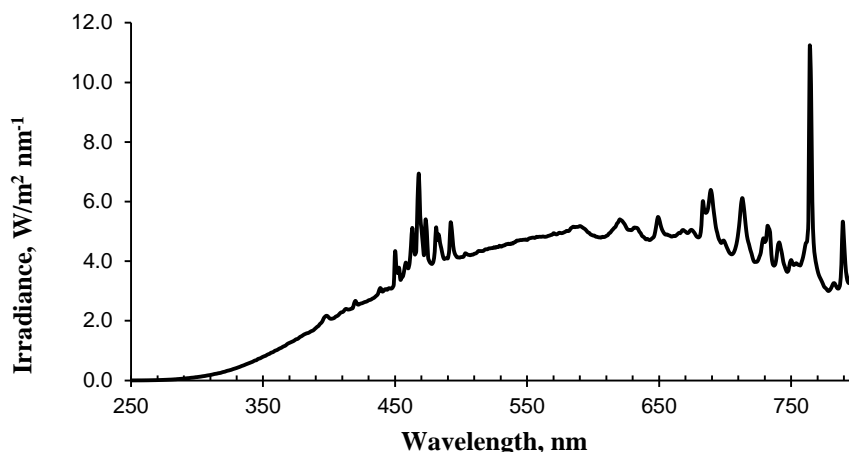


Figure 48. Measured irradiance from 100 W Xe lamp with IR filter.

The gaseous products obtained following irradiation were analyzed by gas chromatography (GC) with a flame ionization detector (FID) and the using Helium (BOC, UN1046, 99.999% purity) as the carrier gas. The GC (Agilent Technologies 7890B) was connected directly to the reactor and samples were analyzed every 30 min leading to a decrease in pressure inside the reactor (0.20 bar) each time a measurement was performed. Tests were replicated to determine the reusability of the material and were named RnCO₂ (where R means the replicate runs and n is the number cycles of CO₂ reduction testing performed). The control test in the absence of CO₂ was carried out with the same sampling time points as the other tests and was designated as RnAr. To investigate the effect of surface contaminants some of the samples were exposed to photocatalytic cleaning in the presence of oxygen prior to testing under standard CO₂ reduction conditions.

3.3.2 Characterisations of pure and O doped C₃N₄ materials

Analysis of the g-C₃N₄ and O_R-C₃N₄ was undertaken using FTIR, XRD, and UV-Vis reflectance techniques. The FTIR analysis correlates to previous reports on g-C₃N₄^{204-206, 301-306}. The finger printing from 807 to 1650 cm⁻¹ and from 3100 to 3500 cm⁻¹ by FTIR analysis demonstrates that the materials synthesized (section 2.2.4) are C₃N₄ structure type (Figure 49). The peaks at 807 cm⁻¹ are due to the

characteristic breathing mode of the s-triazine ring system. The peaks at ca. 1242, 1322, 1412, 1563, and 1634 cm^{-1} are typical stretching vibration modes of C=N and C-N heterocycles. In addition, the broad peak between 3600 and 3000 cm^{-1} is caused by the NH and OH stretches. However C-O and C=O bonds are difficult to distinguish in O doped g- C_3N_4 by FT-IR, as the C-N, C-C and C-O bonds have very similar force constants.³⁰⁷ Due to this constraint and the limited amount of O expected to be incorporated in the $\text{O}_R\text{-C}_3\text{N}_4$, no appreciable changes were observed when comparing it with the g- C_3N_4 catalyst by FTIR.

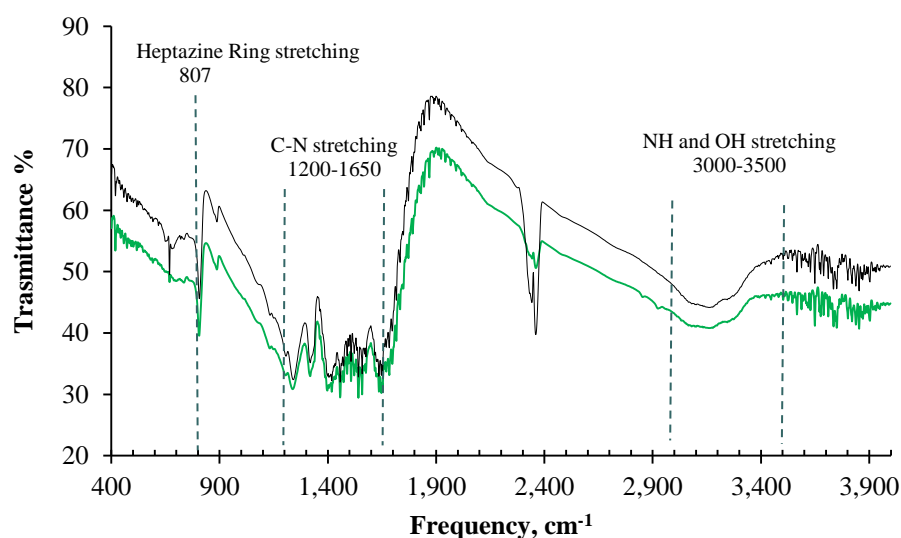


Figure 49. FTIR spectra of as synthesized g- C_3N_4 (green line) and $\text{O}_R\text{-C}_3\text{N}_4$ (black line) showing characteristic g- C_3N_4 fingerprint.

XRD analysis of the synthesized material showed a main 2θ peak at 27.4° which has been assigned to the (002) plane of g- C_3N_4 ,^{195, 308} corresponding to a d-spacing of 0.326 nm. This peak is usually assigned to the distance between the layers of the 2D graphitic material, which undergo a little left-shift in the O doped materials, as reported in the literature.²⁷⁴ The secondary intense peak at 2θ of 13.0° is attributed to the (100) plane, with a d-spacing of 0.680 nm, which is usually reported as the intralayer d-spacing.^{195, 308} From identification of these features in the synthesized g- C_3N_4 material and comparison to tri-s-triazine spectra from literature, the synthesized materials can be confirmed to be the h-g heptazine phase of C_3N_4 . The XRD spectra of the synthesised materials compared to expected peak positions previously reported by Fina et al.³⁰⁸ are shown in Figure 50.

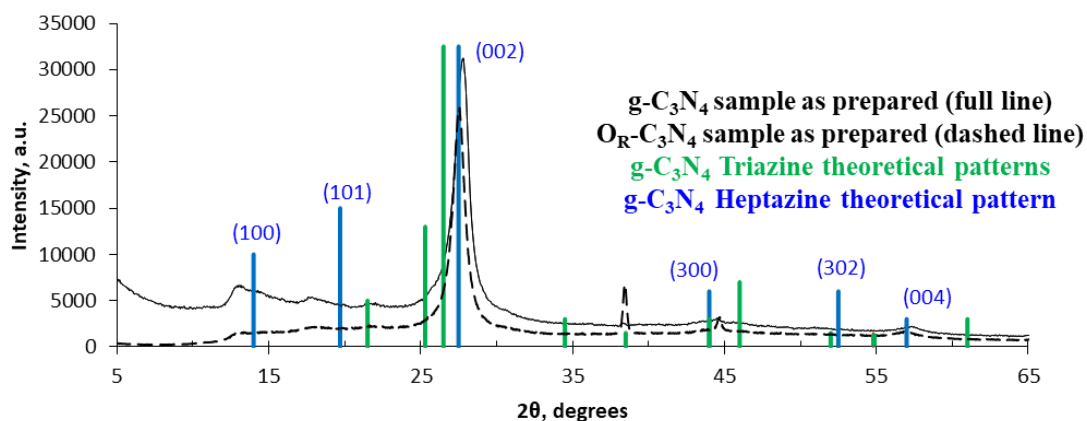


Figure 50. XRD patterns of pure $g\text{-C}_3\text{N}_4$ and $O_R\text{-C}_3\text{N}_4$ as prepared and the peak positions for two phases of $g\text{-C}_3\text{N}_4$ reported by Fina *et al.*^{193, 308} The name reported heptazine (*tri-s-triazine*) represents the melem unit.

To discriminate among the different phases of $g\text{-C}_3\text{N}_4$ and to estimate the band gap energy of the material, the optical band gap was measured. When a semiconductor absorbs light with suitable wavelength, electrons are excited from VB to CB with the simultaneous formation of holes in the VB. These charges produced by photoexcitation can reduce and oxidize the adsorbed surface species, respectively, or give rise to recombination phenomena. A recent study reports a computational method which allows to correlate the thickness of *s*-triazine and *h-g* heptazine C_3N_4 with the band gap energy of the materials.¹⁹⁸ Diffuse reflectance spectroscopy was utilized to determine the band gap of both synthesized $g\text{-C}_3\text{N}_4$ catalysts. These analyses are shown in Figure 51. For pure $g\text{-C}_3\text{N}_4$ and $O_R\text{-C}_3\text{N}_4$ materials optical band gaps of 2.8 and 2.7 eV respectively were estimated. Both values appear consistent with a hexagonally structured *h-g*-heptazine C_3N_4 ,¹⁹³ and in addition, as expected, the samples O doped showed a red shift of the optical band gap with respect to the pristine materials.^{195, 204, 206}

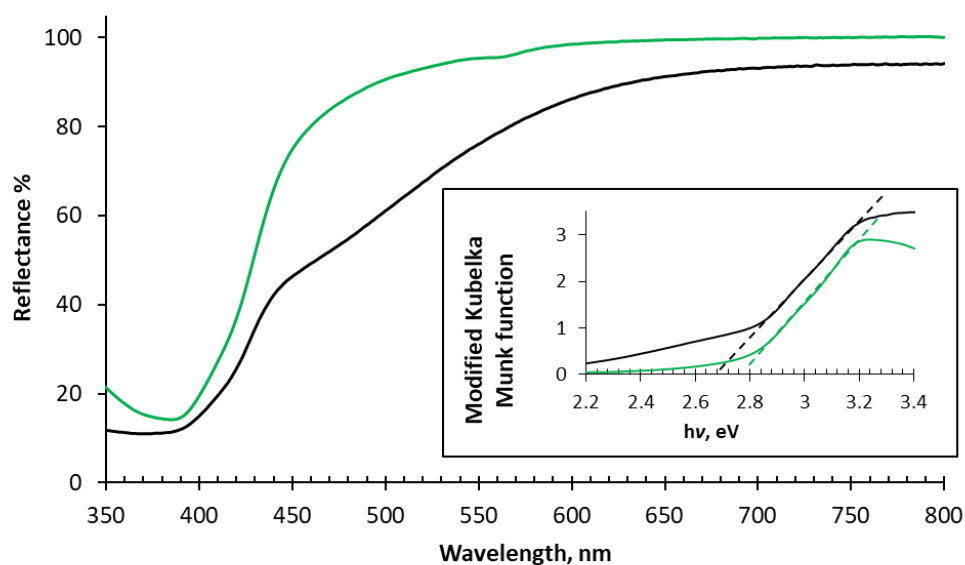


Figure 51. UV-Vis diffuse reflectance spectra of powder of pure $g\text{-C}_3\text{N}_4$ (red line) and $O_R\text{-C}_3\text{N}_4$ (black line) as prepared samples. The inset shows the Kubelka-Munk function vs photon energy, giving the graphic interpolation a band gap energy value equal to 2.8 and 2.7 eV for $g\text{-C}_3\text{N}_4$ and $O_R\text{-C}_3\text{N}_4$, respectively.

3.3.3. Photocatalytic tests

Measurement of photocatalytic activity for CO_2 reduction was performed in a gas phase batch photoreactor testing the $g\text{-C}_3\text{N}_4$, $O_R\text{-C}_3\text{N}_4$ and $O_T\text{-C}_3\text{N}_4$ immobilized samples under the conditions detailed in the section 3.3.1. Chromatographic determination of products from photocatalytic testing yielded only CO , within the limits of detection. No H_2 , O_2 (from water splitting reactions), methane or other hydrocarbons were observed. A typical graph of CO production vs time using $g\text{-C}_3\text{N}_4$ is shown in Figure 52.

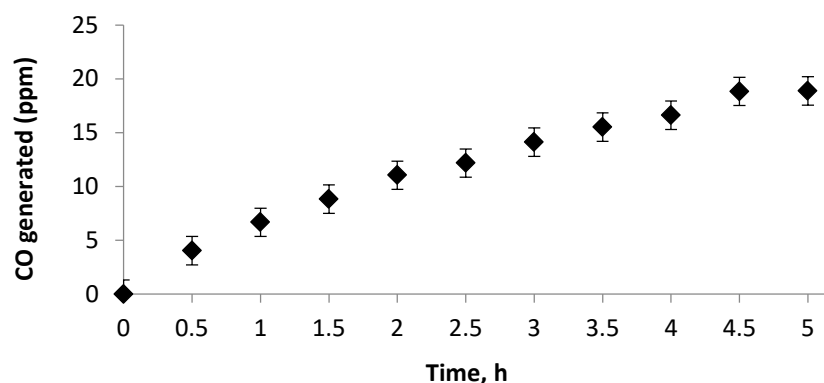


Figure 52. Concentration of CO versus irradiation time in the presence of CO₂ using g-C₃N₄ material.

Having the amount of CO produced with irradiation time, samples were retested to investigate their stability. Reuse of samples showed a decline in the CO concentration (Figure 53) with replicates (R1CO₂ and R2CO₂).

Control runs in the absence of CO₂ were undertaken. In the absence of CO₂, CO was still observed as a product, and a similar trend of lower CO generation on reuse was detected (Figure 53- R1-R3Ar runs).

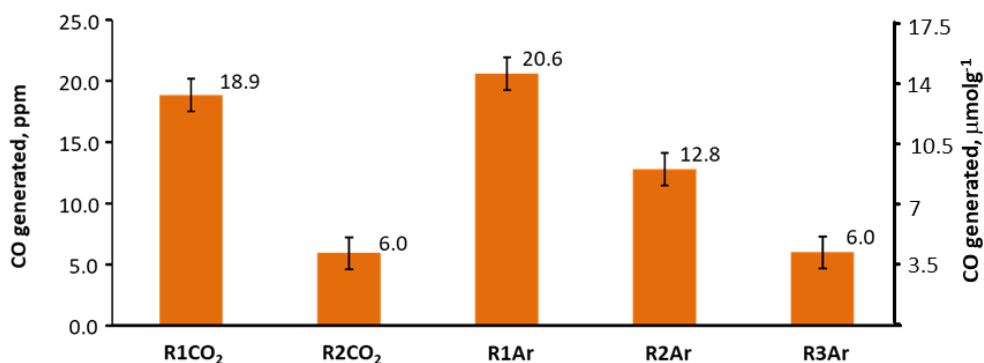


Figure 53. CO concentration obtained after 5 h of irradiation time in the presence (RnCO₂) and in the absence (RnAr) of CO₂ with g-C₃N₄.

The observation of only CO as gaseous product, the declining CO generation rate (on reuse or extended use), and the observation of CO in the absence of CO₂ suggest that some CO₂ molecules from atmosphere remained strongly adsorbed on the catalyst surface. To confirm this behavior a batch test was carried out in inert

atmosphere in absence of CO₂ (N₂ humid) at atmospheric pressure and under visible light. This test confirmed a release of CO₂ with the irradiation time as reported in Figure 54.

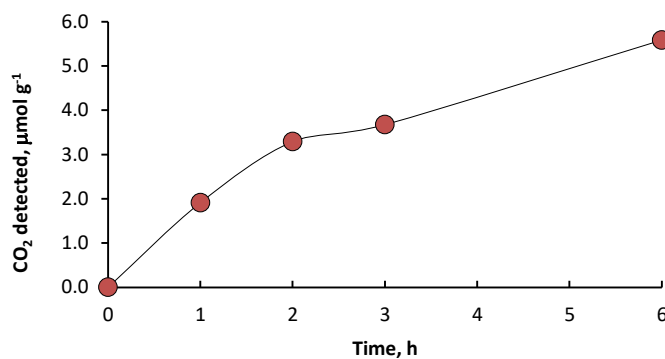


Figure 54. Amount of CO₂ released in a batch reactor under irradiation at ambient pressure and N₂ atmosphere from g-C₃N₄ powder previously cleaned.

Consequently, the adsorbed CO₂ could be responsible for the observed CO. In fact, in the presence of lower CO₂ amounts (just the adsorbed one), a slower catalyst inactivation occurred (**Figure 53**) with respect to the test in presence of higher CO₂ concentration (20% in Ar flow).

To investigate if adsorbed CO₂ or organic fouling was an issue, a twice-used (R2CO₂) sample was photocatalytically cleaned for 3 h in O₂ flow under UV-Vis irradiation. The photocatalytic cleaning with O₂ did not alter the material reactivity within the errors of the analytical system as shown in Figure 55.

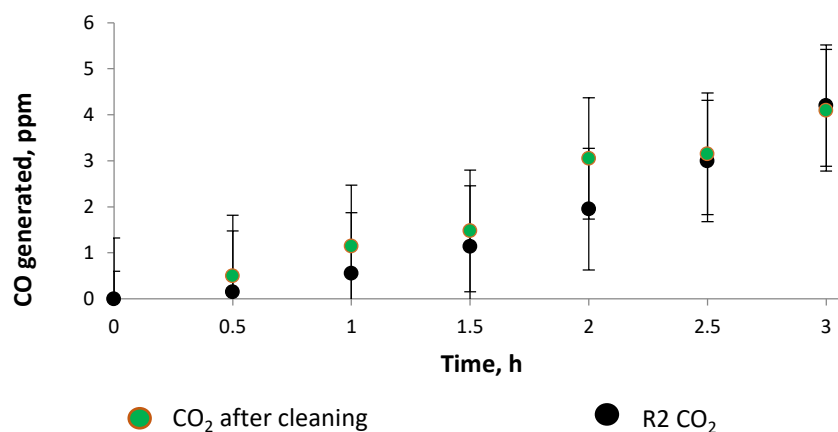


Figure 55. CO photo-generated in the presence of CO₂, before (R2CO₂) and after cleaning (CO₂ after cleaning) versus irradiation time with g-C₃N₄ as photocatalyst.

An oxygen doped carbon nitride, O_T-C₃N₄, was also tested for CO₂ reduction using the same methodology as the one utilized in g-C₃N₄ testing. During this experiment, only CO was detected and the CO generated was observed to decrease with reuse. This is a similar trend to that observed in the case of pure g-C₃N₄. Comparison of activity between pure g-C₃N₄ and O_T-C₃N₄ showed that oxygen modification was detrimental for CO formation (Figure 56). O_R-C₃N₄ was also tested under identical experimental conditions and the yield of CO detected was smaller than that found for the thermal oxygen doped and unmodified C₃N₄ samples.

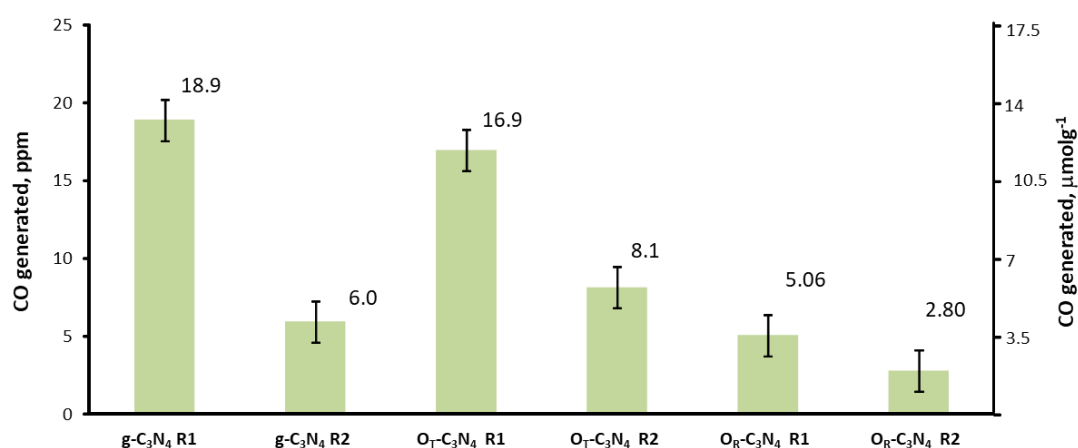


Figure 56. Reproducibly test of CO production in the presence of g-C₃N₄, O_R-C₃N₄ and O_T-C₃N₄ after 5 h of irradiation time in the presence of CO₂.

Table 12 reports the amount of photogenerated CO expressed in terms of both, ppm and $\mu\text{mol g}^{-1}_{\text{catalyst}}$. The apparent Quantum Yield, calculated according to Tan et al.,³⁰⁹ is also reported. Notably, these figures decrease with reuse for of the catalysts tested, being all correlated.

Table 12. Formal Quantum Yield (QY) and CO generated by all sample used and reused after 5 hours of irradiation time in presence of CO₂ and water.

Catalysts	Ppm	$\mu\text{mol g}^{-1}$	QY %
C ₃ N ₄ R1	18.9	13.0	0.0132
C ₃ N ₄ R2	6	4.1	0.0042
O _T -C ₃ N ₄ R1	16.9	11.7	0.0118
O _T -C ₃ N ₄ R2	8.1	5.6	0.0057
O _R -C ₃ N ₄ R1	5.1	3.5	0.0035
O _R -C ₃ N ₄ R2	2.8	1.9	0.0020

Given the limited range of products detected under irradiation, the reduction in product yield with extended use, and the activity decreasing when comparing O_R-C₃N₄ with the O_T-C₃N₄ and unmodified samples, oxidation of g-C₃N₄ was considered as an alternative source of CO observed. Therefore, samples were analyzed before and after use by XPS and FTIR to determine the degree of oxidation consistent with this hypothesis. The structural and functional groups reported for g-C₃N₄ are given in Table 12. FTIR analysis was used to determine if any changes to the functional groups occur during the photocatalytic tests (Figure 56). All samples showed the finger-printing region characteristic for heptazine subunit and functional groups consistent with expected positions for g-C₃N₄ as detailed in Table 13.

Table 13. Peak positions of structural and functional groups observed by FTIR spectra for g-C₃N₄ and O-C₃N₄ samples.

FTIR analysis		Ref.
Frequency, cm ⁻¹	Functional group	

1250-1324-1405-1454-1571-1636	C ₆ N ₇ heptazine heterocycle ring	204-206, 301-306
807-813	triazine ring stretching	204-206, 301-306
892	Cross link heptazine deformation	301
1654	N-H deformation	204, 305
1610	C=N	205, 302, 306
3469-3420	NH ₂ stretching.	204, 205, 302, 305
3337-3137	asymmetric and symmetric stretching N-H	204, 205, 301, 302, 306
3500-3100, 3350	OH	206, 310, 311

A decrease in the absorbance associated with the g-C₃N₄ functional groups was observed following use in the photoreactor (Figure 57). Such changes were also analyzed by XPS.

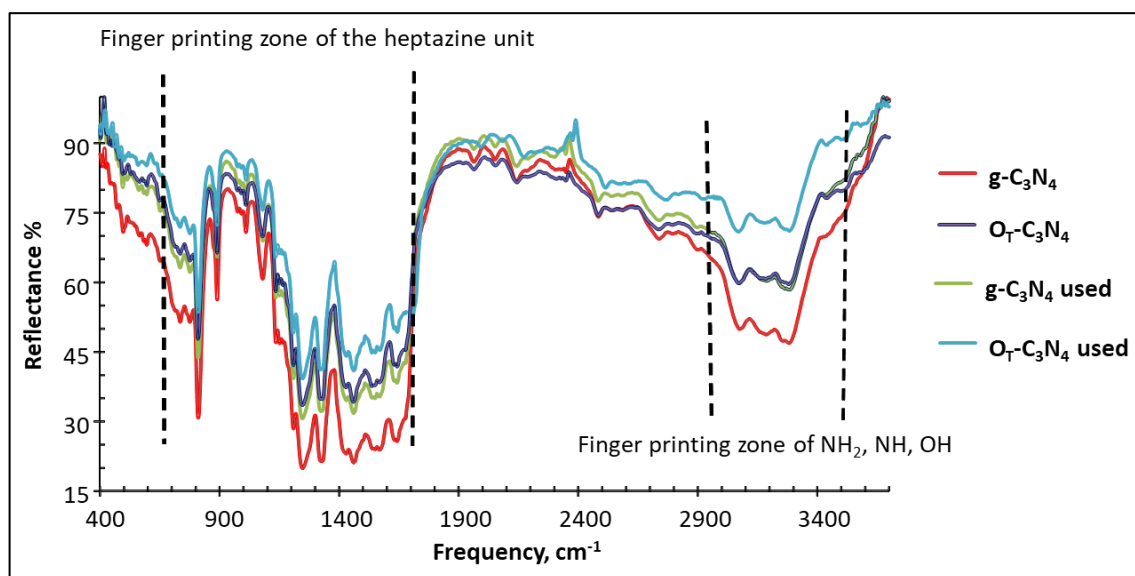


Figure 57. Diffuse FTIR analyses for each sample used and unused.

The XPS elemental profiles and expected position of peaks related to structural and functional groups have previously been reported by researchers investigating g-C₃N₄, as detailed in Table 14. Using this information, in conjunction with analysis

of samples before and after photocatalytic treatment, changes to the photocatalyst surface during CO₂ reduction seem to occur.

Table 14. Structural and peak positions of functional groups which were observed in XPS for g-C₃N₄ and O-C₃N₄

XPS Analysis			
Element	Kind of interaction	Binding energy, eV	Reference
N	400		204-206, 213, 215, 301-306, 310
	N1(N sp ²) C-N=C	398.5	206, 213, 301-306, 310
	N2 (N-H)	399.5	213, 301, 306
	N3 (sp ³) NC ₃	400.2	206, 213, 301, 302, 304, 305, 310
	N4 (NH ₂)	401	206, 301, 303, 304, 310
	<i>N-O, or due to O₂ and H₂O adsorbed</i>	401.8	306
	Nπ-π	404.2	213, 301, 305
C	284.8		204-206, 213, 215, 301-306, 310
	C-C	284.6	204, 206, 213, 301, 302, 304, 310
	C-CH ₂ , C-OH, C-O	286.2	204, 213, 301, 303, 310
	C-N	286.2-287.2	206, 301
	C1	288.2	213, 301-304, 310
	C2	288.8	301
	<i>N-C=O</i>	289.8 -288.9	204, 206, 301, 310

	C π - π	293.8	301
O	532.6		204, 206, 213, 215, 301- 303, 310
	C=O	530	312
	C-OH, O-C-N	531.9	199, 204, 206
	H ₂ O adsorbed	532.9	204, 213, 303
	O-N	533.4	206

Theoretically, XPS should show a C/N molar ratio of 0.75 for g-C₃N₄. However, imperfect carbon nitride crystals can lead to changes to this ratio. Investigation of functional groups, particularly carbon oxygen functionalities, that could alter this ratio are detailed in Table 14. To understand the XPS signal, one must consider the differing bonding configurations that both nitrogen and carbon adopt in the g-C₃N₄ structure (Figure 58). Essentially, as mentioned in the section 1.3.5, carbon has two unique bonding configurations (C1, C2) whilst nitrogen adopts four unique configurations (from N1 to N4) in the carbon nitride structure. This causes a splitting in the XPS signal for each configuration allowing investigation of structure (Figure 58).

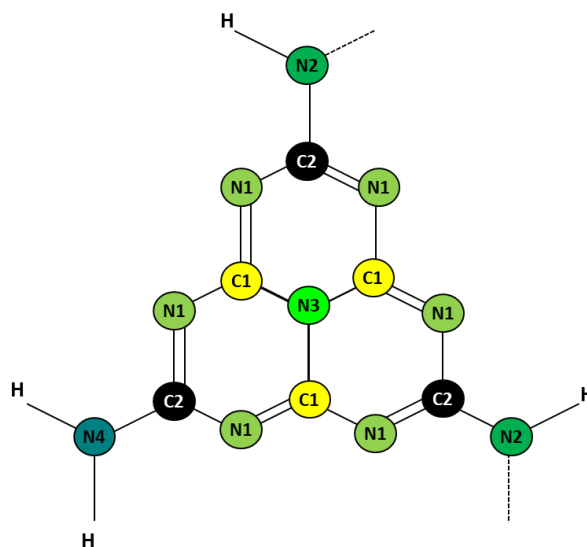


Figure 58. Structure of the repeating heptazine carbon nitride unit with the corresponding atomic assignment according to XPS analysis.

Both elements C and N, in the C_3N_4 graphitic structure, generate the signal due to the π to π^* transition (shake-up) at around 293.8 eV and 404.2 eV respectively, as reported in Table 14. In addition to chemical shifts in XPS due to different bonding configurations of carbon and nitrogen in perfect C_3N_4 crystals, the peak positions due to oxygen functionalities characteristic of $O-C_3N_4$ samples are also reported in italic characters in Table 14.

Analysis of elemental composition via XPS was initiated with a wide energy survey, performed in three locations, to look for contamination and estimate differences in the elemental constitution. Only carbon, nitrogen and oxygen peaks of significant magnitude for quantification were observed (Table 15). The value of binding energy for each element observed showed good agreement with literature (Table 14).

This analysis showed that the quantity of oxygen present in the pure as prepared C_3N_4 is the lowest of all the samples. However, for samples that had undergone thermal annealing and/or testing as a photocatalyst, the oxygen content was increased in comparison to untreated material.

Table 15. Survey analysis average of three (wt %) XPS measurements of used $g-C_3N_4$, unused $g-C_3N_4$ and $O_R-C_3N_4$ reference.

	$O_R-C_3N_4$	$g-C_3N_4$	$g-C_3N_4$ used	$O_T-C_3N_4$	$O_T-C_3N_4$ used
O	5.4	2.0	3.0	2.9	3.6
C	49.6	48.6	49.9	48.5	48.0
N	44.9	49.4	46.8	48.6	48.4

By comparing changes in carbon and nitrogen percentages across sample groups, oxygen inclusion during synthesis of $O_R-C_3N_4$, thermal treated $O_T-C_3N_4$ or used $g-C_3N_4$ data suggests that oxygen incorporated in the structure is likely substituting in one or more of the differing nitrogen positions N1, N2 and N3. In fact, a loss in nitrogen concurrent with increases in oxygen percentage can be observed in Table 14. To discriminate between contributions from strongly adsorbed contaminants and different functional groups, high-resolution scans of N, C and O regions were measured and deconvoluted based on assignments reported in Table 14.

For all samples analyzed, used and unused, a large proportion of the oxygen signal observed came from the water strongly bound to the catalyst. In the as prepared $g-C_3N_4$ sample, all the oxygen observed was from adsorbed contaminants, H_2O and CO_2 . Whilst the used $g-C_3N_4$ sample, thermally and chemically O-doped samples showed increasing intense contributions from oxygen in lattice (N-C-O-C) and oxygen functionalization of periphery aromatic regions ($ArC=O$), as detailed in Table 16.

Table 16. Contributions from different oxygen carbon and nitrogen functionalities (Wt %) estimated from deconvolution of XPS each peak centered about at 288.4, 531.5 and 398.9 eV, respectively.

		Wt %				
		$O_R-C_3N_4$	$g-C_3N_4$	$g-C_3N_4$ used	$O_T-C_3N_4$	$O_T-C_3N_4$ used
Binding energy, eV	O Type	Oxygen				
529.92	O=C Ar	1.37	0.00	0.00	1.35	2.38

531.15	O-C-N _{in lattice}	8.63	0.03	2.34	1.57	2.59
532.28	OH water, CO ₂	90.00	99.97	97.66	97.18	95.03
Binding energy, eV	N Type	Nitrogen				
398.72	N1 edge	68.23	71.34	64.47	65.28	66.88
398.83	N2 external	8.43	3.77	6.83	10.29	7.50
400.08	N3	8.47	9.10	11.12	8.57	10.76
401.08	N4 external	12.79	12.97	14.58	12.90	11.92
404.25	π - π	2.09	2.82	3.01	2.96	2.97
Binding energy, eV	C Type	Carbon				
284.82	C-C	27.49	22.57	27.58	25.29	25.75
286.4	C-OH	5.43	3.30	3.74	1.81	1.83
288	C1	40.82	40.75	29.11	46.63	35.66
288.6	C2	22.28	28.6	33.81	21.33	30.92
289.64	C=O external	1.27	1.74	2.06	1.00	1.94
293.37	π - π	2.72	3.37	3.71	3.96	3.91

This is suggestive that UV-Vis irradiation of g-C₃N₄ in the presence of water leads to photocorrosion and oxidation of the g-C₃N₄. To understand the changes in the carbon nitride structure, due to increasing oxygenation, the nitrogen and carbon regions were also investigated. In the nitrogen region, due to the bonding in the C₆N₁₀H₁₂ heptazine monomer, nitrogen adopts four bonding configurations labeled N1 to N4 in Figure 58, each with a unique binding energy detailed as reported in literature in Table 14 and experimental data found in Table 16. N1 are present on the edges of heptazine base units, N3 are present at the center of a perfect heptazine base, whilst N2 type link heptazine sub units together and N4 represent the groups left upon the termination of polymerization. In a heptazine monomer (Figure 59a) the ratio of N1:N3:N4 is 6:1:3, N2 does not appear in the base unit melem; however as the monomer polymerizes, some N4 type are converted into N2 with the ratio of

N4:N2 groups dependent on the geometry of polymerization (Figure 59c). In the g-h heptazine phase under study here, confirmed by XRD and UV-Vis (see above), heptazine monomers polymerize along parallel zig zag chains linked by single N4 units as illustrated in Figure 59e. Polymerizing in the g-h heptazine structure results in changes in the ratio of N2 to N4 nitrogen, relative to the monomer, as one N4 is replaced with one N2 for every unit extension along the polymerization axis. Illustration of the changes in nitrogen group bonding during polymerization is detailed in Figure 59.

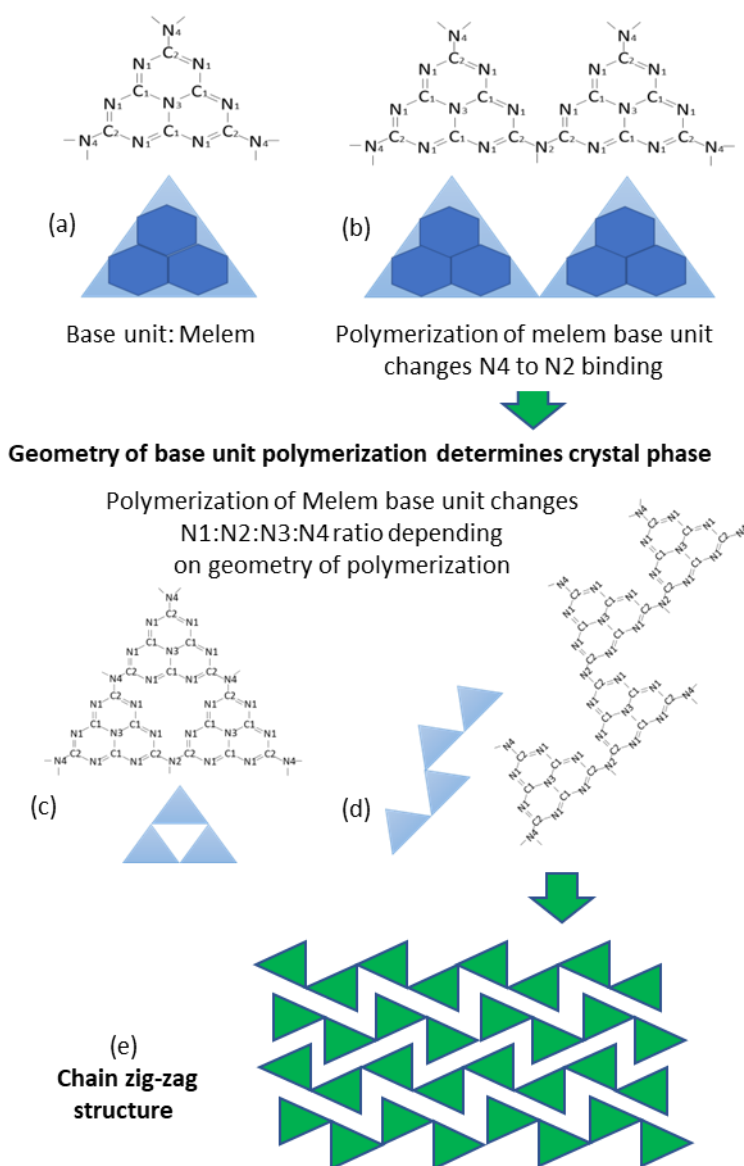


Figure 59. Possible condensation pathway from Melem unit (a) firstly to dimer (b) and then to two different assembling in sheet (c) and linear chains of g-C₃N₄ (d). The chains (d) evolve to g-C₃N₄ zig zag structure (e).

Table 17. Change in nitrogen ratios as a function of chain length for h-g-heptazine structure.

	N1	N2	N3	N4	N1 %	N2 %	N3 %	N4 %
Dimer	12	1	2	4	63.16	5.26	10.52	21.05
Tetramer	12	1	2	3	66.66	5.55	11.11	16.67
Octamer	12	1	2	2.5	68.85	5.71	11.43	14.28
Infinite chain	12	1	2	2	70.58	5.88	11.76	11.76

As reported in Table 17, the short heptazine chains result in N1>N4>N3>N2 ratio, whereas, at the infinite chain lengths, ratios become N1>N4=N3>N2 which is equivalent to a N1:N2:N3:N4 ratio of 12:1:2:2. This corresponds to 70.58:5.88:11.76:11.76 percentage ratios useful when comparing this perfect crystal to the percentages obtained from XPS.

For the synthesized g-C₃N₄, the N1:N2:N3:N4 percentage ratio from XPS was 71.34:3.77:9.10:12.97, which is good match for expected N1 % in g-h-heptazine with largely perfect heptazine base units. Considering N4, it suggests long range but not infinite chains consistent with XRD, the excess of N4 percentage may also be due to unreacted precursor / monomer material or some shorter chains. Deviation, a lower % than expected, in N2 suggests crystal imperfections, defects or branching of the chains removing side N2 groups, whilst contemporaneously increasing N4 groups. Likewise, the N3 ratio was lower than expected for perfect crystals, suggesting vacancies in some of the heptazine blocks.

N1:N2:N3:N4 ratios from carbon nitride oxidized during synthesis, thermally or during photocatalysis are compared in Table 16. All treatments were observed to result in significant reduction in N1 side groups, relative to the starting material, suggestive of damage/distortion to the base of the heptazine unit. Deconvolution of the N2 and N4 (edge and terminal groups) in used g-C₃N₄ shows an increasing N4

percentages, suggesting a reduction in average chain length. In the $O_T-C_3N_4$ sample, higher N2 and N4, with lower N1 ratios than expected for a perfect g-heptazine structure were observed, presumably due to oxygen disrupting periodicity. Its use as a potential photocatalyst showed further changes in the N1:N2:N3:N4, ratio that is consistent with additional restructuring of the polymer towards a more open arrangement.

Deconvolution of XPS C1s region was also used to look at changes in structure following photocatalysis. In this region, the C-C and C-OH peaks are characteristic of adsorbed species or deviance from heptazine structuring / reformation. Both thermal oxidation and use as a potential photocatalyst increased the C-C peak indicative of a material with less heptazine/g- C_3N_4 present. Likewise, signals due to C=O bonding were observed to increase in both sample sets following use as photocatalysts, which is consistent with increasing counts in the oxygen region observed for the same treatment. C1 and C2 regions represent differing carbon nitrogen bonding. In all cases, it showed decreasing C1 and increasing C2 content following photocatalytic use due to changes in nitrogen content during use.

Intentional oxygen doping and repeated use in CO_2 reduction experiments both led to reduced yields of CO in subsequent tests and simultaneous increases in the oxygen content of the g- C_3N_4 with repeated testing. In addition, UV-Vis irradiation was observed to give rise to changes in the g- C_3N_4 structure (N1:N2:N3:N4 ratios).

Another factor to be considered is the role of N in the structure. In particular, as it can be noticed in Table 15 (XPS survey analysis), the increase of O content from the unused to used g- C_3N_4 sample and to O doped samples ($O_T-C_3N_4$ to $O_R-C_3N_4$) corresponds to a decrease of the total content of N. This variation (%), which could be due to a replacement of N with O in the structure, could alter CO_2 adsorption properties adversely.

In photocatalytic, tests carried out in the presence of CO_2 under the experimental conditions used (pressure, temperature, and light intensity); the increase in the O content of the g- C_3N_4 was caused by photocorrosion. It is not easy to determine if H_2O , CO_2 or both are the source(s) of O observed in this work. The photocorrosion means the modification of the C_3N_4 structure, due to the substitution of N with O

during the photoreaction, as shown in Figure 60, as indicated by XPS measurements (Table 14) and reported also by Huang et al. when H_2O_2 was used to dope C_3N_4 with oxygen.²⁰⁴ The mechanism, which led to the final modified C_3N_4 in these experimental conditions, could give rise to formation of a non-stoichiometric or defective solid. Moreover, the figures related to the percentage of the various N types, shown in Table 15, strongly suggest a rearrangement of the g- C_3N_4 structure following use in photocatalytic testing.

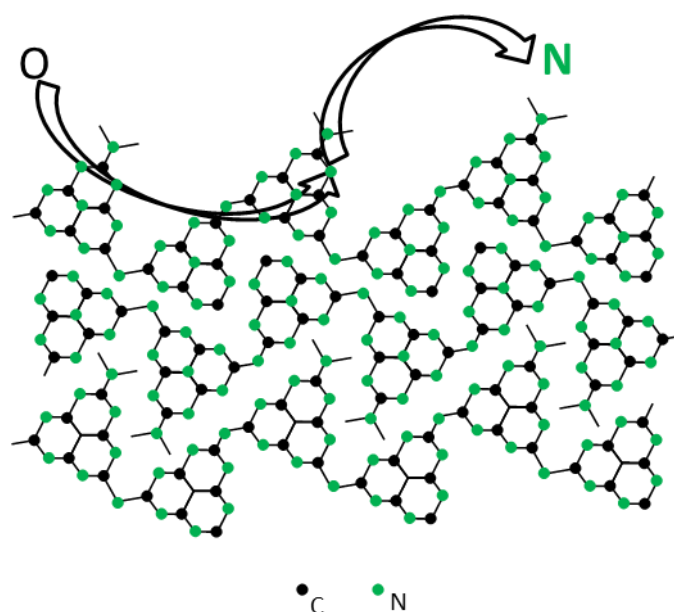


Figure 60. Schematic illustration of N replacement by O in g- C_3N_4 material.

As far as the runs carried out in the absence of CO_2 are concerned, the presence of CO_2 adsorbed on the catalyst surface or as impurity in the system cannot be excluded and it can be compatible with the CO formation.³⁰⁰

In current literature, only a few papers report repeat testing and generally they concern runs carried out by using C_3N_4 composite and or bulk materials with low surface area. Qin et al.,²¹⁴ observed that in the presence of barbituric acid-g- C_3N_4 composite, the photoreduction of CO_2 to CO and H_2 was quite reproducible, at least after three catalytic consecutive tests. Probably, in that case, the presence of barbituric acid stabilized the g- C_3N_4 structure avoiding the replacement of N by O and consequently no decreasing activity was observed. A similar stabilizing effect due to the presence of ceria can be hypothesized in the case of CeO_2 - C_3N_4

composite that showed a constant CH₄ and CO production after 4 runs as reported from Li et al.³¹³

In contrast with the present study, Fu et al. found the reproducibility of CO₂ photoreduction tests in the presence of both bulk g-C₃N₄ and O-C₃N₄ tube photocatalyst. However, it is important to notice that the amount of CO₂ photoreduction products observed by Fu et al. was always lower than the lowest one revealed in this study. Moreover, to the best of my knowledge, no structure studies were carried out after the use of g-C₃N₄ photocatalyst used for CO₂ reduction.²⁰⁶ Interestingly, in that case no CO formation was observed during blank test in the absence of CO₂.

3.3.4 Conclusion

During g-C₃N₄ and oxygen doped g-C₃N₄ photocatalytic tests for CO₂ reduction, the main product detected was CO. No other products were detected. The pure material was observed to be more active than the oxygen modified analogue for CO production. A reduction in the rate of CO generation, under irradiation, was observed during both single runs and repeated test cycles with the same catalyst. During control tests in the absence of CO₂, the production of CO was observed under irradiation, raising questions about the origin of the CO and the stability of g-C₃N₄.

Diffuse reflectance FT-IR analysis showed the expected functional groups characteristic of g-C₃N₄ present in all samples. Functional group peak intensity declined with oxygen doping or photocatalytic use. Given the qualitative nature of FTIR, samples were further investigated with XPS to quantify the changes in the functional groups during photocatalytic use or intentional oxidation.

Both analyses, the diffuse FTIR and XPS, showed that the thermal and the photocatalytic treatments produce similar changes to the functional groups, consistent with oxidation of the C₃N₄ structure. The oxidation of the g-C₃N₄ under UV-Vis irradiation was slightly different to the one obtained with oxygen doping,

but produced the same effect on catalytic behavior, i.e., a reduction in product yield under irradiation.

The XPS data showed an increase in oxygen content, both absolute and bound to carbon, after thermal treatment and after photocatalytic use. This study allowed the examination of where and how oxidation disrupts the material structure, showing changes to the heptazine base units along with changes in bonding between units following oxidation or photocatalytic use.

This research points that under the adopted reactor conditions, the photoexcitation actually leads to oxidation of C_3N_4 rather than water splitting, leading to a loss of photocatalytic activity i.e., photocorrosion. Given that the valence band edge of g- C_3N_4 is close to the water oxidation potential, this material has limited overpotential to drive water oxidation and as such, may accumulate intermediate ROS species that may oxidize the catalyst, changing its activity as observed here. C_3N_4 may still be useful as a photocatalyst; however, the use of a z-scheme or a second co-catalyst material on which to run the oxidation reaction may be necessary to avoid g- C_3N_4 oxidation observed in this work. As aforementioned, many researchers use a z-scheme consisting of g- C_3N_4 in composite materials such as g- C_3N_4 - TiO_2 where the latter material performs the water oxidations steps, reducing the opportunity of g- C_3N_4 oxidation.⁷

3.4 Photocatalytic CO₂ reduction in continuous membrane reactor: C₃N₄ Nafion membrane

The results presented in this chapter have been published:

F. R. Pomilla, A. Brunetti, G. Marci, E. I. Garcia-Lopez, E. Fontananova, L. Palmisano, G. Barbieri. CO₂ to Liquid Fuels: Photocatalytic Conversion in a Continuous Membrane Reactor. *ACS Sustainable Chemistry and Engineering*, **2018**, 6(7), 8743-8753

3.4.1 C₃N₄ powder

3.4.1.1 Powder characterisation

Figure 61 shows XRD analysis of C₃N₄ powder in which two characteristic peaks at 27.3° and 13.1° are clearly defined, in good agreement with patterns reported in the open literature.²¹³ The higher angle peak at 27.3° is characteristic of an interlayer stacking of conjugated aromatic systems, which is indexed to the (002) plane corresponding to the average interlayer distance of 0.326 nm.^{216, 314} The lower diffraction peak at 13.1° is indexed to the (100) plane and assigned to the in-plane structural packing of aromatic systems with an average distance of 0.675 nm, characteristic of heptazine heterocyclic ring (C₆N₇) units.²¹⁶

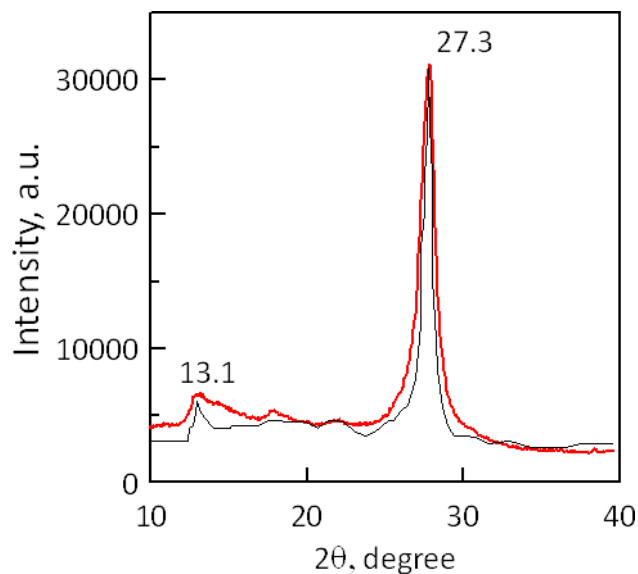


Figure 61. XRD patterns of C_3N_4 (red line) measured for powder and (black line) as reported by Wen et al.¹⁹⁵

The chemical structure is also confirmed by FT-IR whose peaks (Figure 62) at 890, 1250, 1324, 1405, 1454, 1571, and 1636 cm^{-1} correspond to the typical stretching vibration modes of heptazine heterocyclic ring units.³¹⁵ The peak at 804 cm^{-1} belongs to the characteristic breathing mode of triazine units representing the condensed CN heterocycles.³¹⁶

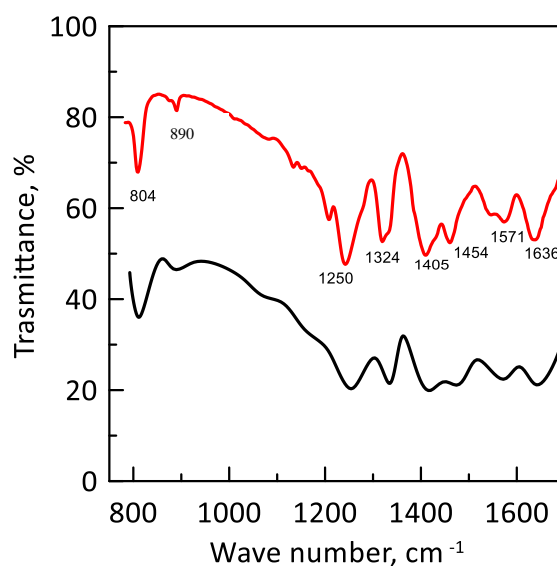


Figure 62. FT-IR spectrum of C_3N_4 powder (red line) and (black line) as reported by Liao et al.³¹⁵

The SEM images (Figure 63a and 63b) show the graphitic structure and the partial exfoliation of C_3N_4 powder caused by the second thermal treatment to which it was subjected.

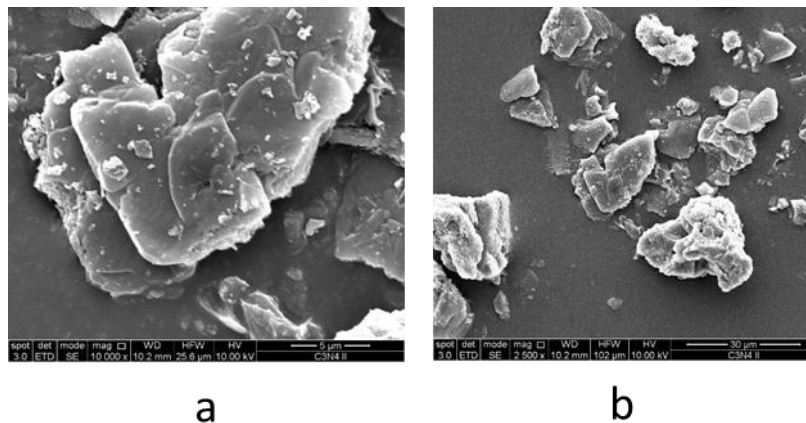


Figure 63. SEM image of C_3N_4 powder at two different magnitude, at a) 5 μm and at b) 30 μm , respectively.

The diffuse reflectance spectra were recorded for investigating the electronic band structure of the C_3N_4 sample, which was determined by the intersection (red spot) of the tangent lines (Figure 64, blue lines) of the Kubelka–Munck modified function, $[F(R'\infty)hv]^{1/2}$ versus the energy of the exciting light. The band gap identified as 2.8 eV (Figure 64) falls in the region of visible light absorption of the photocatalyst corresponding at ca. 443 nm. The discrepancy with the theoretical value of 2.7 eV of the bulk materials is ascribable to the intrinsic superiority of 2D structures of the exfoliated C_3N_4 .¹⁹⁸

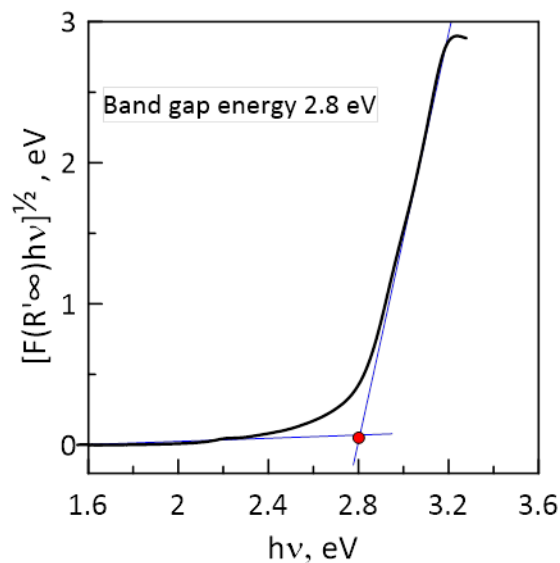


Figure 64. Kubelka-Munck modified function vs. the energy irradiating the C_3N_4 sample.

The BET analysis of the bulk g- C_3N_4 shows a low specific surface area ($7 \text{ m}^2 \text{ g}^{-1}$) as reported by Krivtsov et al.³¹⁷ On the contrary the exfoliated powder sample gave a specific surface area of $154 \text{ m}^2 \text{ g}^{-1}$, in agreement to Zhang et al.³¹⁸ that measured a specific surface area of exfoliated g- C_3N_4 equal to $160 \text{ m}^2 \text{ g}^{-1}$. This relatively high value can be attributed to the two thermal treatments undergone by the melamine, in agreement with Papailias et al.³¹⁹ who stated that structural and optical properties highly depend on the process temperature and, thus, polycondensation degree.¹⁷⁵

3.4.1.2 Preliminary powder photocatalytic test condition and results

For evaluation of the photocatalytic activity, the photocatalytic CO_2 reduction was previously carried out by using powdered C_3N_4 in a batch reactor, which is shown in Figure 26 (section 3.1.1). In detail, 350 mg of C_3N_4 sample was placed in a cylindrical Pirex batch reactor with total volume of 130 mL. As before described (section 3.1.1), the photocatalyst insight the reactor was first cleaned under light with humid He ,¹¹⁴ and subsequently under dark conditions, CO_2 was fluxed for 30 min in the reactor. A $48 \mu\text{L}$ of distillate water was introduced into the reactor by

means of a syringe. Afterward, the batch reactor was placed in a solar box (1500 W, Xe lamp), and the experiments were carried out for 6 h. The concentration of the species was analysed by a Shimadzu gas chromatograph equipped with FID and a Hewlett-Packard GC with TCD, injecting in each a 250 μL sample by means of gas-tight syringe.

During 6 h of irradiation time, the batch reactor conversion was followed for an initial $\text{H}_2\text{O}/\text{CO}_2$ feed molar ratio equal to 0.5, obtaining $0.6 \mu\text{mol g}_{\text{catalyst}}^{-1} \text{h}^{-1}$ of converted carbon. The most abundant products were CH_4 and CO , accordingly to the literature data of gas-phase CO_2 photoreduction.^{320, 321}

3.4.2 Photocatalytic membrane test conditions

Photocatalytic membrane was utilized for CO_2 photoreduction with H_2O as reducing agent. Before the characterization and the photoreduction measurements, the membrane prepared was cleaned. In this procedure carried out by using the membrane reactor set up described above, all the membranes underwent “blank reaction” measurements. An argon stream together with H_2O , instead of CO_2 , was fed continuously for 8-24 h into the reaction module, under the same operating conditions, which were chosen to carry out the photocatalytic experiments including the UV-Vis irradiation. The aim of this procedure was to clean the membrane from any residuals of solvent and other low molecular weight organics eventually present in the polymer solution that could be released during the reaction measurements invalidating the results.

The reactor was equipped with a medium–high mercury vapour pressure lamp (Zs lamp, Helios Ital quartz, Milan) with emittance from 360 nm (UV-Vis) to 600 nm which was used to irradiate the membrane. The flat sheet membrane was assembled in a stainless steel module where a quartz window allowed the UV-Vis irradiation of the catalytic membrane surface.

Once placed in the UV-Vis exposure chamber, the membrane module was continuously fed with CO_2 and H_2O by means of a mass flow controller and an HPLC pump, respectively. Figure 65 shows the experimental apparatus set up. The

membrane reactor mainly consists of three parts: the feed/retentate chamber, the permeate chamber and the catalyst loaded membrane. The two reactor chambers can be considered as lumped parameter systems since reaction takes place in the membrane layer and no concentration gradient of any chemical species is expected, also owing to the low conversion occurring in this specific reaction. Thus, the composition of these two volumes is the same as the related reactor exiting streams, which are retentate and permeate. The module was placed in vertical position to facilitate permeate and retentate sampling, as well as avoiding stagnant zones.

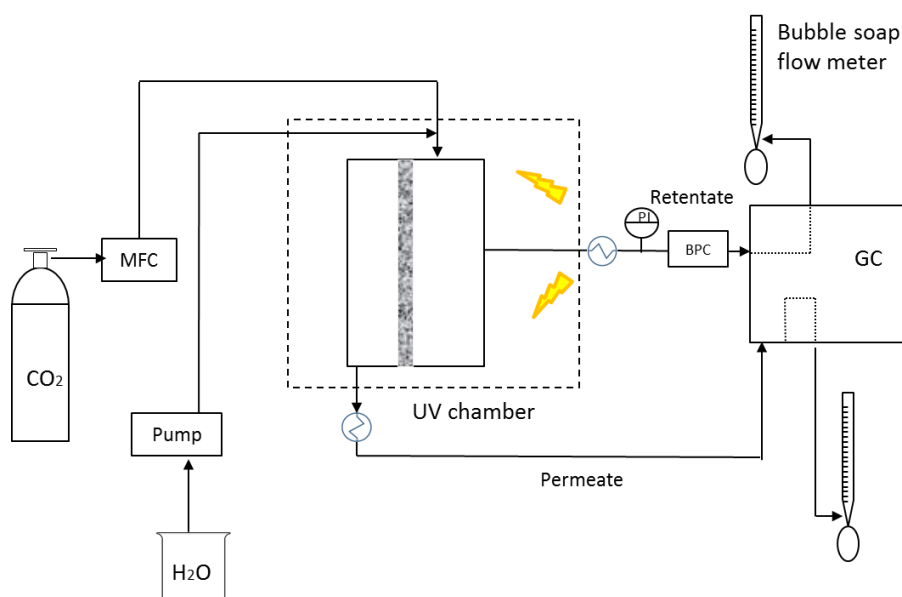


Figure 65. Scheme of Photocatalytic membrane reactor setup.³²²

Table 18 summarizes the operating conditions explored. The trans-membrane pressure difference of 2 bar was regulated by a back pressure controller. The gaseous fraction of retentate and permeate flows was measured by bubble soap flow-meters, after cooling streams outgoing from the reactor with apposite ice traps. The composition of these streams was measured by an Agilent Technologies 7890A gas chromatograph with TCD (HP-PLOT and Molsieve columns). The condensate fraction of the retentate and permeate, periodically sampled, was analysed by an Agilent 6890N gas chromatograph with FID and an HP-5 column.

It has to be highlighted that all the reaction measurements, lasting 25-30 h, were performed in steady state conditions, which were reached within 5 h for all of the species obtained.

The catalytic membrane was used in the continuous photocatalytic membrane reactor for some weeks changing feed molar ratio and feed flow rate as reported in Table 18. During the whole period, C₃N₄ piling out was not evident since no loss in reactor performance and/or selectivity was measured.

Table 18. Operating conditions for C₃N₄ photocatalytic membrane reaction measurements.

CO ₂ flow rate, mL(STP*) min ⁻¹	11-107
H ₂ O/CO ₂ feed molar ratio	0.5; 2; 5
Feed Pressure, bar	2
Permeate Pressure, bar	1
Contact time, s	2; 9.8; 18.7

*STP: standard temperature and pressure, 0°C and 1 bar.

Particular attention was devoted to analysing the effect of contact time on membrane reactor performance. It was defined as the ratio of the catalyst weight dispersed in the membrane to CO₂ feed flow rate, considered as the limiting reagent (Eq. 19).

No difference in CO₂ exiting the reactor from the feed one could be measured practically; therefore, CO₂ conversion did not represent an appreciable value to be considered significant in order to evaluate the reactor performance. Instead, it was evaluated through the produced species flow rate/catalyst weight (Eq. 20), the total converted carbon/catalyst weight ratio (Eq. 21), and reaction selectivity (Eq. 22).

$$\text{Contact time} = \frac{C_3N_4 \text{ catalyst weight embedded in the membrane}}{CO_2 \text{ feed flow rate}}, s \quad \text{Eq. 19}$$

$$\frac{\text{Produced Species flow rate}}{C_3N_4 \text{ catalyst weight}} = \frac{\text{Compound flow rate}}{\text{Amount of catalyst dispersed in membrane} \cdot h} \frac{\mu\text{mol}}{g_{\text{catalyst}}} \quad \text{Eq. 20}$$

$$\frac{\text{Converted carbon}}{C_3N_4 \text{ catalyst weight}} = \frac{\sum \text{Carbon flow rate for each produced species}}{\text{Amount of catalyst dispersed in membrane} \cdot h} \frac{\mu\text{mol}}{g_{\text{catalyst}}} \quad \text{Eq. 21}$$

$$Selectivity_i = \frac{i\text{-species flow rate}}{\sum_i^n \text{species flow rate}}, -$$

Eq. 22

3.4.3 Characterisations of C₃N₄-Nafion membrane

Figure 66a shows FTIR/ATR representative spectra relative to the photocatalytic membrane for both air-facing and casting plate-facing surfaces. Firstly, the analyses confirmed the presence of C₃N₄ catalyst in the membrane matrix as the characteristic chemical structure was maintained by peak presence between ca. 1630 and 1320 cm⁻¹, in agreement with FTIR analysis of C₃N₄ powder (Figure 62). All the signals in the range between 970 and 1400 cm⁻¹ belong to the Nafion structure. In particular, the bands appearing at 970-983 cm⁻¹ are attributed to C–O–C stretching vibrations; the band at ca. 1066 cm⁻¹ can be related to the symmetric stretching of –SO₃–. In the range between 1400 and 1100 cm⁻¹ the asymmetric stretching bands of –SO₃– should be found, but they are covered by the more intense bands of –CF₂ stretching, visible in the spectra.³²³ Moreover, interactions between the Nafion matrix and the loaded C₃N₄ occur as already reported in the literature by Wu et al.³²⁴ The C₃N₄ nanosheets consist of a two-dimensional material that through ammine groups establishes crosslinking interactions with the hydrophilic –SO₃– groups present in the Nafion matrix. FT-IR/ATR analysis of C₃N₄ Nafion membrane shows, with respect to Nafion membrane, a blue-shift of –SO₃– characteristic asymmetric vibration from 1054 cm⁻¹ to 1063 cm⁻¹ (Figure 66a, inset). The g-C₃N₄ nanosheets incorporated in the membrane during membrane formation turns the Nafion original “spherical structure” into a new “lamellar structure” increasing the amorphous phase.³²⁴

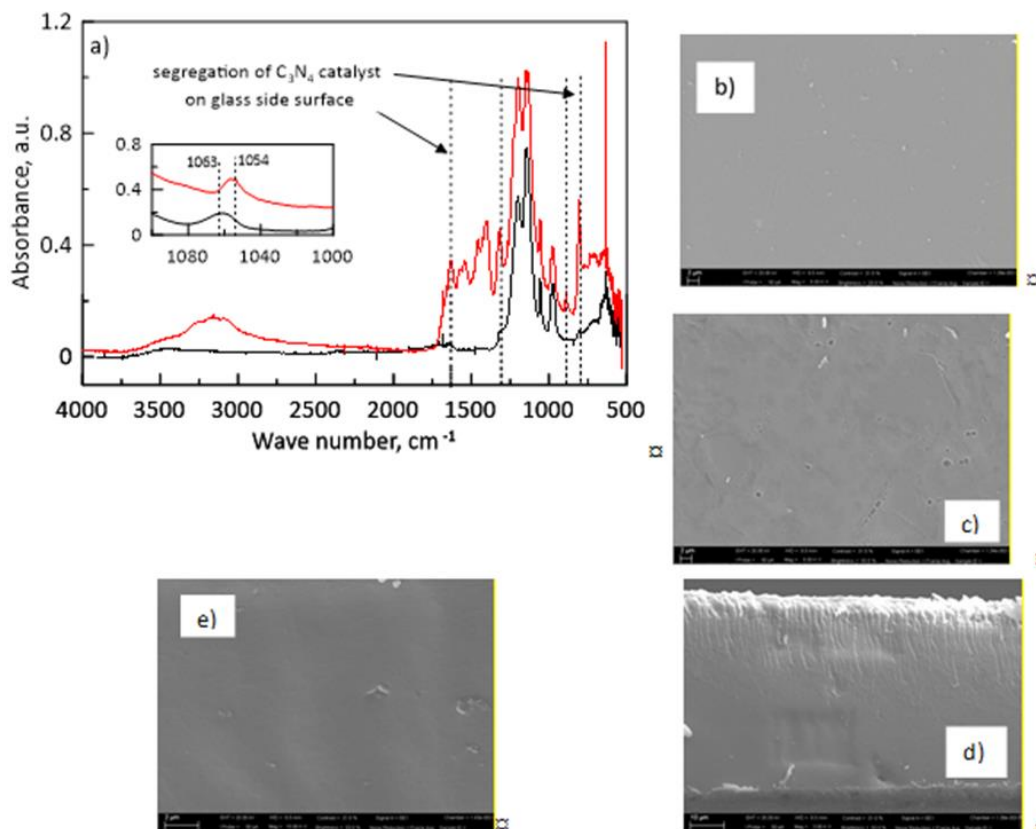


Figure 66. a) FT-IR (ATR) spectra of (black line) air-facing and (red line) casting plate-facing membrane surfaces of C_3N_4 -loaded Nafion membrane (in the inset, the blue shift of $-SO_3$ -groups in the Nafion owing to the presence of the catalyst). SEM of (b) air-facing (magnification 5kX), (c) casting plate-facing surfaces (5 kX), (d) cross-section (3 kX), (e) detail (15 kX), of cross section of C_3N_4 -loaded Nafion membrane.

OH band intensity of the casting plate-facing surface spectrum was higher than the air-facing surface one, most likely owing to the higher catalyst concentration related to its segregation on this membrane side, as also confirmed by SEM images. Indeed, from the perusal of Figure 66b), the air-facing surface of the C_3N_4 -loaded Nafion membrane appears dense in agreement with the expectations for a membrane prepared by solvent evaporation method. On the contrary, the casting plate-facing surface presents some porosities owing to the slow solvent evaporation from the most inner layers of the cast solution that can give rise to local phase separation processes (Figure 66c). Moreover, the SEM image of the casting plate-facing surface highlights a partial segregation of the C_3N_4 partially deposited on the bottom part of the membrane. The SEM images of the cross section (Figure 66d and 66e) confirmed the dense nature of the membrane and the formation of catalyst

micro-aggregates, present in the whole cross section, but more concentrated in the bottom part of the same.

The integrity of catalyst when embedded in membrane matrix was also confirmed by UV–Vis diffuse reflectance spectroscopy analyses that showed a band gap of 2.8 eV for the membranes in dry and wet conditions as for C_3N_4 catalyst powder. Moreover, Nafion matrix was proved to be transparent to UV-visible radiation, as the spectrum was recorded analysing the air-side membrane surface.

3.4.4 Results and discussions

The tests carried out in absence of CO_2 are shown in Figure 67 for both photocatalytic and pure Nafion membrane plotting the species distribution as a function of time on stream. MeOH, EtOH, HCHO and C_3H_6O (acetone) were found in the first sample after 2 h testing at the reactor exit. Their flow rate suddenly decreased along with the time and after 7 h no species were detected at the reactor outlet. This treatment was further continued up to 10-12 h. The continuous operating mode of the membrane reactor, implied a continuous removal of residual species from reactor volume, therefore their decreasing trend confirmed their nature as residues.

The zero values reached by each species profile clearly indicated that the membranes did not longer contain any compound; therefore, the species measured in reaction experiments could only be the result of the photocatalytic activity of the C_3N_4 -Nafion membrane. The presence of the same compounds (Figure 67, right side) in a bare Nafion membrane confirms the previous hypothesis. The difference in the profile evolution along with time could be attributed to the different membrane thickness and the filler (catalyst) presence.

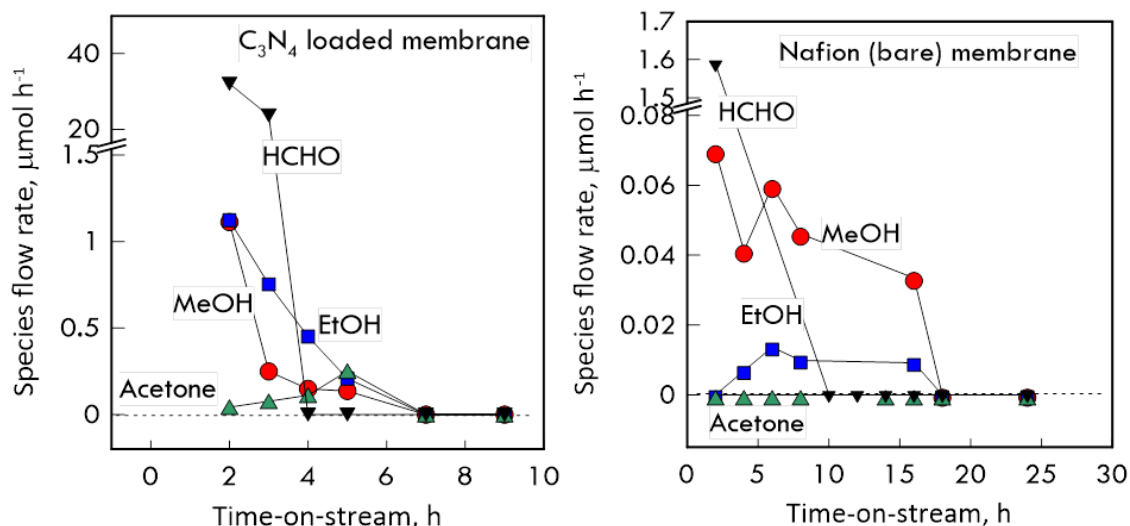


Figure 67. Membrane cleaning (removal of any residuals potentially present) before reaction. C₃N₄ loaded Nafion membrane (active area and thickness respectively 20.4 cm² and 65.8 ± 3.7 µm) and bare Nafion membrane (active area and thickness respectively 4.1 cm² and 81.3 ± 4.3 µm).³²²

As aforementioned, photocatalytic reaction measurements were carried out in presence of H₂O/CO₂ feed analysing the effect of the feed molar ratio and contact time (Eq. 19) on the membrane reactor performance. At a contact time of 2 s, MeOH and EtOH flow rates increased with H₂O/CO₂ feed molar ratio (Figure 68), reaching 17.9 and 14.9 µmol g_{catalyst}⁻¹ h⁻¹, respectively, at a feed molar ratio equal to 5 against 4 and 1.7 µmol g_{catalyst}⁻¹ h⁻¹ obtained at a feed molar ratio of 0.5. Contrarily, to the water defect corresponds a larger HCHO production; therefore, at H₂O/CO₂ feed molar ratio of 0.5, HCHO was the most abundant product, reaching a flow rate of 27 µmol g_{catalyst}⁻¹ h⁻¹ (Figure 68).

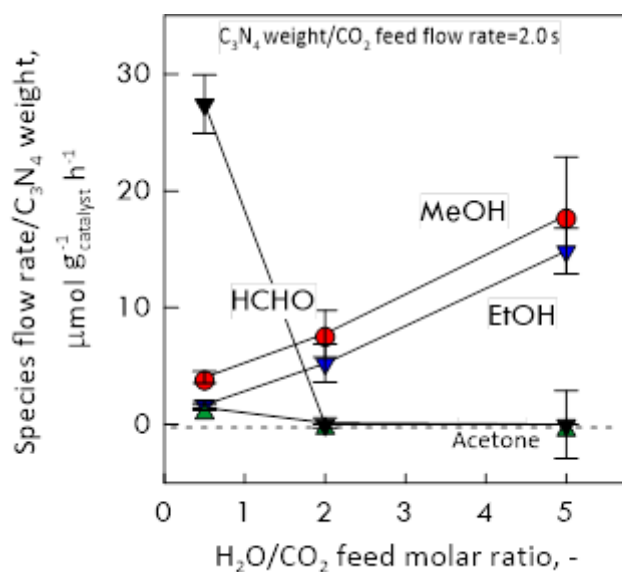
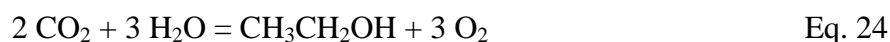
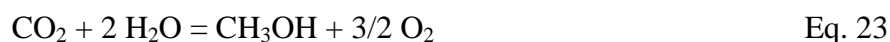


Figure 68. Flow rate/catalyst weight of the various species formed as a function of H₂O/CO₂ feed molar ratio at a contact time of 2 s.

This trend can be explained through the reactions stoichiometry (Eqs 23-25).



A water excess (as in the case of H₂O/CO₂ feed molar ratio=5) leads to MeOH and EtOH as the main products whereas a water defect (as in the case of H₂O/CO₂ feed molar ratio=0.5) leads to HCHO as the main one. Traces of acetone were also found at a feed molar ratio of 0.5, most probably owing to the occurrence of secondary reactions of intermediates not desorbed from the catalytic site, as reported in the literature.^{325, 326}

Similar trends were obtained at a contact time of 9.8 s (Figure 69), where MeOH and EtOH were again the favoured products at a high H₂O/CO₂ feed molar ratio, even though their flow rates were ca. half of that obtained at a contact time of 2 s.

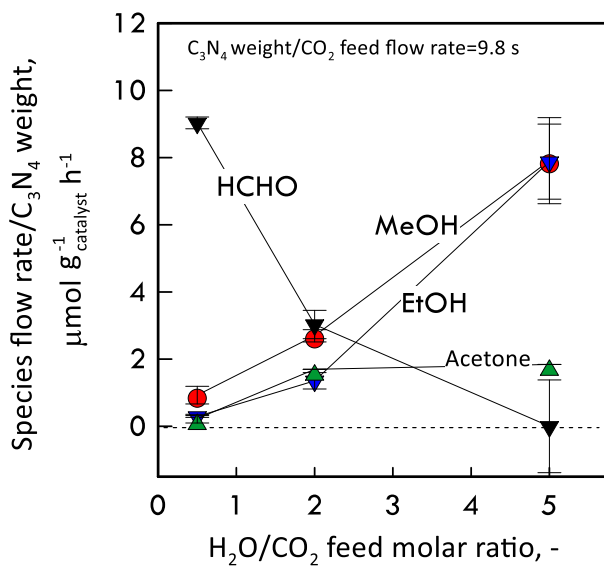


Figure 69. Flow rate/catalyst weight of the various species formed as a function of H₂O/CO₂ feed molar ratio at a contact time of 9.8 s.

This effect can be attributed to the time that the reacting species remain in contact with the catalyst under UV-Vis light. The high contact time, or, in other terms, the slower removal of the reaction mixture from reaction volume can induce MeOH and EtOH to be partially oxidized producing formaldehyde (Eq. 26) or fully oxidized to CO₂ as reaction product. On the contrary, a low contact time implies a fast removal of products from the reaction volume exposed to UV light and, thus, less promotion of secondary reactions.



Analogously, at a feed molar ratio of 0.5, HCHO flow rate/catalyst weight decreased from 27 (at 2 s) to 9 μmol g_{catalyst}⁻¹ h⁻¹ (at 9.8 s) reaching zero at a feed molar ratio equal to 5. Acetone production instead increased as a function of the feed molar ratio up to stable value of ca. 2 μmol g_{catalyst}⁻¹ h⁻¹.

Figure 70 and Figure 71 show the effect of the contact time. MeOH and EtOH were preferential products at the lowest value of contact time.

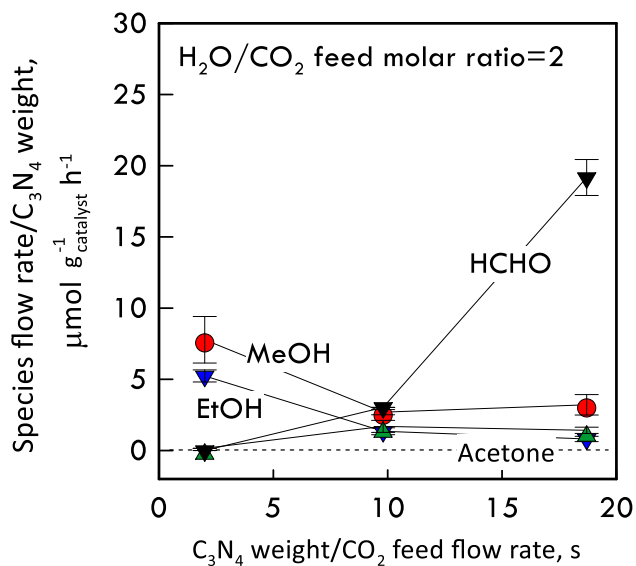


Figure 70. Flow rate/catalyst weight of the various species formed as a function of C₃N₄ weight/CO₂ feed flow rate at H₂O/CO₂ feed molar ratio equal to 2.

As it increased, their flow rate decreased down to a constant value, whereas HCHO and acetone increased as a result of oxidation reaction and secondary reaction between intermediates, respectively. At a feed molar ratio of 5, which means in a water excess, no HCHO was detected (Figure 71). In these conditions, even though MeOH and EtOH decreased along with contact time, they remained the most abundant products in the whole range of contact time considered in the experiments.

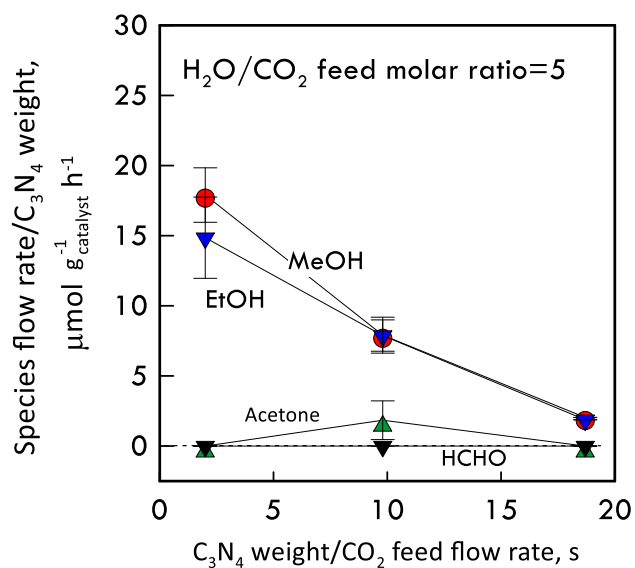


Figure 71. Flow rate/catalyst weight of the various species formed as a function of C₃N₄ weight/CO₂ feed flow rate at H₂O/CO₂ feed molar ratio equal to 5.

The reaction selectivity (Eq. 22) is an important parameter to define the products distribution.

The highest selectivity in alcohols production was observed at low value of contact time and high H₂O/CO₂ feed molar ratio (Figure 72). The best MeOH and EtOH selectivity 54.6% and 45.4 % respectively, were in fact observed at H₂O/CO₂ feed molar ratio equal to 5 and contact time of 2 s, representing 100% of carbon-containing products. Globally, alcohols selectivity tended to increase with feed molar ratio.

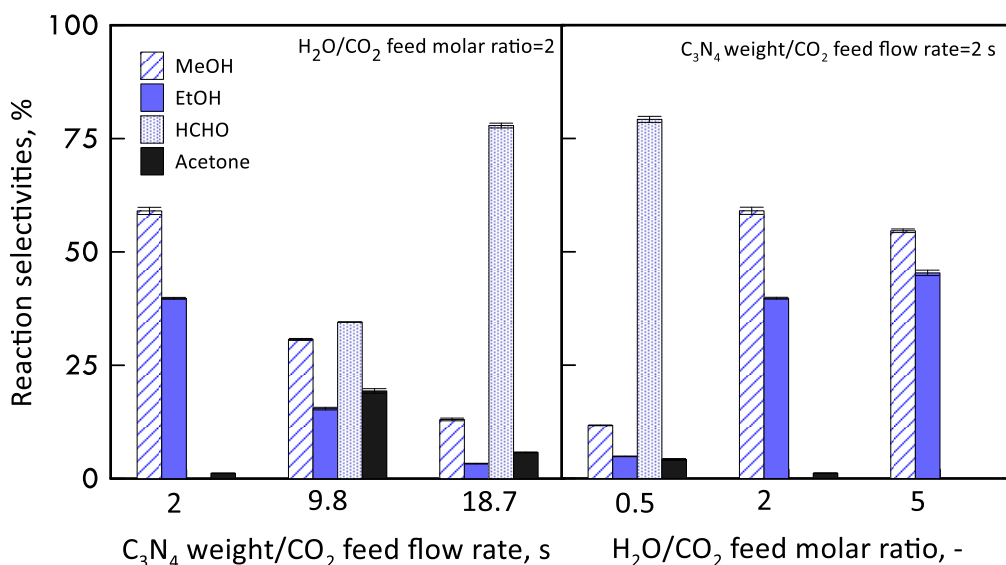


Figure 72. Reaction selectivity as a function of C_3N_4 weight/ CO_2 feed flow rate (left side) and H_2O/CO_2 feed molar ratio (right side).

This behaviour in the CO_2 reduction reaction was previously explained as usual outcome when in the presence of water excess (Eqs. 24-25). Instead, it followed a decreasing trend with contact time, confirming how the slow removal of products from the reaction volume promoted secondary reactions, favouring HCHO and acetone formation.

The capability of the system to convert CO_2 into other carbon-containing species was quantified in terms of total converted carbon/catalyst weight (Eq. 21) and the results are summarized in Figure 73. The highest conversion ($47.6 \mu\text{mol g}_{\text{catalyst}}^{-1} \text{h}^{-1}$) occurred at the highest H_2O/CO_2 feed molar ratio and lowest contact time, with an amount of converted carbon 8 times greater than that measured in the worst conditions (H_2O/CO_2 feed molar ratio=5 and contact time=18.7 s). Comparing the results obtained by the photocatalytic membrane reactor operated in continuous mode with that of the batch system, the membrane reactor converted at least 10 times more carbon than the batch, also in unfavourable conditions. The dispersion in the Nafion matrix increases the active surface of the catalyst implying an easier achievement of the catalytic sites by light and reagents. Moreover, the continuous removals of products from the reaction volume not only favours the reaction, but also promotes the species desorption and the restore of active sites, making them available for further conversion.

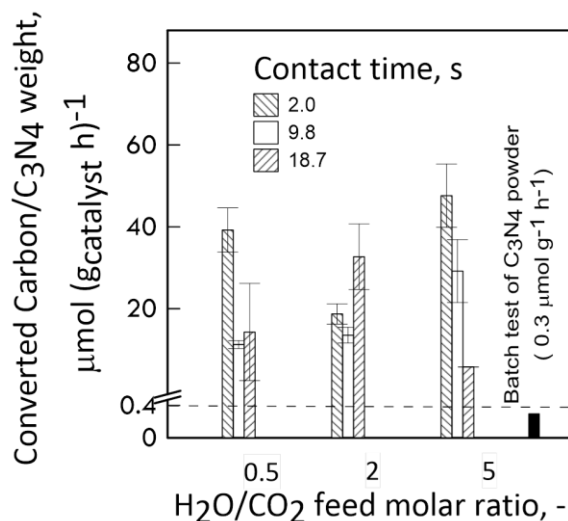
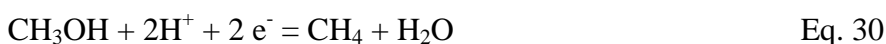
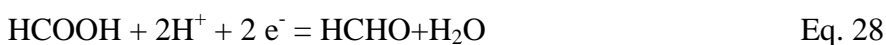


Figure 73. Total Converted Carbon as function of H₂O/CO₂ feed molar ratio and contact time.

Table 19 compares the photocatalytic membrane reactor performance with other results available for C₃N₄ in the literature or obtained by using a continuous reactor. Notably, the MeOH flow rate/catalyst weight of the photocatalytic membrane reactor presented in this work is, under some experimental conditions, significantly higher than the ones obtained with other reaction systems. In comparison with result obtained by Sellaro et al.²⁶⁸ where a TiO₂-based catalyst was embedded in a Nafion matrix, a wider products distribution resulted, with comparable MeOH production. By comparing this work with the data reported for batch systems, the advantage offered by the continuous system is confirmed. The MeOH production is, in fact, higher than most of the ones obtained by using simple C₃N₄ as catalyst and higher or, at least, comparable when it is used as co-catalyst in batch conditions. Moreover, it is worth noticing that, as already observed²⁶⁸ and differently from what can be found in most of the literature for batch reactors, neither CH₄ nor CO were detected, alcohols being the main products. The synergic effect of the use of a photocatalytic membrane and a continuous flow mode reactor allows the substrate to undergo a lower degree of reduction as fresh CO₂ is continuously fed into the system and the produced species are continuously removed from the catalytic sites, reducing the possibility of having over-oxidation.¹¹⁰

Remarks on possible reactions involved are above reported.

A pioneering work of Inoue et al.¹⁰⁵ reported the following reduction reactions:

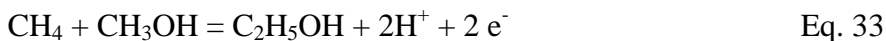


and, the oxidation reaction:



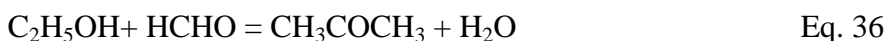
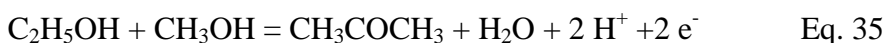
Each of the hypothesized reduction reactions involves two electrons and the various reactions occur in sequence; thus, 8-electrons are required per each CO_2 molecule to obtain CH_4 .

Ethanol and acetone, also experimentally detected in this work, were not included among the above reactions. For ethanol, the below reactions could occur:



To obtain ethanol, two more electrons are needed (12 electrons in total for the reduction of two CO_2 molecules, 6 of which are necessary to obtain one molecule of CH_3OH , 4 for one molecule of HCHO and 2 electrons in Eq. 32 or the presence of CH_4 (Eq. 33). However in this system, no CH_4 was detected; therefore, the first hypothesis is more likely.

Similarly for acetone, the reactions which could occur on the irradiated catalyst surface are:



Equations 35 and 36 do not need any additional electrons. Other solutions can be hypothesized and, in addition, mechanisms based on elementary steps would be useful for understanding the reaction path and then the species produced.

However, it is worth to tentatively correlate the Inoue schemes with some variables used in the present work such as residence time and feed molar ratio.

During CO₂ reduction, the chemical species move from one (feed) membrane face to the permeate one. Along this path, accordingly to the schemes of Inoue et al.¹⁰⁵ and the others reported above, CO₂ conversion to HCOOH, HCOOH to HCHO, HCHO to CH₃OH, CH₃OH and HCHO to C₂H₅OH and acetone take place. CO₂ is always inside the membrane, independently from the feed molar ratio; thus, the first, 2-electrons step, could occur everywhere in the catalytic membrane, although no HCOOH was detected in the exiting stream.

The lower water content (low feed molar ratio) does not favour the oxidative reaction (Eq. 31) and hence the H⁺ production is low. Therefore, the schemes implying four electrons are favoured also for the small availability of this ion (Figure 6, HCHO production). The higher feed molar ratio favours the larger-electrons schemes leading, e.g., to MeOH formation owing to H⁺ large availability.

The feed molar ratio plays a significant role: its lower value favours the low-electrons schemes (e.g., HCHO production, four-electrons), whilst a higher value leads to high-electrons scheme (e.g., MeOH, six-electrons). Therefore, the whole process is a combination of the reactions (2, 4, 6, etc. electrons) since these schemes describe a set of reactions in series and as such, at the end, all the reactants and products of each reaction are in principle expected in the exiting stream.

Table 19. Comparison with results reported in literature

Catalyst	Reactor configuration	Flow rate/catalyst weight, $\mu\text{mol g}_{\text{catalyst}}^{-1} \text{h}^{-1}$							Ref.
		MeOH	EtOH	HCHO	Acetone	HCOOH	CH ₄	CO	
C ₃ N ₄ catalyst embedded in a Nafion membrane	Continuous	0.9-17.9	0.3-14.9	0-27	0-1.8	0	0	0	322 This chapter
C ₃ N ₄	Batch						5		327
C ₃ N ₄ *	Batch	25				1250			303
C ₃ N ₄ catalyst placed in glass fiber	Continuous						0.5	5.2	328
C ₃ N ₄ nanotubes	Batch	0.28							329
C ₃ N ₄	Batch						0.62-1		330
C ₃ N ₄	Batch	0.26					Traces		331
C ₃ N ₄	Batch	10	12						332
C ₃ N ₄	Continuous	Traces							333
3 MEA-C ₃ N ₄	Batch	0.28					0.34		331
AgBr/C ₃ N ₄	Batch				2		21		327
C ₃ N ₄ 3% Cu/TiO ₂ *	Batch	102				1118			303
2 Au-C ₃ N ₄ catalyst placed in glass fiber	Continuous						4.3	6.5	328
C ₃ N ₄ /ZIF 8 (nanocluster on C ₃ N ₄ nanotubes)	Batch	0.75							329
CdIn ₂ S ₄ /C ₃ N ₄ 20% wt.	Continuous	42.7							333
6 SO/0.12B-0.2P-C ₃ N ₄	Batch						6.25-7.5		330
Ag-N doped C ₃ N ₄ -G-50	Batch	20	50						332
TiO ₂ catalyst embedded in a Nafion membrane	Continuous	12.6-45	0	0	0	traces	0	0	268
TiO ₂ nanoparticles in porous cavities of commercial Nafion membranes	Continuous	56 (supercritical CO ₂ as feed)				38			266
Membrane microreactor	Continuous	111							334
TiO ₂ /Y-zeolite anchored on Vycor glass	Batch	5					8		335
Ti-mesoporous zeolite	Batch	3.5					7.5		130

Ti-b(OH) and Ti-b(F)	Batch	5.9					1		336
TiO ₂ and 2% Cu/TiO ₂ in NaOH solution	Batch	0.78							337
Cu/TiO ₂ film supported on optical-fiber	Continuous	0.45							338
Cu/TiO ₂ and Ag/TiO ₂ film supported on optical-fiber	Continuous	4.12							339
TiO ₂ anatase	Batch	0.075					0.40		340
TiO ₂ polymorphs	Continuous					3.15	2.13		341
TiO ₂ polymorphs	Continuous					2.1			342
phtalocyanines /TiO ₂	Batch					26			343

*under UV light

3.4.5 Conclusion

In this work, photocatalytic CO₂ conversion was carried out, as yet not in the literature, in a continuous photocatalytic reactor with an exfoliated C₃N₄-based membrane irradiated by UV light. The effect of H₂O/CO₂ feed molar ratio and contact time on species production, reaction selectivity and converted carbon were investigated.

Total converted carbon per gram of catalyst varied between 5 to 47.6 $\mu\text{mol g}_{\text{catalyst}}^{-1} \text{h}^{-1}$, with the latter value obtained at an H₂O/CO₂ feed molar ratio of 5 and 2 s as contact time with alcohols as prevailing products. The membrane reactor converted at least 10 times more carbon than the batch system, as a result of the better dispersion of catalyst which is embedded in the Nafion matrix.

Overall, alcohols production was promoted by a low contact time as a result of the fast removal of the reaction mixture from the reaction volume exposed to UV light and, thus, with less promotion of oxidation and/or secondary reactions. On the contrary, the slow removal caused a partial oxidation of MeOH and EtOH, favouring HCHO production. In all the cases, a water defect corresponded to a larger HCHO production, reaching a flow rate of 27 $\mu\text{mol g}_{\text{catalyst}}^{-1} \text{h}^{-1}$ at an H₂O/CO₂ feed molar ratio equal to 0.5.

The highest MeOH and EtOH selectivities were 54.6% and 45.4 % respectively, at H₂O/CO₂ feed molar ratio equal to 5 and contact time of 2 s, representing 100% carbon-containing products.

A good alcohols production rate of 32.8 $\mu\text{mol g}_{\text{catalyst}}^{-1} \text{h}^{-1}$ was obtained at the best operating conditions.

3.5 Photocatalytic CO₂ reduction in continuous membrane reactor: C₃N₄-TiO₂/Nafion membrane

The results presented in this chapter will be partially reported in a paper under submission to *Submission to Energy & Environmental Science*.

3.5.1 C₃N₄-TiO₂ powder

3.5.1.1 Powder characterization

The diffuse reflectance spectra of C₃N₄, TiO₂ and C₃N₄-TiO₂ samples were recorded in order to investigate their band gap energy (Figure 74). In particular, the band gap of the C₃N₄-TiO₂ was determined by the intersection (green spot) of the tangent lines indicated in the inset Figure 74.

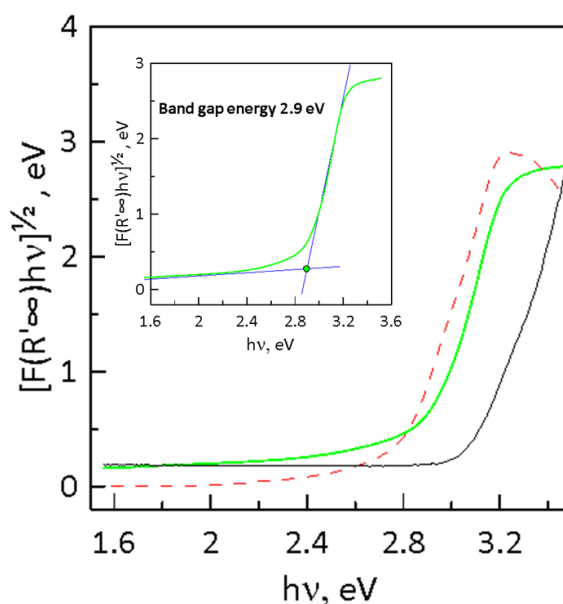


Figure 74. Kubelka-Munck modified function vs. energy for C₃N₄ (dashed red line), TiO₂ (black line) and C₃N₄-TiO₂ (green line) samples. The C₃N₄-TiO₂ band gap energy is reported in the inset.

The band gap of the C₃N₄-TiO₂ sample is 2.9 eV (inset of Figure 74) which falls in the region of visible light absorption and corresponds to ca. 428 nm. Probably due to the

very close band gaps value of the bare samples and the instrumental resolution, in the composite spectrum only one band gap energy was observed instead of two. Thus, by comparing the pure TiO₂ and C₃N₄ reflectance spectra, Li et al. report only one band gap energy for the C₃N₄-TiO₂ sample with an absorption in the visible range accompanying a red shift in the absorption edge, due to the synergistic effect between TiO₂ and C₃N₄.³⁴⁴ The discrepancy with the value of 2.8 eV of the pure C₃N₄ materials, previously found, is ascribable to the presence of TiO₂ which shows a typical band gap energy value of 3.1 eV (black line, Figure 74).

Figure 75 shows the FTIR spectra of TiO₂, C₃N₄ and C₃N₄-TiO₂ samples. According to literature data, the spectrum of the composite material shows the characteristic bands of C₃N₄ and TiO₂.^{221, 345} In particular, as far as C₃N₄ is concerned, the absorption peak at 1644 cm⁻¹ can be ascribed to the *sp*² C=N stretching vibration modes, while the strong peaks at 1248, 1320, and 1416 cm⁻¹ to the *sp*³ C-N heterocycle stretching. Besides, the band at ca. 810 cm⁻¹ is attributed to the typical breathing mode of the tri-s-triazine units.^{207, 209} All of these peaks are representative of the unchanged melem unit structure of C₃N₄ arising after the composite preparation as clearly evidenced by comparing the spectrum of C₃N₄ (red line- Figure75) with that of the composite (green line-Figure75). The spectra between ca. 1250-1650 cm⁻¹ were less defined in the composite with respect to the bare C₃N₄, due to high amount of TiO₂ (75% TiO₂ and 25% C₃N₄). Furthermore, a strong wide band from 400 to 900 cm⁻¹ is due to the TiO₂ presence in the composite C₃N₄-TiO₂, which corresponds to Ti-O and Ti-O-Ti stretching vibration modes.^{221, 345}

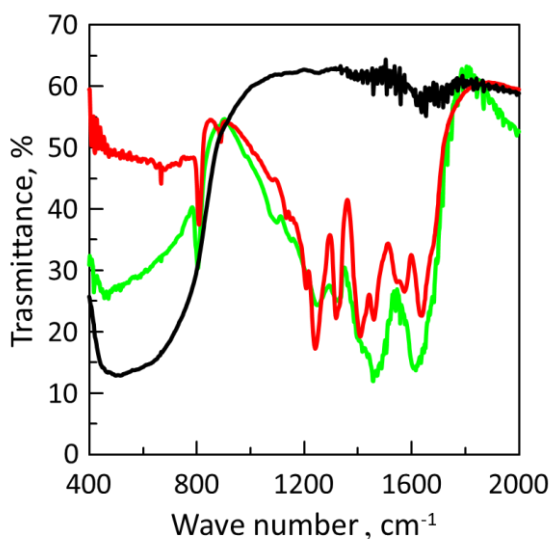


Figure 75. FT-IR spectrum of C_3N_4 powder (red line), TiO_2 (black line) and C_3N_4 - TiO_2 composite (green line).

XRD diffractograms of the C_3N_4 based materials along with the bare TiO_2 and C_3N_4 samples are shown in Figure 76. The pattern of C_3N_4 - TiO_2 composite (red line) shows three main peaks at 13.1° , 25° and 27.3° due to the presence of C_3N_4 and TiO_2 materials. In fact, as in the case of C_3N_4 , C_3N_4 - TiO_2 composite shows two characteristic peaks at 27.3° and 13.1° clearly defined, in good agreement with the patterns reported in the relevant literature and already described in the paragraph 3.4.1.1. The presence of TiO_2 in the composite is confirmed by the intense peak at 25° corresponding to the anatase crystal phase (black line), although the less intense peaks of Anatase phase at 45° and 65° are absent in the composite.

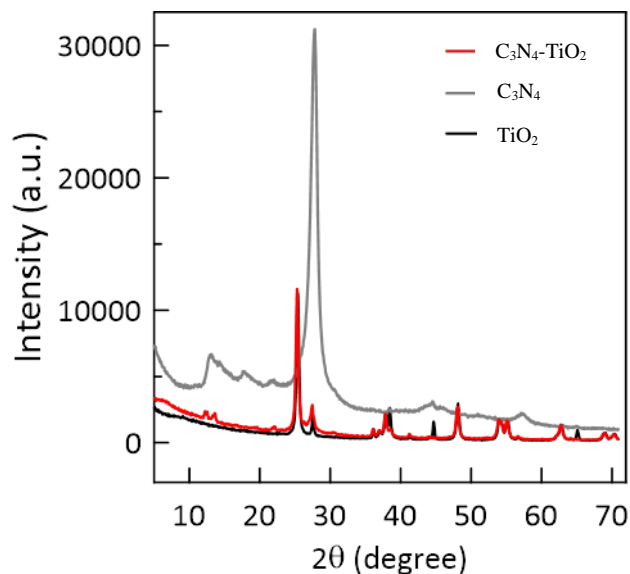


Figure 76. XRD spectra of TiO_2 , C_3N_4 and $\text{C}_3\text{N}_4\text{-TiO}_2$ samples.

3.5.1.2 Preliminary photocatalytic tests: experimental conditions and results by using $\text{C}_3\text{N}_4\text{-TiO}_2$ photocatalyst

The preliminary CO_2 photoreduction tests were carried out by using a batch reactor in Pyrex with a volume of 140 mL and equipped with a septum to permit sampling (Figure 26 section 3.1.1). 0.35g of photocatalyst were dispersed in the bottom of the photoreactor and N_2 was flushed for 2 h inside the system under irradiation in order to photo-desorb possible impurities and/or carbon residues from the catalyst surface. Subsequently, the photoreactor was saturated with CO_2 containing the vapour pressure of water at 25 °C. To start the experiment in the presence of humid CO_2 , the stream of CO_2 was continuously flushed for at least 1 h inside the reactor after bubbling in a water containing flask. In order to evaluate the effect of the amount of water on the CO_2 photoreduction in batch reactor, two tests were preliminary performed by injecting through a syringe 3.6 and 50 μL distilled water, respectively, in the reactor. Then the reactor was closed and irradiated by simulated solar light produced by a SOLARBOX apparatus (CO·FO·ME·GRA) equipped with a 1500W high-pressure Xenon lamp.

The possible presence of products deriving from C impurities was checked by previously irradiating the photocatalysts before the photoactivity experiments in the

presence of CO₂ under a flow of humid He according to Strunk et al.¹¹⁴ This procedure allowed also to clean the surface of the photocatalyst. Notably, no organic species were observed during this treatment.

Aliquots of the gaseous reaction mixture were withdrawn at fixed irradiation times by using a gas-tight micro syringe. The evolution of the formed organic products was followed by a GC-2010 Shimadzu equipped with a Phenomenex Zebron Wax-plus column by using He as the carrier gas and a FID. CO was analysed by a HP 6890 GC equipped with a packed column GC 60/80 Carboxen-1000 and a TCD. The latter analysis was also useful to check that the system was effectively sealed by monitoring the constant amount of N₂ inside the reactor (no air penetrated inside the reactor).

The CO₂ conversion was followed in the presence of two different amounts of H₂O (reductant agent) equal to 3.6 and 50 μL converting 0.26 and 5.27 μmol g_{catalyst}⁻¹ of carbon, respectively (Table 20). In particular, at lower content of H₂O, the only product was CH₄, while at higher content of water, the most abundant products detected were CH₄, MeOH and acetaldehyde with traces of CO. According to the literature data reported in Table 6 (section 1.3.5), the addition of TiO₂ to C₃N₄, increases the photo-converted CO₂ as it is evident by comparing the total carbon converted of test II carried out in the presence of the composite (Table 20) with the results of the test reported in the section 3.4.1.1 in the presence of C₃N₄ sample (0.6 μmol g⁻¹ h⁻¹) carried out under the same experimental conditions.

Table 20. Carbon conversion rate and photogenerated products and total carbon converted after 6 h of irradiation time in batch reactor in the presence of CO₂ and H₂O by using C₃N₄-TiO₂ photocatalyst.

I test: Amount of H ₂ O equal to 3.6 μL		II test: Amount of H ₂ O equal to 50 μL	
Carbon conversion rate, μmol g ⁻¹ h ⁻¹			
0.04		0.9	
Products	μmol g ⁻¹	Products	μmol g ⁻¹
CH ₄	0.26	CH ₄	1.33

		CO	0.1
		Acetaldehyde	1.48
		MeOH	2.36

3.5.2 Photocatalytic membrane test conditions

A photocatalytic membrane was utilized for CO₂ photoreduction with H₂O as the reducing agent. Prior to the characterization and the photoreduction tests, the prepared membrane was cleaned. The cleaning procedure, carried out by using the membrane reactor set up above described, consists in a “blank reaction” where, together with H₂O, an argon stream was fed into the reaction module instead of CO₂, in continuous regime for 8-24 h, at the same operating conditions chosen for the catalytic experiments (under UV-Vis irradiation). The aim of this procedure was to clean the membrane from any residuals of solvent and other low molecular weight organics, possibly present in the polymer solution, that could be released during the reaction measurements thus affecting the results.

The reactor set up used has been described in section 3.4.2 (Figure 65), while the operating conditions applied are summarised in Table 21.

Table 21. Operating conditions for C₃N₄-TiO₂ photocatalytic membrane reaction measurements.

CO ₂ flow rate, mL (STP [*]) min ⁻¹	
H ₂ O/CO ₂ feed molar ratio	0.5; 2; 5
Feed Pressure, bar	3;5
Permeate Pressure, bar	1
Contact time, s	2; 3.5

*STP: standard temperature and pressure, 0°C and 1 bar.

In detail, the trans-membrane pressure difference (3 and 5 bar) was regulated by a back-pressure controller. The gaseous fraction of the retentate and permeate flows, previously cooled down by means of opportune ice traps, was measured by bubble soap flow-meters. The composition of these streams was measured by an Agilent Technologies 7890A gas chromatograph with TCD (HP-PLOT and Molsieve columns). The retentate and permeate condensate fractions were periodically sampled and analysed by an Agilent 6890N gas chromatograph equipped with FID detector and an HP-5 column. All of the tests, lasting 16-20 h, were performed in steady state conditions, which were reached within 5 h for all of the species.

The catalytic membrane was used in the continuous photocatalytic membrane reactor for some weeks changing feed molar ratio, feed pressure, feed flow rate, etc. During the whole period, piling out of C₃N₄-TiO₂ was not evident since no loss in reactor performance and/or selectivity was observed.

Particular attention was devoted to the analysis of the effect of contact time (Eq. 19 section 3.4.2), feed molar ratio and pressure on the membrane reactor performance.

No difference of CO₂ concentration between the feed and the output could be practically measured. Therefore, CO₂ conversion did not represent a significant parameter to be considered to evaluate the reactor performance. Instead, the efficiency of the reaction was evaluated on the basis of produced species by considering the ratios (i) produced species flow rate/catalyst weight (Eq. 20 section 3.4.2), (ii) total converted carbon/catalyst weight ratio (Eq. 21 section 3.4.2), and (iii) the reaction selectivity (Eq. 22 section 3.4.2).

3.5.3 Characterisation of C₃N₄-TiO₂/Nafion membrane

Figure 77a shows two FTIR/ATR representative spectra of the same photocatalytic membrane by considering the air-facing (red spectrum) and casting plate-facing (black spectrum) surfaces. The black spectrum confirmed the presence of C₃N₄-TiO₂ catalyst in the membrane matrix. In fact, the characteristic chemical structure is testified by the bands between ca. 1630 and 1320 cm⁻¹, in agreement with the FTIR analysis of C₃N₄-TiO₂ powder (Figure 75). However, these signals are not evident in the spectrum of the air facing surface of the membrane (red spectrum in Figure 77) due to the catalyst segregation at the bottom of the membrane during the membrane preparation process. In both spectra, all of the signals in the range between 970 and 1400 cm⁻¹ are due to the Nafion structure. In particular, the bands at 970-983 cm⁻¹ are attributed to C–O–C stretching vibrations and the band at ca. 1066 cm⁻¹ can be related to the symmetric stretching of –SO₃–. The asymmetric stretching bands of –SO₃– should occur between 1400 and 1100 cm⁻¹, but they are masked by the more intense bands of –CF₂ stretching.³²³ In this region, the casting plate facing surface spectrum (black line) shows higher intensity than the red spectrum due to the TiO₂ band between 400-900 cm⁻¹, which corresponds to Ti–O and Ti–O–Ti stretching vibration modes as previously described (see Figure 75).

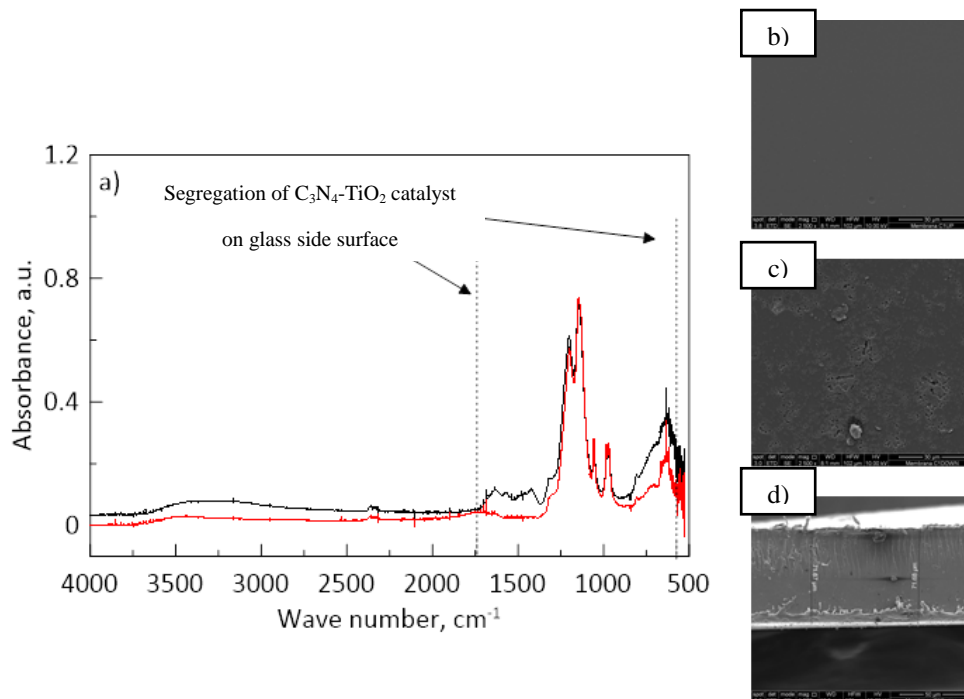


Figure 77. (a) FT-IR (ATR) spectra of (black line) casting plate-facing and (red line) air facing membrane surfaces of C_3N_4 - TiO_2 loaded Nafion membrane. SEM of (b) air-facing (magnification 2.5 kX), (c) casting plate-facing surfaces (2.5 kX), (d) cross-section (1.5 kX) of C_3N_4 - TiO_2 /loaded Nafion membrane.

The difference between the casting plate and the air facing surfaces is confirmed by SEM analyses. Indeed, the air-facing surface of the C_3N_4 - TiO_2 /loaded Nafion membrane shown in Figure 77b appears dense in agreement with the expectations for a membrane prepared by solvent evaporation method. On the contrary, the casting plate-facing surface presents some porosities owing to the slow solvent evaporation from the most internal layers of the cast solution that can give rise to local phase separation processes (Figure 77c). Moreover, the SEM image of the casting plate-facing surface highlights a segregation of the C_3N_4 partially deposited on the bottom part of the membrane confirming the FTIR/ATR analysis. The SEM image of the cross section (Figure 77d) confirmed the dense nature of the membrane and the formation of catalyst micro-aggregates, present in the bottom side.

The integrity of the catalyst, when embedded in the membrane matrix, was also confirmed by UV-vis diffuse reflectance spectroscopy analyses that showed a band gap of 2.9 eV for the membranes in dry and wet conditions as for C_3N_4 - TiO_2 catalyst powder. Moreover, Nafion matrix was proved to be transparent to UV-visible radiation, as the spectrum was recorded analysing the air-side membrane surface.

3.5.4 Results and discussions

Figure 78 shows the results obtained in the tests carried out in the absence of CO₂ (Ar/H₂O stream) by using photocatalytic and pure Nafion membrane plotting the species distribution as a function of time on stream.

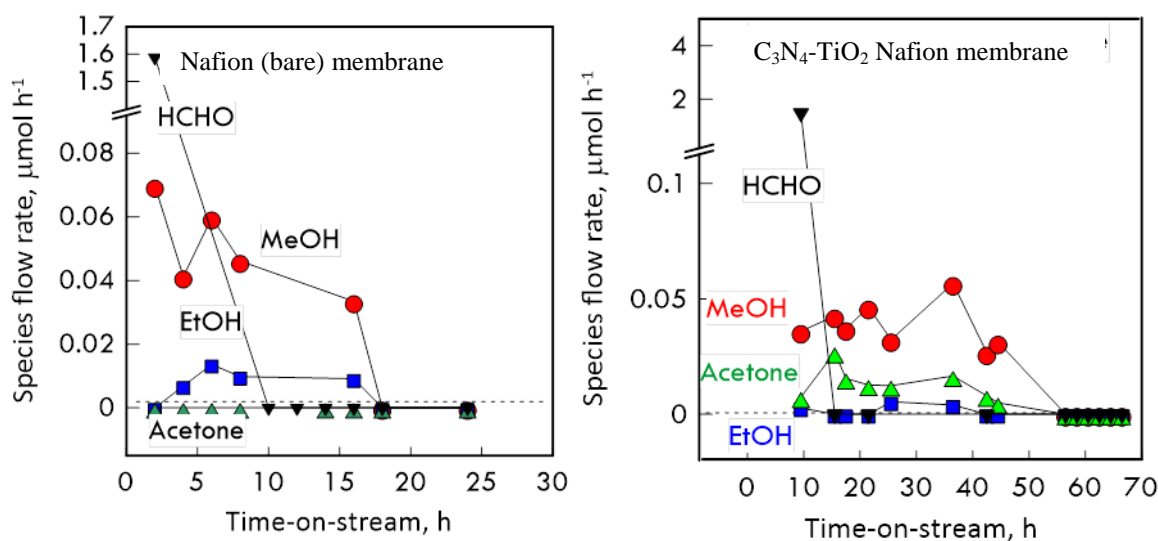


Figure 78. Membrane cleaning (removal of any residuals potentially present) before reaction. C₃N₄-TiO₂ loaded Nafion membrane (active area and thickness respectively 4.1 cm² and 65.8 ± 3.7 μm) and bare Nafion membrane (active area and thickness respectively 4.1 cm² and 78.3 ± 7.8 μm).³²²

MeOH, EtOH, HCHO and C₃H₆O (acetone) were found in the first sample after 2 h of irradiation. In both membrane tests, all of the species flow rate, and especially the HCHO one, decreased with the time until no species could be detected exiting the reactor after 15 and 54 h for the Nafion bare and photocatalytic membrane, respectively. This cleaning treatment was continued up to further 8-12 h. The continuous operating mode of the membrane reactor, implied a continuous removal of residual species from the reactor volume; therefore, their decreasing trend confirms their nature of residues. The zero values reached by each species profile clearly indicates that the membranes did not longer contain residual compound; therefore, the species detected in the reaction experiments in the presence of CO₂ could only be the result of the photocatalytic activity of the C₃N₄-TiO₂-Nafion membrane. The presence of the same compounds in a

bare Nafion membrane (Figure 78) confirms the previous hypothesis. The difference in the profile evolution along with time could be attributed to the different membrane thickness and the filler (catalyst) presence.

When in the Ar-H₂O feed, the Ar is switched to CO₂, the photocatalytic membrane was tested in the reactor (Figure 65) at different feed molar ratios H₂O/CO₂ (0.5, 2 and 5) and contact time (2 and 3.5 s) as reported in Table 21. As previously mentioned, also the pressure effect on the membrane photoreactor performance was evaluated by carrying out CO₂ photoreduction at the pressure of 3 and 5 bar. Generally, these experiments gave MeOH, EtOH, HCHO and acetone as products.

Figure 79 shows both species flow rate and converted carbon obtained in the experiments performed at lower contact time (2 s) as a function of H₂O/CO₂ feed molar ratio. In detail, MeOH and EtOH species flow rate increased reaching 45 and 5 $\mu\text{mol g}^{-1} \text{h}^{-1}$, respectively, by increasing the feed molar ratio from 0.5 to 5. On the other hand, acetone production firstly raised up to 8 $\mu\text{mol g}^{-1} \text{h}^{-1}$ at H₂O/CO₂ feed molar ratio equal to 2 and then decreased to zero at H₂O/CO₂ molar ratio of 5. The MeOH and EtOH trends, as previously reported in the section 3.4.4, are due to the feed molar ratio effect on the products distribution. In fact, by considering the stoichiometric ratio of the alcohol formation from CO₂ and H₂O (Eq. 23-24) the alcohol production is favoured by a water excess. Instead, acetone (C3) formation probably arises from secondary reactions of intermediates not desorbed from the catalytic site, as reported in the literature.^{325, 326}

The total converted carbon/catalyst weight (Eq. 21) was quantified to define the capability of the system to convert CO₂ into other carbon-containing species (Figure 79). MeOH was the main product for all of the feed molar ratio and concurrently the carbon converted increased by increasing the feed molar ratio reaching the highest value of ca. 58 $\mu\text{mol g}^{-1} \text{h}^{-1}$.

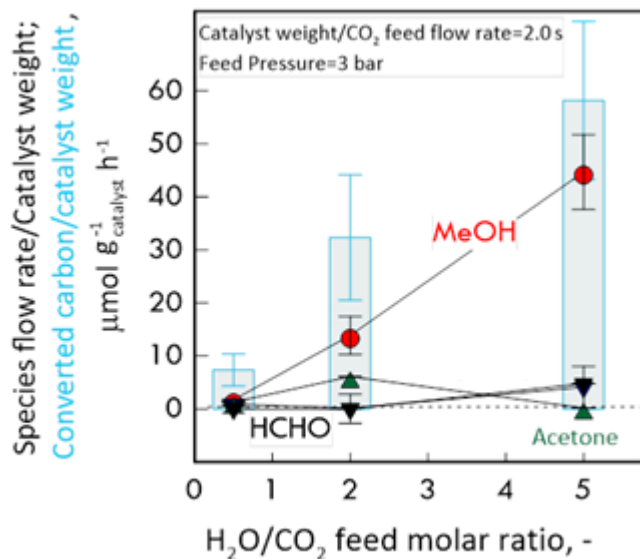


Figure 79. Flow rate/catalyst weight of the various species formed and carbon converted (histogram) as a function of H₂O/CO₂ feed molar ratio at a contact time of 2 s.

Similar trends were obtained at a contact time of 3.5 s (Figure 80), where MeOH was again the favoured product, even though its flow rate was ca. three times less than that obtained at a contact time of 2 s. This lower production is probably due to back reactions (Eq. 26, reported again hereby) oxidizing back to CO₂ the formed MeOH. These reactions are favoured at higher contact times because of the slower removal of O₂ produced in the reactor.



Traces of HCHO were also found at the highest water amount.

Also at a contact time of 3.5 s, the total carbon converted increased with the H₂O/CO₂ molar ratio.

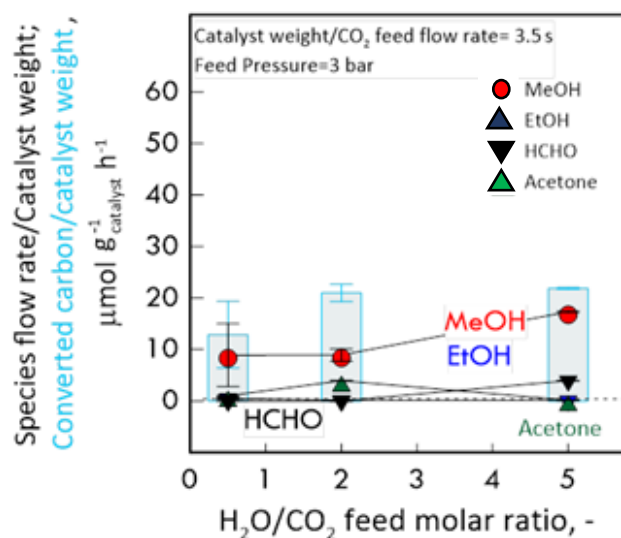


Figure 80. Flow rate/catalyst weight of the various species formed and carbon converted (histogram) as a function of H₂O/CO₂ feed molar ratio at a contact time of 3.5 s.

To define the best membrane reactor performance, Figure 81 shows the total converted carbon/catalyst weight (Eq. 21) obtained in all of the considered experimental conditions. The highest conversion (ca. 58 $\mu\text{mol g}_{\text{catalyst}}^{-1} \text{h}^{-1}$) was achieved at the lowest contact time and highest H₂O/CO₂ feed molar ratio, with an amount of converted carbon 7 times greater than that measured in the worst conditions (H₂O/CO₂ feed molar ratio=0.5 and contact time=2 s). By comparing the results obtained by the photocatalytic membrane reactor operating in continuous mode with that of the batch system reported in Table 21, the membrane reactor converted at least 9 times more carbon than the batch, even in the most unfavourable conditions. As previously reported for the C₃N₄-Nafion membrane, the dispersion of the C₃N₄-TiO₂ in the Nafion matrix increases the active surface of the catalyst thus implying that the catalytic sites are more easily reached by light and reagents than when the powder is not embedded in the membrane. Moreover, by comparing the set of data obtained at contact time of 2 s with the ones at 3.5 s, the continuous removal of products from the reaction volume not only favours the reaction, but also promotes the species desorption and the release of active sites, making them available for further reactions. Furthermore, at fixed contact time of 2 s, a linear trend appears by changing the feed molar ratio, thus confirming the previous observations regarding the H₂O/CO₂ feed molar ratio effect. The same trend was detected for contact time of 3.5 s but with a smaller slope value due to a slower removal

of O_2 produced. In fact, the O_2 presence, as reported in literature, inhibited the photoreduction of CO_2 .³⁴⁶

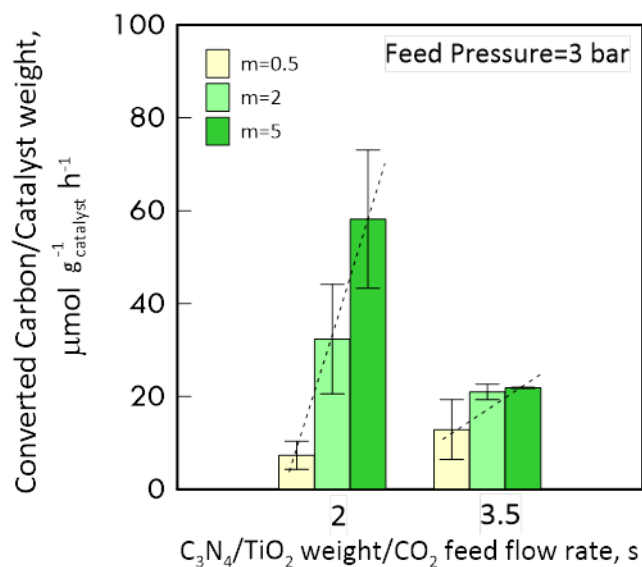


Figure 81. *Converted carbon per gram of catalyst as a function of contact time at different H_2O/CO_2 feed molar ratio.*

The study presented in this dissertation is hereby again reported to compare, at the best contact time (2 s) and reaction pressure (3 bar) the species flow rate obtained from CO_2 photoreduction experiments carried out in the presence of C_3N_4 and C_3N_4 - TiO_2 Nafion membranes at two different feed molar ratios equal to 2 and 5, respectively, in Figure 82.

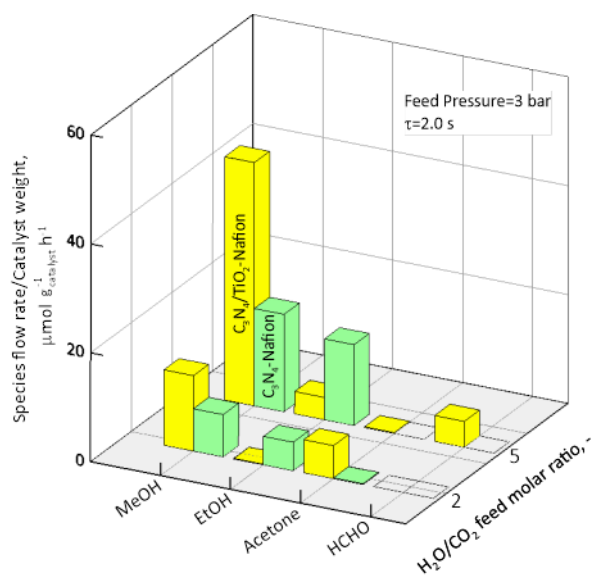
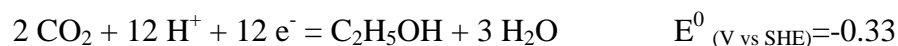
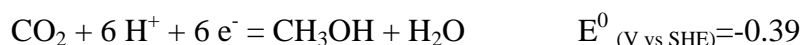


Figure 82. Comparison of the flow rate/catalyst weight of the various species formed at H₂O/CO₂ feed molar ratio of 2 and 5 for C₃N₄-TiO₂-Nafion and C₃N₄-Nafion membranes

The MeOH production was favoured by using the C₃N₄-TiO₂ Nafion membrane, at both feed molar ratios. On the contrary, the C₃N₄-Nafion membrane showed a similar capability in term of MeOH and EtOH production. Nevertheless, at a contact time equal to 2 s, for all of the used catalysts, MeOH was the main product in both feed molar ratio. In fact, by tuning the contact time in order to avoid back reaction, the kinetic favored MeOH production (6 e⁻) compared to the EtOH production (12 e⁻) as shown in equations 12 and 14 as before mentioned in the Chapter 1 (below reported), being in this case the thermodynamic effect negligible.



These evidences are confirmed in the total carbon converted values shown in Figure 83. In detail, the performance to transform CO₂ by using C₃N₄-TiO₂ Nafion membrane was higher than C₃N₄ Nafion membrane at all the feed molar ratios and at fixed pressure and contact time. As reported in literature, generally the heterojunction formation between two semiconductors improves the capability of CO₂ photoreduction. The potential of the holes photogenerated in the g-C₃N₄ valence band is not enough positive to oxidize water and O₂ (see Eq. 9 of Chapter 1). Notably, in H₂O oxidation semi-reaction also H⁺ ions are formed that are required in the CO₂ reduction. The limitation of C₃N₄ valence band

energy²²¹ generates lower amounts of H⁺, and through these, lower yield for all of the products was achieved. The introduction of TiO₂ in the heterojunction C₃N₄-TiO₂, improved the water oxidation^{219, 221} power due to the more positive potential of holes generated in the valence band of TiO₂⁹⁰ (ca. E⁰_{vsSHE} = +2.7 V) with respect to those generated in C₃N₄ (ca. E⁰_{vsSHE} = +1.2 V) (see Figure 13 in Chapter 1).

Again, as previously mentioned, increasing the H₂O/CO₂ feed molar ratio results in higher amount of carbon converted, reaching the highest value of ca. 60 μmol g⁻¹ h⁻¹ by using the C₃N₄-TiO₂ Nafion membrane at molar ratio equal to 5. This value was at least 60 time higher than the carbon converted achieved in the batch test by using the C₃N₄-TiO₂ powder (Figure 83). Even in the worst conditions (0.5 feed molar ratio), the carbon converted in the membrane reactor in the presence of C₃N₄-TiO₂ Nafion membrane was at least 10 times more with respect to the carbon converted values obtained in the batch reactor.

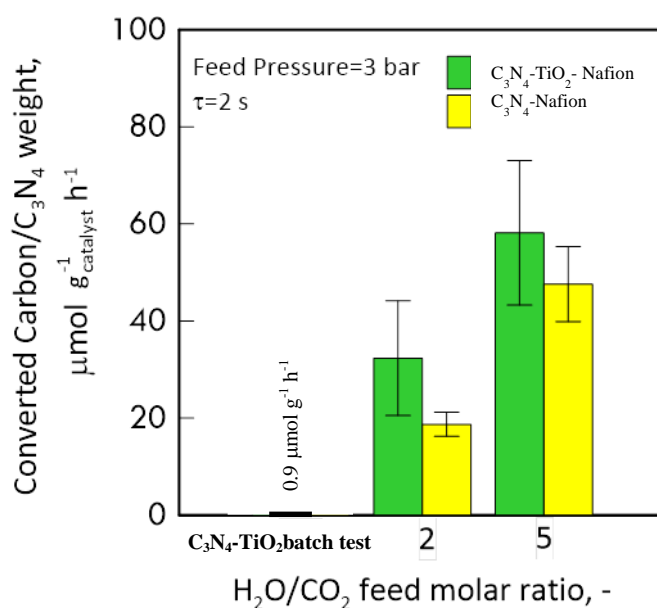


Figure 83. Comparison of converted Carbon/catalyst weight of the various species formed in batch reactor by using C₃N₄-TiO₂ photocatalyst and the photocatalytic membrane as a function of H₂O/CO₂ feed molar ratio.

To evaluate the reaction pressure effect on the photoreduction of CO₂ in the membrane reactor, the C₃N₄-TiO₂ loaded Nafion membrane was tested at reaction pressure of 5 bar.

Figure 84 shows the formed compounds flow rate in the best conditions of fixed feed molar ratio and contact time of 5 and 2 s, respectively at two different feed pressure (3 and 5 bar). The experiment carried out at a feed pressure of 3 bar gave ca. 45, 5 and 6 $\mu\text{mol g}^{-1} \text{h}^{-1}$ of MeOH, EtOH and HCHO, respectively, reaching a carbon converted value of ca. 61 $\mu\text{mol g}^{-1} \text{h}^{-1}$. When the feed pressure increased to 5 bar, the alcohol production decreased, in particular the MeOH fell to 33 $\mu\text{mol g}^{-1} \text{h}^{-1}$ and no EtOH was produced. On the contrary, when the reaction pressure shifted from 3 to 5, the HCHO raised up from 6 to 28 $\mu\text{mol g}^{-1} \text{h}^{-1}$. These results are probably due to the pressure effect on the removal of the photoproducts due to the CO_2 reduction occurring. The higher pressure could reduce the desorption of O_2 photoproducted so that oxygen is available to initiate back reactions of alcohol either photoproducted to HCHO.

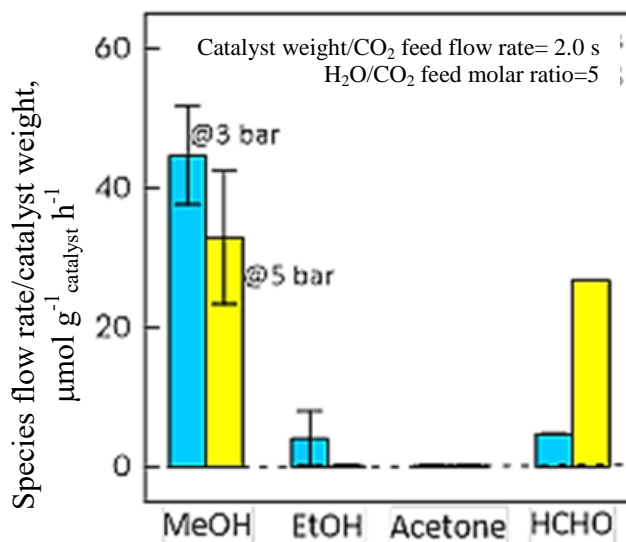


Figure 84. Flow rate/catalyst weight of the various species formed at 3 and 5 bar.

This hypothesis is confirmed by the fact that the carbon converted value obtained at the two reaction pressures did not change (see Table 22). Therefore, the pressure does not influence the photoreduction capability of the photocatalytic membrane but affects the products distribution.

Table 22. Carbon converted at contact time and molar ratio equal to 2s and 5, respectively at 3 and 5 bar as feed pressure by using the $\text{C}_3\text{N}_4\text{-TiO}_2$ loaded Nafion membrane.

Carbon converted, $\mu\text{mol g}^{-1} \text{h}^{-1}$	
at reaction pressure of 3 bar	at reaction pressure of 5 bar
61	61

Figure 85 shows the selectivity values towards the species formed versus the two reaction pressures investigated of 3 and 5 bar. These results highlighted that at a lower reaction pressure the MeOH is the favored product reaching more than 80% of selectivity.

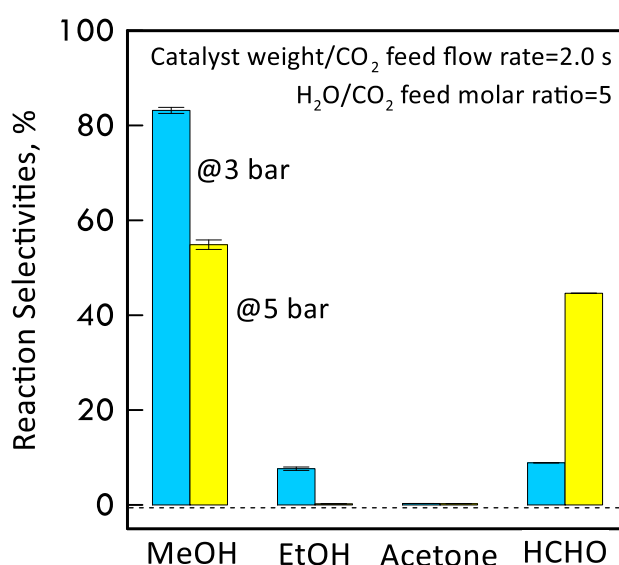


Figure 85. Reaction selectivity of the various species formed at 3 and 5 bar.

Summarizing, the best parameter for both membranes to convert CO₂ to MeOH were lower contact time, higher molar ratio and feed pressure of 3 bar. Figure 86 compares the MeOH selectivity and production rate of the photocatalytic membrane discussed in this dissertation and the results reported from Sellaro et al.²⁶⁸ which investigated the same reaction under the same experimental conditions (feed molar ratio, feed pressure and contact time) but in the presence of a membrane loaded with bare TiO₂. In this last case methanol was the only product detected.

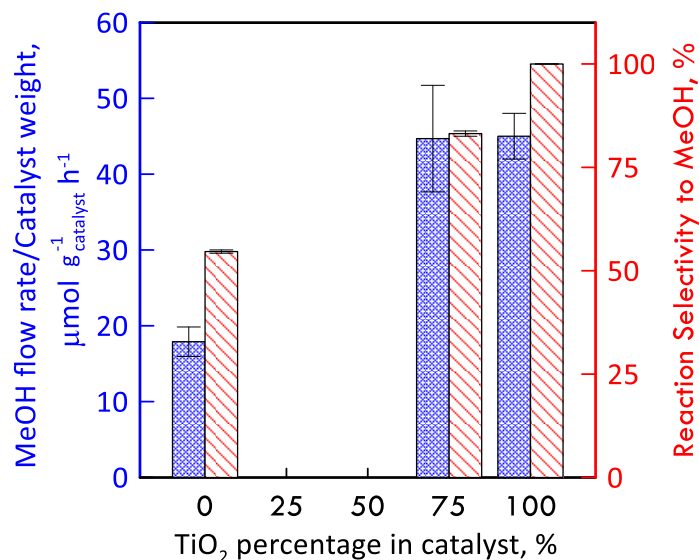


Figure 86. MeOH flow rate per gram of catalyst and relative selectivity as a function of TiO₂ content by comparing literature data.²⁶⁸

In the presence of C₃N₄-TiO₂, the MeOH production rate increased more than two times when the TiO₂ content in the photocatalytic membrane increased from 0% to 75%. Also the selectivity toward MeOH production followed the same trend. When the TiO₂ content raised up to 100%, so without C₃N₄, the MeOH production did not change but the selectivity toward MeOH increased from 80% to 100%. These results suggest that the C₃N₄-TiO₂ composite loaded Nafion membrane was more performant in terms of carbon converted with respect to C₃N₄ and TiO₂ Nafion membranes with a little loss in terms of selectivity towards MeOH with respect to the case of TiO₂ loaded membranes.

3.5.5 Conclusion

For the first time the photocatalytic C₃N₄-TiO₂ loaded Nafion membrane was prepared and used to photocatalytic CO₂ conversion in a continuous photocatalytic reactor irradiated by UV-Vis light. The effects of H₂O/CO₂ feed molar ratio, feed pressure and contact time on species production, reaction selectivity and converted carbon were investigated.

Total converted carbon per gram of catalyst varied between 5 and 61 μmol g_{catalyst}⁻¹ h⁻¹, with the latter value obtained at an H₂O/CO₂ feed molar ratio of 5, 3 bar as feed pressure and 2 s as contact time with MeOH as prevailing product. The membrane

reactor converted at least 10 times more carbon in the worst condition setting than the batch system, as a result of the better dispersion of catalyst which is embedded in the Nafion matrix.

Overall alcohols production was promoted by a low contact time and pressure as a result of the fast removal of the reaction mixture from the reaction volume exposed to UV light and, thus, with less promotion of oxidation and/or secondary reactions. On the contrary, the slow removal caused a partial oxidation of MeOH and EtOH, favouring HCHO production.

By comparing the results obtained in this dissertation with those reported in literature value, the C_3N_4 - TiO_2 Nafion membrane is more efficient in terms of carbon converted than TiO_2 /Nafion membrane. A relationship between the MeOH production and selectivity versus the TiO_2 content in the photocatalyst loaded in polymeric matrix was found.

Conclusions

In the present thesis, promising materials were investigated considering the relationship between physico-chemical features, reactor type, reactor set-up to activity for CO₂ photoreduction by using water as reductant agent.

With the aim to increase the CO₂ photoreduction efficiency were adopted the following different strategies: (i) TiO₂, ZrO₂ based materials were obtained by modifying the bare semiconductors by means of metal and non-metal doping or by coupling them with opportune graphitic materials (such as graphene or graphitic C₃N₄), and (ii) the design of the photocatalytic set-up and the operating parameters influencing the reaction efficiency were tailored by using continuous photocatalytic membrane reactors and different feed molar ratio, residence times and feed pressure.

In particular, the bare semiconductors TiO₂, ZrO₂, and C₃N₄ were obtained by introduction of graphitic materials as C₃N₄ or graphene in TiO₂ composites, or Ce and Er doping in ZrO₂ structure, or again by oxygen doping on C₃N₄.

These materials tested in batch reactors by using water as the reductant showed capability for CO₂ photoreduction. In all the tests, CO₂ photoreduction occurs giving CH₄ and CO or alcohol and acetaldehyde as the main products as a function of catalyst and experimental conditions operated.

The best powder photo-capability in batch reactors was obtained by using 1% G/TiO₂ and 0.5% Er/ZrO₂ materials, giving ca. 44 and 88 μmol g⁻¹ of carbon converted after 6 h of irradiation time, respectively. In the first case, the major products obtained during the CO₂ photoreduction was methane whilst in the second case were ethanol and acetaldehyde.

Also flat sheet photocatalytic C₃N₄ and C₃N₄-TiO₂ Nafion membranes were prepared and tested for CO₂ reduction in a continuous photocatalytic membrane reactor using water as reductant.

Alcohol and formaldehyde were found as the main products and their relative amounts were a function of photocatalytic membrane type and experimental

conditions operated such as the feed H₂O/CO₂ molar ratio, contact time and the reaction pressure.

In all experimental conditions and by using both membrane (C₃N₄ and C₃N₄-TiO₂ membrane) the continuous photocatalytic membrane reactor showed a higher photo-capability for CO₂ reduction with respect to all of the batch results obtained. To convert CO₂ the best parameters were found at the highest feed H₂O/CO₂ molar ratio of 5 and at the smallest contact time (2 s) and reaction pressure (3 bar) for both photocatalytic membrane. In these favourite conditions, furthermore a trend was found between the methanol production/selectivity with the TiO₂ content in the photocatalyst loaded Nafion membrane. The best performance was reached by using the C₃N₄-TiO₂ Nafion membrane obtaining ca. 61 μmol g⁻¹ h⁻¹ of carbon converted with a methanol production equal to ca. 45 μmol g⁻¹ h⁻¹ (ca. 80 % selectivity).

This *Ph.D* dissertation provided (i) an interesting structural study of C₃N₄ before and after use in the CO₂ photoreduction tests, (ii) a remarkable study of catalyst photoactivity by using oxide and graphitic material in batch reaction, (iii) a promising route for the optimisation of the photocatalytic continuous membrane reactor in terms of feed molar ratio, residence time and reaction pressure.

Appendix A. Publications

PUBBLICAZIONI

1. ZrO₂ Based materials as photocatalysts for 2-propanol oxidation by using UV and solar light irradiation and tests for CO₂ reduction. E. I. García-López, G. Marcì, F. R. Pomilla, M. C. Paganini, C. Gionco, E. Giamello, L. Palmisano. *Catalysis Today*, **2018**, 313, 100-105
2. CO₂ to Liquid Fuels: Photocatalytic Conversion in a Continuous Membrane Reactor. F. R. Pomilla, A. Brunetti, G. Marcì, E. I. García-López, E. Fontananova, L. Palmisano, G. Barbieri. *ACS Sustainable Chemistry and Engineering*, **2018**, 6(7), 8743-8753
3. Photocatalytic CO₂ valorization by using TiO₂, ZrO₂ and graphitic based semiconductors. F. R. Pomilla, R. Molinari, G. Marcì, E.I. Garcia-Lopez and L. Palmisano. *Research and Technologies for Society and Industry (IEEE-RTSI)*, ISBN: CFP18C29-ART, Part Number: 978-1-5386-6286-3, **2018**, 478- 483.
4. Graphitic C₃N₄ physical changes following photocatalytic tests in the presence of CO₂ and water. F. R. Pomilla, M. A. L. R. M. Cortes, J. W. J. Hamilton, R. Molinari, G. Barbieri, G. Marcì, L. Palmisano, P. K. Sharma, A. Brown, J. A. Byrne. *Journal of Physical Chemistry C*, **2018**, 122, 28727-28738
5. CO₂ valorisation by using a C₃N₄/TiO₂ Nafion membrane in a photocatalytic membrane reactor: optimisation parameters. *In preparation*.

COMUNICAZIONI A CONGRESSI INTERNAZIONALI

1. ORALE: Photocatalytic CO₂ valorization by using TiO₂, ZrO₂ and graphitic based semiconductors. F. R. Pomilla, R. Molinari, G. Marcì, E.I. Garcia-Lopez and L. Palmisano. Research and Technologies for Society and Industry (RTSI), ISBN: CFP18C29-ART, Part Number: 978-1-5386-6286-3, from pag. 478 to pag. 483, **2018**. 4° International Forum EEI, RTSI, section Nanomaterials for 4.0, 10-13 September **2018**, Scuola Politecnica of University of Palermo, Palermo, Italy.
2. CO₂ reduction in photocatalytic membrane reactor: products selectivity study. F.R: Pomilla, A. Brunetti, G. Marcì, E. I. Garcia-Lopez, E. Fontananova, L. Palmisano, G. Barbieri. European meeting on Solar Chemistry and Photocatalysis: Environmental Applications (SPEA) 10, Almeria, Spain, 4-8 June **2018**. (P15)
3. ZrO₂ base materials: preparation, characterization and photocatalytic activity for 2-propanol oxidation and CO₂ reduction. E. I. Garcia-Lopez, G. Marci, F. R. Pomilla, M. C. Paganini, C. Gionco, E. Giamello and L. Palmisano. 5th European Conference Environmental Applications of Advanced Oxidation Processes- EAAOP5, 25-29th June **2017**, Prague, Czech Republic.
4. Photocatalytic membrane reactor for CO₂ conversion, F. R. Pomilla, A. Brunetti, G. Marcì, E. Fontananova, L. Palmisano and G. Barbieri, CO₂ Summit III: Pathways to Carbon Capture, Utilization, and Storage Deployment ECI Cetraro (CS), Italy , May 22-26, **2017**
5. CO₂ conversion in continuous photocatalytic membrane reactor, F.R. Pomilla , A. Brunetti, G. Marcì, E. Fontananova, E. I. Garcia-Lòpez, L. Palmisano and G. Barbieri. 10th Korea-Italy workshop on the “Membrane Technology for Climate Change”, page 91, Didimol Plaza KRICT, Daejeon, Republic of Korea, **2017**

COMUNICAZIONI A CONGRESSI NAZIONALI

(INVITED, ORAL O POSTERS)

- I. Foto-reattori a membrana per la valorizzazione del CO₂. F. R. Pomilla, A. Brunetti, G. Marcì, E. I. Garcìa –Lopez, E. Fontananova, G. Marcì, L. Palmisano and G. Barbieri. Congresso Società Chimica Italiana congiunto delle sezioni Sicilia e Calabria, Palermo, Italy, 01-02 Marzo **2019**, Oral presentation
- II. Photocatalytic membranes for CO₂ reduction, F. R. Pomilla, A. Brunetti, E. Fontananova, G. Marcì, L. Palmisano and G. Barbieri. Seminar Day, CNR-ITM, Arcavacata di Rende (CS), Italy, 01 December **2016**, Oral presentation

Periodo all'estero.

Periodo di sei mesi all'estero presso i laboratori del NIBEC dell'Università della Ulster, Jordanstown, Belfast sotto la supervisione del prof John Anthony Byrne.

Partecipazioni a progetti all'estero.

Partecipazione, dal 19/09/2016 al 06/10/2016, ad un progetto internazionale dal titolo " Innovative Oxide materials for the solar Photocatalytic degradation" (IOSPEP) all'interno del progetto SFERA nella Piattaforma Solare di Almeria.

Appendix B. Training *Ph.D* school activity

Attività didattica

ELENCO DEI SEMINARI SEGUITI

- 1) 8/02/2016 (tramite videoconferenza) ore 15:00-16:00 The LCH, Dark Matter and beyond by professor Tomer Volansky of Tel Aviv University (<https://physics.tau.ac.il/>), 16:30-17:30 Dark Matter from cosmological observations and connection with the searches at colliders by professor Pasquale Serpico of LAPTH-CNRS (<https://lapth.cnrs.fr/>)
- 2) 18/05/2016, (ore 10:00-13:30) in Aula Magna dell'Università delle Calabria. Convegno "L'affascinante fisica del neutrino e l'evoluzione cosmica" promosso dal Prof. Marco Schioppa.
- 3) 18/05/2016, (ore 14:00 – 17:30) Aula Caldora – Università della Calabria. “Approccio sostenibile al recupero delle strutture esistenti”
- 4) Giovedì 19 (ore 15:00-18:30) e Venerdì 20 (ore 9:00-17:00) Maggio 2016 Aula Magna dell'Università della Calabria. "Pianeta Acqua - La qualità della risorsa idrica in Calabria: stato dell'arte e prospettive".
- 5) 07/06/2016 (ore 15:30), Cubo 15B aula E, dell'Università della Calabria, tenuta dal professore Salvator Dominguez-Bella dal titolo “Roman raw materials in the Hispania Baetica, the case of the maritime baths mosaic in Baelo Claudia, Cadiz, Spain.”
- 6) 08/06/2016 (ore 9:00), Cubo 15B aula E, dell'Università della Calabria, tenuta dal professore Salvator Dominguez-Bella dal titolo “Archeometric research applications of the mXRF. Same examples in the South Spain.”
- 7) 27 /06/ 2016 (Ore 15:30 - 18:30), Aula PT3, Cubo 45 B, Piano Terra, dell'Università della Calabria, dal titolo "In-situ π -Anchor for Delaying Debonding of U-wrap FRP in Shear Strengthened RC Beams".

- 8) Mercoledì 29 giugno 2016, ore 15:30, Aula Magna DiBEST, III piano, cubo 15b, dell'Università della Calabria, tenuto dal Prof. Josè Arribas, dal titolo "Identification of diagenetic aspects in sandstones: examples and practices".
- 9) 28-03-2017, Seminario "Intuvo Roadshow", Responsabile Nicola Cimino, Agilent Technologies Italia, Arcavacata di Rende, Università degli studi della Calabria. 8 ore
- 10) 05/06/2018. Seminario su analisi topografiche dei materiali. Responsabile: Prof.ssa Monica Santamaria. Università degli Studi di Palermo, Dipartimento DICAM, Viale delle Scienze. 8 ore
- 11) 04/04/2018. Seminario dal titolo "Inside the review process". Responsabile: Prof. Davide Ravasi, Università degli Studi di Palermo, aula Capitò, ed. 7, Viale delle Scienze. 10 ore

ATTIVITA' FORMATIVE GENERALI EFFETTUATE

- 1) Scienza e tecnologia delle membrane – Preparazione di membrane. ITM-CNR 19-22/04/2016. Docenti: L. Giorno, A. Figoli, A. Gugliuzza (4CFU).
- 2) Analytical techniques for environmental studies. 24, 26 Maggio - 7,13,14 Giugno 2016 presso le aule e i laboratori dei cubo 15A /B e 14 A /B. Docenti: Donatella Barca, Paola Donato, Fabio Scarciglia (4CFU).
- 3) Scienza e tecnologia delle membrane – Applicazione di membrane. ITM-CNR 9,14,15,16 Giugno 2016. Docenti: E. Drioli, A. Criscuoli, G. Di Profio, G. Barbieri (4CFU).
- 4) Writing a scientific paper: Guidelines and Tips. Docente: Alessio Caravella (4 CFU). 27/06-01/07 2016.
- 5) Scienza e tecnologia delle membrane – Caratterizzazione di membrane. ITM-CNR 01-07/07/2016. Docenti: A. Figoli, A. Gugliuzza (4CFU)
- 6) Corsi LIO presso il Laison Office dell'Università della Calabria. (4 CFU)

- 7) Corso di “Calcolo scientifico”, Responsabile Prof. Pantano, Università degli studi della Calabria. Dal 13/03 al 22/05/2017. (4 CFU)
- 8) Corso di “Materiali per la catalisi eterogenea”. Responsabile Prof. Giuseppe Marci, Università degli studi di Palermo. Dal 26-09 al 15-12-2017. (6CFU)
- 9) Corso: Corso: English for everyday life. Responsabile: Prof. Deborah Cully. Ulster University, Jordanstown, Belfast, Northern Ireland. Da Agosto a Dicembre 2017. 1 semestre.
- 10) Corso: Academic writing. Responsabile: Prof. Deborah Cully. Ulster University, Jordanstown, Belfast, Northern Ireland. Da Agosto a Dicembre 2017. 1 semestre.

Acknowledgements

The completion of this doctoral dissertation was possible with the support of several people. I would like to express my sincere gratitude to all of them.

First of all, I am extremely grateful to my research guides, professor Giuseppe Marcì, engineer Giuseppe Barbieri and professor Raffaele Molinari for their valuable guidance, scholar inputs and consistent encouragement. They have always made himself available to clarify my doubts despite their busy schedules. It has been a great opportunity to do my doctoral programme under their guidance and to learn from their research expertise.

I am also grateful to Adele Brunetti for her trust and encouragement that supported me in this research, especially for sharing her expertise so willingly. I miss our morning coffee!

This work was possible also thanks to the unconditioned support provided by professor Leonardo Palmisano and professor Elisa Isabel García Lòpez. Their professional, amicable and positive disposition helped me in many occasions.

Professor Monica Santamaria and her research group, and Dr. Bartolo Megna are kindly acknowledged for XRD and Raman analysis, respectively.

A special mention to Tony Byrne and Jeremy Hamilton and to their research group in general. It was fantastic to have the opportunity to work in your facilities. What a cracking place to work!

A lot of people have been very close to me and facilitated my staying in Cosenza, in particular I am grateful to Leonardo for his support and sincere friendship and to his family for having adopted me as a daughter. Thanks also to Francesca that offered me her funny and generous friendship.

Very special thanks to Samira, Dili, Bruno, Darragh, Stergos and Sophia for the amazing moments during my staying in Belfast. Thanks especially to Maria Ana for her sincere friendship.

Thanks to all of my best friends that I keep with me over the distances, in particular thanks to Alessia and Andrea for precious time and support they provided in many occasions. Unforgettable, the best skype calls in my life.

I am indebted to my family for their daily sacrifices and love which allowed me to reach this goal, and to my Bruno, who supported me in every possible way, every time close to me and on my side.

And finally, last but not least, to my colleague and friend Francesco Rita. It was great sharing laboratory, difficulties, happiness and goals with you during these years. The thesis would not have come to successful completion, without his support.

I also gratefully acknowledge the “SIACE” Ph.D. Course at the University of Calabria and the Institute for Membrane Technology - Council National Research (ITM-CNR) of Cosenza (Italy) for financial support.

Index Figure

Figure 1. Global temperature and CO ₂ atmosphere concentration (ppm) trend from 1880 to 2016. ²	20
Figure 2. Average emissions per capita from 1960 to 2012. ³	22
Figure 3. (a)Anthropogenic sources of Carbon dioxide and (b) Carbon dioxide emissions from fossil fuel combustion.	22
Figure 4. The main reaction/process type from CO ₂ transformation to obtain high added value compounds. ^{7,8}	25
Figure 5. Modes of bonding of carbon dioxide with transition metal.	26
Figure 6. Schematic illustration of the three major categories of electrocatalysts for CO ₂ reduction. ⁵⁸	28
Figure 7.Simplified scheme of natural photosynthesis process by plant.	31
Figure 8. Schematic key processes representation of a photocatalytic reaction at level of a semiconductor particle.	33
Figure 9. Catalytic and photocatalytic simplified mechanisms.	34
Figure 10. Schematic presentation of principal catalyst modifications.	36
Figure 11. Separation charges in the different types of heterojunctions as reported from Li et al. ⁹³	38
Figure 12. Z scheme representation.	39
Figure 13. Potentials for various redox couples in water (pH 7) and the band-edge positions of semiconductor photocatalysts reported by Kou et al. ⁸⁸	42
Figure 14. Different reaction mechanisms in liquid and gas phase reported from Olivo et al. ¹⁰⁶	44
Figure 15. Band positions and potential applications of some typical photocatalysts at pH = 7 in aqueous solutions, reported from Li et al. ¹⁷³	51
Figure 16.The redox potentials of the relevant products of CO ₂ reduction with respect to the estimated position of the g-C ₃ N ₄ conduction and valence band edges (CB and CV) at pH 7. ¹⁹³	54
Figure 17. Schematic g-C ₃ N ₄ synthesis by three different precursors, reported by Ong et al. ¹⁸⁹	54
Figure 18. Thermal synthesis to obtain pure and non-metal doped g-C ₃ N ₄ , reported by Ong et al. ¹⁸⁹	56

Figure 19. Melem structure repeated in the polymeric C ₃ N ₄ with the corresponding atomic assignment according to XPS analysis as Dante et al. report. ²⁰³	57
Figure 20. Diameter range of tubular membranes.	64
Figure 21. Simplified scheme of symmetric and asymmetric membrane ²⁴⁴	66
Figure 22. Permeation through a membrane of liquids or gases where ΔC , ΔP , ΔE are the concentration, pressure and electrochemical gradient, respectively.	67
Figure 23. Membrane production methods and application fields of the obtained membranes.	68
Figure 24. Chemical structure of Nafion polymer.	69
Figure 25. Module arrangements: two types of single pass (a and b) and recirculation mode.	70
Figure 26. Photocatalytic apparatus consisting by Solar Box and glass batch reactor equipped with GC TCD-FID instruments.	85
Figure 27. XRD patterns of the prepared samples. Ce doped (A) and Er doped (B) ZrO ₂ samples, along with the pristine ZrO ₂ . (A): ZrO ₂ (a); 0.5%Ce/ZrO ₂ (b) and 10%Ce/ZrO ₂ (c) and (B): ZrO ₂ (a); 0.5%Er/ZrO ₂ (b) and 10%Er/ZrO ₂ (c). ¹⁴⁵	86
Figure 28. Raman spectra of the samples: ZrO ₂ (a); 0.5% Ce/ZrO ₂ (b) and 10% Ce/ZrO ₂ (c). ¹⁴⁵	87
Figure 29. Raman spectra of the samples: ZrO ₂ (a); 0.5% Er/ZrO ₂ (b) and 10% Er/ZrO ₂ (c). ¹⁴⁵	89
Figure 30. Absorbance spectra of the samples obtained by applying the Kubelka-Munk function, $F(R_{\infty})$, to the diffuse reflectance spectra. (A): ZrO ₂ (a), 0.5% Ce/ZrO ₂ (b), 10% CeZrO ₂ (c) and (B): ZrO ₂ (a), 0.5% Er/ZrO ₂ (b), and 10% Er/ZrO ₂ (c) The inset is a magnification of the squared region. ¹⁴⁵	90
Figure 31. Photoluminescence spectra of (A): ZrO ₂ (a); 0.5% Ce/ZrO ₂ (b) and 10% Ce/ZrO ₂ (c) and (B): ZrO ₂ (a); 0.5% Er/ZrO ₂ (b) and 10% Er/ZrO ₂ (c). ¹⁴⁵	91
Figure 32. EPR spectra recorded at liquid nitrogen temperature for the Ce/ZrO ₂ (A) samples: (a) 0.5% Ce/ZrO ₂ before irradiation; (b) 0.5% Ce/ZrO ₂ after irradiation; (c) 10% Ce/ZrO ₂ before irradiation; (b) 10% Ce/ZrO ₂ after irradiation and Er/ZrO ₂ (B) samples: (a) 0.5% Er/ZrO ₂ before irradiation; (b) 0.5% Er/ZrO ₂ after irradiation; (c) 10% Er/ZrO ₂ before irradiation; (d) 10% Er/ZrO ₂ after irradiation. Irradiation time: 15 min. ¹⁴⁵	93

Figure 33. Photogenerated products versus irradiation time in the presence of ZrO ₂ catalyst, CO ₂ and H ₂ O.	94
Figure 34. Photocatalytic reactivity (in terms of $\mu\text{mol g}^{-1}$) towards CO ₂ reduction after 6 hours of irradiation time obtained with the following catalysts ZrO ₂ , 0.5% Er/ZrO ₂ , 10% Er/ZrO ₂ , 0.5% Ce/ZrO ₂ and 10% Ce/ZrO ₂ coloured green, yellow, blue, red and grey, respectively.	95
Figure 35. Carbon converted obtained after 6 hour of irradiation time with the following catalyst ZrO ₂ , 0.5% Er/ZrO ₂ , 10% Er/ZrO ₂ , 0.5% Ce/ZrO ₂ and 10% Ce/ZrO ₂	97
Figure 36. CO ₂ adsorption on defective (a) and perfect (b) ZrO ₂ surface.	98
Figure 37. FTIR spectra recorded from 400 to 4000 cm^{-1} of pure graphene oxide (black) and G/TiO ₂ composites at different graphene loading. The vertical black dashed and full black lines indicate the graphene oxide (GO) and graphene (G) characteristic peaks, respectively.	101
Figure 38. Raman spectra analysis of G/TiO ₂ composites, pure GO and TiO ₂ by using a laser at 532 nm. The TiO ₂ Raman spectrum is shown in the inset (dashed line).	102
Figure 39. Microscopy images of a) GO, b) 0.5% G/TiO ₂ , and c) 3% G/TiO ₂ samples.	103
Figure 40. Diffuse Reflectance spectra recorded for all G/TiO ₂ composites.	104
Figure 41. Methane photo-generated versus irradiation time in the presence of G/TiO ₂ composites.	106
Figure 42. Methanol photo-generated versus irradiation time in the presence of G/TiO ₂ composites.	107
Figure 43. Carbon monoxide photo-generated versus irradiation time in the presence of G/TiO ₂ composites.	107
Figure 44. Acetaldehyde photo-generated versus irradiation time in the presence of G/TiO ₂ composites.	108
Figure 45. Total carbon converted after 6 h of irradiation time in the presence of G/TiO ₂ composites.	109
Figure 46. Selectivity of methane, carbon monoxide, acetaldehyde and methanol photogenerated after 6 h of irradiation in the presence of G/TiO ₂ composites.	109

Figure 47. Batch photoreactor scheme equipped with a mass flow controller and light source reported from Cortes et al. ²⁹⁸ The system is on line connected with a GC-FID/TCD.....	112
Figure 48. Measured irradiance from 100 W Xe lamp with IR filter.	113
Figure 49. FTIR spectra of as synthesized g-C ₃ N ₄ (green line) and O _R -C ₃ N ₄ (black line) showing characteristic g-C ₃ N ₄ fingerprint.	114
Figure 50. XRD patterns of pure g-C ₃ N ₄ and O _R -C ₃ N ₄ as prepared and the peak positions for two phases of g-C ₃ N ₄ reported by Fina et al. ^{191, 306} The name reported heptazine (tri-s-triazine) represents the melem unit.	115
Figure 51. UV-Vis diffuse reflectance spectra of powder of pure g-C ₃ N ₄ (red line) and O _R -C ₃ N ₄ (black line) as prepared samples. The inset shows the Kubelka-Munk function vs photon energy, giving the graphic interpolation a band gap energy value equal to 2.8 and 2.7 eV for g-C ₃ N ₄ and O _R -C ₃ N ₄ , respectively.	116
Figure 52. Concentration of CO versus irradiation time in the presence of CO ₂ using g-C ₃ N ₄ material.	117
Figure 53. CO concentration obtained after 5 h of irradiation time in the presence (RnCO ₂) and in the absence (RnAr) of CO ₂ with g-C ₃ N ₄	117
Figure 54. Amount of CO ₂ released in a batch reactor under irradiation at ambient pressure and N ₂ atmosphere from g-C ₃ N ₄ powder previously cleaned.	118
Figure 55. CO photo-generated in the presence of CO ₂ , before (R2CO ₂) and after cleaning (CO ₂ after cleaning) versus irradiation time with g-C ₃ N ₄ as photocatalyst....	119
Figure 56. Reproducibly test of CO production in the presence of g-C ₃ N ₄ , O _R -C ₃ N ₄ and O _T -C ₃ N ₄ after 5 h of irradiation time in the presence of CO ₂	119
Figure 57. Diffuse FTIR analyses for each sample used and unused.	121
Figure 58. Structure of the repeating heptazine carbon nitride unit with the corresponding atomic assignment according to XPS analysis.....	124
Figure 59. Possible condensation pathway from Melem unit (a) firstly to dimer (b) and then to two different assembling in sheet (c) and linear chains of g-C ₃ N ₄ (d). The chains (d) evolve to g-C ₃ N ₄ zig zag structure (e).....	127
Figure 60. Schematic illustration of N replacement by O in g-C ₃ N ₄ material.....	130
Figure 61. XRD patterns of C ₃ N ₄ (red line) measured for powder and (black line) as reported by Wen et al. ¹⁹³	134

Figure 62. FT-IR spectrum of C ₃ N ₄ powder (red line) and (black line) as reported by Liao et al. ³¹³	134
Figure 63. SEM image of C ₃ N ₄ powder at two different magnitude, at a) 5 μm and at b) 30 μm, respectively.....	135
Figure 64. Kubelka-Munck modified function vs. the energy irradiating the C ₃ N ₄ sample.....	136
Figure 65. Scheme of Photocatalytic membrane reactor setup. ³²⁰	138
Figure 66. a) FT-IR (ATR) spectra of (black line) air-facing and (red line) casting plate-facing membrane surfaces of C ₃ N ₄ -loaded Nafion membrane (in the inset, the blue shift of -SO ₃ -groups in the Nafion owing to the presence of the catalyst). SEM of (b) air-facing (magnification 5kX), (c) casting plate-facing surfaces (5 kX), (d) cross-section (3 kX), (e) detail (15 kX), of cross section of C ₃ N ₄ -loaded Nafion membrane.	141
Figure 67. Membrane cleaning (removal of any residuals potentially present) before reaction. C ₃ N ₄ loaded Nafion membrane (active area and thickness respectively 20.4 cm ² and 65.8 ± 3.7 μm) and bare Nafion membrane (active area and thickness respectively 4.1 cm ² and 81.3 ± 4.3 μm). ³²⁰	143
Figure 68. Flow rate/catalyst weight of the various species formed as a function of H ₂ O/CO ₂ feed molar ratio at a contact time of 2 s.....	144
Figure 69. Flow rate/catalyst weight of the various species formed as a function of H ₂ O/CO ₂ feed molar ratio at a contact time of 9.8 s.....	145
Figure 70. Flow rate/catalyst weight of the various species formed as a function of C ₃ N ₄ weight/CO ₂ feed flow rate at H ₂ O/CO ₂ feed molar ratio equal to 2.	146
Figure 71. Flow rate/catalyst weight of the various species formed as a function of C ₃ N ₄ weight/CO ₂ feed flow rate at H ₂ O/CO ₂ feed molar ratio equal to 5.	147
Figure 72. Reaction selectivity as a function of C ₃ N ₄ weight/CO ₂ feed flow rate (left side) and H ₂ O/CO ₂ feed molar ratio (right side).....	148
Figure 73. Total Converted Carbon as function of H ₂ O/CO ₂ feed molar ratio and contact time.	149
Figure 74. Kubelka-Munck modified function vs. energy for C ₃ N ₄ (dashed red line), TiO ₂ (black line) and C ₃ N ₄ -TiO ₂ (green line) samples. The C ₃ N ₄ -TiO ₂ band gap energy is reported in the inset.....	155

Figure 75. FT-IR spectrum of C ₃ N ₄ powder (red line), TiO ₂ (black line) and C ₃ N ₄ -TiO ₂ composite (green line).	157
Figure 76. XRD spectra of TiO ₂ , C ₃ N ₄ and C ₃ N ₄ -TiO ₂ samples.	158
Figure 77. (a) FT-IR (ATR) spectra of (black line) casting plate-facing and (red line) air facing membrane surfaces of C ₃ N ₄ -TiO ₂ loaded Nafion membrane. SEM of (b) air-facing (magnification 2.5 kX), (c) casting plate-facing surfaces (2.5 kX), (d) cross-section (1.5 kX) of C ₃ N ₄ -TiO ₂ /loaded Nafion membrane.	163
Figure 78. Membrane cleaning (removal of any residuals potentially present) before reaction. C ₃ N ₄ -TiO ₂ loaded Nafion membrane (active area and thickness respectively 4.1 cm ² and 65.8 ± 3.7 μm) and bare Nafion membrane (active area and thickness respectively 4.1 cm ² and 78.3 ± 7.8 μm). ³²⁰	164
Figure 79. Flow rate/catalyst weight of the various species formed and carbon converted (histogram) as a function of H ₂ O/CO ₂ feed molar ratio at a contact time of 2 s.	166
Figure 80. Flow rate/catalyst weight of the various species formed and carbon converted (histogram) as a function of H ₂ O/CO ₂ feed molar ratio at a contact time of 3.5 s.	167
Figure 81. Converted carbon per gram of catalyst as a function of contact time at different H ₂ O/CO ₂ feed molar ratio.	168
Figure 82. Comparison of the flow rate/catalyst weight of the various species formed at H ₂ O/CO ₂ feed molar ratio of 2 and 5 for C ₃ N ₄ -TiO ₂ -Nafion and C ₃ N ₄ -Nafion membranes	169
Figure 83. Comparison of converted Carbon/catalyst weight of the various species formed in batch reactor by using C ₃ N ₄ -TiO ₂ photocatalyst and the photocatalytic membrane as a function of H ₂ O/CO ₂ feed molar ratio.	170
Figure 84. Flow rate/catalyst weight of the various species formed at 3 and 5 bar.....	171
Figure 85. Reaction selectivity of the various species formed at 3 and 5 bar.	172
Figure 86. MeOH flow rate per gram of catalyst and relative selectivity as a function of TiO ₂ content by comparing literature data. ²⁶⁶	173

References

1. Anderegg, W. R. L.; Prall, J. W.; Harold, J.; Schneider, S. H., Expert credibility in climate change. *Proceedings of the National Academy of Sciences* **2010**, *107* (27), 12107.
2. Allen, M. R.; Frame, D. J.; Huntingford, C.; Jones, C. D.; Lowe, J. A.; Meinshausen, M.; Meinshausen, N., Warming caused by cumulative carbon emissions towards the trillionth tonne. *Nature* **2009**, *458*, 1163.
3. <http://www.climatecentral.org/gallery/graphics/co2-and-rising-global-temperatures>.
4. Commission, E. Climate Action. https://ec.europa.eu/clima/policies/strategies_en (accessed 28 May 2018, 15:13).
5. Le Quéré, C.; Andres, R. J.; Boden, T.; Conway, T.; Houghton, R. A.; House, J. I.; Marland, G.; Peters, G. P.; van der Werf, G. R.; Ahlström, A.; Andrew, R. M.; Bopp, L.; Canadell, J. G.; Ciais, P.; Doney, S. C.; Enright, C.; Friedlingstein, P.; Huntingford, C.; Jain, A. K.; Jourdain, C.; Kato, E.; Keeling, R. F.; Klein Goldewijk, K.; Levis, S.; Levy, P.; Lomas, M.; Poulter, B.; Raupach, M. R.; Schwinger, J.; Sitch, S.; Stocker, B. D.; Viovy, N.; Zaehle, S.; Zeng, N., The global carbon budget 1959–2011. *Earth Syst. Sci. Data* **2013**, *5* (1), 165-185.
6. Le Quéré, C.; Andrew, R. M.; Friedlingstein, P.; Sitch, S.; Pongratz, J.; Manning, A. C.; Korsbakken, J. I.; Peters, G. P.; Canadell, J. G.; Jackson, R. B.; Boden, T. A.; Tans, P. P.; Andrews, O. D.; Arora, V. K.; Bakker, D. C. E.; Barbero, L.; Becker, M.; Betts, R. A.; Bopp, L.; Chevallier, F.; Chini, L. P.; Ciais, P.; Cosca, C. E.; Cross, J.; Currie, K.; Gasser, T.; Harris, I.; Hauck, J.; Haverd, V.; Houghton, R. A.; Hunt, C. W.; Hurtt, G.; Ilyina, T.; Jain, A. K.; Kato, E.; Kautz, M.; Keeling, R. F.; Klein Goldewijk, K.; Körtzinger, A.; Landschützer, P.; Lefèvre, N.; Lenton, A.; Lienert, S.; Lima, I.; Lombardozzi, D.; Metzl, N.; Millero, F.; Monteiro, P. M. S.; Munro, D. R.; Nabel, J. E. M. S.; Nakaoka, S. I.; Nojiri, Y.; Padin, X. A.; Pregon, A.; Pfeil, B.; Pierrot, D.; Poulter, B.; Rehder, G.; Reimer, J.; Rödenbeck, C.; Schwinger, J.; Séférian, R.; Skjelvan, I.; Stocker, B. D.; Tian, H.; Tilbrook, B.; Tubiello, F. N.; van der Laan-Luijkx, I. T.; van der Werf, G. R.; van Heuven, S.; Viovy, N.; Vuichard, N.; Walker, A. P.; Watson, A. J.; Wiltshire, A. J.; Zaehle, S.; Zhu, D., Global Carbon Budget 2017. *Earth Syst. Sci. Data* **2018**, *10* (1), 405-448.
7. Nakamura, S.; Hatakeyama, M.; Wang, Y.; Ogata, K.; Fujii, K., A Basic Quantum Chemical Review on the Activation of CO₂. In *Advances in CO₂ Capture, Sequestration, and Conversion*, American Chemical Society: 2015; Vol. 1194, pp 123-134.
8. Narayanan, H.; Viswanathan, B.; Yesodharan, S., Photocatalytic Reduction of Carbon Dioxide: Issues and Prospects. *Current Catalysis* **2016**, *5* (2), 79-107.
9. Sakakura, T.; Choi, J.-C.; Yasuda, H., Transformation of Carbon Dioxide. *Chemical Reviews* **2007**, *107* (6), 2365-2387.
10. Chang, X.; Wang, T.; Gong, J., CO₂ photo-reduction: insights into CO₂ activation and reaction on surfaces of photocatalysts. *Energy & Environmental Science* **2016**, *9* (7), 2177-2196.
11. Gibson, D. H., The Organometallic Chemistry of Carbon Dioxide. *Chemical Reviews* **1996**, *96* (6), 2063-2096.

12. Aresta, M., Carbon Dioxide Utilization: Greening Both the Energy and Chemical Industry: An Overview. In *Utilization of Greenhouse Gases*, American Chemical Society: **2003**; Vol. 852, pp 2-39.
13. Boyd, C. L.; Clot, E.; Guiducci, A. E.; Mountford, P., Pendant Arm Functionalized Benzamidinate Titanium Imido Compounds: Experimental and Computational Studies of Their Reactions with CO₂. *Organometallics* **2005**, *24* (10), 2347-2367.
14. McCowan, C. S.; Groy, T. L.; Caudle, M. T., Synthesis, Structure, and Preparative Transamination of Tetrazinc Carbamate Complexes Having the Basic Zinc Carboxylate Structure. *Inorganic Chemistry* **2002**, *41* (5), 1120-1127.
15. Darensbourg, D. J.; Sanchez, K. M.; Reibenspies, J. H.; Rheingold, A. L., Synthesis, structure, and reactivity of zerovalent group 6 metal pentacarbonyl aryl oxide complexes. Reactions with carbon dioxide. *Journal of the American Chemical Society* **1989**, *111* (18), 7094-7103.
16. Tam, E. C. Y.; Johnstone, N. C.; Ferro, L.; Hitchcock, P. B.; Fulton, J. R., Carbon Dioxide Activation by "Non-nucleophilic" Lead Alkoxides. *Inorganic Chemistry* **2009**, *48* (18), 8971-8976.
17. Tsuda, T.; Saegusa, T., Reaction of cupric methoxide and carbon dioxide. *Inorganic Chemistry* **1972**, *11* (10), 2561-2563.
18. Chisholm, M. H.; Cotton, F. A.; Extine, M. W.; Reichert, W. W., The molybdenum-molybdenum triple bond. 4. Insertion reactions of hexakis(alkoxy)dimolybdenum compounds with carbon dioxide and single-crystal x-ray structural characterization of bis(tert-butylcarbonato)tetrakis(tert-butoxy)dimolybdenum. *Journal of the American Chemical Society* **1978**, *100* (6), 1727-1734.
19. Mandal, S. K.; Ho, D. M.; Orchin, M., Reaction of electrophiles with manganese(I) and rhenium(I) alkoxide complexes: reversible absorption of atmospheric carbon dioxide. *Organometallics* **1993**, *12* (5), 1714-1719.
20. Darensbourg, D. J.; Lee, W.-Z.; Phelps, A. L.; Guidry, E., Kinetic Study of the Insertion and Deinsertion of Carbon Dioxide into fac-(CO)₃(dppe)MnOR Derivatives. *Organometallics* **2003**, *22* (26), 5585-5588.
21. Choi, J.-C.; Sakakura, T.; Sako, T., Reaction of Dialkyltin Methoxide with Carbon Dioxide Relevant to the Mechanism of Catalytic Carbonate Synthesis. *Journal of the American Chemical Society* **1999**, *121* (15), 3793-3794.
22. Kim, H. S.; Kim, J. J.; Lee, B. G.; Jung, O. S.; Jang, H. G.; Kang, S. O., Isolation of a Pyridinium Alkoxy Ion Bridged Dimeric Zinc Complex for the Coupling Reactions of CO₂ and Epoxides. *Angewandte Chemie International Edition* **2000**, *39* (22), 4096-4098.
23. Archibald, S. J.; Foxon, S. P.; Freeman, J. D.; Hobson, J. E.; Perutz, R. N.; Walton, P. H., Preparation of cationic cobalt phenoxide and ethoxide complexes and their reversible reaction with carbon dioxide. *Journal of the Chemical Society, Dalton Transactions* **2002**, (14), 2797-2799.
24. Simpson, R. D.; Bergman, R. G., Comparison of the reactivity of (CO)₃L₂ReOR, (CO)₃L₂ReOAr and (CO)₃L₂ReNHAr with carbon dioxide and other electrophiles. *Organometallics* **1992**, *11* (12), 4306-4315.
25. Razuvaev, G. A.; Vyshinskaya, L. I.; Drobotenko, V. V.; Mal'kova, G. Y.; Vyshinsky, N. N., Synthesis and properties of alkylvanadium(III) alkoxides. *Journal of Organometallic Chemistry* **1982**, *239* (2), 335-343.

26. Chisholm, M. H.; Folting, K.; Huffman, J. C.; Tatz, R. J., Quadruple bonds between molybdenum atoms supported by alkoxide ligands. Structural effects and reactivity patterns. *Journal of the American Chemical Society* **1984**, *106* (4), 1153-1154.
27. Parrino, F.; Deiana, C.; Chierotti, M. R.; Martra, G.; Palmisano, L., Formation of dibutyl carbonate and butylcarbamate via CO₂ insertion in titanium(IV) butoxide and reaction with n-butylamine. *Journal of CO₂ Utilization* **2016**, *13*, 90-94.
28. Tomishige, K.; Sakaihorii, T.; Ikeda, Y.; Fujimoto, K., A novel method of direct synthesis of dimethyl carbonate from methanol and carbon dioxide catalyzed by zirconia. *Catalysis Letters* **1999**, *58* (4), 225-229.
29. Wu, X. L.; Xiao, M.; Meng, Y. Z.; Lu, Y. X., Direct synthesis of dimethyl carbonate on H₃PO₄ modified V₂O₅. *Journal of Molecular Catalysis A: Chemical* **2005**, *238* (1), 158-162.
30. Dibenedetto, A.; Pastore, C.; Aresta, M., Direct carboxylation of alcohols to organic carbonates: Comparison of the Group 5 element alkoxides catalytic activity: An insight into the reaction mechanism and its key steps. *Catalysis Today* **2006**, *115* (1), 88-94.
31. Ballivet-Tkatchenko, D.; Jerphagnon, T.; Ligabue, R.; Plasseraud, L.; Poinso, D., The role of distannoxanes in the synthesis of dimethyl carbonate from carbon dioxide. *Applied Catalysis A: General* **2003**, *255* (1), 93-99.
32. Zhao, T.; Han, Y.; Sun, Y., Novel reaction route for dimethyl carbonate synthesis from CO₂ and methanol. *Fuel Processing Technology* **2000**, *62* (2), 187-194.
33. Aresta, M.; Dibenedetto, A.; Pastore, C., Synthesis and Characterization of Nb(OR)₄[OC(O)OR] (R = Me, Et, Allyl) and Their Reaction with the Parent Alcohol To Afford Organic Carbonates. *Inorganic Chemistry* **2003**, *42* (10), 3256-3261.
34. Montini, T.; Monai, M.; Beltram, A.; Romero-Ocaña, I.; Fornasiero, P., H₂ production by photocatalytic reforming of oxygenated compounds using TiO₂-based materials. *Materials Science in Semiconductor Processing* **2016**, *42*, 122-130.
35. Cui, Y.; Zhang, H.; Xu, H.; Li, W., Kinetic study of the catalytic reforming of CH₄ with CO₂ to syngas over Ni/ α -Al₂O₃ catalyst: The effect of temperature on the reforming mechanism. *Applied Catalysis A: General* **2007**, *318*, 79-88.
36. Rostrup-Nielsen, J. R.; Sehested, J.; Nørskov, J. K., Hydrogen and synthesis gas by steam- and CO₂ reforming. In *Advances in Catalysis*, Academic Press: 2002; Vol. 47, pp 65-139.
37. Hershkowitz, F.; Deckman, H. W.; Frederick, J. W.; Fulton, J. W.; Socha, R. F., Pressure Swing Reforming: A novel process to improve cost and efficiency of CO₂ capture in power generation. *Energy Procedia* **2009**, *1* (1), 683-688.
38. Pakhare, D.; Spivey, J., A review of dry (CO₂) reforming of methane over noble metal catalysts. *Chemical Society Reviews* **2014**, *43* (22), 7813-7837.
39. Chawl, S. K.; George, M.; Patel, F.; Patel, S., Production of Synthesis Gas by Carbon Dioxide Reforming of Methane over Nickel based and Perovskite Catalysts. *Procedia Engineering* **2013**, *51*, 461-466.
40. Barbieri, G.; Marigliano, G.; Golemme, G.; Drioli, E., Simulation of CO₂ hydrogenation with CH₃OH removal in a zeolite membrane reactor. *Chemical Engineering Journal* **2002**, *85* (1), 53-59.
41. Appel, A. M.; Bercaw, J. E.; Bocarsly, A. B.; Dobbek, H.; DuBois, D. L.; Dupuis, M.; Ferry, J. G.; Fujita, E.; Hille, R.; Kenis, P. J. A.; Kerfeld, C. A.; Morris, R. H.; Peden, C. H. F.; Portis, A. R.; Ragsdale, S. W.; Rauchfuss, T. B.; Reek, J. N. H.; Seefeldt, L. C.; Thauer, R. K.; Waldrop, G. L., Frontiers, Opportunities, and Challenges

- in Biochemical and Chemical Catalysis of CO₂ Fixation. *Chemical Reviews* **2013**, *113* (8), 6621-6658.
42. Costentin, C.; Robert, M.; Saveant, J.-M., Catalysis of the electrochemical reduction of carbon dioxide. *Chemical Society Reviews* **2013**, *42* (6), 2423-2436.
43. Lu, Q.; Rosen, J.; Jiao, F., Nanostructured Metallic Electrocatalysts for Carbon Dioxide Reduction. *ChemCatChem* **2014**, *7* (1), 38-47.
44. Lu, Q.; Rosen, J.; Zhou, Y.; Hutchings, G. S.; Kimmel, Y. C.; Chen, J. G.; Jiao, F., A selective and efficient electrocatalyst for carbon dioxide reduction. *Nature Communications* **2014**, *5*, 3242.
45. Zhang, X.; Wu, Z.; Zhang, X.; Li, L.; Li, Y.; Xu, H.; Li, X.; Yu, X.; Zhang, Z.; Liang, Y.; Wang, H., Highly selective and active CO₂ reduction electrocatalysts based on cobalt phthalocyanine/carbon nanotube hybrid structures. *Nature Communications* **2017**, *8*, 14675.
46. Rosen, J.; Hutchings, G. S.; Lu, Q.; Rivera, S.; Zhou, Y.; Vlachos, D. G.; Jiao, F., Mechanistic Insights into the Electrochemical Reduction of CO₂ to CO on Nanostructured Ag Surfaces. *ACS Catalysis* **2015**, *5* (7), 4293-4299.
47. Chen, Y.; Kanan, M. W., Tin Oxide Dependence of the CO₂ Reduction Efficiency on Tin Electrodes and Enhanced Activity for Tin/Tin Oxide Thin-Film Catalysis. *Journal of the American Chemical Society* **2012**, *134* (4), 1986-1989.
48. Li, C. W.; Kanan, M. W., CO₂ Reduction at Low Overpotential on Cu Electrodes Resulting from the Reduction of Thick Cu₂O Films. *Journal of the American Chemical Society* **2012**, *134* (17), 7231-7234.
49. Ma, S.; Lan, Y.; Perez Gaby, M. J.; Moniri, S.; Kenis Paul, J. A., Silver Supported on Titania as an Active Catalyst for Electrochemical Carbon Dioxide Reduction. *ChemSusChem* **2014**, *7* (3), 866-874.
50. Hsieh, Y.-C.; Senanayake, S. D.; Zhang, Y.; Xu, W.; Polyansky, D. E., Effect of Chloride Anions on the Synthesis and Enhanced Catalytic Activity of Silver Nanocoral Electrodes for CO₂ Electroreduction. *ACS Catalysis* **2015**, *5* (9), 5349-5356.
51. Min, S.; Yang, X.; Lu, A.-Y.; Tseng, C.-C.; Hedhili, M. N.; Lai, Z.; Li, L.-J.; Huang, K.-W., Surface-reconstructed Cu electrode via a facile electrochemical anodization-reduction process for low overpotential CO₂ reduction. *Journal of Saudi Chemical Society* **2017**, *21* (6), 708-712.
52. Kortlever, R.; Peters, I.; Koper, S.; Koper, M. T. M., Electrochemical CO₂ Reduction to Formic Acid at Low Overpotential and with High Faradaic Efficiency on Carbon-Supported Bimetallic Pd–Pt Nanoparticles. *ACS Catalysis* **2015**, *5* (7), 3916-3923.
53. Rasul, S.; Anjum Dalaver, H.; Jedidi, A.; Minenkov, Y.; Cavallo, L.; Takanebe, K., A Highly Selective Copper–Indium Bimetallic Electrocatalyst for the Electrochemical Reduction of Aqueous CO₂ to CO. *Angewandte Chemie International Edition* **2014**, *54* (7), 2146-2150.
54. Liu, Y.; Chen, S.; Quan, X.; Yu, H., Efficient Electrochemical Reduction of Carbon Dioxide to Acetate on Nitrogen-Doped Nanodiamond. *Journal of the American Chemical Society* **2015**, *137* (36), 11631-11636.
55. Varela Ana, S.; Ranjbar Sahraie, N.; Steinberg, J.; Ju, W.; Oh, H. S.; Strasser, P., Metal-Doped Nitrogenated Carbon as an Efficient Catalyst for Direct CO₂ Electroreduction to CO and Hydrocarbons. *Angewandte Chemie International Edition* **2015**, *54* (37), 10758-10762.

56. Asadi, M.; Kumar, B.; Behranginia, A.; Rosen, B. A.; Baskin, A.; Reprin, N.; Pisasale, D.; Phillips, P.; Zhu, W.; Haasch, R.; Klie, R. F.; Král, P.; Abiade, J.; Salehi-Khojin, A., Robust carbon dioxide reduction on molybdenum disulphide edges. *Nature Communications* **2014**, *5*, 4470.
57. Kumar, B.; Asadi, M.; Pisasale, D.; Sinha-Ray, S.; Rosen, B. A.; Haasch, R.; Abiade, J.; Yarin, A. L.; Salehi-Khojin, A., Renewable and metal-free carbon nanofibre catalysts for carbon dioxide reduction. *Nature Communications* **2013**, *4*, 2819.
58. Nakata, K.; Ozaki, T.; Terashima, C.; Fujishima, A.; Einaga, Y., High-Yield Electrochemical Production of Formaldehyde from CO₂ and Seawater. *Angewandte Chemie International Edition* **2013**, *53* (3), 871-874.
59. Lin, S.; Diercks, C. S.; Zhang, Y.-B.; Kornienko, N.; Nichols, E. M.; Zhao, Y.; Paris, A. R.; Kim, D.; Yang, P.; Yaghi, O. M.; Chang, C. J., Covalent organic frameworks comprising cobalt porphyrins for catalytic CO₂ reduction in water. *Science* **2015**, *349* (6253), 1208.
60. Lu, Q.; Jiao, F., Electrochemical CO₂ reduction: Electrocatalyst, reaction mechanism, and process engineering. *Nano Energy* **2016**, *29*, 439-456.
61. Fuchs, G., Alternative Pathways of Carbon Dioxide Fixation: Insights into the Early Evolution of Life? *Annual Review of Microbiology* **2011**, *65* (1), 631-658.
62. Bassham, J. A.; Benson, A. A.; Calvin, M., THE PATH OF CARBON IN PHOTOSYNTHESIS: VIII. THE RÔLE OF MALIC ACID. *Journal of Biological Chemistry* **1950**, *185* (2), 781-787.
63. Benemann, J. R., CO₂ mitigation with microalgae systems. *Energy Conversion and Management* **1997**, *38*, S475-S479.
64. Usui, N.; Ikenouchi, M., The biological CO₂ fixation and utilization project by RITE(1) — Highly-effective photobioreactor system —. *Energy Conversion and Management* **1997**, *38*, S487-S492.
65. Lee Jun, C.; Kim Jae, H.; Chang Won, S.; Pak, D., Biological conversion of CO₂ to CH₄ using hydrogenotrophic methanogen in a fixed bed reactor. *Journal of Chemical Technology & Biotechnology* **2012**, *87* (6), 844-847.
66. Ma, J.; Sun, N.; Zhang, X.; Zhao, N.; Xiao, F.; Wei, W.; Sun, Y., A short review of catalysis for CO₂ conversion. *Catalysis Today* **2009**, *148* (3), 221-231.
67. Westerhoff, P.; Hu, Q.; Esparza-Soto, M.; Vermaas, W., Growth parameters of microalgae tolerant to high levels of carbon dioxide in batch and continuous-flow photobioreactors. *Environmental Technology* **2010**, *31* (5), 523-532.
68. Kumar, K.; Dasgupta, C. N.; Nayak, B.; Lindblad, P.; Das, D., Development of suitable photobioreactors for CO₂ sequestration addressing global warming using green algae and cyanobacteria. *Bioresource Technology* **2011**, *102* (8), 4945-4953.
69. Chiu, S.-Y.; Kao, C.-Y.; Tsai, M.-T.; Ong, S.-C.; Chen, C.-H.; Lin, C.-S., Lipid accumulation and CO₂ utilization of *Nannochloropsis oculata* in response to CO₂ aeration. *Bioresource Technology* **2009**, *100* (2), 833-838.
70. Adamczyk, M.; Lasek, J.; Skawińska, A., CO₂ Biofixation and Growth Kinetics of *Chlorella vulgaris* and *Nannochloropsis gaditana*. *Applied Biochemistry and Biotechnology* **2016**, *179*, 1248-1261.
71. Cotton, C. A. R.; Douglass, J. S.; De Causmaecker, S.; Brinkert, K.; Cardona, T.; Fantuzzi, A.; Rutherford, A. W.; Murray, J. W., Photosynthetic Constraints on Fuel from Microbes. *Frontiers in Bioengineering and Biotechnology* **2015**, *3*, 36.
72. Singh, S. P.; Singh, P., Effect of CO₂ concentration on algal growth: A review. *Renewable and Sustainable Energy Reviews* **2014**, *38*, 172-179.

73. Hamed, R. B.; Batchelar, E. T.; Clifton, I. J.; Schofield, C. J., Mechanisms and structures of crotonase superfamily enzymes – How nature controls enolate and oxyanion reactivity. *Cellular and Molecular Life Sciences* **2008**, *65* (16), 2507-2527.
74. Knowles, J. R., The Mechanism of Biotin-Dependent Enzymes. *Annual Review of Biochemistry* **1989**, *58* (1), 195-221.
75. Waldrop Grover, L.; Holden Hazel, M.; Maurice Martin, S., The enzymes of biotin dependent CO₂ metabolism: What structures reveal about their reaction mechanisms. *Protein Science* **2012**, *21* (11), 1597-1619.
76. Ciamician, G., THE PHOTOCHEMISTRY OF THE FUTURE. *Science* **1912**, *36* (926), 385.
77. Heindel, N. D.; Pfau, M. A., A profitable partnership: Giacomo Ciamician and Paul Silber. *Journal of Chemical Education* **1965**, *42* (7), 383.
78. Gaya, U. I.; Abdullah, A. H., Heterogeneous photocatalytic degradation of organic contaminants over titanium dioxide: A review of fundamentals, progress and problems. *Journal of Photochemistry and Photobiology C: Photochemistry Reviews* **2008**, *9* (1), 1-12.
79. Izumi, I.; Fan, F.-R. F.; Bard, A. J., Heterogeneous photocatalytic decomposition of benzoic acid and adipic acid on platinized titanium dioxide powder. The photo-Kolbe decarboxylative route to the breakdown of the benzene ring and to the production of butane. *The Journal of Physical Chemistry* **1981**, *85* (3), 218-223.
80. Carp, O.; Huisman, C. L.; Reller, A., Photoinduced reactivity of titanium dioxide. *Progress in Solid State Chemistry* **2004**, *32* (1), 33-177.
81. Fujishima, A.; Honda, K., Electrochemical Photolysis of Water at a Semiconductor Electrode. *Nature* **1972**, *238*, 37.
82. Frank, S. N.; Bard, A. J., Heterogeneous photocatalytic oxidation of cyanide and sulfite in aqueous solutions at semiconductor powders. *The Journal of Physical Chemistry* **1977**, *81* (15), 1484-1488.
83. Parrino, F.; Di Paola, A.; Loddo, V.; Pibiri, I.; Bellardita, M.; Palmisano, L., Photochemical and photocatalytic isomerization of trans-caffeic acid and cyclization of cis-caffeic acid to esculetin. *Applied Catalysis B: Environmental* **2016**, *182*, 347-355.
84. Scandura, G.; Palmisano, G.; Yurdakal, S.; Tek, B. S.; Özcan, L.; Loddo, V.; Augugliaro, V., Selective photooxidation of ortho-substituted benzyl alcohols and the catalytic role of ortho-methoxybenzaldehyde. *Journal of Photochemistry and Photobiology A: Chemistry* **2016**, *328*, 122-128.
85. Herrmann, J.-M., Heterogeneous photocatalysis: fundamentals and applications to the removal of various types of aqueous pollutants. *Catalysis Today* **1999**, *53* (1), 115-129.
86. Palmisano, G.; Albin, A.; Marci, G.; Palmisano, L.; Ravelli, D., CHAPTER 11 New Synthetic Routes in Heterogeneous Photocatalysis. In *Photocatalysis: Applications*, The Royal Society of Chemistry: 2016; pp 303-344.
87. Kraeutler, B.; Bard, A. J., Heterogeneous photocatalytic preparation of supported catalysts. Photodeposition of platinum on titanium dioxide powder and other substrates. *Journal of the American Chemical Society* **1978**, *100* (13), 4317-4318.
88. Palmisano, L.; Loddo, V.; Yurdakal, S., Heterogeneous photocatalysis from fundamentals to possible applications. *Catalysis Today* **2017**, *281*, 1.
89. Bellardita, M.; García-López, E. I.; Marci, G.; Krivtsov, I.; García, J. R.; Palmisano, L., Selective photocatalytic oxidation of aromatic alcohols in water by using P-doped g-C₃N₄. *Applied Catalysis B: Environmental* **2018**, *220*, 222-233.

90. Kou, J.; Lu, C.; Wang, J.; Chen, Y.; Xu, Z.; Varma, R. S., Selectivity Enhancement in Heterogeneous Photocatalytic Transformations. *Chemical Reviews* **2017**, *117* (3), 1445-1514.
91. Rajeshwar, K.; Thomas, A.; Janáky, C., Photocatalytic Activity of Inorganic Semiconductor Surfaces: Myths, Hype, and Reality. *The Journal of Physical Chemistry Letters* **2015**, *6* (1), 139-147.
92. Patrocínio, A. O. T.; Schneider, J.; Franca, M. D.; Santos, L. M.; Caixeta, B. P.; Machado, A. E. H.; Bahnemann, D. W., Charge carrier dynamics and photocatalytic behavior of TiO₂ nanopowders submitted to hydrothermal or conventional heat treatment. *RSC Advances* **2015**, *5* (86), 70536-70545.
93. Wang, J.; Shen, Y.; Li, Y.; Liu, S.; Zhang, Y., Crystallinity Modulation of Layered Carbon Nitride for Enhanced Photocatalytic Activities. *Chemistry (Weinheim an Der Bergstrasse, Germany)* **2016**, *22* (35), 12449-12454.
94. Sun, Z.; Talreja, N.; Tao, H.; Texter, J.; Muhler, M.; Strunk, J.; Chen, J., Catalysis of Carbon Dioxide Photoreduction on Nanosheets: Fundamentals and Challenges. *Angewandte Chemie International Edition* **2017**, *57* (26), 7610-7627.
95. Li, X.; Shen, R.; Ma, S.; Chen, X.; Xie, J., Graphene-based heterojunction photocatalysts. *Applied Surface Science* **2018**, *430*, 53-107.
96. Low, J.; Jiang, C.; Cheng, B.; Wageh, S.; Al-Ghamdi Ahmed, A.; Yu, J., A Review of Direct Z-Scheme Photocatalysts. *Small Methods* **2017**, *1* (5), 1700080.
97. Stolarczyk, J. K.; Bhattacharyya, S.; Polavarapu, L.; Feldmann, J., Challenges and Prospects in Solar Water Splitting and CO₂ Reduction with Inorganic and Hybrid Nanostructures. *ACS Catalysis* **2018**, *8* (4), 3602-3635.
98. Karamian, E.; Sharifnia, S., On the general mechanism of photocatalytic reduction of CO₂. *Journal of CO₂ Utilization* **2016**, *16*, 194-203.
99. Yuan, L.; Xu, Y.-J., Photocatalytic conversion of CO₂ into value-added and renewable fuels. *Applied Surface Science* **2015**, *342*, 154-167.
100. He, H.; Zapol, P.; Curtiss, L. A., Computational screening of dopants for photocatalytic two-electron reduction of CO₂ on anatase (101) surfaces. *Energy & Environmental Science* **2012**, *5* (3), 6196-6205.
101. Strunk, J., 10 - Requirements for efficient metal oxide photocatalysts for CO₂ reduction. In *Metal Oxides in Energy Technologies*, Wu, Y., Ed. Elsevier: 2018; pp 275-301.
102. Tahir, M.; Amin, N. S., Advances in visible light responsive titanium oxide-based photocatalysts for CO₂ conversion to hydrocarbon fuels. *Energy Conversion and Management* **2013**, *76*, 194-214.
103. Kočí, K.; Matějů, K.; Obalová, L.; Krejčíková, S.; Lacný, Z.; Plachá, D.; Čapek, L.; Hospodková, A.; Šolcová, O., Effect of silver doping on the TiO₂ for photocatalytic reduction of CO₂. *Applied Catalysis B: Environmental* **2010**, *96* (3), 239-244.
104. Liu, G.; Hoivik, N.; Wang, K.; Jakobsen, H., Engineering TiO₂ nanomaterials for CO₂ conversion/solar fuels. *Solar Energy Materials and Solar Cells* **2012**, *105*, 53-68.
105. Inoue, T.; Fujishima, A.; Konishi, S.; Honda, K., Photoelectrocatalytic reduction of carbon dioxide in aqueous suspensions of semiconductor powders. *Nature* **1979**, *277*, 637.
106. Benson, E. E.; Kubiak, C. P.; Sathrum, A. J.; Smieja, J. M., Electrocatalytic and homogeneous approaches to conversion of CO₂ to liquid fuels. *Chemical Society Reviews* **2009**, *38* (1), 89-99.

107. Kudo, A.; Miseki, Y., Heterogeneous photocatalyst materials for water splitting. *Chemical Society Reviews* **2009**, *38* (1), 253-278.
108. Olivo, A.; Ghedini, E.; Signoretto, M.; Compagnoni, M.; Rossetti, I., Liquid vs. Gas Phase CO₂ Photoreduction Process: Which Is the Effect of the Reaction Medium? *Energies* **2017**, *10* (9).
109. Tsega, M.; Dejene, F. B., Influence of acidic pH on the formulation of TiO₂ nanocrystalline powders with enhanced photoluminescence property. *Heliyon* **2017**, *3* (2), e00246.
110. Marianna, B.; Agatino Di, P.; Elisa, G.-L.; Vittorio, L.; Giuseppe Marcì and Leonardo, P., Photocatalytic CO₂ Reduction in Gas-Solid Regime in the Presence of Bare, SiO₂ Supported or Cu-Loaded TiO₂ Samples. *Current Organic Chemistry* **2013**, *17* (21), 2440-2448.
111. Bickley, R. I.; Gonzalez-Carreno, T.; Lees, J. S.; Palmisano, L.; Tilley, R. J. D., A structural investigation of titanium dioxide photocatalysts. *Journal of Solid State Chemistry* **1991**, *92* (1), 178-190.
112. Mo, S.-D.; Ching, W. Y., Electronic and optical properties of three phases of titanium dioxide: Rutile, anatase, and brookite. *Physical Review B* **1995**, *51* (19), 13023-13032.
113. Yang, C.-C.; Yu, Y.-H.; van der Linden, B.; Wu, J. C. S.; Mul, G., Artificial Photosynthesis over Crystalline TiO₂-Based Catalysts: Fact or Fiction? *Journal of the American Chemical Society* **2010**, *132* (24), 8398-8406.
114. Mei, B.; Pougin, A.; Strunk, J., Influence of photodeposited gold nanoparticles on the photocatalytic activity of titanate species in the reduction of CO₂ to hydrocarbons. *Journal of Catalysis* **2013**, *306*, 184-189.
115. Pougin, A.; Dilla, M.; Strunk, J., Identification and exclusion of intermediates of photocatalytic CO₂ reduction on TiO₂ under conditions of highest purity. *Physical Chemistry Chemical Physics* **2016**, *18* (16), 10809-10817.
116. Monai, M.; Montini, T.; Fornasiero, P., Brookite: Nothing New under the Sun? *Catalysts* **2017**, *7* (10).
117. Anpo, M.; Yamashita, H.; Ichihashi, Y.; Ehara, S., Photocatalytic reduction of CO₂ with H₂O on various titanium oxide catalysts. *Journal of Electroanalytical Chemistry* **1995**, *396* (1), 21-26.
118. Mizuno, T.; Adachi, K.; Ohta, K.; Saji, A., Effect of CO₂ pressure on photocatalytic reduction of CO₂ using TiO₂ in aqueous solutions. *Journal of Photochemistry and Photobiology A: Chemistry* **1996**, *98* (1), 87-90.
119. Kaneco, S.; Kurimoto, H.; Ohta, K.; Mizuno, T.; Saji, A., Photocatalytic reduction of CO₂ using TiO₂ powders in liquid CO₂ medium. *Journal of Photochemistry and Photobiology A: Chemistry* **1997**, *109* (1), 59-63.
120. Ku, Y.; Lee, W.-H.; Wang, W.-Y., Photocatalytic reduction of carbonate in aqueous solution by UV/TiO₂ process. *Journal of Molecular Catalysis A: Chemical* **2004**, *212* (1), 191-196.
121. Mele, G.; Annese, C.; Accolti, L.; De Riccardis, A.; Fusco, C.; Palmisano, L.; Scarlino, A.; Vasapollo, G., Photoreduction of Carbon Dioxide to Formic Acid in Aqueous Suspension: A Comparison between Phthalocyanine/TiO₂ and Porphyrin/TiO₂ Catalysed Processes. *Molecules* **2015**, *20* (1).
122. Marcì, G.; García-López, E. I.; Palmisano, L., Photocatalytic CO₂ reduction in gas–solid regime in the presence of H₂O by using GaP/TiO₂ composite as photocatalyst under simulated solar light. *Catalysis Communications* **2014**, *53*, 38-41.

123. Qin, S.; Xin, F.; Liu, Y.; Yin, X.; Ma, W., Photocatalytic reduction of CO₂ in methanol to methyl formate over CuO–TiO₂ composite catalysts. *Journal of Colloid and Interface Science* **2011**, *356* (1), 257-261.
124. Abdullah, H.; Khan, M. R.; Pudukudy, M.; Yaakob, Z.; Ismail, N. A., CeO₂-TiO₂ as a visible light active catalyst for the photoreduction of CO₂ to methanol. *Journal of Rare Earths* **2015**, *33* (11), 1155-1161.
125. Xie, T.-f.; Wang, D.-j.; Zhu, L.-j.; Li, T.-j.; Xu, Y.-j., Application of surface photovoltage technique in photocatalysis studies on modified TiO₂ photo-catalysts for photo-reduction of CO₂. *Materials Chemistry and Physics* **2001**, *70* (1), 103-106.
126. Zhao, Z.; Fan, J.; Wang, J.; Li, R., Effect of heating temperature on photocatalytic reduction of CO₂ by N–TiO₂ nanotube catalyst. *Catalysis Communications* **2012**, *21*, 32-37.
127. Luo, D.; Bi, Y.; Kan, W.; Zhang, N.; Hong, S., Copper and cerium co-doped titanium dioxide on catalytic photo reduction of carbon dioxide with water: Experimental and theoretical studies. *Journal of Molecular Structure* **2011**, *994* (1), 325-331.
128. Yan, Y.; Yu, Y.; Cao, C.; Huang, S.; Yang, Y.; Yang, X.; Cao, Y., Enhanced photocatalytic activity of TiO₂-Cu/C with regulation and matching of energy levels by carbon and copper for photoreduction of CO₂ into CH₄. *CrystEngComm* **2016**, *18* (16), 2956-2964.
129. Yang, C.-C.; Vernimmen, J.; Meynen, V.; Cool, P.; Mul, G., Mechanistic study of hydrocarbon formation in photocatalytic CO₂ reduction over Ti-SBA-15. *Journal of Catalysis* **2011**, *284* (1), 1-8.
130. Yamashita, H.; Fujii, Y.; Ichihashi, Y.; Zhang, S. G.; Ikeue, K.; Park, D. R.; Koyano, K.; Tatsumi, T.; Anpo, M., Selective formation of CH₃OH in the photocatalytic reduction of CO₂ with H₂O on titanium oxides highly dispersed within zeolites and mesoporous molecular sieves. *Catalysis Today* **1998**, *45* (1), 221-227.
131. Wang, C.; Thompson, R. L.; Baltrus, J.; Matranga, C., Visible Light Photoreduction of CO₂ Using CdSe/Pt/TiO₂ Heterostructured Catalysts. *The Journal of Physical Chemistry Letters* **2010**, *1* (1), 48-53.
132. Pan, J.; Wu, X.; Wang, L.; Liu, G.; Lu, G. Q.; Cheng, H.-M., Synthesis of anatase TiO₂ rods with dominant reactive {010} facets for the photoreduction of CO₂ to CH₄ and use in dye-sensitized solar cells. *Chemical Communications* **2011**, *47* (29), 8361-8363.
133. Hua Xu and Shuxin Ouyang and Lequan Liu and Defa Wang and Tetsuya Kako and Jinhua, Y., Porous-structured Cu₂O/TiO₂ nanojunction material toward efficient CO₂ photoreduction. *Nanotechnology* **2014**, *25* (16), 165402.
134. Ong, W.-J.; Gui, M. M.; Chai, S.-P.; Mohamed, A. R., Direct growth of carbon nanotubes on Ni/TiO₂ as next generation catalysts for photoreduction of CO₂ to methane by water under visible light irradiation. *RSC Advances* **2013**, *3* (14), 4505-4509.
135. Khataee, A.; Kayan, B.; Gholami, P.; Kalderis, D.; Akay, S.; Dinpazhoh, L., Sonocatalytic degradation of Reactive Yellow 39 using synthesized ZrO₂ nanoparticles on biochar. *Ultrasonics Sonochemistry* **2017**, *39*, 540-549.
136. Sreethawong, T.; Ngamsinlapasathian, S.; Yoshikawa, S., Synthesis of crystalline mesoporous-assembled ZrO₂ nanoparticles via a facile surfactant-aided sol-gel process and their photocatalytic dye degradation activity. *Chemical Engineering Journal* **2013**, *228*, 256-262.

137. Fathima, J. B.; Pugazhendhi, A.; Venis, R., Synthesis and characterization of ZrO₂ nanoparticles-antimicrobial activity and their prospective role in dental care. *Microbial Pathogenesis* **2017**, *110*, 245-251.
138. Heshmatpour, F.; Aghakhanpour, R. B., Synthesis and characterization of nanocrystalline zirconia powder by simple sol-gel method with glucose and fructose as organic additives. *Powder Technology* **2011**, *205* (1), 193-200.
139. Oetzel, C.; Clasen, R., Preparation of zirconia dental crowns via electrophoretic deposition. *Journal of Materials Science* **2006**, *41* (24), 8130-8137.
140. Elshazly, E. S.; El-Hout, S. M.; Ali, M. E.-S., Ytria Tetragonal Zirconia Biomaterials: Kinetic Investigation. *Journal of Materials Science & Technology* **2011**, *27* (4), 332-337.
141. Taghizadeh, M. T.; Vatanparast, M., Ultrasonic-assisted synthesis of ZrO₂ nanoparticles and their application to improve the chemical stability of Nafion membrane in proton exchange membrane (PEM) fuel cells. *Journal of Colloid and Interface Science* **2016**, *483*, 1-10.
142. Jacob, K.-H.; Knozinger, E.; Benier, S., Adsorption sites on polymorphic zirconia. *Journal of Materials Chemistry* **1993**, *3* (6), 651-657.
143. Yamaguchi, T., Application of ZrO₂ as a catalyst and a catalyst support. *Catalysis Today* **1994**, *20* (2), 199-217.
144. Corma, A., Inorganic Solid Acids and Their Use in Acid-Catalyzed Hydrocarbon Reactions. *Chemical Reviews* **1995**, *95* (3), 559-614.
145. Navío, J. A.; Colón, G.; Macías, M.; Sánchez-Soto, P. J.; Augugliaro, V.; Palmisano, L., ZrO₂ · SiO₂ mixed oxides: surface aspects, photophysical properties and photoreactivity for 4-nitrophenol oxidation in aqueous phase. *Journal of Molecular Catalysis A: Chemical* **1996**, *109* (3), 239-248.
146. Basahel, S. N.; Ali, T. T.; Mokhtar, M.; Narasimharao, K., Influence of crystal structure of nanosized ZrO₂ on photocatalytic degradation of methyl orange. *Nanoscale Research Letters* **2015**, *10* (1), 73.
147. García-López, E.; Marcì, G.; Pomilla, F. R.; Paganini, M. C.; Gionco, C.; Giamello, E.; Palmisano, L., ZrO₂ Based materials as photocatalysts for 2-propanol oxidation by using UV and solar light irradiation and tests for CO₂ reduction. *Catalysis Today* **2018**, *313*, 100-105.
148. Sayama, K.; Arakawa, H., Photocatalytic decomposition of water and photocatalytic reduction of carbon dioxide over zirconia catalyst. *The Journal of Physical Chemistry* **1993**, *97* (3), 531-533.
149. Gionco, C.; Paganini, M. C.; Giamello, E.; Burgess, R.; Di Valentin, C.; Pacchioni, G., Paramagnetic Defects in Polycrystalline Zirconia: An EPR and DFT Study. *Chemistry of Materials* **2013**, *25* (11), 2243-2253.
150. Lo, C.-C.; Hung, C.-H.; Yuan, C.-S.; Wu, J.-F., Photoreduction of carbon dioxide with H₂ and H₂O over TiO₂ and ZrO₂ in a circulated photocatalytic reactor. *Solar Energy Materials and Solar Cells* **2007**, *91* (19), 1765-1774.
151. He, D.; Peng, Z.; Gong, W.; Luo, Y.; Zhao, P.; Kong, L., Mechanism of a green graphene oxide reduction with reusable potassium carbonate. *RSC Advances* **2015**, *5* (16), 11966-11972.
152. Park, S.; Ruoff, R. S., Chemical methods for the production of graphenes. *Nature Nanotechnology* **2009**, *4*, 217.
153. Brodie, B. C., Sur le poids atomique du graphite. *Ann. Chim. Phys.* **1860**, *59*, 466-472.

154. Staudenmaier, L., Verfahren zur Darstellung der Graphitsäure. *Berichte der deutschen chemischen Gesellschaft* **1898**, 31 (2), 1481-1487.
155. Hummers, W. S.; Offeman, R. E., Preparation of Graphitic Oxide. *Journal of the American Chemical Society* **1958**, 80 (6), 1339-1339.
156. Ambrosi, A.; Chua, C. K.; Bonanni, A.; Pumera, M., Electrochemistry of Graphene and Related Materials. *Chemical Reviews* **2014**, 114 (14), 7150-7188.
157. Chang, C.-Y.; Ju, S.-P.; Chang, J.-W.; Huang, S.-C.; Yang, H.-W., The thermal conductivity and mechanical properties of poly(p-phenylene sulfide)/oxidized-graphene and poly(p-phenylene sulfide)/defect-graphene nano-composites by molecular dynamics simulation. *RSC Advances* **2014**, 4 (50), 26074-26080.
158. Zhu, J.; Chen, M.; He, Q.; Shao, L.; Wei, S.; Guo, Z., An overview of the engineered graphene nanostructures and nanocomposites. *RSC Advances* **2013**, 3 (45), 22790-22824.
159. Geim, A. K., Graphene: Status and Prospects. *Science* **2009**, 324 (5934), 1530.
160. Zhang, N.; Yang, M.-Q.; Liu, S.; Sun, Y.; Xu, Y.-J., Waltzing with the Versatile Platform of Graphene to Synthesize Composite Photocatalysts. *Chemical Reviews* **2015**, 115 (18), 10307-10377.
161. Han, C.; Zhang, N.; Xu, Y.-J., Structural diversity of graphene materials and their multifarious roles in heterogeneous photocatalysis. *Nano Today* **2016**, 11 (3), 351-372.
162. Yoo, E.; Zhou, H., Influence of CO₂ on the stability of discharge performance for Li-air batteries with a hybrid electrolyte based on graphene nanosheets. *RSC Advances* **2014**, 4 (23), 11798-11801.
163. Routh, P.; Layek, R. K.; Nandi, A. K., Negative differential resistance and improved optoelectronic properties in Ag nanoparticles-decorated graphene oxide-riboflavin hybrids. *Carbon* **2012**, 50 (10), 3422-3434.
164. Bhattacharya, P.; Dhibar, S.; Hatui, G.; Mandal, A.; Das, T.; Das, C. K., Graphene decorated with hexagonal shaped M-type ferrite and polyaniline wrapper: a potential candidate for electromagnetic wave absorbing and energy storage device applications. *RSC Advances* **2014**, 4 (33), 17039-17053.
165. Liu, J.; Bai, H.; Wang, Y.; Liu, Z.; Zhang, X.; Sun Darren, D., Self-Assembling TiO₂ Nanorods on Large Graphene Oxide Sheets at a Two-Phase Interface and Their Anti-Recombination in Photocatalytic Applications. *Advanced Functional Materials* **2010**, 20 (23), 4175-4181.
166. Xiang, Q.; Yu, J.; Jaroniec, M., Graphene-based semiconductor photocatalysts. *Chemical Society Reviews* **2012**, 41 (2), 782-796.
167. Sun, Y.; Wu, Q.; Shi, G., Graphene based new energy materials. *Energy & Environmental Science* **2011**, 4 (4), 1113-1132.
168. Lightcap, I. V.; Kosel, T. H.; Kamat, P. V., Anchoring Semiconductor and Metal Nanoparticles on a Two-Dimensional Catalyst Mat. Storing and Shuttling Electrons with Reduced Graphene Oxide. *Nano Letters* **2010**, 10 (2), 577-583.
169. Yu, J.; Jin, J.; Cheng, B.; Jaroniec, M., A noble metal-free reduced graphene oxide-CdS nanorod composite for the enhanced visible-light photocatalytic reduction of CO₂ to solar fuel. *Journal of Materials Chemistry A* **2014**, 2 (10), 3407-3416.
170. Gan, Z.; Wu, X.; Meng, M.; Zhu, X.; Yang, L.; Chu, P. K., Photothermal Contribution to Enhanced Photocatalytic Performance of Graphene-Based Nanocomposites. *ACS Nano* **2014**, 8 (9), 9304-9310.

171. Loh, K. P.; Bao, Q.; Ang, P. K.; Yang, J., The chemistry of graphene. *Journal of Materials Chemistry* **2010**, *20* (12), 2277-2289.
172. Jia, L.; Wang, D.-H.; Huang, Y.-X.; Xu, A.-W.; Yu, H.-Q., Highly Durable N-Doped Graphene/CdS Nanocomposites with Enhanced Photocatalytic Hydrogen Evolution from Water under Visible Light Irradiation. *The Journal of Physical Chemistry C* **2011**, *115* (23), 11466-11473.
173. Zhang, N.; Zhang, Y.; Pan, X.; Fu, X.; Liu, S.; Xu, Y.-J., Assembly of CdS Nanoparticles on the Two-Dimensional Graphene Scaffold as Visible-Light-Driven Photocatalyst for Selective Organic Transformation under Ambient Conditions. *The Journal of Physical Chemistry C* **2011**, *115* (47), 23501-23511.
174. Tang, Y.; Hu, X.; Liu, C., Perfect inhibition of CdS photocorrosion by graphene sheltering engineering on TiO₂ nanotube array for highly stable photocatalytic activity. *Physical Chemistry Chemical Physics* **2014**, *16* (46), 25321-25329.
175. Li, X.; Yu, J.; Jaroniec, M., Hierarchical photocatalysts. *Chemical Society Reviews* **2016**, *45* (9), 2603-2636.
176. Zhang, H.; Lv, X.; Li, Y.; Wang, Y.; Li, J., P25-Graphene Composite as a High Performance Photocatalyst. *ACS Nano* **2010**, *4* (1), 380-386.
177. Low, J.; Yu, J.; Ho, W., Graphene-Based Photocatalysts for CO₂ Reduction to Solar Fuel. *The Journal of Physical Chemistry Letters* **2015**, *6* (21), 4244-4251.
178. Liang, Y. T.; Vijayan, B. K.; Gray, K. A.; Hersam, M. C., Minimizing Graphene Defects Enhances Titania Nanocomposite-Based Photocatalytic Reduction of CO₂ for Improved Solar Fuel Production. *Nano Letters* **2011**, *11* (7), 2865-2870.
179. Zhang, Q.; Lin, C.-F.; Jing, Y. H.; Chang, C.-T., Photocatalytic reduction of carbon dioxide to methanol and formic acid by graphene-TiO₂. *Journal of the Air & Waste Management Association* **2014**, *64* (5), 578-585.
180. Liang, Y. T.; Vijayan, B. K.; Lyandres, O.; Gray, K. A.; Hersam, M. C., Effect of Dimensionality on the Photocatalytic Behavior of Carbon-Titania Nanosheet Composites: Charge Transfer at Nanomaterial Interfaces. *The Journal of Physical Chemistry Letters* **2012**, *3* (13), 1760-1765.
181. Tu, W.; Zhou, Y.; Liu, Q.; Yan, S.; Bao, S.; Wang, X.; Xiao, M.; Zou, Z., An In Situ Simultaneous Reduction-Hydrolysis Technique for Fabrication of TiO₂-Graphene 2D Sandwich-Like Hybrid Nanosheets: Graphene-Promoted Selectivity of Photocatalytic-Driven Hydrogenation and Coupling of CO₂ into Methane and Ethane. *Advanced Functional Materials* **2012**, *23* (14), 1743-1749.
182. Ong, W.-J.; Tan, L.-L.; Chai, S.-P.; Yong, S.-T.; Mohamed, A. R., Self-assembly of nitrogen-doped TiO₂ with exposed {001} facets on a graphene scaffold as photo-active hybrid nanostructures for reduction of carbon dioxide to methane. *Nano Research* **2014**, *7* (10), 1528-1547.
183. Xing, M.; Shen, F.; Qiu, B.; Zhang, J., Highly-dispersed Boron-doped Graphene Nanosheets Loaded with TiO₂ Nanoparticles for Enhancing CO₂ Photoreduction. *Scientific Reports* **2014**, *4*, 6341.
184. Wang, P.-Q.; Bai, Y.; Luo, P.-Y.; Liu, J.-Y., Graphene-WO₃ nanobelt composite: Elevated conduction band toward photocatalytic reduction of CO₂ into hydrocarbon fuels. *Catalysis Communications* **2013**, *38*, 82-85.
185. Kumar, P.; Mungse, H. P.; Khatri, O. P.; Jain, S. L., Nitrogen-doped graphene-supported copper complex: a novel photocatalyst for CO₂ reduction under visible light irradiation. *RSC Advances* **2015**, *5* (68), 54929-54935.

186. Lv, X.-J.; Fu, W.-F.; Hu, C.-Y.; Chen, Y.; Zhou, W.-B., Photocatalytic reduction of CO₂ with H₂O over a graphene-modified NiO_x-Ta₂O₅ composite photocatalyst: coupling yields of methanol and hydrogen. *RSC Advances* **2013**, *3* (6), 1753-1757.
187. Hurtado, L.; Natividad, R.; García, H., Photocatalytic activity of Cu₂O supported on multi layers graphene for CO₂ reduction by water under batch and continuous flow. *Catalysis Communications* **2016**, *84*, 30-35.
188. Pastrana-Martínez, L. M.; Silva, A. M. T.; Fonseca, N. N. C.; Vaz, J. R.; Figueiredo, J. L.; Faria, J. L., Photocatalytic Reduction of CO₂ with Water into Methanol and Ethanol Using Graphene Derivative-TiO₂ Composites: Effect of pH and Copper(I) Oxide. *Topics in Catalysis* **2016**, *59* (15), 1279-1291.
189. Tu, W.; Zhou, Y.; Liu, Q.; Tian, Z.; Gao, J.; Chen, X.; Zhang, H.; Liu, J.; Zou, Z., Robust Hollow Spheres Consisting of Alternating Titania Nanosheets and Graphene Nanosheets with High Photocatalytic Activity for CO₂ Conversion into Renewable Fuels. *Advanced Functional Materials* **2012**, *22* (6), 1215-1221.
190. Jiang, L.; Yuan, X.; Zeng, G.; Wu, Z.; Liang, J.; Chen, X.; Leng, L.; Wang, H.; Wang, H., Metal-free efficient photocatalyst for stable visible-light photocatalytic degradation of refractory pollutant. *Applied Catalysis B: Environmental* **2018**, *221* (Supplement C), 715-725.
191. Ong, W.-J.; Tan, L.-L.; Ng, Y. H.; Yong, S.-T.; Chai, S.-P., Graphitic Carbon Nitride (g-C₃N₄)-Based Photocatalysts for Artificial Photosynthesis and Environmental Remediation: Are We a Step Closer To Achieving Sustainability? *Chemical Reviews* **2016**, *116* (12), 7159-7329.
192. Osorio-Guillén, J. M.; Espinosa-García, W. F.; Moyses Araujo, C., Assessing photocatalytic power of g-C₃N₄ for solar fuel production: A first-principles study involving quasi-particle theory and dispersive forces. *The Journal of Chemical Physics* **2015**, *143* (9), 094705.
193. Xu, Y.; Gao, S.-P., Band gap of C₃N₄ in the GW approximation. *International Journal of Hydrogen Energy* **2012**, *37* (15), 11072-11080.
194. Ye, S.; Wang, R.; Wu, M.-Z.; Yuan, Y.-P., A review on g-C₃N₄ for photocatalytic water splitting and CO₂ reduction. *Applied Surface Science* **2015**, *358* (Part A), 15-27.
195. Wen, J.; Xie, J.; Chen, X.; Li, X., A review on g-C₃N₄-based photocatalysts. *Applied Surface Science* **2017**, *391* (Part B), 72-123.
196. Zhang, H.; Yu, A., Photophysics and Photocatalysis of Carbon Nitride Synthesized at Different Temperatures. *The Journal of Physical Chemistry C* **2014**, *118* (22), 11628-11635.
197. Zhang, Y.; Pan, Q.; Chai, G.; Liang, M.; Dong, G.; Zhang, Q.; Qiu, J., Synthesis and luminescence mechanism of multicolor-emitting g-C₃N₄ nanopowders by low temperature thermal condensation of melamine. *Scientific Reports* **2013**, *3*, 1943.
198. Zhang, H.; Zuo, X.; Tang, H.; Li, G.; Zhou, Z., Origin of photoactivity in graphitic carbon nitride and strategies for enhancement of photocatalytic efficiency: insights from first-principles computations. *Physical Chemistry Chemical Physics* **2015**, *17* (9), 6280-6288.
199. Jiang, L.; Yuan, X.; Pan, Y.; Liang, J.; Zeng, G.; Wu, Z.; Wang, H., Doping of graphitic carbon nitride for photocatalysis: A review. *Applied Catalysis B: Environmental* **2017**, *217* (Supplement C), 388-406.
200. Zhang, L.; Zhang, Y.; Shi, R.; Bao, S.; Wang, J.; Amini, A.; Chandrashekar, B. N.; Cheng, C., Phosphorous doped graphitic-C₃N₄ hierarchical architecture for

hydrogen production from water under visible light. *Materials Today Energy* **2017**, *5*, 91-98.

201. Yuan, Y.-P.; Cao, S.-W.; Liao, Y.-S.; Yin, L.-S.; Xue, C., Red phosphor/g-C₃N₄ heterojunction with enhanced photocatalytic activities for solar fuels production. *Applied Catalysis B: Environmental* **2013**, *140-141*, 164-168.

202. Shalom, M.; Guttentag, M.; Fettkenhauer, C.; Inal, S.; Neher, D.; Llobet, A.; Antonietti, M., In Situ Formation of Heterojunctions in Modified Graphitic Carbon Nitride: Synthesis and Noble Metal Free Photocatalysis. *Chemistry of Materials* **2014**, *26* (19), 5812-5818.

203. Zhang, J.; Chen, X.; Takahabe, K.; Maeda, K.; Domen, K.; Epping, J. D.; Fu, X.; Antonietti, M.; Wang, X., Synthesis of a Carbon Nitride Structure for Visible-Light Catalysis by Copolymerization. *Angewandte Chemie International Edition* **2009**, *49* (2), 441-444.

204. Huang, Z.-F.; Song, J.; Pan, L.; Wang, Z.; Zhang, X.; Zou, J.-J.; Mi, W.; Zhang, X.; Wang, L., Carbon nitride with simultaneous porous network and O-doping for efficient solar-energy-driven hydrogen evolution. *Nano Energy* **2015**, *12* (Supplement C), 646-656.

205. Dante, R. C.; Martín-Ramos, P.; Correa-Guimaraes, A.; Martín-Gil, J., Synthesis of graphitic carbon nitride by reaction of melamine and uric acid. *Materials Chemistry and Physics* **2011**, *130* (3), 1094-1102.

206. Fu, J.; Zhu, B.; Jiang, C.; Cheng, B.; You, W.; Yu, J., Hierarchical Porous O-Doped g-C₃N₄ with Enhanced Photocatalytic CO₂ Reduction Activity. *Small* **2017**, *13* (15), 1603938-n/a.

207. Hao, R.; Wang, G.; Jiang, C.; Tang, H.; Xu, Q., In situ hydrothermal synthesis of g-C₃N₄/TiO₂ heterojunction photocatalysts with high specific surface area for Rhodamine B degradation. *Applied Surface Science* **2017**, *411*, 400-410.

208. Li, K.; Peng, B.; Jin, J.; Zan, L.; Peng, T., Carbon nitride nanodots decorated brookite TiO₂ quasi nanocubes for enhanced activity and selectivity of visible-light-driven CO₂ reduction. *Applied Catalysis B: Environmental* **2017**, *203*, 910-916.

209. Wang, H.; Li, J.; Ma, C.; Guan, Q.; Lu, Z.; Huo, P.; Yan, Y., Melamine modified P25 with heating method and enhanced the photocatalytic activity on degradation of ciprofloxacin. *Applied Surface Science* **2015**, *329*, 17-22.

210. Yu, J.; Wang, S.; Low, J.; Xiao, W., Enhanced photocatalytic performance of direct Z-scheme g-C₃N₄-TiO₂ photocatalysts for the decomposition of formaldehyde in air. *Physical Chemistry Chemical Physics* **2013**, *15* (39), 16883-16890.

211. Zhang, G.; Zhang, T.; Li, B.; Jiang, S.; Zhang, X.; Hai, L.; Chen, X.; Wu, W., An ingenious strategy of preparing TiO₂/g-C₃N₄ heterojunction photocatalyst: In situ growth of TiO₂ nanocrystals on g-C₃N₄ nanosheets via impregnation-calcination method. *Applied Surface Science* **2018**, *433*, 963-974.

212. Zhou, J.; Zhang, M.; Zhu, Y., Photocatalytic enhancement of hybrid C₃N₄/TiO₂ prepared via ball milling method. *Physical Chemistry Chemical Physics* **2015**, *17* (5), 3647-3652.

213. Mao, J.; Peng, T.; Zhang, X.; Li, K.; Ye, L.; Zan, L., Effect of graphitic carbon nitride microstructures on the activity and selectivity of photocatalytic CO₂ reduction under visible light. *Catalysis Science & Technology* **2013**, *3* (5), 1253-1260.

214. Qin, J.; Wang, S.; Ren, H.; Hou, Y.; Wang, X., Photocatalytic reduction of CO₂ by graphitic carbon nitride polymers derived from urea and barbituric acid. *Applied Catalysis B: Environmental* **2015**, *179* (Supplement C), 1-8.

215. Wang, H.; Sun, Z.; Li, Q.; Tang, Q.; Wu, Z., Surprisingly advanced CO₂ photocatalytic conversion over thiourea derived g-C₃N₄ with water vapor while introducing 200–420nm UV light. *Journal of CO₂ Utilization* **2016**, *14* (Supplement C), 143-151.
216. Wang, K.; Li, Q.; Liu, B.; Cheng, B.; Ho, W.; Yu, J., Sulfur-doped g-C₃N₄ with enhanced photocatalytic CO₂-reduction performance. *Applied Catalysis B: Environmental* **2015**, *176* (Supplement C), 44-52.
217. Dong, G.; Zhang, L., Porous structure dependent photoreactivity of graphitic carbon nitride under visible light. *Journal of Materials Chemistry* **2012**, *22* (3), 1160-1166.
218. Huang, Y.; Wang, Y.; Bi, Y.; Jin, J.; Ehsan, M. F.; Fu, M.; He, T., Preparation of 2D hydroxyl-rich carbon nitride nanosheets for photocatalytic reduction of CO₂. *RSC Advances* **2015**, *5* (42), 33254-33261.
219. Raziq, F.; Qu, Y.; Zhang, X.; Humayun, M.; Wu, J.; Zada, A.; Yu, H.; Sun, X.; Jing, L., Enhanced Cocatalyst-Free Visible-Light Activities for Photocatalytic Fuel Production of g-C₃N₄ by Trapping Holes and Transferring Electrons. *The Journal of Physical Chemistry C* **2016**, *120* (1), 98-107.
220. Zhou, S.; Liu, Y.; Li, J.; Wang, Y.; Jiang, G.; Zhao, Z.; Wang, D.; Duan, A.; Liu, J.; Wei, Y., Facile in situ synthesis of graphitic carbon nitride (g-C₃N₄)-N-TiO₂ heterojunction as an efficient photocatalyst for the selective photoreduction of CO₂ to CO. *Applied Catalysis B: Environmental* **2014**, *158-159*, 20-29.
221. Reli, M.; Huo, P.; Šihor, M.; Ambrožová, N.; Troppová, I.; Matějová, L.; Lang, J.; Svoboda, L.; Kuštrowski, P.; Ritz, M.; Praus, P.; Kočí, K., Novel TiO₂/C₃N₄ Photocatalysts for Photocatalytic Reduction of CO₂ and for Photocatalytic Decomposition of N₂O. *The Journal of Physical Chemistry A* **2016**, *120* (43), 8564-8573.
222. Adekoya, D. O.; Tahir, M.; Amin, N. A. S., g-C₃N₄/(Cu/TiO₂) nanocomposite for enhanced photoreduction of CO₂ to CH₃OH and HCOOH under UV/visible light. *Journal of CO₂ Utilization* **2017**, *18*, 261-274.
223. Roy, S. C.; Varghese, O. K.; Paulose, M.; Grimes, C. A., Toward Solar Fuels: Photocatalytic Conversion of Carbon Dioxide to Hydrocarbons. *ACS Nano* **2010**, *4* (3), 1259-1278.
224. Indrakanti, V. P.; Kubicki, J. D.; Schobert, H. H., Photoinduced activation of CO₂ on Ti-based heterogeneous catalysts: Current state, chemical physics-based insights and outlook. *Energy & Environmental Science* **2009**, *2* (7), 745-758.
225. Levenspiel, O., Chemical Reaction Engineering. *Industrial & Engineering Chemistry Research* **1999**, *38* (11), 4140-4143.
226. Cassano, A. E.; Martin, C. A.; Brandi, R. J.; Alfano, O. M., Photoreactor Analysis and Design: Fundamentals and Applications. *Industrial & Engineering Chemistry Research* **1995**, *34* (7), 2155-2201.
227. Emenike, V. N.; Schenkendorf, R.; Krewer, U., A systematic reactor design approach for the synthesis of active pharmaceutical ingredients. *European Journal of Pharmaceutics and Biopharmaceutics* **2018**, *126*, 75-88.
228. Cristaldi, D. A.; Yanar, F.; Mosayyebi, A.; García-Manrique, P.; Stulz, E.; Carugo, D.; Zhang, X., Easy-to-perform and cost-effective fabrication of continuous-flow reactors and their application for nanomaterials synthesis. *New Biotechnology* **2018**.

229. Esteves, B. M.; Rodrigues, C. S. D.; Madeira, L. M., Wastewater treatment by heterogeneous fenton-like processes in continuous reactors. In *Handbook of Environmental Chemistry*, 2019; Vol. 67, pp 211-255.
230. Ahmad, J. S. M.; Cai, W.; Zhao, Z.; Zhang, Z.; Shimizu, K.; Lei, Z.; Lee, D.-J., Stability of algal-bacterial granules in continuous-flow reactors to treat varying strength domestic wastewater. *Bioresource Technology* **2017**, *244*, 225-233.
231. Chakraborty, B.; Basu, S., Treatment of wastewater by mixed bacterial consortium in continuous reactors packed with solid waste. *Journal of Water Process Engineering* **2017**, *17*, 135-142.
232. Tang, Z.; Kim, W.-S.; Yu, T., Continuous synthesis of silver plates in a continuous stirring tank reactor (CSTR). *Journal of Industrial and Engineering Chemistry* **2018**.
233. Aghbashlo, M.; Tabatabaei, M.; Rastegari, H.; Ghaziaskar, H. S.; Valijanian, E., Exergy-based optimization of a continuous reactor applied to produce value-added chemicals from glycerol through esterification with acetic acid. *Energy* **2018**, *150*, 351-362.
234. Casademont, P.; Cardozo-Filho, L.; Meurer, E.; Sánchez-Oneto, J.; Portela, J. R., Gasification of Olive Oil Mill Waste by Supercritical Water in a Continuous Reactor. *The Journal of Supercritical Fluids* **2018**.
235. Chattopadhyay, S.; Sen, R., Development of a novel integrated continuous reactor system for biocatalytic production of biodiesel. *Bioresource Technology* **2013**, *147*, 395-400.
236. Sim, L. C.; Leong, K. H.; Saravanan, P.; Ibrahim, S., Rapid thermal reduced graphene oxide/Pt-TiO₂ nanotube arrays for enhanced visible-light-driven photocatalytic reduction of CO₂. *Applied Surface Science* **2015**, *358*, 122-129.
237. Pan, P.-W.; Chen, Y.-W., Photocatalytic reduction of carbon dioxide on NiO/InTaO₄ under visible light irradiation. *Catalysis Communications* **2007**, *8* (10), 1546-1549.
238. Akhter, P.; Hussain, M.; Saracco, G.; Russo, N., Novel nanostructured-TiO₂ materials for the photocatalytic reduction of CO₂ greenhouse gas to hydrocarbons and syngas. *Fuel* **2015**, *149*, 55-65.
239. Singhal, N.; Kumar, U., Noble metal modified TiO₂: selective photoreduction of CO₂ to hydrocarbons. *Molecular Catalysis* **2017**, *439*, 91-99.
240. Wang, W.-N.; An, W.-J.; Ramalingam, B.; Mukherjee, S.; Niedzwiedzki, D. M.; Gangopadhyay, S.; Biswas, P., Size and Structure Matter: Enhanced CO₂ Photoreduction Efficiency by Size-Resolved Ultrafine Pt Nanoparticles on TiO₂ Single Crystals. *Journal of the American Chemical Society* **2012**, *134* (27), 11276-11281.
241. Li, H.; Lei, Y.; Huang, Y.; Fang, Y.; Xu, Y.; Zhu, L.; Li, X., Photocatalytic reduction of carbon dioxide to methanol by Cu₂O/SiC nanocrystallite under visible light irradiation. *Journal of Natural Gas Chemistry* **2011**, *20* (2), 145-150.
242. Ola, O.; Maroto-Valer, M. M., Transition metal oxide based TiO₂ nanoparticles for visible light induced CO₂ photoreduction. *Applied Catalysis A: General* **2015**, *502*, 114-121.
243. Susanto, H.; Ulbricht, M., Polymeric Membranes for Molecular Separations. *Membrane Operations* **2009**.
244. Staude, E., Marcel Mulder: Basic Principles of Membrane Technology, Kluwer Academic Publishers, Dordrecht, Boston, London, 1991, ISBN 0-7923-0978-2, 363

- Seiten, Preis: DM 200,—. *Berichte der Bunsengesellschaft für physikalische Chemie* **1992**, 96 (5), 741-742.
245. Saier, H. D.; Strathmann, H., Asymmetric Membranes: Preparation and Applications. *Angewandte Chemie International Edition in English* **1975**, 14 (7), 452-459.
246. Hylton, K.; Mitra, S., Automated, on-line membrane extraction. *Journal of Chromatography A* **2007**, 1152 (1), 199-214.
247. Guo, X.; Mitra, S., On-line membrane extraction liquid chromatography for monitoring semi-volatile organics in aqueous matrices. *Journal of Chromatography A* **2000**, 904 (2), 189-196.
248. Kamata, K.; Iyoda, T., CHAPTER 5 - Nanocylinder Array Structures in Block Copolymer Thin Films. In *Nanomaterials*, Hosono, H.; Mishima, Y.; Takezoe, H.; MacKenzie, K. J. D.; MacKenzie, K.; Mishima, Y.; Takezoe, H., Eds. Elsevier Science Ltd: Oxford, 2006; pp 171-223.
249. Murphy Tom, M.; Offord Grant, T.; Paul Don, R., Fundamentals of Membrane Gas Separation. *Membrane Operations* **2009**.
250. Alberti, G.; Di Vona, M. L.; Narducci, R., New results on the visco-elastic behaviour of ionomer membranes and relations between T–RH plots and proton conductivity decay of Nafion® 117 in the range 50–140 C. *International Journal of Hydrogen Energy* **2012**, 37 (7), 6302-6307.
251. Tai, C.-C.; Chen, C.-L.; Liu, C.-W.; Huang, Y.-R., Investigation the proton transport in highly hydrated Nafion membrane doping with SiO₂ nanoparticles by molecular dynamics simulation. *Thin Solid Films* **2018**.
252. Cao, K.; Jiang, Z.; Zhang, X.; Zhang, Y.; Zhao, J.; Xing, R.; Yang, S.; Gao, C.; Pan, F., Highly water-selective hybrid membrane by incorporating g-C₃N₄ nanosheets into polymer matrix. *Journal of Membrane Science* **2015**, 490, 72-83.
253. Peng, K.-J.; Lai, J.-Y.; Liu, Y.-L., Nanohybrids of graphene oxide chemically-bonded with Nafion: Preparation and application for proton exchange membrane fuel cells. *Journal of Membrane Science* **2016**, 514, 86-94.
254. Lee, A.; Elam, J. W.; Darling, S. B., Membrane materials for water purification: design, development, and application. *Environmental Science: Water Research & Technology* **2016**, 2 (1), 17-42.
255. Schlosser, Š., Extractive Separations in Contactors with One and Two Immobilized L/L Interfaces: Applications and Perspectives. *Membrane Operations* **2009**.
256. Barbieri, G.; Scura, F., Fundamental of Chemical Membrane Reactors. *Membrane Operations* **2009**.
257. Giorno, L.; De Luca, G.; Figoli, A.; Piacentini, E.; Drioli, E., Membrane Emulsification: Principles and Applications. *Membrane Operations* **2009**.
258. Morelli, S.; Salerno, S.; Piscioneri, A.; Rende, M.; Campana, C.; Drioli, E.; De Bartolo, L., Membranes in Regenerative Medicine and Tissue Engineering. *Membrane Operations* **2009**.
259. Koros William, J.; Kratochvil, A.; Shu, S.; Husain, S., Energy and Environmental Issues and Impacts of Membranes in Industry. *Membrane Operations* **2009**.
260. Baker Richard, W., Membrane Gas-Separation: Applications. *Membrane Operations* **2009**.

261. Molinari, R.; Caruso, A.; Palmisano, L., Photocatalytic Membrane Reactors in the Conversion or Degradation of Organic Compounds. *Membrane Operations* **2009**.
262. Camera-Roda, G.; Santarelli, F., Intensification of Water Detoxification by Integrating Photocatalysis and Pervaporation. *Journal of Solar Energy Engineering* **2005**, *129* (1), 68-73.
263. Pandikumar, A.; Manonmani, S.; Ramaraj, R., TiO₂-Au nanocomposite materials embedded in polymer matrices and their application in the photocatalytic reduction of nitrite to ammonia. *Catalysis Science & Technology* **2012**, *2* (2), 345-353.
264. Molinari, R.; Lavorato, C.; Argurio, P., Photocatalytic reduction of acetophenone in membrane reactors under UV and visible light using TiO₂ and Pd/TiO₂ catalysts. *Chemical Engineering Journal* **2015**, *274*, 307-316.
265. Iglesias, O.; Rivero, M. J.; Urriaga, A. M.; Ortiz, I., Membrane-based photocatalytic systems for process intensification. *Chemical Engineering Journal* **2016**, *305*, 136-148.
266. Pathak, P.; Mezziani, M. J.; Li, Y.; Cureton, L. T.; Sun, Y.-P., Improving photoreduction of CO₂ with homogeneously dispersed nanoscale TiO₂ catalysts. *Chemical Communications* **2004**, (10), 1234-1235.
267. Pathak, P.; Mezziani, M. J.; Castillo, L.; Sun, Y.-P., Metal-coated nanoscale TiO₂ catalysts for enhanced CO₂ photoreduction. *Green Chemistry* **2005**, *7* (9), 667-670.
268. Sellaro, M.; Bellardita, M.; Brunetti, A.; Fontananova, E.; Palmisano, L.; Drioli, E.; Barbieri, G., CO₂ conversion in a photocatalytic continuous membrane reactor. *RSC Advances* **2016**, *6* (71), 67418-67427.
269. Chen, R.; Cheng, X.; Zhu, X.; Liao, Q.; An, L.; Ye, D. D.; He, X. F.; Wang, Z. B., High-performance optofluidic membrane microreactor with a mesoporous CdS/TiO₂/SBA-15@carbon paper composite membrane for the CO₂ photoreduction. *Chemical Engineering Journal* **2017**, *316*, 911-918.
270. Geyer, K.; Codée Jeroen, D. C.; Seeberger Peter, H., Microreactors as Tools for Synthetic Chemists—The Chemists' Round-Bottomed Flask of the 21st Century? *Chemistry – A European Journal* **2006**, *12* (33), 8434-8442.
271. Westermann, T.; Melin, T., Flow-through catalytic membrane reactors—Principles and applications. *Chemical Engineering and Processing: Process Intensification* **2009**, *48* (1), 17-28.
272. Poe Sarah, L.; Cummings Meredith, A.; Haaf Michael, P.; McQuade, D. T., Solving the Clogging Problem: Precipitate-Forming Reactions in Flow. *Angewandte Chemie International Edition* **2006**, *45* (10), 1544-1548.
273. Nethravathi, C.; Rajamathi, M., Chemically modified graphene sheets produced by the solvothermal reduction of colloidal dispersions of graphite oxide. *Carbon* **2008**, *46* (14), 1994-1998.
274. Dong, G.; Ai, Z.; Zhang, L., Efficient anoxic pollutant removal with oxygen functionalized graphitic carbon nitride under visible light. *RSC Advances* **2014**, *4* (11), 5553-5560.
275. Gionco, C.; Paganini, M. C.; Giamello, E.; Sacco, O.; Vaiano, V.; Sannino, D., Rare earth oxides in zirconium dioxide: How to turn a wide band gap metal oxide into a visible light active photocatalyst. *Journal of Energy Chemistry* **2017**, *26* (2), 270-276.
276. Popa, N. C.; Balzar, D., Size-broadening anisotropy in whole powder pattern fitting. Application to zinc oxide and interpretation of the apparent crystallites in terms of physical models. *Journal of Applied Crystallography* **2008**, *41* (3), 615-627.

277. Srinivasan, R.; Rice, L.; Davis, B. H., Critical Particle Size and Phase Transformation in Zirconia: Transmission Electron Microscopy and X-ray Diffraction Studies. *Journal of the American Ceramic Society* **1990**, *73* (11), 3528-3530.
278. Yamamoto, T.; Tanaka, T.; Takenaka, S.; Yoshida, S.; Onari, T.; Takahashi, Y.; Kosaka, T.; Hasegawa, S.; Kudo, M., Structural Analysis of Iron and Manganese Species in Iron- and Manganese-Promoted Sulfated Zirconia. *The Journal of Physical Chemistry B* **1999**, *103* (13), 2385-2393.
279. Zhang, J.; Yan, S.; Yuan, M.; Wang, X.; Li, C., UV Raman spectroscopic study on the surface phase of ZrO₂ modified with Nd₂O₃. *Materials Letters* **2011**, *65* (2), 201-204.
280. Wu, H.; Li, Y.; Wang, Y.; Zhang, P.; Rao, W., Study on preparation, microstructure and luminescent properties of Er-ZrO₂ layer. *Journal of Rare Earths* **2016**, *34* (9), 958-962.
281. Takanaka, K.; Yamamoto, R., Temperature-dependent multi-ion interactions in simple metals. *physica status solidi (b)* **1977**, *84* (2), 813-816.
282. Remeika, J. P.; Glass, A. M., The growth and ferroelectric properties of high resistivity single crystals of lead titanate. *Materials Research Bulletin* **1970**, *5* (1), 37-45.
283. Muñoz-Batista, M. J.; Gómez-Cerezo, M. N.; Kubacka, A.; Tudela, D.; Fernández-García, M., Role of Interface Contact in CeO₂-TiO₂ Photocatalytic Composite Materials. *ACS Catalysis* **2014**, *4* (1), 63-72.
284. Kumari, L.; Du, G. H.; Li, W. Z.; Vennila, R. S.; Saxena, S. K.; Wang, D. Z., Synthesis, microstructure and optical characterization of zirconium oxide nanostructures. *Ceramics International* **2009**, *35* (6), 2401-2408.
285. Cong, Y.; Li, B.; Lei, B.; Li, W., Long lasting phosphorescent properties of Ti doped ZrO₂. *Journal of Luminescence* **2007**, *126* (2), 822-826.
286. Zhang, H. T.; Wu, G.; Chen, X. H., Thermal stability and photoluminescence of Zr_{1-x}Ce_xO₂ (0 ≤ x ≤ 1) nanoparticles synthesized in a non-aqueous process. *Materials Chemistry and Physics* **2007**, *101* (2), 415-422.
287. Che, M.; Kibblewhite, J. F. J.; Tench, A. J.; Dufaux, M.; Naccache, C., Oxygen species adsorbed on CeO₂/SiO₂ supported catalysts. *Journal of the Chemical Society, Faraday Transactions 1: Physical Chemistry in Condensed Phases* **1973**, *69* (0), 857-863.
288. Craciun, R., Characterization of mixed amorphous/crystalline cerium oxide supported on SiO₂. *Solid State Ionics* **1998**, *110* (1), 83-93.
289. Aboukais, A.; Zhilinskaya, E. A.; Lamonier, J.-F.; Filimonov, I. N., EPR study of ceria-silica and ceria-alumina catalysts: Localization of superoxide radical anions. *Colloids and Surfaces A: Physicochemical and Engineering Aspects* **2005**, *260* (1), 199-207.
290. Pipornpong, W.; Wanbayor, R.; Ruangpornvisuti, V., Adsorption CO₂ on the perfect and oxygen vacancy defect surfaces of anatase TiO₂ and its photocatalytic mechanism of conversion to CO. *Applied Surface Science* **2011**, *257* (24), 10322-10328.
291. Casiraghi, C., Doping dependence of the Raman peaks intensity of graphene close to the Dirac point. *Physical Review B* **2009**, *80* (23), 233407.
292. Ferrari, A. C.; Robertson, J., Raman spectroscopy of amorphous, nanostructured, diamond-like carbon, and nanodiamond. *Philosophical Transactions of the Royal Society of London. Series A: Mathematical, Physical and Engineering Sciences* **2004**, *362* (1824), 2477.

293. Tuinstra, F.; Koenig, J. L., Raman Spectrum of Graphite. *The Journal of Chemical Physics* **1970**, *53* (3), 1126-1130.
294. Ferrari, A. C.; Meyer, J. C.; Scardaci, V.; Casiraghi, C.; Lazzeri, M.; Mauri, F.; Piscanec, S.; Jiang, D.; Novoselov, K. S.; Roth, S.; Geim, A. K., Raman Spectrum of Graphene and Graphene Layers. *Physical Review Letters* **2006**, *97* (18), 187401.
295. Basko, D. M., Theory of resonant multiphonon Raman scattering in graphene. *Physical Review B* **2008**, *78* (12), 125418.
296. Thomsen, C.; Reich, S., Double Resonant Raman Scattering in Graphite. *Physical Review Letters* **2000**, *85* (24), 5214-5217.
297. Johra, F. T.; Lee, J.-W.; Jung, W.-G., Facile and safe graphene preparation on solution based platform. *Journal of Industrial and Engineering Chemistry* **2014**, *20* (5), 2883-2887.
298. Schonfelder, R.; Rummeli, M. H.; Gruner, W.; Loffler, M.; Acker, J.; Hoffmann, V.; Gemming, T.; Buchner, B.; Pichler, T. Purification-induced sidewall functionalization of magnetically pure single-walled carbon nanotubes. *Nanotechnology* **2007**, *18* (37), 375601.
299. Moon, I. K.; Lee, J.; Ruoff, R. S.; Lee, H., Reduced graphene oxide by chemical graphitization. *Nature Communications* **2010**, *1*, 73.
300. Cortes, M. A. L. R. M.; Hamilton, J. W. J.; Sharma, P. K.; Brown, A.; Nolan, M.; Gray, K. A.; Byrne, J. A., Formal quantum efficiencies for the photocatalytic reduction of CO₂ in a gas phase batch reactor. *Catalysis Today* **2018**.
301. Dante, R. C.; Sánchez-Arévalo, F. M.; Chamorro-Posada, P.; Vázquez-Cabo, J.; Huerta, L.; Lartundo-Rojas, L.; Santoyo-Salazar, J.; Solorza-Feria, O.; Diaz-Barrios, A.; Zoltan, T.; Vargas, F.; Valenzuela, T.; Muñoz-Bisesti, F.; Quiroz-Chávez, F. J., Synthesis and characterization of Cu-doped polymeric carbon nitride. *Fullerenes, Nanotubes and Carbon Nanostructures* **2016**, *24* (3), 171-180.
302. Li, X.; Zhang, J.; Shen, L.; Ma, Y.; Lei, W.; Cui, Q.; Zou, G., Preparation and characterization of graphitic carbon nitride through pyrolysis of melamine. *Applied Physics A* **2009**, *94* (2), 387-392.
303. Adekoya, D. O.; Tahir, M.; Amin, N. A. S., g-C₃N₄/(Cu/TiO₂) nanocomposite for enhanced photoreduction of CO₂ to CH₃OH and HCOOH under UV/visible light. *Journal of CO₂ Utilization* **2017**, *18* (Supplement C), 261-274.
304. Ren, J.; Chai, Y.; Liu, Q.; Zhang, L.; Dai, W.-L., Intercorrelated Ag₃PO₄ nanoparticles decorated with graphitic carbon nitride: Enhanced stability and photocatalytic activities for water treatment. *Applied Surface Science* **2017**, *403* (Supplement C), 177-186.
305. Zhou, Z.; Wang, J.; Yu, J.; Shen, Y.; Li, Y.; Liu, A.; Liu, S.; Zhang, Y., Dissolution and Liquid Crystals Phase of 2D Polymeric Carbon Nitride. *Journal of the American Chemical Society* **2015**, *137* (6), 2179-2182.
306. Montigaud, H.; Tanguy, B.; Demazeau, G.; Alves, I.; Courjault, S., C₃N₄: Dream or reality? Solvothermal synthesis as macroscopic samples of the C₃N₄ graphitic form. *Journal of Materials Science* **2000**, *35* (10), 2547-2552.
307. She, X.; Liu, L.; Ji, H.; Mo, Z.; Li, Y.; Huang, L.; Du, D.; Xu, H.; Li, H., Template-free synthesis of 2D porous ultrathin nonmetal-doped g-C₃N₄ nanosheets with highly efficient photocatalytic H₂ evolution from water under visible light. *Applied Catalysis B: Environmental* **2016**, *187*, 144-153.

308. Fina, F.; Callear, S. K.; Carins, G. M.; Irvine, J. T. S., Structural Investigation of Graphitic Carbon Nitride via XRD and Neutron Diffraction. *Chemistry of Materials* **2015**, *27* (7), 2612-2618.
309. Tan, L.-L.; Ong, W.-J.; Chai, S.-P.; Mohamed, A. R., Photocatalytic reduction of CO₂ with H₂O over graphene oxide-supported oxygen-rich TiO₂ hybrid photocatalyst under visible light irradiation: Process and kinetic studies. *Chemical Engineering Journal* **2017**, *308*, 248-255.
310. Oh, J.; Yoo, R. J.; Kim, S. Y.; Lee, Y. J.; Kim, D. W.; Park, S., Oxidized Carbon Nitrides: Water-Dispersible, Atomically Thin Carbon Nitride-Based Nanodots and Their Performances as Bioimaging Probes. *Chemistry – A European Journal* **2015**, *21* (16), 6241-6246.
311. Bai, G.; Song, Z.; Geng, H.; Gao, D.; Liu, K.; Wu, S.; Rao, W.; Guo, L.; Wang, J., Oxidized Quasi-Carbon Nitride Quantum Dots Inhibit Ice Growth. *Advanced Materials* **2017**, *29* (28), 1606843-n/a.
312. Beamson, G.; Briggs, D., *High Resolution XPS of Organic Polymers: The Scienta ESCA300 Database*. Wiley: 1992.
313. Li, M.; Zhang, L.; Wu, M.; Du, Y.; Fan, X.; Wang, M.; Zhang, L.; Kong, Q.; Shi, J., Mesostructured CeO₂/g-C₃N₄ nanocomposites: Remarkably enhanced photocatalytic activity for CO₂ reduction by mutual component activations. *Nano Energy* **2016**, *19* (Supplement C), 145-155.
314. Zhao, H.; Yu, H.; Quan, X.; Chen, S.; Zhang, Y.; Zhao, H.; Wang, H., Fabrication of atomic single layer graphitic-C₃N₄ and its high performance of photocatalytic disinfection under visible light irradiation. *Applied Catalysis B: Environmental* **2014**, *152-153*, 46-50.
315. Liao, G.; Chen, S.; Quan, X.; Yu, H.; Zhao, H., Graphene oxide modified g-C₃N₄ hybrid with enhanced photocatalytic capability under visible light irradiation. *Journal of Materials Chemistry* **2012**, *22* (6), 2721-2726.
316. Yu, J.; Wang, S.; Cheng, B.; Lin, Z.; Huang, F., Noble metal-free Ni(OH)₂-g-C₃N₄ composite photocatalyst with enhanced visible-light photocatalytic H₂-production activity. *Catalysis Science & Technology* **2013**, *3* (7), 1782-1789.
317. Krivtsov, I.; García-López, E. I.; Marci, G.; Palmisano, L.; Amghouz, Z.; García, J. R.; Ordóñez, S.; Díaz, E., Selective photocatalytic oxidation of 5-hydroxymethyl-2-furfural to 2,5-furandicarboxyaldehyde in aqueous suspension of g-C₃N₄. *Applied Catalysis B: Environmental* **2017**, *204*, 430-439.
318. Zhang, J.; Zhang, M.; Yang, C.; Wang, X., Nanospherical Carbon Nitride Frameworks with Sharp Edges Accelerating Charge Collection and Separation at a Soft Photocatalytic Interface. *Advanced Materials* **2014**, *26* (24), 4121-4126.
319. Papailias, I.; Giannakopoulou, T.; Todorova, N.; Demotikali, D.; Vaimakis, T.; Trapalis, C., Effect of processing temperature on structure and photocatalytic properties of g-C₃N₄. *Applied Surface Science* **2015**, *358*, 278-286.
320. Ong, W.-J.; Tan, L.-L.; Chai, S.-P.; Yong, S.-T., Heterojunction engineering of graphitic carbon nitride (g-C₃N₄) via Pt loading with improved daylight-induced photocatalytic reduction of carbon dioxide to methane. *Dalton Transactions* **2015**, *44* (3), 1249-1257.
321. Shi, H.; Chen, G.; Zhang, C.; Zou, Z., Polymeric g-C₃N₄ Coupled with NaNbO₃ Nanowires toward Enhanced Photocatalytic Reduction of CO₂ into Renewable Fuel. *ACS Catalysis* **2014**, *4* (10), 3637-3643.

322. Pomilla, F. R.; Brunetti, A.; Marci, G.; Garcia-Lopez, E. I.; Fontananova, E.; Palmisano, L.; Barbieri, G., CO₂ to liquid fuels: photocatalytic conversion in a continuous membrane reactor. *ACS Sustainable Chemistry & Engineering* **2018**.
323. Albu-Yaron, A.; Arcan, L.; Heitner-Wirguin, C., TiO₂-loaded Nafion membranes: An electron microscope investigation. *Thin Solid Films* **1990**, *185* (1), 181-188.
324. Wu, C.; Lu, S.; Zhang, J.; Xiang, Y., Inducing microstructural changes in Nafion by incorporating graphitic carbon nitride to enhance the vanadium-blocking effect. *Physical Chemistry Chemical Physics* **2018**, *20* (11), 7694-7700.
325. Shi, D. X.; Feng, Y. Q.; Zhong, S. H., Photocatalytic conversion of CH₄ and CO₂ to oxygenated compounds over Cu/CdS-TiO₂/SiO₂ catalyst. *Catalysis Today* **2004**, *98* (4), 505-509.
326. Hori, Y.; Takahashi, R.; Yoshinami, Y.; Murata, A., Electrochemical Reduction of CO at a Copper Electrode. *The Journal of Physical Chemistry B* **1997**, *101* (36), 7075-7081.
327. Murugesan, P.; Narayanan, S.; Manickam, M., Experimental studies on photocatalytic reduction of CO₂ using AgBr decorated g-C₃N₄ composite in TEA mediated system. *Journal of CO₂ Utilization* **2017**, *22*, 250-261.
328. Li, H.; Gao, Y.; Xiong, Z.; Liao, C.; Shih, K., Enhanced selective photocatalytic reduction of CO₂ to CH₄ over plasmonic Au modified g-C₃N₄ photocatalyst under UV-vis light irradiation. *Applied Surface Science* **2018**, *439*, 552-559.
329. Liu, S.; Chen, F.; Li, S.; Peng, X.; Xiong, Y., Enhanced photocatalytic conversion of greenhouse gas CO₂ into solar fuels over g-C₃N₄ nanotubes with decorated transparent ZIF-8 nanoclusters. *Applied Catalysis B: Environmental* **2017**, *211*, 1-10.
330. Raziq, F.; Qu, Y.; Humayun, M.; Zada, A.; Yu, H.; Jing, L., Synthesis of SnO₂/B-P codoped g-C₃N₄ nanocomposites as efficient cocatalyst-free visible-light photocatalysts for CO₂ conversion and pollutant degradation. *Applied Catalysis B: Environmental* **2017**, *201*, 486-494.
331. Huang, Q.; Yu, J.; Cao, S.; Cui, C.; Cheng, B., Efficient photocatalytic reduction of CO₂ by amine-functionalized g-C₃N₄. *Applied Surface Science* **2015**, *358*, 350-355.
332. Li, H.; Gan, S.; Wang, H.; Han, D.; Niu, L., Intercorrelated Superhybrid of AgBr Supported on Graphitic-C₃N₄-Decorated Nitrogen-Doped Graphene: High Engineering Photocatalytic Activities for Water Purification and CO₂ Reduction. *Advanced Materials* **2015**, *27* (43), 6906-6913.
333. Liu, H.; Zhang, Z.; Meng, J.; Zhang, J., Novel visible-light-driven CdIn₂S₄/mesoporous g-C₃N₄ hybrids for efficient photocatalytic reduction of CO₂ to methanol. *Molecular Catalysis* **2017**, *430*, 9-19.
334. Cheng, X.; Chen, R.; Zhu, X.; Liao, Q.; He, X.; Li, S.; Li, L., Optofluidic membrane microreactor for photocatalytic reduction of CO₂. *International Journal of Hydrogen Energy* **2016**, *41* (4), 2457-2465.
335. Dhakshinamoorthy, A.; Navalon, S.; Corma, A.; Garcia, H., Photocatalytic CO₂ reduction by TiO₂ and related titanium containing solids. *Energy & Environmental Science* **2012**, *5* (11), 9217-9233.
336. Ikeue, K.; Yamashita, H.; Anpo, M.; Takewaki, T., Photocatalytic Reduction of CO₂ with H₂O on Ti-β Zeolite Photocatalysts: Effect of the Hydrophobic and Hydrophilic Properties. *The Journal of Physical Chemistry B* **2001**, *105* (35), 8350-8355.

337. Tseng, I. H.; Chang, W.-C.; Wu, J. C. S., Photoreduction of CO₂ using sol-gel derived titania and titania-supported copper catalysts. *Applied Catalysis B: Environmental* **2002**, *37* (1), 37-48.
338. Wu, J. C. S.; Lin, H.-M.; Lai, C.-L., Photo reduction of CO₂ to methanol using optical-fiber photoreactor. *Applied Catalysis A: General* **2005**, *296* (2), 194-200.
339. Wu, J. C. S., Photocatalytic Reduction of Greenhouse Gas CO₂ to Fuel. *Catalysis Surveys from Asia* **2009**, *13* (1), 30-40.
340. Kočí, K.; Obalová, L.; Matějová, L.; Plachá, D.; Lacný, Z.; Jirkovský, J.; Šolcová, O., Effect of TiO₂ particle size on the photocatalytic reduction of CO₂. *Applied Catalysis B: Environmental* **2009**, *89* (3), 494-502.
341. Liu, L.; Zhao, H.; Andino, J. M.; Li, Y., Photocatalytic CO₂ Reduction with H₂O on TiO₂ Nanocrystals: Comparison of Anatase, Rutile, and Brookite Polymorphs and Exploration of Surface Chemistry. *ACS Catalysis* **2012**, *2* (8), 1817-1828.
342. Zhao, H.; Liu, L.; Andino, J. M.; Li, Y., Bicrystalline TiO₂ with controllable anatase-brookite phase content for enhanced CO₂ photoreduction to fuels. *Journal of Materials Chemistry A* **2013**, *1* (28), 8209-8216.
343. Mele, G.; Annese, C.; De Riccardis, A.; Fusco, C.; Palmisano, L.; Vasapollo, G.; D'Accolti, L., Turning lipophilic phthalocyanines/TiO₂ composites into efficient photocatalysts for the conversion of CO₂ into formic acid under UV-vis light irradiation. *Applied Catalysis A: General* **2014**, *481*, 169-172.
344. Li, K.; Gao, S.; Wang, Q.; Xu, H.; Wang, Z.; Huang, B.; Dai, Y.; Lu, J., In-Situ-Reduced Synthesis of Ti³⁺ Self-Doped TiO₂/g-C₃N₄ Heterojunctions with High Photocatalytic Performance under LED Light Irradiation. *ACS Applied Materials & Interfaces* **2015**, *7* (17), 9023-9030.
345. Zhu, H.; Chen, D.; Yue, D.; Wang, Z.; Ding, H., In-situ synthesis of g-C₃N₄-P25 TiO₂ composite with enhanced visible light photoactivity. *Journal of Nanoparticle Research* **2014**, *16* (10), 2632.
346. Dilla, M.; Schlögl, R.; Strunk, J., Photocatalytic CO₂ Reduction Under Continuous Flow High-Purity Conditions: Quantitative Evaluation of CH₄ Formation in the Steady-State. *ChemCatChem* **2017**, *9* (4), 696-704.